UNIVERSITY OF OXFORD

Characterisation of novel cardiac and skeletal ion channels on intracellular Ca^{2+} stores.

THESIS SUBMITTED FOR THE AWARD OF A DPHIL IN CARDIOVASCULAR SCIENCE

DAVID RICHARD EBERHARDT

HERTFORD COLLEGE

Word count: 41602

Abstract

Excitation-contraction (EC) coupling is the process by which Ca^{2+} is released from the sarcoplasmic reticulum (SR) and is fundamental to cardiac and skeletal muscle function. The SR contains many uncharacterised ion channels and proteins which may influence EC coupling and in this thesis I have investigated the biophysical properties of some of these channels.

I have demonstrated that the single-channel gating and conducting properties of SR K^+ channels from various mammalian species (rabbit, sheep and mouse) are very similar. I investigated the actions of possible physiological regulators of these channels and demonstrated that luminal Ca^{2+} and Mg^{2+} can block K^+ flux in a voltage-dependent manner, while luminal Ca^{2+}, Ni^{2+}, and alkaline pH can reduce Po by additional mechanisms. I also characterised the single-channel properties of the various SR anion channels that are observed after incorporating mammalian SR vesicles into artificial membranes.

The trimeric intracellular cation channels (TRIC-A and TRIC-B) and Mitsugumin 23 (MG23) are suggested to be SR cation channels. I have therefore utilised *Tric-a* KO and *Mg23* KO mice to study SR membranes devoid of TRIC-A and MG23. Additionally, I have begun to investigate the single-channel properties of purified *c. elegans* TRIC-B1 and human TRIC-A. I found that SR K^+ channel function was altered in SR from *Tric*-a KO or *Mg23* KO tissue, however the underlying mechanisms for the observed changes appear to be complex. My initial studies of the purified TRIC-A and TRIC-B proteins show that they are permeable to K^+, Ca^{2+}, choline, and Cl^-, properties which deviate from those of SR K^+ channels from rabbit, mouse and sheep. This may reflect species differences or alterations to protein function caused during the purification process or that SR K^+ channels remain an unidentified class of ion channel.

Acknowledgments

I would like convey my sincerest gratitude my supervisor, Professor Rebecca Sitsapesan, for providing me the opportunity to undertake this DPhil. I would like to thank her for all her hard work in mentoring me and helping me with the writing of this thesis. I would also like to convey my thanks to the members of the Sitsapesan group for their help in this project and for their friendship and for the entertaining coffee breaks. Special thanks should go to Dr Elisa Venturi, Dr Fiona O'Brien and Dr Sam El-Ajouz for the experimental data which they provided to this thesis.

I would also like to thank our collaborators in the Takashima laboratory for their provision of the CHO cells over-expressing TRIC-A, and *Tric-a* KO and *Mg23* KO mouse tissue. Thanks also to our collaborators in the Zhenfeng Liu laboratory (Laboratory of Protein and Peptide Pharmaceuticals &Laboratory of Proteomics, Institute of Biophysics, Chinese Academy of Sciences, Beijing 100101, China) for the provision of their *c. elegans* TRIC-B1 protein preparations and to the Carpenter laboratory (Structural Genomics Consortium, University of Oxford, UK), especially to Simon Bushell, for their work in purifying the human TRIC-A protein. Additionally, I would like to thank the members of the Galione laboratory, especially to Lianne Davis, for their support in the TPC2 arm of this project which unfortunately was not completed in time for use in this thesis.

I would like to thank my wonderful wife, Emma, for contending with me through the stress of writing this thesis. You are my best friend and the love of my life. Even in the darkest days, you never fail to put a smile on my face. I look forward to many wonderful years of marriage. Thanks also to all of my family, especially to my parents, Martin and Lynette, for their support and unconditional love.

"It is the glory of God to conceal a thing: but the honour of kings is to search out a matter." Proverbs 25v2 (KJV).

Glory to God who is my Creator and my Saviour.

Author declaration

I declare that the work in this dissertation was carried out in accordance with the requirements of the University's Regulations and Code of Practice for Research Degree Programmes and that it has not been submitted for any other academic award. Except where indicated by specific reference in the text, the work is the candidate's own work. Work done in collaboration with, or with the assistance of, others, is indicated as such. Any views expressed in the dissertation are those of the author.

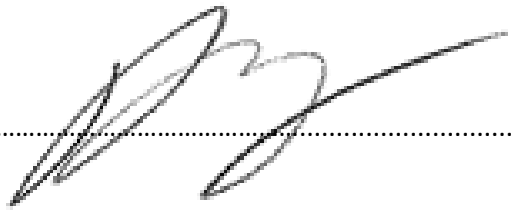
SIGNED……  DATE **31/05/18**

Table of contents

Chapter 1. Introduction 1

1.1 Ca^{2+} 1

1.2 EC-coupling 1

1.2.1 EC-coupling in skeletal muscle 2

1.2.2 EC-coupling in cardiac muscle 2

1.3 Proteins involved in EC-coupling 4

1.3.1 The ryanodine receptor 4

1.3.2 Structural proteins of the triads and dyads 4

1.3.3 ATPase proteins 4

1.4 The need for a countercurrent 5

1.4.1 SR K^+ channels 8

1.4.1.1 Trimeric intracellular cations (TRIC) channels 10

1.4.2 SR Cl^- channels 22

1.4.2.1 SR Cl^- channels observed in the bilayer 22

1.4.2.2 Cl^- channels identified as present in the SR 25

1.4.3 Non-selective SR ion channels 28

1.4.3.1 Mitsugumin23 (MG23) 28

1.5 Aims of this thesis 31

Chapter 2. General methods 33

2.1 Method for isolation of light SR, heavy SR and mixed membrane fractions 34

2.1.1 Collection of animal tissue 34

2.1.1.1 Sheep cardiac tissue 34

2.1.1.2 Rabbit skeletal muscle 34

2.1.1.3 Mouse cardiac and skeletal muscle 35

2.1.2 Collection of cells for membrane preparations 35

2.1.2.1 CHO cells 35

2.1.3 Heavy SR (HSR), light SR (LSR) and “mixed membrane” isolation procedure from mammalian tissue 36

2.1.4 Isolation of HSR and LSR from cell cultures 39

2.2 Measurement of protein concentration 41

2.3 The planar lipid bilayer technique 41

2.3.1 The bilayer apparatus 42

2.3.2 Electrical equipment used for experimentation and data acquisition 44

2.4 Forming an artificial bilayer 47

2.4.1 Lipids 47

2.4.2 Priming 47

2.4.3 Painting an artificial bilayer 47

2.4.4 Thinning of the bilayer 48

2.4.5 The voltage clamp technique 48

2.4.6 Bilayer detection and estimate of the area 49

2.5 Incorporating liposomes containing native or recombinant protein 51

2.5.1 Fusion events 51

2.5.2 Incorporation of native SR vesicles 54

2.6 Solutions used in planar lipid bilayer experiments 55

2.6.1 Choosing the right ion 55

2.6.2 Typical electrophysiological bath solutions used in this thesis 56

2.6.3 Liquid Junction potentials 57

2.7 Protocol for the study of proteins in the bilayer system 59

2.7.1 Native membranes 59

2.7.1.1 The SR K^+ channel and the RyR1 and RyR2 proteins 59

2.7.1.2 The Sarcoplasmic Reticulum Anion Selective (SRAS) channel 60

2.7.1.3 The Sarcoplasmic Reticulum Anion Leak (SRAL) channel 60

2.7.2 Purified TRIC-A and TRIC-B 60

2.7.2.1 KCl experiments 60

2.7.2.2 Choline-Cl experiments 61

2.8 Measuring the pH of solutions 61

2.9 Measurement of free [Ca^{2+}] 61

2.10 Analysis of single-channel recordings 61

2.10.1 Data acquisition 61

2.10.2 Single-channel analysis 62

2.10.2.1 Single-channel conductance 63

2.10.2.1.1 Relative permeability 65

2.10.2.2 Open probability calculations for the SR K^+ channel 67

2.10.2.3 Modelling the SR K^+ channel and idealisation 68

2.10.2.4 Open probability 72

2.10.2.5 Analysis of multiple SR K^+ channels gating in the bilayer 72

2.10.2.6 Noise analysis 74

2.10.2.7 Log-Likelihood ratio tests 75

2.11 Chemical compounds 76

2.12 Statistics 76

Chapter 3. Properties of the SR K^+ channel 77

3.1 Introduction 78

3.2 Results 79

3.2.1 Species differences in SR K^+ channel gating 79

3.2.2 Finding a ligand for the SR K^+ channel 86

3.2.3 Ca^{2+} as a ligand of the SR K^+ channel 86

3.2.3.1 The SR K^+ channel in low [Ca^{2+}] 86

3.2.3.2 The effect of increasing luminal [Ca^{2+}] on SR K^+ channel function 94

3.2.3.3 The effect of increasing cytosolic [Ca^{2+}] on SR K^+ channel function 104

3.2.3.4 The effect of increasing symmetrical [Ca^{2+}] on SR K^+ channel function 109

3.2.4 Mg^{2+} as a ligand of the SR K^+ channel 113

3.2.5 Ni^{2+} as a ligand of the SR K^+ channel 128

3.2.6 ATP as a ligand of the SR K^+ channel 132

3.2.7 Effect of high pH on the SR K^+ channel 136

3.3 Discussion 141

3.3.1 Gating differences between mammalian SR K^+ channel isoforms 141

3.3.2 Pharmacological properties of the SR K^+ channel 142

Chapter 4. SR Cl^- channels 145

4.1 Introduction 146

4.2 Results 146

4.2.1 The different flavours of SR Cl- channels 146

4.2.2 The SR anion-selective (SRAS) channel 149

4.2.3 The SR anion leak (SRAL) channel 157

4.2.4 The Type 3 SR Cl^- channel 164

4.3 Discussion 166

4.3.1 SRAS channels 166

4.3.2 SRAL channels 170

4.3.3 The Type 3 SR Cl^- channel 173

Chapter 5. TRIC-A proteins from native membranes 174

5.1 Introduction 175

5.2 Results 176

5.2.1 The study of CHO cell membranes over-expressing human TRIC-A 176

5.2.2 SR ion channels in *Tric-a* KO tissue 178

5.2.3 SR K^+ channels from *Tric-a* KO tissue 178

5.2.3.1 Studying the gating of multiple SR K^+ channels gating in bilayers 190

5.2.4 The RyR1 channel in *Tric-a* KO tissue 198

5.2.5 +SR Cl^- currents *Tric-a* KO mice 202

5.3 Discussion 206

Chapter 6. Purified TRIC-A and TRIC-B proteins 213

6.1 Introduction 214

6.2 Results 215

6.2.1 The study of reconstituted *c. elegans* TRIC-B1 protein 215

6.2.1.1 Initial experiments: The four channels 215

6.2.1.2 The type I channel 215

6.2.1.3 The type II channel 221

6.2.1.4 The Type III channel 226

6.2.1.5 The Type IV channel 228

6.2.2 Which Channel Type is the *c. elegans* TRIC-B1 channel? 230

6.2.3 Control liposome studies 230

6.2.4 Extruded liposomes 232

6.2.5 Similarity to native SR channels 233

6.2.5.1 Similarities to other native proteins 238

6.2.6 Properties of the type I protein 238

6.2.6.1 Further permeability studies 238

6.2.6.2 Modelling the gating of the *c. elegans* TRIC-B1 protein 241

6.2.6.3 An alternative mechanism for *c. elegans* TRIC-B1 channel gating 243

6.2.6.4 Pharmacological evidence for the existence of sub-conductance unresolved fast gating 249

6.2.7 The purified human TRIC-A protein 253

6.2.7.1 Permeability properties of the human TRIC-A protein 253

6.2.8 A comparison of the *c. elegans* TRIC-B1 and human TRIC-A channels 258

6.3 Discussion 263

6.3.1 Permeability of the Type I channel/*c. elegans* TRIC-B1 264

6.3.2 Gating of the *c. elegans* TRIC-B1 channel 269

6.3.3 Comparison to published data 270

6.3.4 Is TRIC responsible for SR K^+ channel currents? 272

6.4 Further experiments 272

Chapter 7. SR channels from *Mg23* KO mouse tissue 274

7.1 Introduction 275

7.2 Results 277

7.2.1 SR K^+ channel from *Mg23* KO mice 277

7.2.2 The SR K^+ channel from *Mg23* KO tissue gates in a cooperative manner 285

7.2.3 RyR1 channels from *Mg23* KO mice 289

7.2.4 Cl^- currents from *Mg23* KO mice 289

7.2.5 The effect of the cytotoxic small molecule, C-6, on SR ion channels 293

7.2.6 pH may be an activator of MG23 296

7.3 Discussion 299

Chapter 8. Conclusions 301

Table of Figures

Figure 1.1. A schematic of EC-coupling in mammalian cardiac muscle 3

Figure 1.2. Schematic of the SR during Ca^{2+} release showing the two proposed pathways for a countercurrent 7

Figure 1.3. Gating of the mouse skeletal SR K^{+} channel, adapted from Matyjaszkiewicz *et al.* (2015) [104] 10

Figure 1.4. Predictions for the structure of TRIC from EM images taken from Yazawa *et al.* 2007 [81] 13

Figure 1.5. The TRIC family of proteins adapted from Silverio and Saier, Jr (2011) [114] 15

Figure 1.6. Sequence alignment for the various identified TRIC structures and Human TRIC for comparison 18

Figure 1.7. The structure of the *c. elegans* TRIC-B1/B2 channel and the monomeric pore region adapted from Yang *et al.* (2016) [112] 19

Figure 1.8. Current-fluctuations through the *c. elegans* TRIC-B1 channel adapted from Yang *et al.* (2016) [112] 21

Figure 1.9. The effect of Ca^{2+} on *c. elegans* TRIC- B1/B2 protein structure, adapted from Yang *et al.* (2016) [112] 22

Figure 1.10. SR Cl^{-} channels observed in artificial bilayers 24

Figure 1.11. The BCl and SCl channel taken from Kourie *et al*. (1996) [121] 25

Figure 1.12. Identified SR Cl^- channels 27

Figure 1.13. The proposed shape of MG23 in its fully constructed (left) and monomeric (right) form taken from Venturi *et al.* (2011) [165] 30

Figure 2.1. Schematic illustration of 20-40 % sucrose density gradient and LSR/HSR collection 38

Figure 2.2. Schematic illustration of 1.1 M-1.6 M sucrose density gradient and LSR/HSR collection .. 40

Figure 2.3. Schematic of the block and cup apparatus. 43

Figure 2.4. A schematic of the electrical equipment used for data acquisition during planar lipid bilayer experiments. 46

Figure 2.5. Schematic showing examples of Current-fluctuations through unfiltered traces when ion channels incorporate into the bilayer 53

Figure 2.6. A schematic illustration of the cis and trans chambers showing the contributing factors to a liquid junction potential. 57

Figure 2.7. A schematic of a current-voltage relationship 65

Figure 2.8. Assigning the levels to the model for use in idealisation 70

Figure 2.9. Gaussian curves fitted to an amplitude-histogram in QuB 71

Figure 2.10. Current-fluctuations showing single and multiple SR K^+ channels gating in the bilayer .. 73

Figure 3.1. Comparison of gating of various mammalian SR K^+ channels 81

Figure 3.2. Po of the various mammalian SR K^+ channels 84

Figure 3.3. Comparison of the single-channel conductance of various mammalian SR K^+ channels 86

Figure 3.4. The SR K^+ channel from sheep cardiac muscle and rabbit skeletal muscle in low free [Ca^{2+}] 89

Figure 3.5. The effect of lowering Ca^{2+} on sheep cardiac and rabbit skeletal SR K^+ channel function . 93

Figure 3.6. The mouse skeletal SR K^+ channel in the presence of increasing luminal [Ca^{2+}]..... 95

Figure 3.7. The effect of increasing luminal [Ca^{2+}] on the Po of mouse skeletal SR K^+ channels..... 98

Figure 3.8. Single-channel event analysis of mouse skeletal SR K^+ channels with increasing luminal [Ca^{2+}] 102

Figure 3.9. Block of the mouse skeletal SR K^+ channel by 5 mM *trans* Ca^{2+}..... 103

Figure 3.10. The mouse skeletal SR K^+ channel in the presence of increasing cytosolic [Ca^{2+}]..... 105

Figure 3.11. The effect of increasing cytosolic [Ca^{2+}] on the single-channel properties of mouse skeletal SR K^+ channels 108

Figure 3.12. The mouse skeletal SR K^+ channel in the presence of increasing symmetrical [Ca^{2+}]..... 110

Figure 3.13. The effect of increasing symmetrical [Ca^{2+}] on the Po of mouse skeletal SR K^+ channels 112

Figure 3.14. The mouse skeletal SR K^+ channel in the presence of increasing luminal [Mg^{2+}] 115

Figure 3.15. The effect of increasing luminal [Mg^{2+}] on the Po of mouse skeletal SR K^+ channels..... 117

Figure 3.16. The mouse skeletal SR K^+ channel in the presence of increasing cytosolic [Mg^{2+}] 118

Figure 3.17. The effect of increasing cytosolic [Mg^{2+}] on the Po of mouse skeletal SR K^+ channels... 120

Figure 3.18. The mouse skeletal SR K^+ channel in the presence of increasing symmetrical [Mg^{2+}] ... 121

Figure 3.19. The effect of increasing symmetrical [Mg^{2+}] on the Po of mouse skeletal SR K^+ channels 123

Figure 3.20. The effect of Mg^{2+} on the current-voltage relationships of mouse skeletal muscle SR K^+ channels 125

Figure 3.21. A comparison of the current-voltage relationships for mouse skeletal SR K^+ channels in the presence of 5 mM Ca^{2+} and 5 mM Mg^{2+} 126

Figure 3.22. The pore of the mouse skeletal muscle SK K^+ channel is impermeable to Mg^{2+} 127

Figure 3.23. The mouse skeletal SR K^+ channel in the presence of 0.5 mM luminal [Ni^{2+}] 129

Figure 3.24. The effect of 0.5 mM luminal [Ni^{2+}] on the Po of mouse skeletal SR K^+ channels 131

Figure 3.25. The sheep cardiac SR K^+ channel in the presence of 1 mM cytosolic Na-ATP 133

Figure 3.26. The effect of 1 mM cytosolic Na-ATP on the single-channel properties of sheep cardiac SR K^+ channels 135

Figure 3.27. The mouse skeletal SR K^+ channel in the presence cytosolic pH 9.2 137

Figure 3.28. The effect of cytosolic pH 9.2 on the single-channel properties of mouse skeletal SR K^+ channels 139

Figure 3.29. The effect of cytosolic pH 9.2 on voltage sensitivity of mouse skeletal SR K^+ channels 140

Figure 3.30. A schematic of the proposed Ca^{2+} inhibition of the SR K^+ channel during diastole (left) and systole (right) 143

Figure 4.1. Cl^- channel currents observed in the rabbit HSR 149

Figure 4.2. The SRAS channel from sheep cardiac muscle 151

Figure 4.3. Sheep cardiac SRAS channel amplitude-histograms 152

Figure 4.4. The SRAS channel from mouse skeletal muscle 154

Figure 4.5. Mouse skeletal SRAS channel amplitude-histograms 155

Figure 4.6. Current-voltage relationships for the SRAS channel 156

Figure 4.7. Current-fluctuations through the mouse skeletal SRAL channel. 159

Figure 4.8. Current-voltage relationships for the SRAL channel in choline-chloride 160

Figure 4.9. Current-voltage relationships for the SRAL channel in NMDG-Chloride 161

Figure 4.10. Current-voltage relationships of the SRAL channel with increasing ionic concentrations 162

Figure 4.11. Conductance-concentration relationships of the SRAL channel 163

Figure 4.12. Current-fluctuations through the Type 3 SR Cl^- channel observed in the rabbit skeletal SR 165

Figure 4.13. A schematic showing a current-voltage relationship of a Cl^--selective channel in asymmetrical solutions with 600 mM Cl^- in the *cis* chamber and 0 mM Cl^- in the *trans* chamber 168

Figure 4.14. Examples of gating of the SRAS channel and a Cl^--selective channel observed in previous studies 169

Figure 4.15. A comparison of the SCl and SRAS channels adapted from by Kourie *et al.* in 1996 [120] 170

Figure 4.16. Current-fluctuations through the SRAL channel and the BCl channel adapted from Kourie *et al.* 1996 [121] 172

Figure 5.1. Current-fluctuations through a possible TRIC-A channel 178

Figure 5.2. Current-fluctuations through SR K^+ channels from WT and *Tric-a* KO mouse skeletal muscle 181

Figure 5.3. Current-fluctuations through SR K^+ channels from WT and *Tric-a* KO mouse cardiac muscle 182

Figure 5.4. Single-channel properties of SR K^+ channels from WT and *Tric-a* KO mouse skeletal and cardiac muscle..... 184

Figure 5.5. A comparison of the single-channel properties of the SR K^+ channel from WT and *Tric-a* KO mouse skeletal muscle 187

Figure 5.6. Examples of current-fluctuations through SR K^+ channels from WT and *Tric-a* KO mouse skeletal muscle..... 188

Figure 5.7. Event analysis of SR K^+ channels from WT and *Tric-a* KO mouse skeletal muscle 189

Figure 5.8. The spread of data for the Po_{total} of SR K^+ channels from WT and *Tric-a* KO mice 190

Figure 5.9. Representative channel recordings showing a single SR K^+ channel gating in the bilayer (A) and multiple channels gating in the bilayer (B)..... 193

Figure 5.10. The Po of single and multiple SR K^+ channels from WT and *Tric-a* KO skeletal muscle . 194

Figure 5.11. The Po of SR K^+ channels as a function of the number of channels gating in the bilayer 195

Figure 5.12. The binomial statistical prediction for three SR K^+ channels gating in the bilayer 196

Figure 5.13. A comparison of experimental data to the binomial statistical prediction 198

Figure 5.14. Mg^{2+} inhibition of RyR1 channels from WT and *Tric-a* KO tissue 200

Figure 5.15. Effect of PKA-dependent phosphorylation on the Ca^{2+}-dependence of gating of RyR1 from WT and *Tric-a* KO mice 202

Figure 5.16 Representative recordings of SR Cl^-/SRAL channel currents observed in *Tric-a* KO tissue 204

Figure 5.17. Permeability properties of SRAL channels from WT and *Tric-a* KO mouse skeletal muscle 205

Figure 5.18. Sequence alignment of mouse TRIC-A and TRIC-B showing sequence similarities 208

Figure 5.19. The SR membrane in WT and *Tric-a* KO tissue adapted from El-Ajouz *et al.* (2017)[197] 210

Figure 5.20. A schematic of proposed crowding of ion channels in the WT SR membrane 211

Figure 6.1. Current-fluctuations through the type I channel 218

Figure 6.2. The permeability properties of the type I channel 221

Figure 6.3. Current-fluctuations through the type II channel 222

Figure 6.4. Permeability properties of the type II channel 225

Figure 6.5. The type III channel 227

Figure 6.6. The type IV channel 229

Figure 6.7 Current-fluctuations through the channels observed in control empty liposomes at ±30 mV 231

Figure 6.8. A schematic showing the state of liposomes before extrusion (left) and after extrusion (right) through a 400 nM membranes 232

Figure 6.9 Native SR K^+ channel from sheep cardiac muscle 234

Figure 6.10. Native SR K^+ channel from mouse skeletal 235

Figure 6.11. A sequence alignment of the TRIC-B protein 237

Figure 6.12 Current-fluctuations through the *c. elegans* TRIC-B1channel 240

Figure 6.13. The 5-state model of *c. elegans* TRIC-B1 gating 242

Figure 6.14. A simplified schematic showing how a single-channel recording and a amplitude histogram would appear if an ion channel with three identical pores were gating in the bilayer 243

Figure 6.15. The 4-state model of *c. elegans* TRIC-B1 gating 244

Figure 6.16. The 7-state model of *c. elegans* TRIC-B1 gating 246

Figure 6.17. The native TRIC channel from mouse skeletal muscle 248

Figure 6.18. The effect of decamethonium on the *c. elegans* TRIC-B1 channel 251

Figure 6.19. The effect of decamethonium on the mouse skeletal SR K^+ channel 252

Figure 6.20. Current-fluctuations through the human TRIC-A channel 255

Figure 6.21. The permeability properties of the human TRIC-A channel 257

Figure 6.22. Current-fluctuations through the *c. elegans* TRIC-B1 channel and the human TRIC-B channel 259

Figure 6.23. A comparison of the biophysical properties of the *c. elegans* TRIC-B1 and the human TRIC-A channels 263

Figure 6.24. Current-voltage relationships for the *c. elegans* TRIC-B1 channel in KCl and choline-chloride showing the shift from symmetrical solutions (red) to asymmetrical solutions (blue)..... 265

Figure 6.25. A schematic of how decamethonium block could alter the channel behaviour of the TRIC-B1 channel 270

Figure 6.26. Published electrophysiological data of TRIC channels..... 271

Figure 7.1. Current-fluctuations through purified MG23 channels..... 276

Figure 7.2. The SR K^+ channel from *Mg23* KO mouse skeletal muscle..... 280

Figure 7.3. Gating properties of the SR K^+ channel from WT and *Mg23* KO tissue..... 281

Figure 7.4. The gating properties of the mouse skeletal muscle SR K^+ channel from WT and *Mg23* KO mice..... 283

Figure 7.5. Event analysis of SR K^+ channels from WT and *Mg23* KO mouse skeletal muscle..... 284

Figure 7.6. The Po of the SR K^+ channel as a function of the number of channels gating in the bilayer 286

Figure 7.7 The binomial statistical prediction for three SR K^+ channels gating in the bilayer 287

Figure 7.8. A comparison of experimental data to the binomial statistical prediction 288

Figure 7.9. RyR1 channels from WT and *Mg23* KO tissue..... 290

Figure 7.10. Representative recordings of SR Cl^- currents observed in *Mg23* KO tissue..... 291

Figure 7.11. Permeability properties of SR Cl^- currents from WT and *Mg23* KO mouse skeletal muscle 292

Figure 7.12. The structure of C-6 293

Figure 7.13. The effect of C-6 on the RyR1 channel. 296

Figure 7.14. The effect of pH 9.2 on membranes containing SR proteins from *Mg23* KO mice and WT mice 298

Publication list

Full papers

D. Eberhardt and R. Sitsapesan, Connecting Two-Pore Channel Structure with Single-channel Permeability Measurements, Messenger, vol. 4, no. 1, pp. 34–45, 2015.

S. El-Ajouz, E. Venturi, K. Witschas, M. Beech, AD. Wilson, C. Lindsay, **D. Eberhardt**, F. O'Brien, T. Iida, M. Nishi, H. Takeshima, R. Sitsapesan. Dampened activity of ryanodine receptor channels in mutant skeletal muscle lacking TRIC-A, J Physiol, 595(14):4769-4784, 2017.

Published abstracts

Katja Witschas, Fiona O'Brien, Elisa Venturi, Sam El-Ajouz, Matthew Beech, **David Eberhardt**, Tsunaki Iida, Miyuki Nishi, Hiroshi Takeshima, Rebecca Sitsapesan (2016), Dampened activity of single ryanodine receptor channels in mice devoid of TRIC-A, Biophysical society annual meeting 2016 (Los Angeles, CA, USA). Biophysical Journal vol: 110 (3) pp: 266a.

David Eberhardt, Fiona O'Brien, Elisa Venturi, Katja Witschas, Sam El-Ajouz, Tsunaki Iida, Miyuki Nishi, Hiroshi Takeshima & Rebecca Sitsapesan. (2016), Cardiac and skeletal sarcoplasmic reticulum K^+ channels from TRIC-A knockout mice show distinct gating characteristics to those derived from wild type mice, Physiology 2016 (Dublin, Ireland), Proc Physiol Soc 37, PCA054.

Fiona O'Brien, **David Eberhardt**, Elisa Venturi, Elena Galfre, Sam El-Ajouz, Tsunaki Iida, Miyuki Nishi, Hiroshi Takeshima & Rebecca Sitsapesan (2016) SR K^+ channels from TRIC-A knockout mice gate in a cooperative manner, Physiology 2016 (Dublin, Ireland), Proc Physiol Soc 37, PCB094

K. Witschas, S. El-Ajouz, E. Venturi, M. Beech, F. O'Brien, **D. Eberhardt**, T. Iida, M. Nishi, H. Takeshima, R. Sitsapesan (2016) Single ryanodine receptor channels from the skeletal muscle of

TRIC-A knockout mice show reduced activation by Mg^{2+}ATP, Physiology 2016 (Dublin, Ireland), Proc Physiol Soc 37, PCA051

Poster presentations

David Eberhardt, Rebecca Sitsapesan, (2015), Divalent cation concentration regulates the activity of the cardiac sarcoplasmic reticulum K^+ channel. BHF 4-year DPhil day 2014, (Manchester, UK).

David Eberhardt, Fiona O'Brien, Elisa Venturi, Katja Witschas, Sam El-Ajouz, Tsunaki Iida, Miyuki Nishi, Hiroshi Takeshima & Rebecca Sitsapesan. (2016), Cardiac and skeletal sarcoplasmic reticulum K^+ channels from TRIC-A knockout mice show distinct gating characteristics to those derived from wild type mice, Physiology 2016 (Dublin, Ireland), Proc Physiol Soc 37, PCA054. (**Published and shown above**).

David Eberhardt, Fiona O'Brien, Elisa Venturi, Katja Witschas, Sam El-Ajouz, Tsunaki Iida, Miyuki Nishi, Hiroshi Takeshima & Rebecca Sitsapesan. Sarcoplasmic reticulum K^+ channels from TRIC-A knockout mice show distinct gating characteristics to those derived from wild type mice. Oxion, 2016 (Oxford, UK).

David Eberhardt, Fiona O'Brien, Elisa Venturi, Tsunaki Iida, Miyuki Nishi, Hiroshi Takeshima & Rebecca Sitsapesan (2017), Distinct gating characteristics of sarcoplasmic reticulum K^+ channels from *Tric-a* knockout mice, GRC meeting on Excitation-contraction coupling, 2017 (Les Diablerets, Switzerland).

Table of contribution

Figure number	Contributor(s)	Work contributed
Figure 3.2	Dr Elisa Venturi	2 recordings of SR K^+ channels from sheep cardiac muscle at +30 mV.
	Dr Fiona O'Brien	21 recordings of SR K^+ channels from mouse skeletal muscle at ±30 mV.
Figure 2.3	Dr Elisa Venturi	2 recordings of SR K^+ channels from sheep cardiac muscle at +30 mV.
	Dr Fiona O'Brien	21 recordings of SR K^+ channels from mouse skeletal muscle at ±30 mV.
Figure 5.4	Dr Elisa Venturi	2 recordings of SR K^+ channels from WT sheep cardiac muscle at +30 mV.
	Dr Fiona O'Brien	8 recordings of SR K^+ channels from WT mouse skeletal muscle and 18 recordings of SR K^+ channels from *Tric-a* KO mouse skeletal muscle at ±30 mV.
Figure 5.5	Dr Fiona O'Brien	8 recordings of SR K^+ channels from WT mouse skeletal muscle and 18 recordings of SR K^+ channels from *Tric-a* KO mouse skeletal muscle at ±30 mV.
Figure 5.7	Dr Fiona O'Brien	8 recordings of SR K^+ channels from WT mouse skeletal muscle and 18 recordings of SR K^+ channels from *Tric-a* KO mouse skeletal muscle at ±30 mV.
Figure 5.10	Dr Fiona O'Brien	Single-channels: 8 recordings of SR K^+ channels from WT mouse skeletal muscle and 18 recordings of SR K^+ channels from *Tric-a* KO mouse skeletal muscle at ±30 mV. Multiple channels: 13 recordings of SR K^+ channels from WT mouse skeletal muscle and 14 recordings of SR K^+ channels from *Tric-a* KO mouse skeletal muscle at ±30 mV.
Figure 5.11	Dr Fiona O'Brien	1 channel: 8 recordings of SR K^+ channels from WT mouse skeletal muscle and 18 recordings of SR K^+ channels from *Tric-a* KO mouse skeletal muscle at ±30 mV. 2 channels: 10 recordings of SR K^+ channels from WT mouse skeletal muscle and 9 recordings of SR K^+ channels from *Tric-a* KO mouse skeletal muscle at ±30 mV. 3 channels: 3 recordings of SR K^+ channels from WT mouse skeletal muscle and 5 recordings of SR K^+ channels from *Tric-a* KO mouse skeletal muscle at ±30 mV.
Figure 5.12	Dr Fiona O'Brien	1 channel: 8 recordings of SR K^+ channels from WT mouse skeletal muscle and 18 recordings of SR K^+ channels from *Tric-a*

		KO mouse skeletal muscle at ±30 mV. 2 channels: 10 recordings of SR K^+ channels from WT mouse skeletal muscle and 9 recordings of SR K^+ channels from *Tric-a* KO mouse skeletal muscle at ±30 mV. 3 channels: 3 recordings of SR K^+ channels from WT mouse skeletal muscle and 5 recordings of SR K^+ channels from *Tric-a* KO mouse skeletal muscle at ±30 mV.
Figure 5.13	Dr Fiona O'Brien	1 channel: 8 recordings of SR K^+ channels from WT mouse skeletal muscle and 18 recordings of SR K^+ channels from *Tric-a* KO mouse skeletal muscle at ±30 mV. 2 channels: 10 recordings of SR K^+ channels from WT mouse skeletal muscle and 9 recordings of SR K^+ channels from *Tric-a* KO mouse skeletal muscle at ±30 mV. 3 channels: 3 recordings of SR K^+ channels from WT mouse skeletal muscle and 5 recordings of SR K^+ channels from *Tric-a* KO mouse skeletal muscle at ±30 mV.
Figure 5.14	Dr Elisa Venturi	6 recordings of ryanodine receptors from WT mouse skeletal muscle and 10 recordings of ryanodine receptors from *Tric-a* KO mouse skeletal muscle at +30 mV.
	Dr Sam El-Ajouz	6 recordings of ryanodine receptors from WT mouse skeletal muscle and 9 recordings of ryanodine receptors from *Tric-a* KO mouse skeletal muscle at +30 mV.
Figure 5.15	Dr Elisa Venturi	8 recordings of ryanodine receptors from WT mouse skeletal muscle and 8 recordings of ryanodine receptors from *Tric-a* KO mouse skeletal muscle at +30 mV.
	Dr Sam El-Ajouz	2 recordings of ryanodine receptors from WT mouse skeletal muscle and 2 recordings of ryanodine receptors from *Tric-a* KO mouse skeletal muscle at +30 mV.

Table of abbreviations

ADP	Adenosine diphosphate
ATP	Adenosine triphosphate
BCl	'Big' Cl^- channel
BSA	Bovine Serum Albumin
C. Elegans	*Caenorhabditis elegans*
CAM	Calmodulin
CF	Cystic fibrosis
CFTR	Cystic fibrosis transmembrane conductance regulator
CHO	Chinese hampster ovary
CICR	Ca^{2+}-induced Ca^{2+}-release
CLIC	Phloride intracellular channel
Cp	*Colwellia psychrerythraea*
DHPR	Dihydropyridine receptors (L-type Ca^{2+} channels)
DIDS	4,4'-Diisothiocyano-2,2'-stilbenedisulfonic acid
DM	n-Decyl-beta-D-maltopyranoside
DTT	Dithiothreitol
EC-coupling	Excitation-contraction coupling
EGTA	ethylene glycol-bis(β-aminoethyl ether)-N,N,N',N'-tetraacetic acid)
EM	Electron microscopy
ER	Endoplasmic reticulum
GST	Glutathione S-transferase
HEPES	N'-2-hydroxethylpiperazine-N'-2-ethanesulphonic acid
HSR	'Heavy' sarcoplasmic reticulum
KO	Knock-out
LSR	'Light' sarcoplasmic reticulum
MG23	Mitsugumin23
MG29	Mitsugumin29
MM	Mixed membrane
NCX	Na^+/Ca^{2+} exchanger
NMDG	N-Methyl-D-glucamin
NPPB	Nitro-2-(3-phenylpropylamino)benzoic acid
PE	Phosphatidylethanolamide
PI(4,5)P2	Phosphatidylinositol4,5-bisphosphate
PIPES	Piperazine-N,N'-bis [ethanesulfonic acid]
PKA	Protein Kinase type A
PMCA	Plasma membrane Ca^{2+}-ATPase
PMSF	Phenylmethylsulfonyl fluoride
Po	Open probability
PoFull	Open probability of the fully open channel level
PoSub	Open probability of the sub-conductance state
PoTotal	Open probability of both the fully open and sub-conductance channel levels
Rs	*Rhodobacter sphaeroides*
RyR	Ryanodine receptor

RyR1	Type 1 ryanodine receptor
RyR2	Type 2 ryanodine receptor
Sa	*Sulfolobus acidocaldarius*
SCl	'Small' Cl^- channel
SD	Standard deviation
SEM	Standard error of the mean
SERCA	Sarcoplasmic/Endoplasmic reticulum Ca^{2+}-ATPase
SKM	segmental k-means algorithm
SR	Sarcoplasmic reticulum
Ss	*Sulfolobus solfataricus*
TEA	Tetraethyl ammonium
TM	Trans-membrane
TRIC	Trimeric intracellular cation channel
TRIC-A	Trimeric intracellular cation channel sub-type A
TRIC-B	Trimeric intracellular cation channel sub-type B
Tris	Tris(hydroxymethyl)methylamine
T-tubules	Transverse tubules
VDAC	Voltage-dependent anion-channel
VICR	Voltage-induced Ca^{2+}-release

Chapter 1. Introduction

1.1 Ca^{2+}

It could be argued that Ca^{2+} is the most important signalling molecule in eukaryotic organisms. It affects a number of processes including apoptosis, excitability, exocytosis, fertilisation, motility and transcription [1]. In cardiac and skeletal muscle, it is responsible for triggering muscle contraction through a process called excitation-contraction coupling (EC-coupling).

1.2 EC-coupling

EC coupling is the process by which depolarisation of the cell surface membrane results, through specialised cellular sub-structures, in the mechanical contraction of muscle cells [2]–[4].The process is summarised in Figure 1.1. In skeletal and cardiac muscle, this occurs through an increase in intracellular Ca^{2+} from cellular stores such as the sarcoplasmic reticulum (SR) in response to membrane depolarisation [5]–[8]. This process is dependent on invaginations of the plasma membrane, called transverse tubules (t-tubules) [9], and the adjoining area of the SR, termed the junctional SR [10]–[12]. The t-tubule and the junctional SR regions form triads in skeletal muscle [13][14] and dyads in cardiac muscle [15]–[18]. Triads and dyads form the basic EC-coupling units [9].

Important differences exist between the EC coupling process in mammalian cardiac muscle and in mammalian skeletal muscle, especially in the transmission of the stimuli between the t-tubules and the SR [19].

1.2.1 EC-coupling in skeletal muscle

In skeletal muscle cells, EC-coupling occurs when depolarisation of the sarcolemmal membrane (plasma membrane) results in the activation of voltage sensitive Ca^{2+} channels, known as dihydropyridine receptors (DHPRs), which are located within the t-tubule invaginations [20]–[23]. The DHPRs in skeletal muscle t-tubules are directly coupled to the skeletal isoform of the ryanodine receptor (RyR1) in the SR [20], [23]–[27]. The physical linking leads to activated DHPRs in turn activating RyR1 proteins [9], [22], [24], [25], [28]. RyR1 is a high molecular mass membrane spanning ion channel expressed in the membrane of the SR in the junctional regions, and is the pathway for the rapid intracellular Ca^{2+}-release from the SR [29]–[35]. Activation of the RyR1 channels by activated DHPRs therefore results in a release of Ca^{2+} from the SR and the activation of myofilaments (cellular contractile proteins) [36]–[39]. In skeletal muscle, this process is referred to as voltage-induced Ca^{2+} release (VICR).

1.2.2 EC-coupling in cardiac muscle

Cardiac EC-coupling is dependent on extracellular Ca^{2+} levels whereas skeletal EC-coupling is not (40). In cardiac muscle cells, the process by which EC-coupling occurs is referred to as calcium-induced calcium release (CICR) [8], [36], [40]–[44]. In cardiac EC-coupling, voltage activation of the DHPRs results in the channels opening and producing an influx of Ca^{2+} into the junctional region from the extracellular solution [37]. This Ca^{2+} influx is not enough to activate the myofilaments, but instead activates localised cardiac ryanodine receptor isoforms (RyR2) [38]. Ca^{2+} is thus released from SR stores through RyR2 channels which results in activation of the myofilaments [36]–[39].

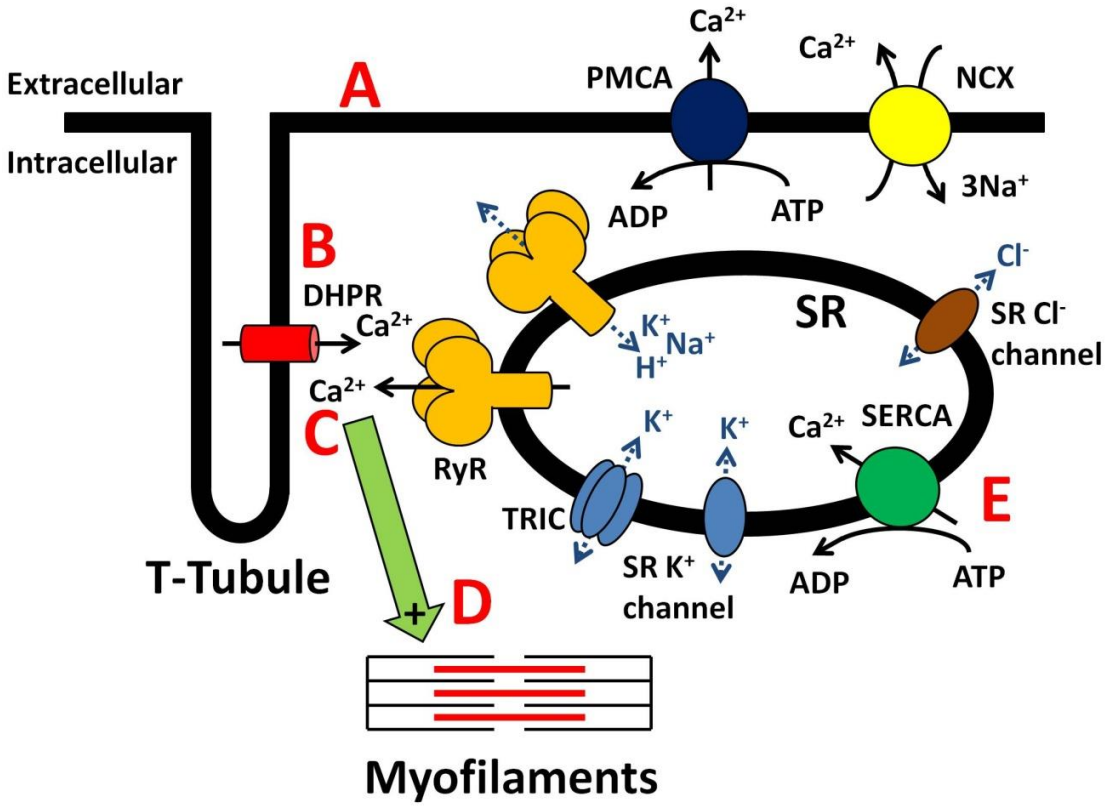


Figure 1.1. A schematic of EC-coupling in mammalian cardiac muscle
A schematic showing the plasma membrane of a mammalian striated muscle cell with a t-tubule structure and a section of the SR. Bilayer membranes are shown as thick black lines. The ion channels and molecules represented are as follows: PMCA = plasma membrane Ca^{2+}-ATPase, NCX = Na^{+}/Ca^{2+} exchanger, DHPR = Dihydropyridine receptors (L-type Ca^{2+} channel), ADP = Adenosine diphosphate, ATP = Adenosine triphosphate, RyR = Ryanodine receptor, SERCA = Sarcoplasmic/Endoplasmic reticulum Ca^{2+}-ATPase, TRIC = Trimeric intracellular cation channel. 5 phases of EC-coupling are labelled A to E. A = depolarisation of the plasma membrane, B = activation of voltage-sensitive DHPRs, allowing Ca^{2+} to flow into the cleft region, C = activation of the RyRs by either CICR (cardiac muscle), or by the DHPRs (skeletal muscle), releasing Ca^{2+} from the SR into the cell cytosol, D = Ca^{2+} activation of myofilaments, causing cellular contraction, and E = re-loading of the SR.

1.3 Proteins involved in EC-coupling

1.3.1 The ryanodine receptor

As discussed previously, in skeletal and cardiac muscle tissue, RyR1 and RyR2, respectively are the main isoforms of RyR responsible for Ca^{2+} release from the SR during EC-coupling [20], [23]–[27], [36]–[39]. RyR proteins are localised mainly to the junctional regions of the SR , and due to their large size (~3000 kDa) and localisation, are responsible for the distinction between 'heavy' SR (HSR) and 'light' SR (LSR) [29]. HSR is so called because of its high concentration of RyR proteins, which causes it to be denser, and consists of the junctional region of the SR. LSR consists of the non-junctional SR and has a lower concentration of RyRs. HSR and LSR can be separated from the HSR in a sucrose density gradient. In this thesis, SR membrane fractions were often divided into HSR and LSR fractions for use in bilayer experiments.

1.3.2 Structural proteins of the triads and dyads

Research into the SR over the past four decades has revealed it to be a complex organelle which contains many additional proteins which are thought to play important roles in the structural organisation of the triads and dyads. Notable examples include junctophilins which are thought to maintain the close proximity between the t-tubule and SR structures required for efficient Ca^{2+} release during EC-coupling [18], [45], [46], triadin and junctin which are suggested to play a role as anchors for the RyR protein [47]–[49], and mitsugumin 29 (MG-29) which may act as a tethering protein to facilitate correct alignment of triad structures [50]–[52].

1.3.3 ATPase proteins

After Ca^{2+} release from the SR in both skeletal and cardiac muscle, basal intracellular [Ca^{2+}] is restored. In the membrane of the SR, the Sarcoplasmic/Endoplasmic reticulum Ca^{2+}-ATPase

(SERCA) protein works to reload the SR with Ca^{2+} to allow for the next Ca^{2+} release event [53][54]. In the sarcolemma, the plasma membrane Ca^{2+}-ATPase (PMCA) [55][56] and the Na^{+}/Ca^{2+} exchanger (NCX) [57][58] move Ca^{2+} from the cell cytosol into the extracellular solution. This process is summarised in Figure 1.1.

1.4 The need for a countercurrent

As discussed earlier in this chapter, during EC-coupling Ca^{2+} is released from the SR which triggers muscle contraction in skeletal and cardiac muscle. It is also well established that, without an additional flow of ions to balance the charge asymmetry across the SR due to the Ca^{2+} efflux, Ca^{2+} release during EC coupling would be impossible [59]–[71].

Two pathways have been suggested for the production of a countercurrent during EC-coupling, summarised in Figure 1.2. The first pathway is due to fluctuations in monovalent ions through specialised countercurrent channels. It has long been know that the SR was selectively permeable to small monovalent ions, mediated by SR ion channels [72]–[75]. The most plausible candidate for a counter ion channel is that of SR K^{+} channels [61], [68], [76]–[80], such as the TRIC-A and TRIC-B channels [81] which would allow K^{+} to flow into the SR lumen, thus correcting the charge asymmetry caused by Ca^{2+} release. It is unlikely that this is the only pathway however as the block of SR K^{+} channel current does not result in the elimination of Ca^{2+} from the SR release as would be expected if this were the sole pathway for the provision of countercurrent [66][82]. Additionally, recent studies with TRIC KO models have revealed impaired Ca^{2+} release, but not prevented it completely [81], [83]–[85], suggesting that TRIC channels are not the sole countercurrent carrying channels. SR countercurrents have also been suggested to be carried by ions other than K^{+} such as Cl^{-} [86] and H^{+} [87][88].

The second pathway is a countercurrent carried through RyRs. It has been suggested that the RyR channel can provide its own countercurrent [67][89]. If this is so, then the necessity for the counter-ion flux through SR ion channels may not as critical as first assumed, although equilibration of ions across the SR will still be important.

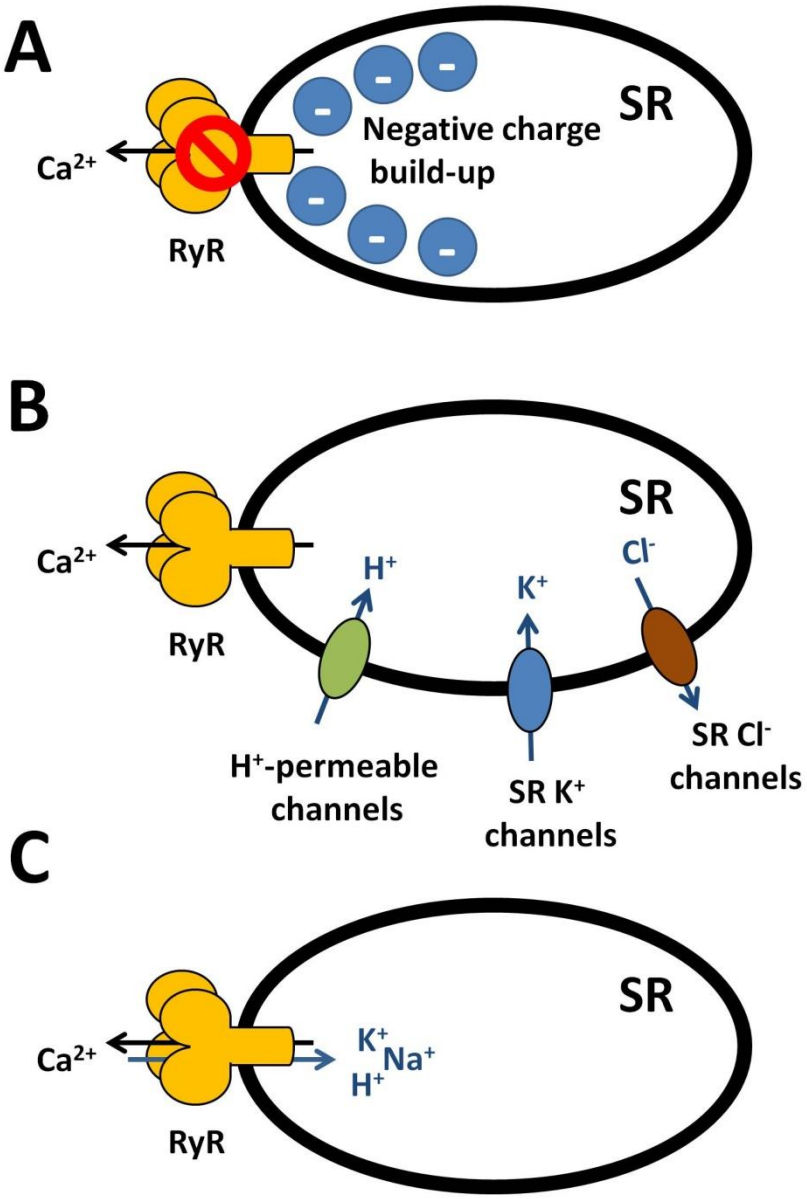


Figure 1.2. Schematic of the SR during Ca^{2+} release showing the two proposed pathways for a countercurrent

(A) Without a countercurrent, Ca^{2+} release from the SR is prevented by a rapid build-up of negative charge. A countercurrent is therefore required to allow Ca^{2+} release to occur. **(B)** It has been suggested that countercurrent could be carried by the movement of monovalent ions through SR ion channels. **(C)** It has also been suggested that RyR channels can provide their own countercurrent during EC coupling negating the need for other ion channels. It is probable that both the RyR and other SR ion channels are involved in providing a countercurrent.

1.4.1 SR K^+ channels

SR K^+ channels have been proposed as a possible candidate for carrying countercurrent across the SR membrane during EC coupling [75], [90]–[96]. K^+ and Cl^- channel fluctuations after incorporation of skeletal muscle SR membrane vesicles into an artificial planar phospholipid bilayer were first observed by Miler in 1978 [72]. The K^+ component of these current-fluctuations was later identified as channels referred to as 'the SR K^+ channel' [75], [90]–[96], however more recently, it has been suggested that SR K^+ channel currents consist of more than one class of ion channel [97]. SR K^+ channels have been reported to be permeable to a range of monovalent cations with a permeability sequence of $K^+ > NH_4^+ > Rb^+ > Na^+ > Li^+ > Cs^+$, but impermeable to Ca^{2+} [75]. The channels are thought to be sensitive to low pH, with a reduction in K^+ conductance observed in pH 5.0 [72], and have been found to be blocked by Ca^{2+} [72], [75], [98], [99] and known K^+ channel blockers such as tetraethyl ammonium (TEA) [90], decamethonium [100][96], hexamethonium [100], 4-aminopyridine [101], and gallamine [93]. A specific ligand for SR K^+ channels is yet to be reported, however. The size of the SR K^+ channel conductance pathway was also postulated using the channel permeability to a range of large organic cations [102], a minimum pore area of 20 $Å^2$ was speculated [90], although as stated earlier, it is possible that more than one SR K^+ channel exists [97].

Early studies of the gating of SR K^+ channels in SR isolated from frog skeletal muscle, observed them to gate with long opening bursts which contained both fully open and sub-conductance channel open levels [61]. The channel conductance was recorded at 150 pS in 100 mM KCl and the conductance for the channel sub-conductance level was reported at 50 pS, 30 % of the fully open channel level [61]. Later studies using SR K^+ channels isolated from mammalian skeletal muscle, reported a sub-conductance level of 60-70 % of the fully open channel level

[92], [103]. Improvements in resolution of single-channel recordings have allowed more recent studies to analyse the gating of SR K^+ channels in more detail. Figure 1.3 shows representative single-channel traces from a recent paper recorded at a higher resolution [104]. The figure shows a long channel opening burst at +30 mV in symmetrical 210 mM K^+ solutions and with a conductance of 211 pS. The channel exhibited long opening bursts to the fully open channel level which contained both brief sojourns and extended periods gating to a sub-conductance level. Most notable are the regions at the beginning and at the end of the open burst where the channel dwelt predominately in the sub-conductance level; these were referred to as the 'shoulders' and the 'tails' of the channel opening events [105][104]. This gating was seen as typical SR K^+ channel gating, and is described as such in this thesis. Additionally, these recent studies have suggested that mouse SR K^+ channels may contain as many as four distinct sub-conductance levels [105][104] as is shown in Figure 1.3B. A further important feature of SR K^+ channel gating is its apparent voltage sensitivity [72][105][104]. Under voltage clamp conditions and with K^+ as the permeant ion, the SR K^+ channel was found to have a lower Po at negative potentials compared with positive potentials as is shown in Figure 1.3A.

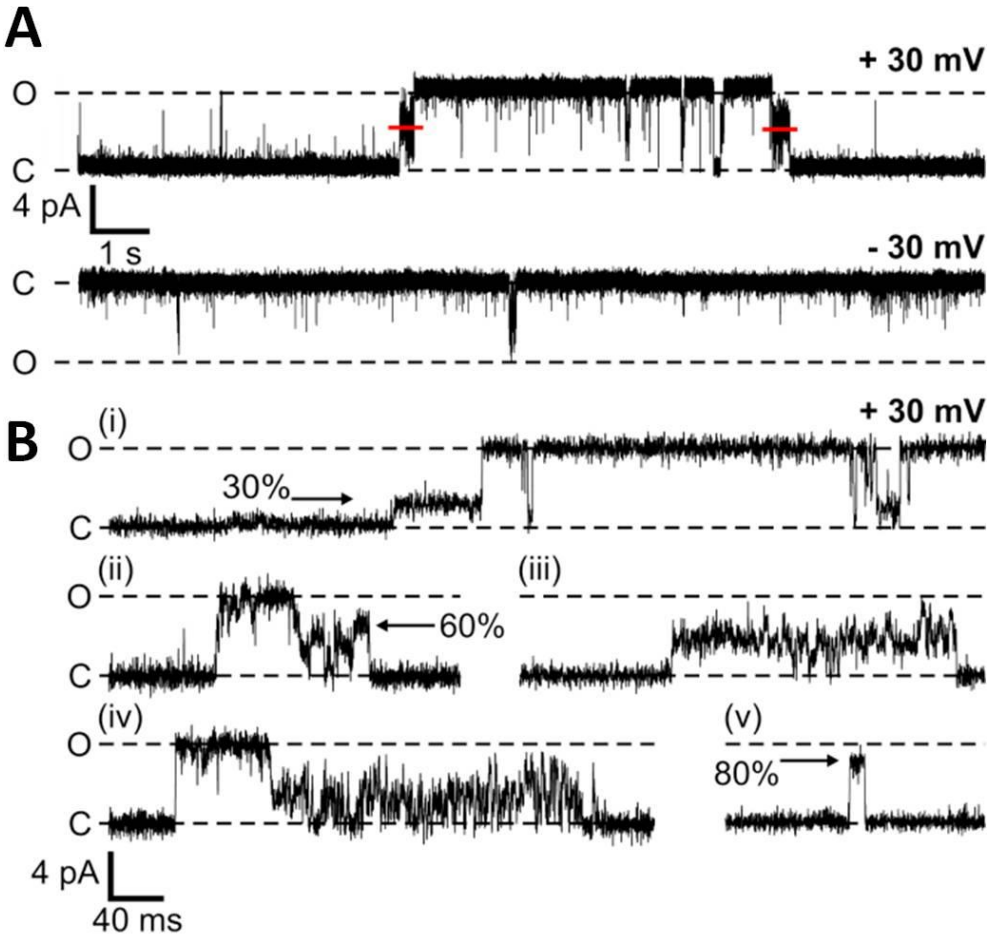


Figure 1.3. Gating of the mouse skeletal SR K^+ channel, adapted from Matyjaszkiewicz *et al.* (2015) [104]
(A) Typical gating of the SR K^+ channel in 210 mM K^+ at +30 mV and -30 mV holding potentials. **(B)** Examples of sub-conductance levels at 30%, 60%, 80% and rapid gating between states. Channel closed levels are shown by C and fully open channel levels by O.

1.4.1.1 Trimeric intracellular cations (TRIC) channels

It has been suggested that trimeric intracellular cation (TRIC) channels could be the SR K^+ channels that are observed when SR vesicles are incorporated into planer phospholipid bilayers [97]. The TRIC channel is an intracellular ion channel, where two isoforms have been cloned and identified, termed TRIC-A and TRIC-B [106][81]. TRIC-A is especially abundant in excitable tissues, such as cardiac and skeletal muscle, while TRIC-B is found in most tissues

[106]. TRIC proteins were purified and reconstituted into liposomes for study using a planar lipid bilayer [97][106]. Both TRIC-A and TRIC-B proteins were found to form K^+ selective ion channels in artificial bilayers which were also found to exhibit voltage and Ca^{2+} sensitivity [97][106], similar to that of the SR K^+ channel [72], [104], [105], [107]. Purified TRIC-A was reported to not be blocked by decamethonium at concentrations up to 100 µM [81], and it was suggested that the lack of effect of decamethonium could be evidence that TRIC-A is not equivalent to the usually observed SR K^+ channels [81]. However, according to the effects of decamethonium on SR K^+ channels that we observe in the Sitsapesan lab, this concentration is too low (at 300 mM K^+ in the *cis* chamber) to observe a change in single-channel conductance and, at most, a slight reduction in mean open lifetimes and Po might be observed. In this report there is no analysis of channel gating [100].

The physiological role of TRIC channels is not yet established, however, as has been suggested for SR K^+ channels, evidence exists which implies that TRIC channels may play a role in providing a counter-current to Ca^{2+} flux during EC-coupling [83][106]. Much of this evidence comes from the study of pathologies in *Tric* knockout (KO) mouse models [81], [83]–[85]. Three *tric* KO mouse models were developed in the Takeshima laboratory: *Tric* double KO (lacking both the TRIC-A and TRIC-B proteins) [81], *Tric-a* KO [83], and *Tric-b* KO [85]. Each of these phenotypes exhibited impaired Ca^{2+} release with over-loaded Ca^{2+} stores [81], [83]–[85]. In *Tric* double KO mice, the cardiac SR becomes swollen and heavily overloaded with Ca^{2+} [81]. Embryonic cardiac arrest was observed after embryonic day E9.5 [81]. In *Tric-b* KO mice, alveolar epithelial cells exhibit inadequate Ca^{2+}-release from overloaded ER stores [85]. These mice were observed to die of respiratory failure following birth [85]. *Tric-a* KO mice survived until adulthood; however the ability of the skeletal muscle cells to respond to stress was found to be defective, and instability existed in the Ca^{2+}-release process [83]. Moreover, this knockout mouse phenotype was observed to develop hypertension due to impaired

hyperpolarisation signalling evoked by Ca^{2+} spark/release in vascular smooth muscle [84]. Further to these experiments, Mutations in *tric-b* genes are responsible for osteogenesis imperfecta [108][109][110].

The structure of the TRIC channel was first predicated using electron microscopy (EM) [81]. EM images were used to generate a 3-dimentional prediction for the shape of the TRIC protein. The TRIC channels were shown to be trimeric in structure, with each ion channel formed from three individual monomers of ∼30 kDa in molecular mass [81][111][112]. TRIC has been described as being akin to a bullet-shaped protein, spanning the membrane of the SR as shown in Figure 1.4 [97][106][81].

.

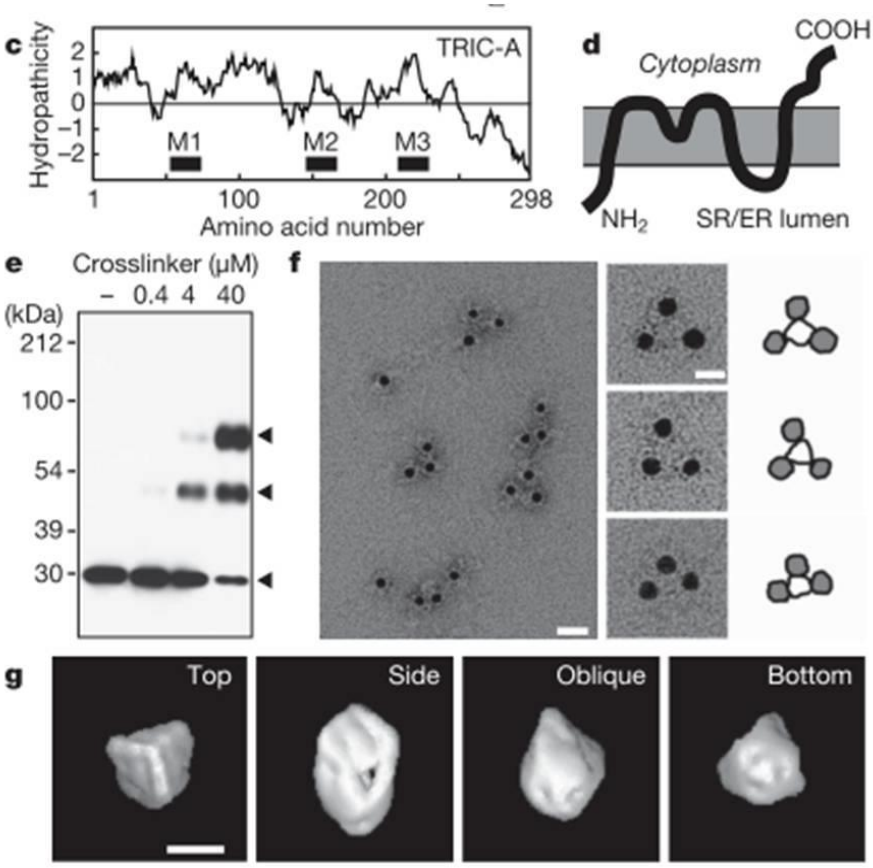


Figure 1.4. Predictions for the structure of TRIC from EM images taken from Yazawa *et al.* 2007 [81]
c, Hydropathicity profile of TRIC-A in the Kyte–Doolittle algorithm (window size, 19 residues). M1–M3, putative transmembrane segments. **d**, Topology model of TRIC-A proposed in Supplementary Fig. 2. **e**, Chemical cross-linking of TRIC-A with 1,11-bis-maleimidotetraethyleneglycol. Arrowheads, monomeric, dimeric and trimeric forms. **f**, Electron microscopy images of native TRIC-A bound with gold-conjugated Fab fragment (left panel; scale bar, 200Å). High-magnification images of the immuno-complexes and their contours are also shown (right panels; scale bar, 100Å). **g**, Surface representations of three-dimensional reconstruction of native TRIC-A. Scale bar, 50Å. [81].

Recently, three different groups have published high resolution crystal structures of TRIC-B channels [111]–[113]. The structures were of one eukaryotic TRIC isoform from the TRIC-B subtype (TRIC-B1 and TRIC-B2 at resolutions of 3.3 Å and 2.3 Å, respectively), from *Caenorhabditis elegans* (*c. elegans)* [112], and four prokaryotic TRIC isoforms, *Rhodobacter sphaeroides* (Rs), *Sulfolobus solfataricus* (Ss) [111], *Sulfolobus acidocaldarius* (Sa), and *Colwellia*

psychrerythraea (Cp) [113] at resolutions of 3.4 Å, 2.6 Å, 1.6 Å, 2.4 Å, respectively. Previously, a bioinformatics analysis study predicted the existence of prokaryotic homologues, and that these formed the majority of TRIC isoforms (Figure 1.5) [114].

The structures confirmed the trimeric nature of TRIC channels, and suggested three identical cation pores through the centre of each monomer [111]–[113]. For the purposes of this thesis, the structure of the TRIC-B protein from *c. elegans* will be discussed, as this structure shares more sequence homology with mammalian TRIC channels (Figure 1.6). The *c. elegans* TRIC-B1 structure suggested a protein with three 7-TM monomers, each with a central pore (Figure 1.7) [112]. Interestingly, the *c. elegans* TRIC-B1/2 was found to contain an Phosphatidylinositol4,5-bisphosphate ($PI(4,5)P_2$) molecule as part of the channel structure, with the charged head group of the lipid molecule forming part of the channel pore (Figure 1.7) [112]. This was not observed in the prokaryotic TRIC isoforms [111][113]. *Rs*TRIC was found to contain carbon acyl chains as part of the channel structure, but in a different area and configuration to that of the *c. elegans* TRIC-B1/B2 [111]. $PI(4,5)P_2$ binds to the KEV region of the TRIC channel [112] which is highly conserved in mammalian TRIC channels [106][112], but is not present in prokaryotic TRIC proteins (highlighted in blue in Figure 1.6).

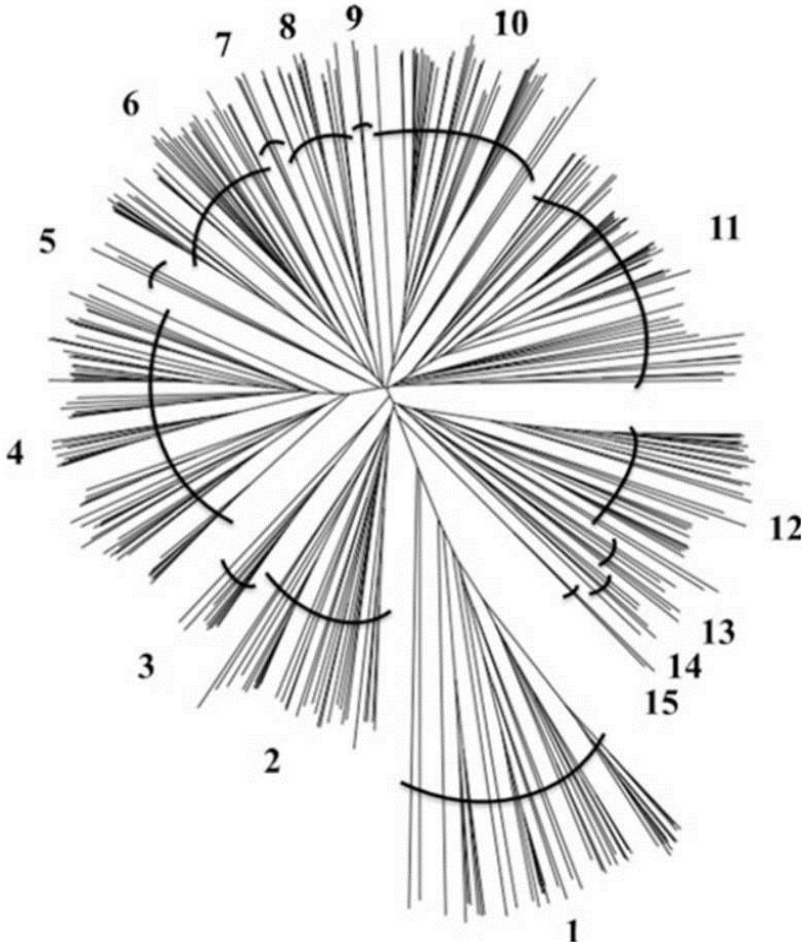
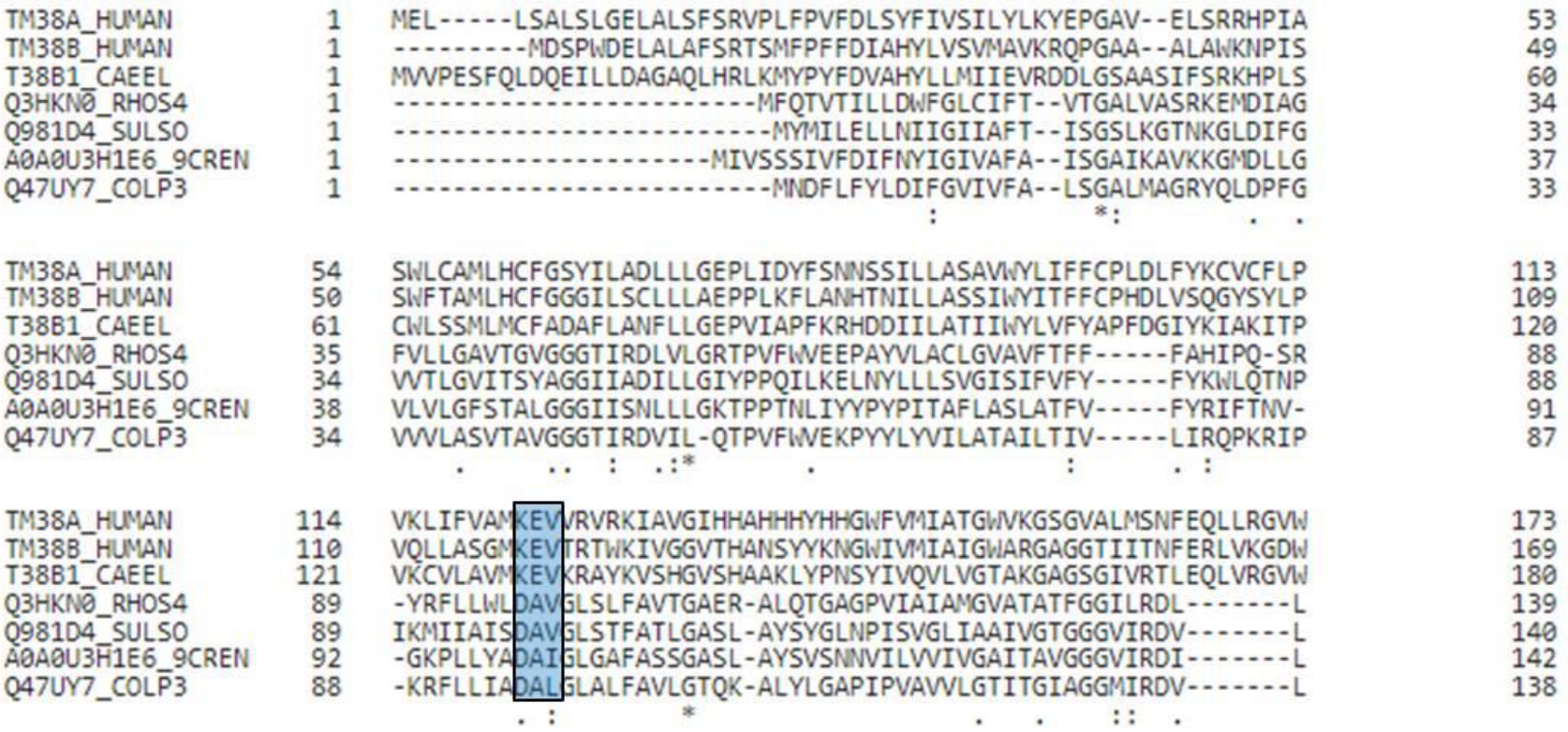


Figure 1.5. The TRIC family of proteins adapted from Silverio and Saier, Jr (2011) [114]
The TRIC family of proteins adapted from Silverio and Saier, Jr (2011). **1** represents the eukaryotic TRIC isoforms and **2-15** represent the prokaryotic isoforms [114].


TM38A_HUMAN 1 MEL-----LSALSLGELALSFSRVPLFPVFDLSYFIVSILYLKYEPGAV--ELSRRHPIA 53
TM38B_HUMAN 1 ---------MDSPWDELALAFSRTSMFPFFDIAHYLVSVMAVKRQPGAA--ALAWKNPIS 49
T38B1_CAEEL 1 MVVPESFQLDQEILLDAGAQLHRLKMYPYFDVAHYLLMIIEVRDDLGSAASIFSRKHPLS 60
Q3HKN0_RHOS4 1 ------------------------MFQTVTILLDWFGLCIFT--VTGALVASRKEMDIAG 34
Q981D4_SULSO 1 ------------------------MYMILELLNIIGIIAFT--ISGSLKGTNKGLDIFG 33
A0A0U3H1E6_9CREN 1 ---------------------MIVSSSIVFDIFNYIGIVAFA--ISGAIKAVKKGMDLLG 37
Q47UY7_COLP3 1 ------------------------MNDFLFYLDIFGVIVFA--LSGALMAGRYQLDPFG 33
TM38A_HUMAN 54 SWLCAMLHCFGSYILADLLLGEPLIDYFSNNSSILLASAVWYLIFFCPLDLFYKCVCFLP 113
TM38B_HUMAN 50 SWFTAMLHCFGGGILSCLLLAEPPLKFLANHTNILLASSIWYITFFCPHDLVSQGYSYLP 109
T38B1_CAEEL 61 CWLSSMLMCFADAFLANFLLGEPVIAPFKRHDDIILATIIWYLVFYAPFDGIYKIAKITP 120
Q3HKN0_RHOS4 35 FVLLGAVTGVGGGTIRDLVLGRTPVFWVEEPAYVLACLGVAVFTFF-----FAHIPQ-SR 88
Q981D4_SULSO 34 VVTLGVITSYAGGIIADILLGIYPPQILKELNYLLLSVGISIFVFY-----FYKWLQTNP 88
A0A0U3H1E6_9CREN 38 VLVLGFSTALGGGIISNLLLGKTPPTNLIYYPYPITAFLASLATFV-----FYRIFTNV- 91
Q47UY7_COLP3 34 VVVLASVTAVGGGTIRDVIL-QTPVFWVEKPYYLYVILATAILTIV-----LIRQPKRIP 87
TM38A_HUMAN 114 VKLIFVAMKEVVRVRKIAVGIHHAHHHYHHGWFVMIATGWVKGSGVALMSNFEQLLRGVW 173
TM38B_HUMAN 110 VQLLASGMKEVTRTWKIVGGVTHANSYYKNGWIVMIAIGWARGAGGTIITNFERLVKGDW 169
T38B1_CAEEL 121 VKCVLAVMKEVKRAYKVSHGVSHAAKLYPNSYIVQVLVGTAKGAGSGIVRTLEQLVRGVW 180
Q3HKN0_RHOS4 89 -YRFLLWLDAVGLSLFAVTGAER-ALQTGAGPVIAIAMGVATATFGGILRDL-------L 139
Q981D4_SULSO 89 IKMIIAISDAVGLSTFATLGASL-AYSYGLNPISVGLIAAIVGTGGGVIRDV-------L 140
A0A0U3H1E6_9CREN 92 -GKPLLYADAIGLGAFASSGASL-AYSVSNNVILVVIVGAITAVGGGVIRDI-------L 142
Q47UY7_COLP3 88 -KRFLLIADALGLALFAVLGTQK-ALYLGAPIPVAVVLGTITGIAGGMIRDV-------L 138

```
TM38A_HUMAN         174   KPETNEILHMSFPTKASLYGAILFTLQQTRWLPVSKASLIFIFTL-FMVSCKVFLTATHS          232
TM38B_HUMAN         170   KPEGDEWLKMSYPAKVTLLGSVIFTFQHTQHLAISKHNLMFLYTI-FIVATKITMMTTQT          228
T38B1_CAEEL         181   LPTHNELLRPSFATKACVVAASVLALEKSGTYLTAPHDLVYLVIVGFFVYFKLS-AVILH          239
Q3HKN0_RHOS4        140   GGESPVILRREIYITAALLGAAAFVALDAFGA--PRELALG---AGFAAAFLS-------          187
Q981D4_SULSO        141   VNEIPMVLTKEIYATAALLSGFIYYFTTPYLH----HDSLF---VAFLGSFLL-------          186
A0A0U3H1E6_9CREN    143   SNEVPLILTREFYATTAVIGSFVYFIASDLSV--PEDVALI---VSFLITLIL-------          190
Q47UY7_COLP3        139   CNVIPMILREEIYALAAMLGGSLFIILHGLNW--NDTNAMI---VSISAALAL-------          186
                                 *  .    . : ..                  :     :

TM38A_HUMAN         233   HSSPFDALEGYICPVLFGSACGGDHHHD-----NHGGSHSGGGPGAQHSAMPAKSKEELS          287
TM38B_HUMAN         229   STMTFAPFEDTLSWMLFGWQQPFSSCEK-----KSEAKSPSNGVGSL----ASKPVDVAS          279
T38B1_CAEEL         240   VTDPFAPIENLFCAIFMGGIWDAVSRALAASRDRRAAGAHSNENGSSIST-PEK------          292
Q3HKN0_RHOS4        188   ----------RAAGLVWGLSLPRYRARP----------GRPEGRG---------------          212
Q981D4_SULSO        187   ----------RILSIKYNFNLPKREDNK----------S---------------------          205
A0A0U3H1E6_9CREN    191   ----------RILAMELKWELPRKKIE-----------------------------------          207
Q47UY7_COLP3        187   ----------RLAAIYWHVSLPAFHIVE----------KPKKEKGTTKI--IEK------          218
                                     :

TM38A_HUMAN         288   EGSRKKKAKKAD                                                    299
TM38B_HUMAN         280   DNVKKKHTKKNE                                                    291
T38B1_CAEEL         293   ----KDQ-----                                                    295
Q3HKN0_RHOS4        213   ------------                                                    212
Q981D4_SULSO        206   ------------                                                    205
A0A0U3H1E6_9CREN    208   ------------                                                    207
Q47UY7_COLP3        219   ---------K--                                                    219
```

Figure 1.6. Sequence alignment for the various identified TRIC structures and Human TRIC for comparison

Human TRIC-A (TMEM38A_HUMAN), Human TRIC-B (TMEM38B_HUMAN), *c. elegans* TRIC-B1 (T38B1_CAEEL), *Rs*TRIC (Q3HKNO_RHOS4), *Ss*TRIC (Q981D4_SULSO), *Sa*TRIC (AOAOU3HIE6_9CREN), and *Cp*TRIC (Q47UY7_COLP3). This figure was produced using the database and the online tools provided by Uniprot (http://www.uniprot.org/). Highlighted in blue is the KEV region which is thought to bind the PI(4,5)P_2 molecule; this is conserved in eukaryotic, but not prokaryotic TRIC channels .

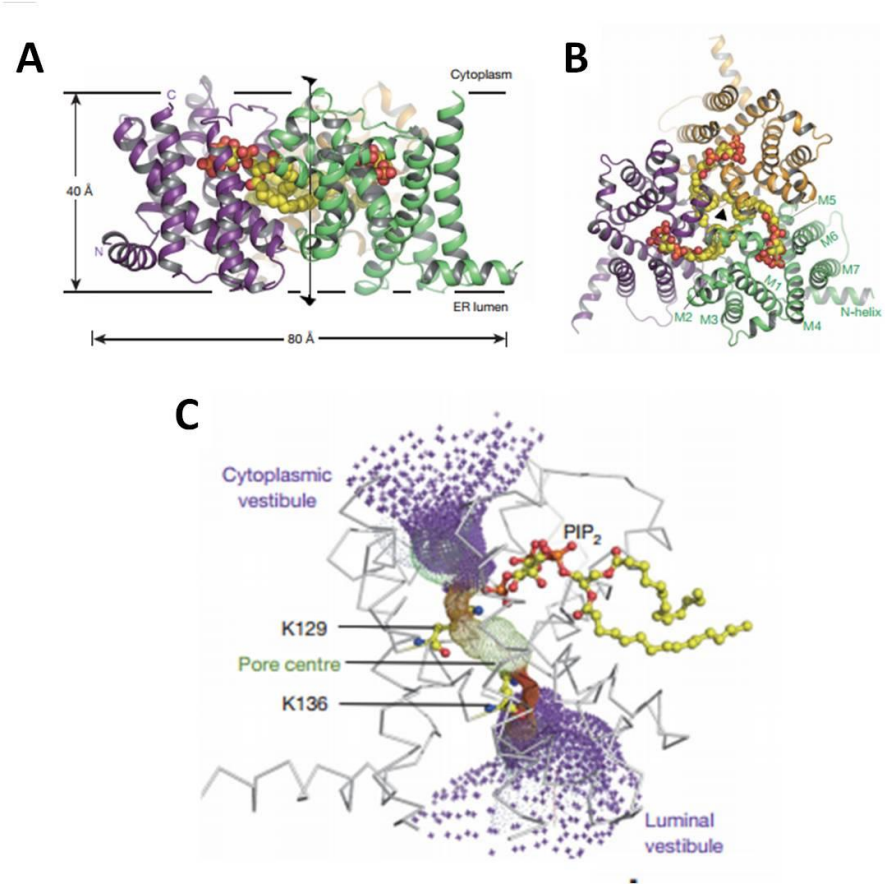


Figure 1.7. The structure of the *c. elegans* TRIC-B1/B2 channel and the monomeric pore region adapted from Yang *et al.* (2016) [112]
(A, B) The homotrimeric TRIC-B1 channel in complex with PIP2. The protein subunits are presented as ribbon models, while the PIP2 molecules are shown as yellow-and-red sphere models. The views are along the membrane plane **(A)** or along the C3 axis from the cytoplasmic side **(B)**. **(C)** The profile of an hourglass-shaped pore within the C. elegans TRIC-B1 monomer. Colour codes: red, low radius surface (pore radius 2.3Å). The protein backbones are shown as ribbon models. The two bottlenecks of the pore coloured in red are located near two lysine residues and the PIP2 molecule (shown as the ball-and-stick models) [112].

The pore of the *c. elegans* TRIC-B1/B2 channel was found to be an hour glass shape with two constrictions of <1.5 Å and a central reservoir of between 1.5-2.3 Å (Figure 1.8) [112]. The central reservoir was found to contain both water and monovalent binding sites, accessible to a Rb^+ ion. A second cation binding site which binds Cs^+ was also identified on the luminal side of the pore [112].

Single-channel properties of the *c. elegans* TRIC-B1 channel were studied by inside-out patch-clamp electrophysiology on reconstituted giant unilamellar vesicles containing the purified *c. elegans* TRIC-B1 protein [112]. The channel exhibited a fully open conductance of 153 pS in 210 mM symmetrical KCl solution and two sub-conductance states at 33 % (45.8 pS) and 67 % (101.5 pS) which are thought to correspond to the open level of one or more of the monomeric pores [112]. The channel was found to be activated by Ca^{2+} added to the cytosolic side of the channel, but inhibited by symmetrical Ca^{2+} [112]. It was suggested that a Ca^{2+} binding side was present on the cytosolic side of the *c. elegans* TRIC-B1 protein which was confirmed by mutagenesis. It was found that, in the presence of Ca^{2+}, the TRIC protein underwent a conformational change which resulted in channel activation (Figure 1.9). Mutations of the KEV region of the *c. elegans* TRIC-B1 channel were also studied. A K129A/R133L mutant was developed which lacked the capacity to bind a $PI(4,5)P_2$ [112]. This mutant exhibited fewer channel events to the fully open channel level and dwelt for longer periods in the sub-conductance level. It has been suggested that the presence of $PI(4,5)P_2$ is important for normal TRIC trimeric assembly [112]; however prokaryotic TRIC proteins were found to form trimers without any similar lipid structures [111][113]. Further to this, prokaryotic TRIC channels, although found to contain sub-conductance states and similar conductance values, were not observed to gate in a monomeric form [111][113] as is the case with *c. elegans* TRIC-B1 protein [112]. Cation binding sites were also not present in prokaryotic TRIC channels [111][113] which suggests differing modulation between prokaryotic and eukaryotic TRIC channels.

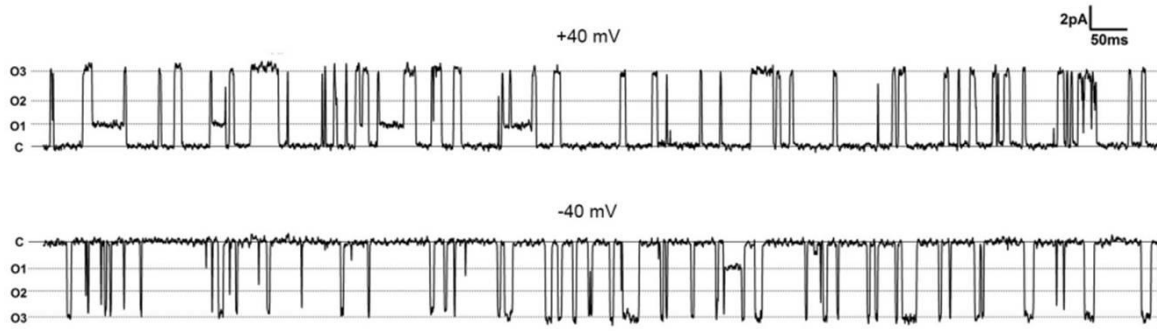


Figure 1.8. Current-fluctuations through the *c. elegans* TRIC-B1 channel adapted from Yang *et al.* (2016) [112]
Current-fluctuations through the *c. elegans* TRIC-B1 channel at the indicated holding potentials. The closed state is given by C and the open states by O1-O3 where O1 and O2 constitute sub-conductance states. Recordings were made in symmetrical 210 mM KCl solutions [112].

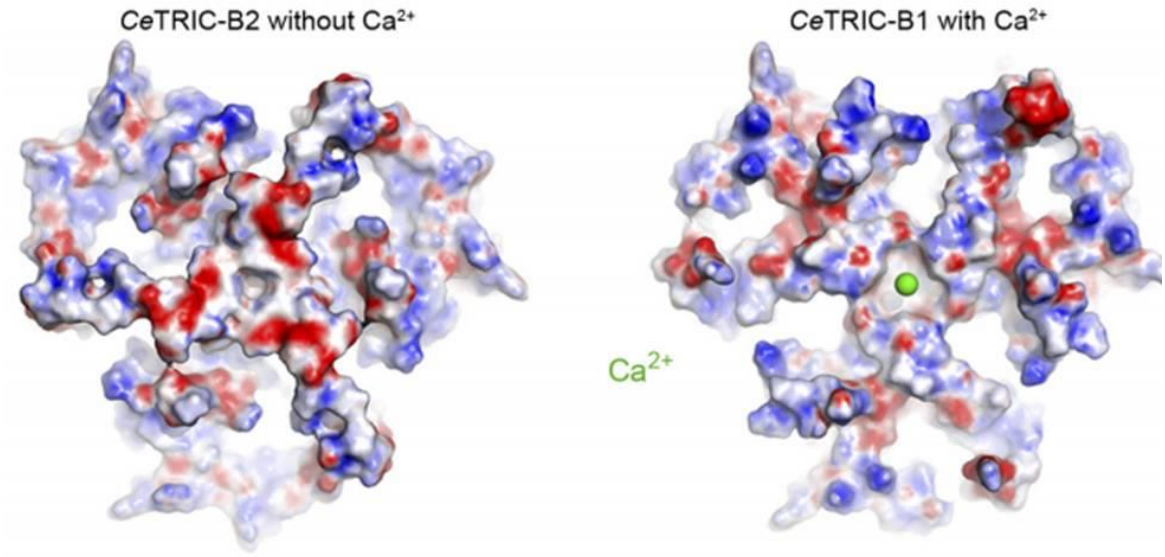


Figure 1.9. The effect of Ca^{2+} on *c. elegans* TRIC- B1/B2 protein structure, adapted from Yang *et al.* (2016) [112]**.**
Electrostatic surface presentations of TRIC-B2 trimer (without Ca^{2+} bound) and TRIC-B1 trimer (with Ca^{2+} bound). The colour codes for the electrostatic potential on the surfaces of the TRIC-B1/B2 trimers are: red, −15 kTe−1 ; white, neutral; blue, +15 kTe−1 . The Ca^{2+} ion bound to TRIC-B1 trimer is presented as a green sphere. The green arrows indicate the regions around the trimeric centres involved in binding Ca^{2+}. The magenta stars label the pore region within each monomer [112].

1.4.2 SR Cl^- channels

1.4.2.1 SR Cl^- channels observed in the bilayer

In 1978, Miller first described both K^+ and Cl^- currents across the membrane of the SR from rabbit skeletal muscle using planar lipid bilayer techniques [72]. A number of subsequent studies into SR anion selective channels after reconstitution into bilayers of cardiac and skeletal SR membrane were conducted which revealed a number of SR Cl^- channels with varying biophysical and pharmacological properties [79], [115]–[121]. The reported Cl^- channels fell broadly into two groups. The first group consisted of a Cl^- selective channel with defined sub-conductance levels [86][116][122][123][118][119] which was blocked by Cl^-

channels blockers such as 4,4'-Diisothiocyano-2,2'-stilbenedisulfonic acid (DIDS) [116] and 5-Nitro-2-(3-phenylpropylamino)benzoic acid (NPPB) [118], modulated by calmodulin (CaM) [123], and shut down by Zn^{2+} [118]. The second group consisted of a non-selective channel, permeable to Cl^-, but also large cations such as Tris and choline [117], [124]–[126]. Examples of channels from both groups are shown in Figure 1.10. In Figure 1.10, both currents were recorded in similar solutions of choline-chloride and the E_{rev} values, detailed in the figure legend, show the first channel to be selective for both choline and Cl^- [124], and the second to be only permeable to Cl^- [116]. A third group of SR Cl^- channels also appears to exist which appear as voltage-sensitive porin channels [79][115].

The majority of the SR Cl^- channels studied exhibited voltage sensitivity and gated with sub-conductance levels [79], [115]–[121], [127], although the number of such states reported varied from 2 states [79][118] to 13 states [121]. It is possible, however, that the apparent sub-conductance gating in some of these channels was due to the coordinated openings of multiple channels [118][120]. SR Cl^- channels were reported to be both sensitive [115][120][127], and insensitive [79][116][118][122] to Ca^{2+}. It has also been shown that some SR Cl^- channels are pH-sensitive [72][118][128][129] and Kawano et al. in 1992 and again in 1999 [122][130], reported Cl^- channels in SR membranes that appeared permeable to adenine nucleotides and which were activated by protein kinase A (PKA) [122][130]. In 1996, a paper by Kourie *et al*. [121] described two distinct types of Cl^- channels in artificial bilayers. The channels gated with different conductances, and were named the 'big' Cl^- (BCl) and 'small' Cl^- (SCl) channels, respectively. Examples of these two channel types are shown in Figure 1.11. The BCl channel was observed to exhibit a high Po and multiple sub-conductance states with a single-channel conductance of 210-250 pS in 250/50 mM *cis*/*trans* CsCl. The SCl channel exhibited a lower Po and more closings to the zero current level. The SCl channel was also

observed to gate with multiple sub-conductance levels, but less than were observed in the BCl channel gating, and a conductance of 56-75 ps in 250/50 mM *cis*/*trans* CsCl [121].

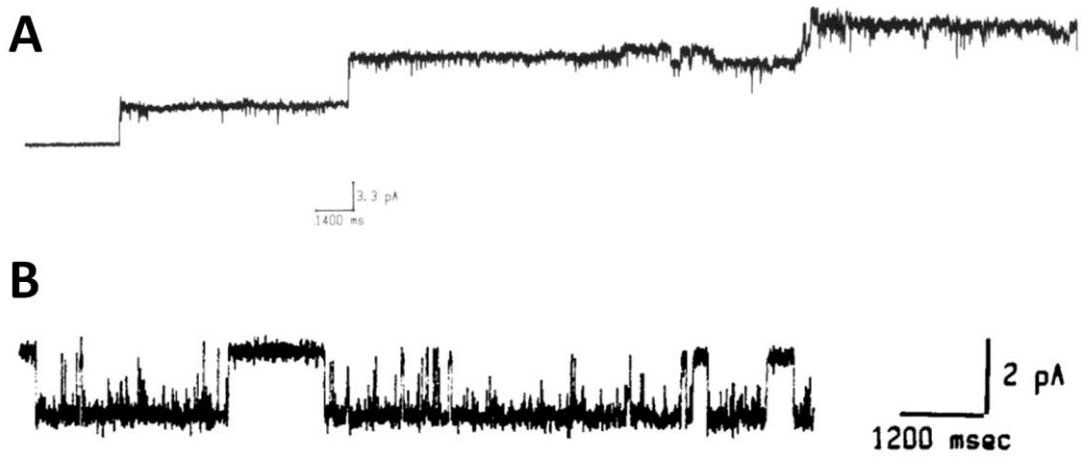


Figure 1.10. SR Cl^- channels observed in artificial bilayers
(A) An example of the non-selective Cl^- channel incorporations observed in bilayer experiments at 0 mV. The channel was recorded in 250/50 mM *cis*/*trans* choline-chloride solutions and reversed at +25 mV (the calculated E_{rev} for Cl^- was -41 mV). The figure is adapted from Figure 3 of Smith *et al*, 1986 [124]. **(B)** An example of the small Cl^--selective channels observed in bilayer experiments at 0 mV. The channel was recorded in 260/60 mM *cis*/*trans* choline-chloride solutions and reversed at +31 mV, close to the Cl^- E_{rev} of 36.7 mV. The figure is adapted from Rousseau, 1989 [116].

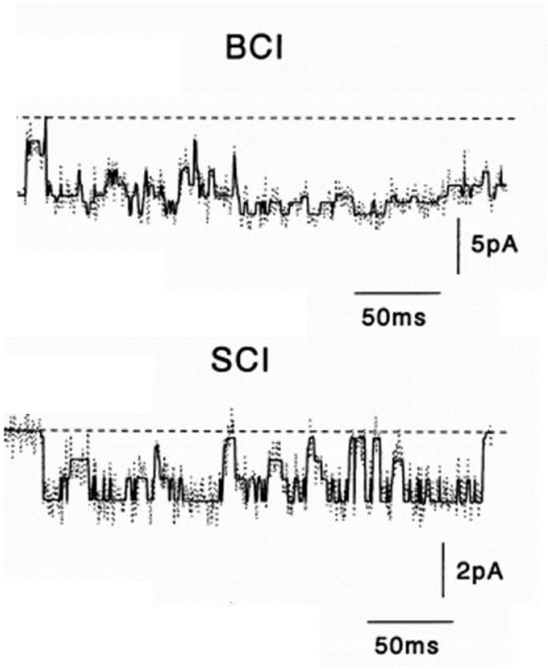


Figure 1.11. The BCl and SCl channel taken from Kourie *et al*. (1996) [121]
The BCl (top) and SCl (bottom) channels as described by Kourie *et al*. (1996) [121]. Recordings were taken at 0 mV in 250 mM CsCl in the *cis* chamber and 50 mM CsCl in the *trans* chamber. The zero current level is shown with a black dashed line.

1.4.2.2 Cl^- channels identified as present in the SR

More recently, cystic fibrosis transmembrane conductance regulator (CFTR) Cl^--channel was detected on the SR membrane of human skeletal muscle [131]. The CFTR protein is a phosphorylation-dependent epithelial Cl^- channel. Dysfunction of CFTR channels results in the genetic disease, cystic fibrosis (CF) through the disruption of ion transport across epithelial cells [132]. The CFTR protein exhibits a small conductance of 6-10 pS in symmetrical 140 mM N-Methyl-D-glucamin (NMDG)-chloride and has been shown to activated by PKA-dependent phosphorylation [133]. An example of CFTR gating is shown in Figure 1.12A.

A, porin-like, Cl^- channel has also been identified in the SR termed the voltage-dependent anion-channel (VDAC) [134][135]. VDAC is a beta-barrel proteins which spans the

membrane of intracellular organelles such as mitochondria [136][137]. In humans and most other higher eukaryotic organisms, three VDAC isoforms exist, VDAC1, VDAC2, VDAC3 [138]. VDAC has a suggested physiological role of providing charge compensation during Ca^{2+}-release [134]. VDAC is also thought to be permeable to ATP and as such may also be involved in ATP transport into the SR lumen [139]. VDAC channel properties are similar to those described in some native SR Cl^- channel recordings [79][115]. An example of VDAC gating is shown in Figure 1.12B.

It is also possible that chloride intracellular channel (CLIC) proteins are responsible for Cl^- currents observed in the SR. CLIC proteins are members of the glutathione S-transferase (GST) superfamily and are a novel class of membrane-bound proteins that have been grouped together on the basis of their sequence similarity [140][141]. Purified CLIC1 proteins have been shown to form functional Cl- channels [142][143][144][145]. After reconstitution into planar lipid bilayers, CLIC1 channels, exhibited a conductance of 38±3 pS in 500:50 mM *cis:trans* KCl solution and gated with two sub-conductance states at 22% and 45% of the fully open channel level [146]. Examples of CLIC1 channel gating are shown in Figure 1.12C. CLIC2, which shares sequence similarity with CLIC1, has been suggested to limit Ca^{2+} release from the SR by directly regulating RyR2 channels [147][148].

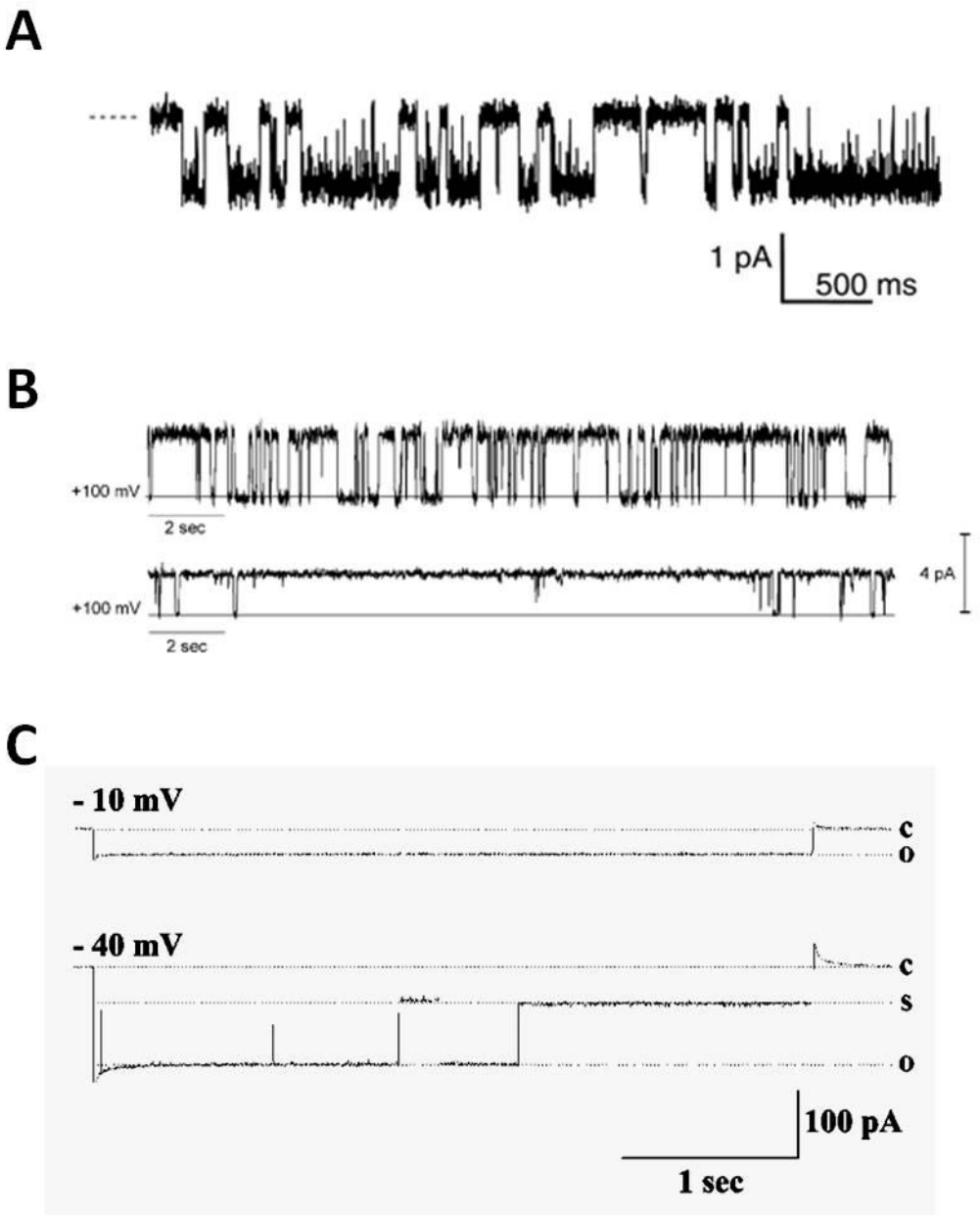


Figure 1.12. Identified SR Cl^- channels
(A) Single-channel recordings of a purified CFTR channel at -80 mV in symmetrical 140 mM NMDG-chloride solutions. Adapted from Cotton and Welsh, 1997 [149]. **(B)** Single-channel recordings of a purified CLIC1 channel in 500:50 mM *cis*/*trans* KCl solutions. Adapted from Singh and Ashley, 2006 [146]. **(C)** Single-channel recordings of a purified VDAC channel in symmetrical 400 mM NaCl. Adapted from Shoshan-Barmatz and Gincel, 2003 [135].

1.4.3 Non-selective SR ion channels

A number of non-selective ion channels are thought to exist in the SR. These include the BRI3-binding protein (BRI3BP) [150], mitsugumin23 (MG23) [151], pannexin channels (PanX1, PanX2, and PanX3) [152]–[154], presenilins [155][156] and transient receptor potential (TRP) proteins (TRPV1, TRPP2, and TRPM8) [157]. The role of these ion channels in unclear. Several, such as BRI3BP, MG23 and PanX1 are thought to play a role in apoptosis [150], [158]–[161]. I have focussed on one of these Ca^{2+}-leak channels: MG23.

1.4.3.1 Mitsugumin23 (MG23)

MG23, also known as TMEM109, is a novel 23 kDa protein which is abundantly expressed in the membranes of the ER/SR, especially in fast-twitch striated muscle fibres [151]. MG23 was first identified by the laboratory of Hiroshi Takeshima (Graduate School of Pharmaceutical Sciences, Kyoto, Japan) in 1998 [162] and shares a close sequence homology with BRI3BP, also a novel protein with unknown functional properties or physiological roles [163][151]. Immunofluorescence analysis of rabbit skeletal and cardiac muscle showed that MG23 was present in the triad (skeletal) and diad (cardiac) junctions and the outer nuclear membranes [162]. After sucrose density gradient centrifugation, MG23 proteins were found not to separate into a specific SR fraction, which suggests that MG23 is not localised to the functional regions of the SR [162].

A physiological role for MG23 is yet to be established, however it has been suggested that MG23 may play a role in promoting apoptosis by generating lethal signals from the SR/ER [158][159]. A recent paper, published through collaboration between the Sitsapesan and Takeshima laboratories, focused on the structure and electrophysiological properties of MG23 [164]. MG23 was found to form a large, 'bowl-shaped', structure in the SR membrane (see Figure 1.13). It was speculated that this structure was formed by six crescent-shaped

monomers. The single-channel properties of purified MG23 protein were also studied. MG23 was found to be a cation selective channel with a single-channel conductance of 85.1±5.3 pS in symmetrical 260 mM KCl and 88.2±2.9 pS in symmetrical 260 mM KPIPES solution. The channel was found to have a low Po and gate with brief open events to a fully open state. Multiple MG23 channels were also observed to gate in the bilayer. Despite these findings, currents from the MG23 channel are yet to be identified in native SR, and it is unclear whether any potential role for this channel exists in EC coupling.

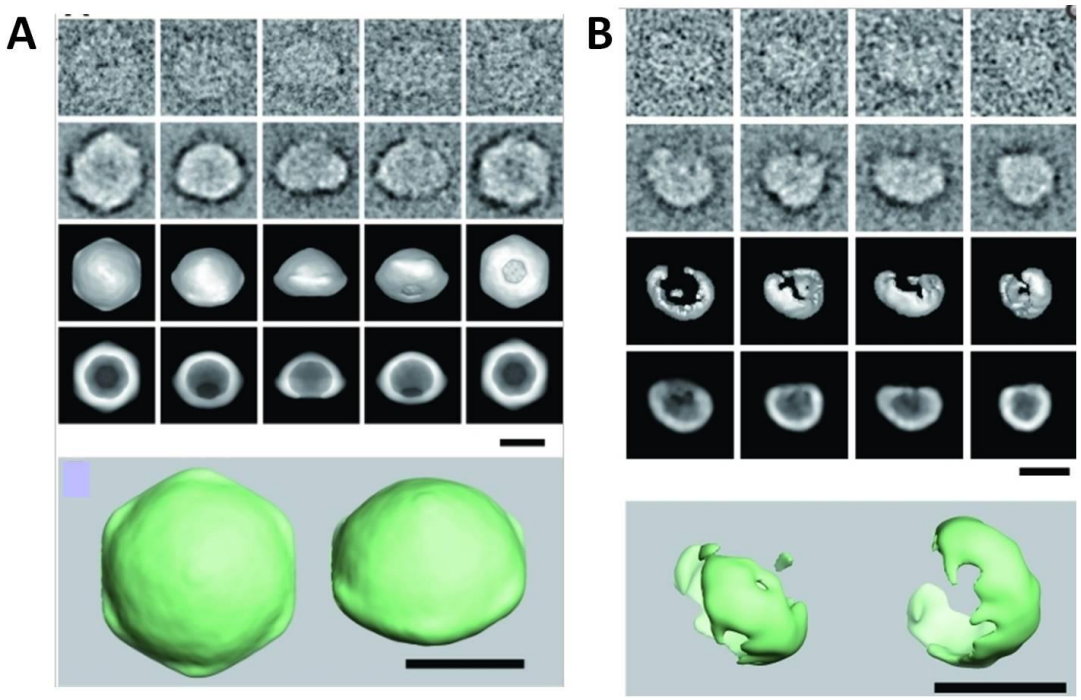


Figure 1.13. The proposed shape of MG23 in its fully constructed (left) and monomeric (right) form taken from Venturi *et al.* (2011) [165]
(A) Reconstruction of the larger-sized MG23 particle. First row, representative raw images; second row, corresponding class averages; third row, surface representations of the 3D reconstruction; fourth row, projections of the 3D reconstruction. Consistency among data sets is very high in size, shape, and inner structure, indicating successful 3D reconstruction from the original images of recombinant MG23 particles. Surface representation of two MG23 structures from top (left) and oblique (right) views. Dimensions of the larger-sized bowl-shaped structure are 12 nm (height), 16 nm (wide side length), and 17 nm (diagonally at the widest transmembrane region). The scale bars are 10 nm. (B) Reconstruction of the smaller-sized MG23 particle. First row, representative raw images; second row, corresponding class averages; third row, surface representations; fourth row, projections of the 3D reconstruction. Dimensions of the smaller-sized crescent-shaped molecule are 14 nm (height), 11 nm (wide side length), and 6 nm (narrow side length). The massive bowl-shaped particle is considered to be an assembly of multiples of this small subunit. The scale bars are 10 nm. Taken from Venturi et al. (2011) [165].

1.5 Aims of this thesis

The major aim of this thesis was to incorporate SR vesicles or purified SR proteins into artificial membranes under voltage-clamp conditions in order to study and identify the various SR K^+ and Cl^- channels which may be involved in providing a countercurrent during Ca^{2+} flux in skeletal and cardiac muscle. I studied SR K^+ channels from rabbit, mouse and sheep cardiac and skeletal muscle and identified similarities and differences between the species. A specific ligand for SR K^+ channels is yet to be identified and so I sought to study the effect of Ca^{2+}, Mg^{2+}, Ni^{2+}, high pH and ATP on SR K^+ channels with the aim of better understanding SR K^+ channel function and regulation.

SR Cl^- channels have been observed in planar lipid bilayer experiments, but have not yet been fully characterised. I therefore attempted to study SR Cl^- channel gating and permeability properties and establish whether they could be identified as currently known Cl^- channels such as the CFTR, VDAC or CLIC channels, or whether they were novel entities.

TRIC channels were recently identified SR K^+ channels, and have been shown to be important for Ca^{2+} release from the SR in a number of studies [81], [83]–[85]. I therefore aimed to characterise the biophysical properties of TRIC channels and their possible regulatory effects on other SR ion channels. I utilised the *Tric-a* KO mouse developed by the Takeshima laboratory [85] to study whether any differences existed between SR ion$^-$ channels from WT and *Tric-a* KO muscle. In order to study TRIC channels directly, I incorporated purified TRIC-A and TRIC-B proteins, reconstituted into liposomes, into bilayers to observe current-fluctuations through the purified channels. I also examined whether TRIC-like gating could be observed in native SR K^+ channel recordings. Finally, MG23 is a novel protein which is localised to the SR. In order to examine how MG23 may interact with other SR ion channels, I studied SR vesicles isolated from *Mg23* KO mice to ascertain whether any differences exist between SR ion$^-$

channels from WT and *Mg23* KO muscle. I also tested a number of potential activators of MG23 on SR from WT and *Mg23* KO mice in an attempt to find an activator of MG23.

Chapter 2. General methods

2.1 Method for isolation of light SR, heavy SR and mixed membrane fractions

Native SR was isolated from skeletal or cardiac animal tissue (rabbit and mouse hind leg or sheep or mouse ventricular muscle) or from cell cultures.

2.1.1 Collection of animal tissue

2.1.1.1 Sheep cardiac tissue

Sheep cardiac tissue was collected from an abattoir (Long Compton Abattoir, Warwickshire, UK). Lambs were slaughtered at 6-8 months. The animals were stunned with a captive bolt and the hearts immediately removed and placed into ice cold bathing solution consisting of 1 l of Hartmann's Solution (28.7 mM sodium lactate, 5.4 mM potassium chloride, 102.7 mM sodium chloride and 2.4 mM calcium chloride dihydrate) and 20 ml of cardoplegia infusion (1.7 M magnesium chloride, 800 mM potassium chloride, 58 mM procaine hydrochloride; Martindale Pharmaceuticals, Buckinghamshire, UK).

The left ventricle of each heart, including the septal wall, was isolated and the excess fat and connective tissue removed. The remaining cardiac tissue was discarded. Each ventricle was cut into two segments and stored in liquid N_2.

2.1.1.2 Rabbit skeletal muscle

Skeletal muscle was collected from the hind leg of adult white New Zealand rabbits of varying ages that had been sacrificed for use in other procedures and was snap frozen and stored in liquid N_2.

2.1.1.3 Mouse cardiac and skeletal muscle

The mouse tissue used was taken from four separate colonies. All *Tric-a* KO mouse tissue originated from a colony of C57-BL6 mice, genetically altered to be devoid of the TRIC-A protein [81], and C57-BL6 mice devoid of MG23 protein were obtained from the University of Kyoto in Japan and were collected by members of the Takashima laboratory (Department of Biological Chemistry, Graduate School of Pharmaceutical Sciences, Kyoto University, Kyoto 606-8501, Japan). WT mice were also taken from the C57-BL6 mice colonies belonging to the Takashima laboratory and the Dora laboratory (Department of Pharmacology, University of Oxford, UK). Mice were sacrificed at 11-16 weeks and their whole hearts and hind leg skeletal muscle were removed and immediately snap frozen and stored in liquid N_2.

2.1.2 Collection of cells for membrane preparations

The cells used for the over expression and purification of intracellular ion channels were Chinese hamster ovary (CHO) cells.

2.1.2.1 CHO cells

Cells were maintained Minimum Essential Medium (MEM) Alpha (Gibco) supplemented with 10% (v/v) FBS (Biosera). Cells over expressing TRIC proteins also included 400 µg/ml Geneticin® (G418; Gibco) and 2% (v/v) penicillin and streptomycin antibiotics (Invitrogen). The cells were kept at 37◦C in a humidified culture incubator supplied with 5% CO_2. After reaching confluency (around 80%), cells were dislodged with 0.05% trypsin (Invitrogen) to give a cell suspension and then either diluted in the desired medium and propagated in new flasks, or they were collected to use for isolating specific membrane fractions.

2.1.3 Heavy SR (HSR), light SR (LSR) and "mixed membrane" isolation procedure from mammalian tissue

All procedures for isolating SR membranes were carried out at 4^{o}C in a cold room. The isolation of mouse cardiac and skeletal SR was performed with half quantities of each solution.

The mammalian muscle was removed from liquid nitrogen storage and was moved on ice to the cold room. The tissue was ground with a liquid N_2-cooled pestle and mortar into pieces approximately 1 cm^3 prior to homogenisation in 300 ml of solution containing 300 mM sucrose, 20 mM piperazine-N,N'-bis [ethanesulfonic acid] (PIPES), protease inhibitors (300 nM aprotinin, 1 µM leupeptin, 1 mM benzamidine, 1 mM phenylmethylsulfonyl fluoride (PMSF)), 2.5 mM dithiothreitol (DTT), pH 7.2. The resultant mixture was then centrifuged at 10,000 x g, for 20 min, at 4°C, in a Sorvall GSA rotor. The pellet was discarded, and the supernatant was ultracentrifuged at 100,000 x g, for 1 h, at 4°C (in a Beckman Type 45i rotor). The pellet at this point contained the mixed membrane fraction.

For a mixed membrane preparation, the pellet would be resuspended in a minimal amount of a solution containing 400 mM sucrose, 5 mM N'-2-hydroxethylpiperazine-N'-2-ethanesulphonic acid (HEPES), buffered to pH 7.2 with Tris. The resuspended pellet was then aliquoted, snap frozen in liquid N_2, and stored at -80^{o}C.

For an HSR and LSR membrane preparation, the pellet was re resuspended in a solution containing 400 mM KCl, 0.1 mM CaCl2, 0.1 mM ethylene glycol-bis(β-aminoethyl ether)-N,N,N',N'-tetraacetic acid) (EGTA), 5 mM PIPES, and 10% w/v sucrose, pH 7.2 and was loaded onto the top of a discontinuous sucrose gradient, prepared using three different concentrations of sucrose: 20 %, 30 %, and 40 % w/v also dissolved in a solution containing 400 mM KCl, 0.1 mM $CaCl_2$, 0.1 mM EGTA, 5 mM PIPES, pH 7.2. The solutions were layered on top of each other in a 32 ml Beckman tube, as shown in Figure 2.1, using a 10 ml glass syringe

attached to a 10 cm needle with a 14 mm diameter. The sarcolemma remained at the top of the tube , the LSR membranes sedimented to the 20-30% interface and the HSR membranes sedimented to the 30-40% interface [166]. The LSR and HSR were collected and diluted in 400 mM KCl, 10 mM PIPES, pH 7.2. The mixture was ultracentrifuged at 100,000 x g, for 1 h, at 4°C (in a Beckman 45i rotor) to remove the excess sucrose and the pellets were resuspended in a solution containing 400 mM sucrose, 5 mM N'-2-hydroxethylpiperazine-N'-2-ethanesulphonic acid (HEPES), buffered to pH 7.2 with Tris, aliquoted, snap frozen in liquid N_2, and stored at -80 °C.

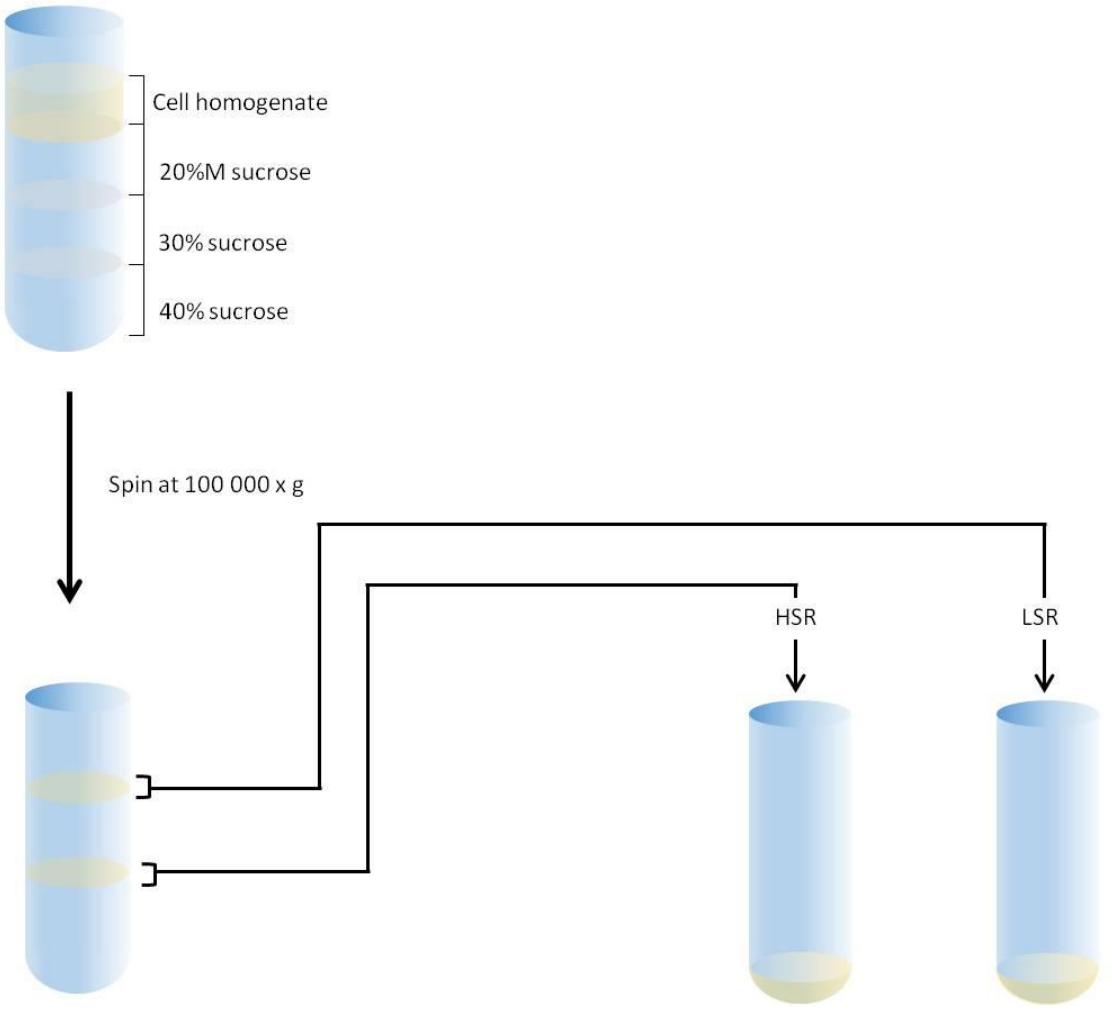


Figure 2.1. Schematic illustration of 20-40 % sucrose density gradient and LSR/HSR collection
10 ml of 40 % sucrose, 30 % sucrose and 20 % sucrose were sequentially added to a Beckman tube. The mixed membrane, diluted in 10 % sucrose was layered on top (top left). Following centrifugation, the LSR and HSR were detected at the 20%-30% and the 30%-40% (w/v) interfaces, respectively (bottom left). The LSR and HSR fractions were collected (bottom right).

2.1.4 Isolation of HSR and LSR from cell cultures

The cells were removed from liquid nitrogen storage and moved on ice to the cold room at 4^{o}C. At each stage of the procedure, a 50 µl aliquot was set aside for western blot analysis. The cells were resuspended in 15 ml of 10 mM HCl buffered to pH 7.2 with Tris and homogenised thoroughly using a 15 ml glass homogeniser and rod. The cell homogenate was then transferred to a 50 ml centrifuge tube and mixed in a 1:1 ratio with 600 mM sucrose, 10 mM HCl buffered to pH 7.2 with Tris and centrifuged at 4 ^{o}C at 10 000 x g for 10 min in a Sorvall GSA rotor. The supernatant was collected and centrifuged at 4 ^{o}C at 100 000 x g for 1 hour in a in a Beckman SW32 Ti rotor. The pellet was then removed and resuspended in 1 ml of 300 mM sucrose, 10mM HCl buffered to pH 7.2 with Tris and homogenised using a 3 ml glass homogeniser and rod. The homogenate was then layered on top of a discontinuous sucrose gradient with sucrose bands of 1.1 M, 1.3 M and 1.6 M as shown in Figure 2.2. The gradient was centrifuged at 100 000 x g for 2 hours at 4 ^{o}C (Beckman SW55 Ti rotor). The sediment at each interface was collected in centrifuge tubes (Figure 2.2) and diluted in 10mM HCl buffered to pH 7.2 with Tris such that the sediment in interface I was diluted 2x (v/v), interface II was diluted 3x (v/v), and interface III was diluted 4x (v/v). The tubes where centrifuged at 100 000 x g for 1 hour at 4 ^{o}C (Beckman SW55 Ti rotor). The pellet was resuspended in a minimal amount of 300 mM sucrose, 10mM HCl buffered to pH 7.2 with Tris, aliquoted, snap frozen in liquid N_2, and stored at -80 ^{o}C.

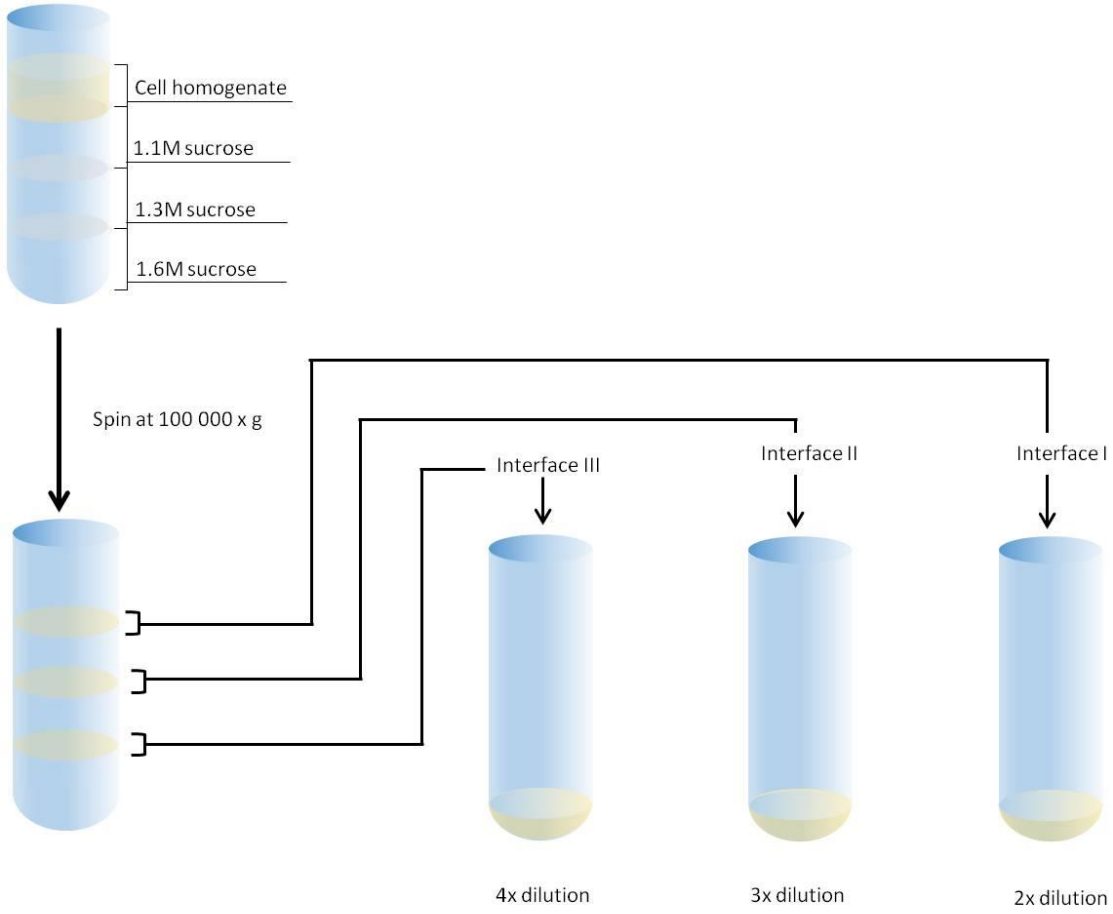


Figure 2.2. Schematic illustration of 1.1 M-1.6 M sucrose density gradient and LSR/HSR collection

10 ml of 1.6 M sucrose, 1.3 M sucrose and 1.1 M sucrose were sequentially added to a Beckman tube. The cell homogenate, diluted in 1 M sucrose was layered on top (top). Following centrifugation, the LSR and HSR were detected at the three interfaces (bottom).

2.2 Measurement of protein concentration

Protein concentration was measured using a Bradford assay [167]. The Bradford assay takes advantage of the innate acidity of proteins to cause a colour change in the pH sensitive dye, Coomassie Brilliant Blue G-250. The colour results in difference absorbance properties of solutions which contain protein. By comparing the absorbance to standards with known protein concentrations, the protein concentration of the solution can be calculated.

The standards were made with Bovine Serum Albumin (BSA, Protein Standard 1 mg/ml, Sigma Aldrich) diluted in water to the following percentages (w/v): 100 %, 75 %, 50 %, 25 %, and 12.5 %. Bradford reagent dye was diluted in water to a 1:4 dilution. 20 µl of each standard was added to a cuvette and mixed with 1 ml of the diluted Bradford reagent dye. The absorbance of each standard plus a blank (water) was measured using a Biomate 3 Series Spectophotometer (Thermo Electron Limited, Cambridge, UK) and the BSA standard curve plotted. The protein sample to be measured was diluted 1:1000 and 20 µl was mixed with diluted Bradford reagent dye at a 1:4 dilution and its absorbance measured. The protein reading was repeated three times and the mean value taken. The protein concentration was obtained by extrapolation from the BSA linear standard curve.

2.3 The planar lipid bilayer technique

The planar lipid bilayer technique is an electrophysiological technique first described by Mueller et al (1962) [168]. Planar lipid bilayer experiments are useful in recording currents across intracellular membranes, such as the SR which are difficult to study using traditional patch clamp techniques, and allows the study of intracellular ion channels at a single molecule level under highly controlled conditions.

2.3.1 The bilayer apparatus

Bilayer experiments were conducted using a specialised planar lipid bilayer apparatus consisting of a Delrin (acetyl resin) cup (Warner Instrument, Hamden, USA) shown in Figure 2.3A which contained an aperture with a diameter of 150-200 µm, and a Perspex block (Warner Instrument, Hamden, USA) which contained a figure-of-eight-shaped cavity (Figure 2.3B). The cup was placed into one side of the cavity to form two chambers (Figure 2.3C). The chambers are designated the *cis* chamber (the cup) and the *trans* chamber (the remaining empty side of the block cavity). The two smaller cavities shown on the left side of the block in Figure 2.3 were filled with 200 µl of 3M LiCl which each respectively accommodating a silver chloride electrode, connected to a head stage, and an agar bridge, connecting the cavity to its corresponding chamber. The agar bridges were formed from glass capillaries bent into a U-shape over a Bunsen burner and filled with 3M LiCl and 2 % (w/v) agar as shown in Figure 2.3C. The bridges were stored in 3M LiCl. To conduct bilayer experiments, the *cis* and *trans* chambers were filled with 1 ml of the bath solution and the *cis* chamber was voltage clamped relative to the ground (*trans* chamber).

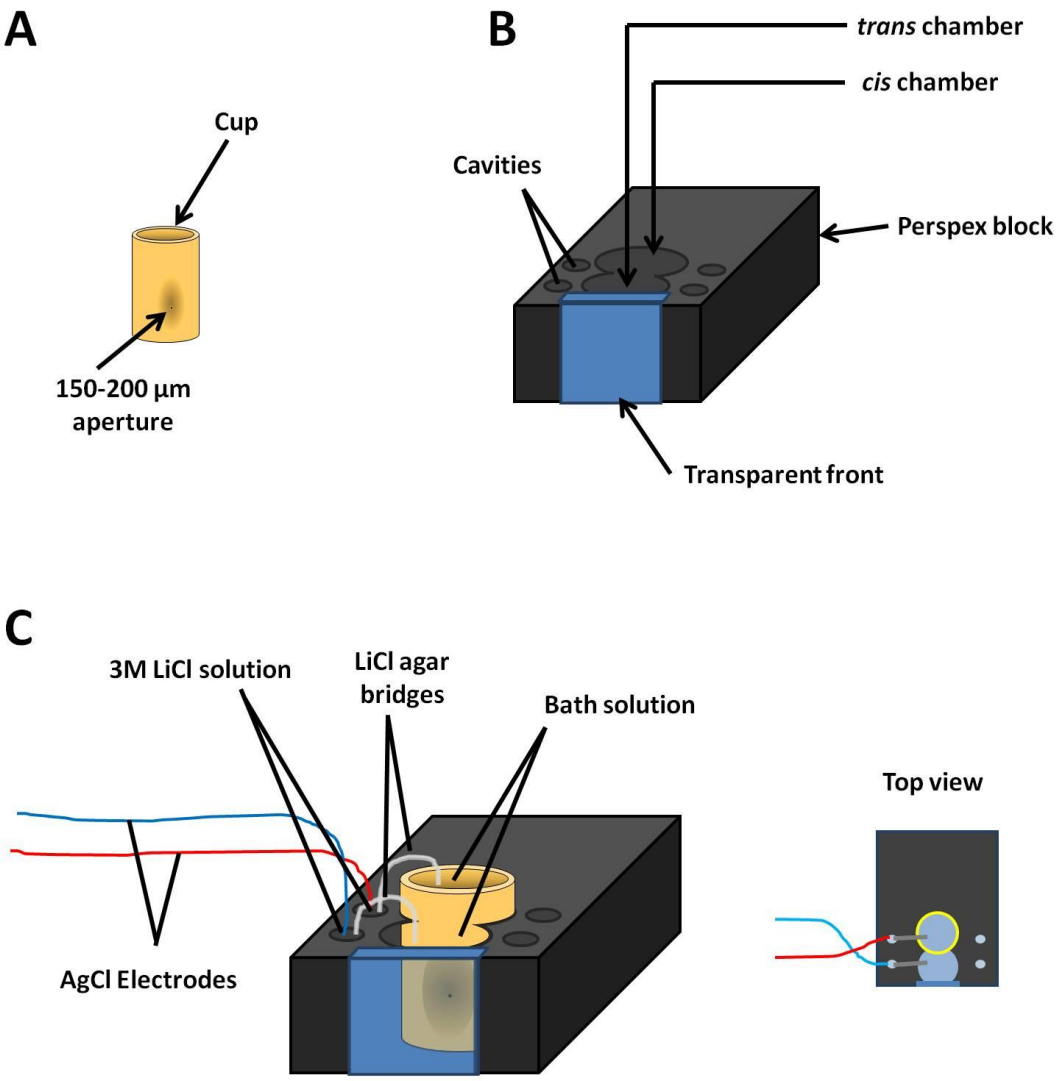


Figure 2.3. Schematic of the block and cup apparatus.
(A) The Delrin cup with the 150-200 µm aperture labelled. **(B)** The Perspex block showing the positions of the *cis* and *trans* chambers. **(C)** The bilayer setup showing the positions of each solution, the electrodes and the agar bridges.

2.3.2 Electrical equipment used for experimentation and data acquisition

The electrical equipment used to acquire electrophysiological recordings was as follows:

- BC-525 bilayer clamp amplifier (Warner Instruments, Hamden, USA) and a headstage which the silver chloride electrodes from the bilayer apparatus were attached. The amplifier contained a 4-pole Bessel filter which was used to filter the outgoing signal to the computer. A filter of 10 kHz was applied to the recordings in this thesis.

- InstruTECH ITC-18 Interface (HEKA, Elektronik Lambrecht/Pfalz, Germany) was used to convert the analogue signal from the amplifier into a digital form that could be stored on the computer.

- A computer (Viglen DQ35JO, Intel core) was used for data acquisition and analysis (Windows 7 professional, 32 bit). The computer ran WinEDR software (University of Strathclyde, UK), which was used to record the digital data.

- A low pass 8-pole Bessel filter (Frequency Devices Inc, Ottawa, Canada) was used to filter the signal from the amplifier for real time visualisation of the single-channel current fluctuations

- An oscilloscope (Hitachi VC-6545, UK) was used to preview the data (filtered through the low pass 8-pole Bessel filter) during the acquisition.

- A magnetic stirring system (Spin-2 stir plate, Warner Instruments, LLC, Hamden, CT, USA) on which was seated the block with the cup. The system allowed solutions to be mixed in both chambers using small magnetic stir bars.

- An aluminium box which acts as a faraday cage. The block/cup apparatus together with the stirring system and the head stage were held within the faraday cage to prevent background radiation from interfering with experiments.

The equipment was set-up as shown in Figure 2.4 and grounded through the central grounding point of the system located on the rear panel of the BC-525 amplifier to maintain background electrical noise at a minimal level.

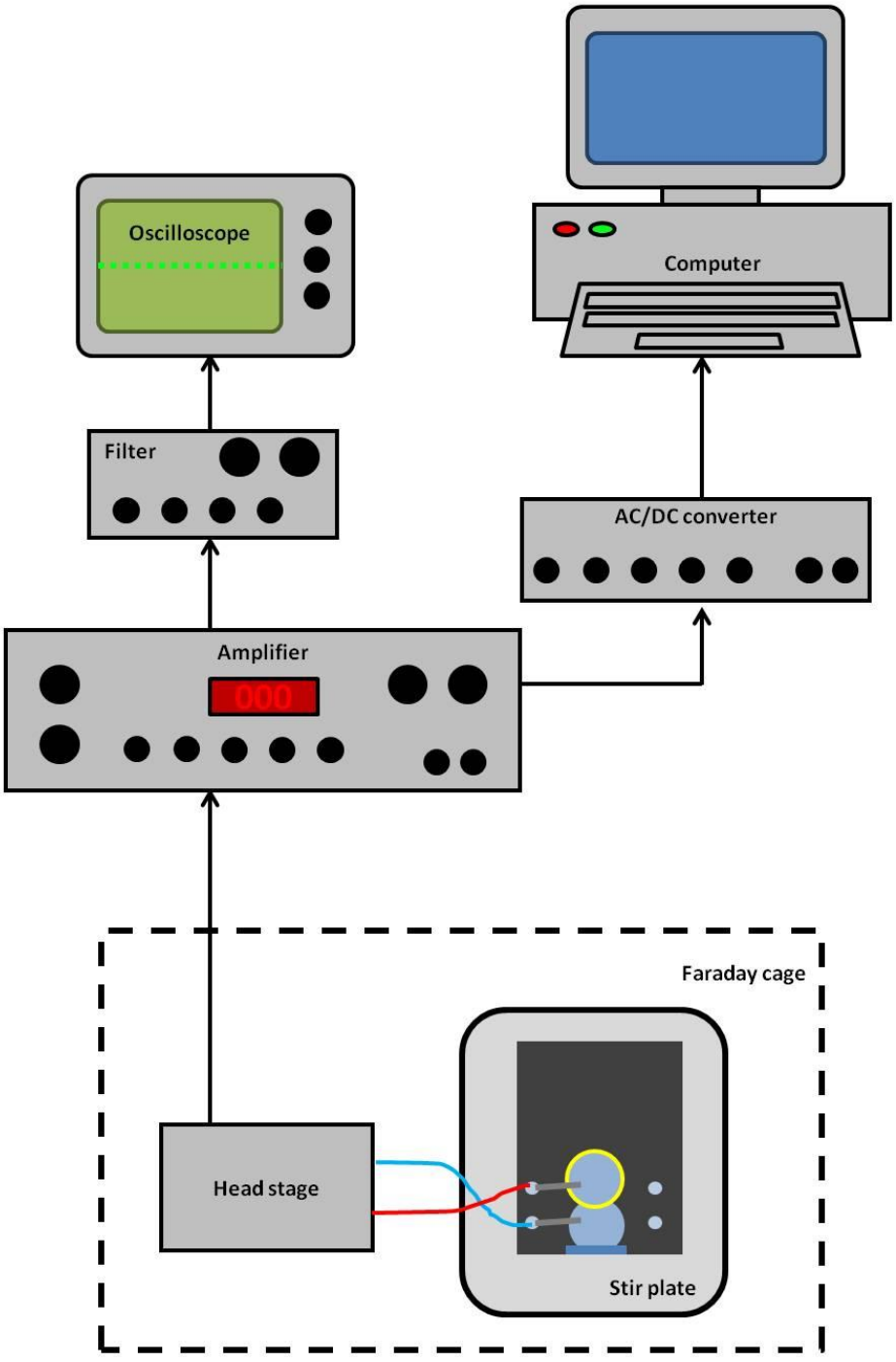


Figure 2.4. A schematic of the electrical equipment used for data acquisition during planar lipid bilayer experiments.
The black arrows correspond to electrical connections and the flow of data. The black dashed line represents the limit of the Faraday cage.

2.4 Forming an artificial bilayer

Planar lipid bilayer recordings require the incorporation of vesicles containing the protein of interest into artificial bilayers. To accomplish this, artificial planar lipid bilayers were formed following the method first described by Miller (1978) [72].

2.4.1 Lipids

Phosphatidylethanolamide (PE) lipids were purchased from Avanti Polar Lipids (Birmingham, AL, USA) and stored at a concentration of 50 mg/ml in chloroform at -80°C. Prior to use, the chloroform was evaporated off using N_2 gas and the PE was resuspended in decane to obtain a final concentration of 35 mg/ml.

2.4.2 Priming

Before an artificial bilayer can be painted, the cup aperture must be treated with lipid to allow a stable bilayer to form. This process is called priming. 1 µl of the PE lipid-decane mixture was applied to the outside of the cup covering the aperture and was allowed to dry. The cup was then placed into the block as described earlier.

2.4.3 Painting an artificial bilayer

Once the cup had been primed and the bilayer apparatus was set up as described above, the *cis* and *trans* chambers were filled with 1 ml of the desired bath salt solution. An artificial bilayer was formed by covering the end of a clean pipette tip with the PE lipid-decane mixture described in Section 2.3.1, and using the tip to 'paint' the lipid over the aperture from the inside of the cup. The lipid covers the aperture, disrupting the current flow between the *cis* and *trans* chambers. Initially, the lipid is several micrometers thick and cannot be considered

to be a bilayer, however after several seconds, the centre of the bilayer will become thinner due a number of forces [169][170][171].

2.4.4 Thinning of the bilayer

Due to the nature of the membrane in the circular aperture, the lipid will form into a thick torus around the rim of the aperture with the centre portion thinning out, this is as a result of the Plateau-Gibbs border suction force [171]. Due to the pressure being greater at the membranes thinnest point, the surrounding solution either side of the membrane is pushed to the sides of the aperture which thins the membrane. As areas of the membrane thin to a bilayer, Van der Waals forces between the aqueous phases in each bath solution increase the pressure on the thinner areas of the membrane, which results in additional thinning of the bilayer [169]. Eventually, steric repulsion prevents the membrane from thinning further and the Van der Waals forces counteract the Plateau-Gibbs border suction force by preventing solution from moving to the sides of the aperture. Equilibrium of these forces is required to form a stable bilayer.

2.4.5 The voltage clamp technique

When the *cis* and *trans* chambers are filled with salt solutions, a current can flow between the two chambers connecting the electrodes, thus a simple circuit exists from the head stage (connected to the amplifier), along one electrode to the *cis* chamber, from the *cis* to the *trans* chamber, along the second electrode and back to the head stage. Forming a bilayer in the cup aperture between the two chambers prevents this current from flowing and breaks the circuit. Under these conditions, the bilayer behaves like a capacitor and stores energy as electrical charge either side of the membrane. When an ion channel is present and in an open state in the bilayer, ions can pass through the pore of the channel, re-connecting the circuit. Ionic movement through the pore of an ion channel is limited however and thus the channel pore

acts as a resistor. The units for the resistance of the pore are given in GΩ. Ion channel conductance is therefore given as the inverse of this in the units, pS.

A system in which an artificial bilayer is present separating the *cis* and *trans* chambers, but which contains an ion channel in an open state can therefore be thought of as a circuit which contains a capacitor (the bilayer) and a resistor (the ion channel pore). Under these conditions, the total current through the bilayer (I_b) is the sum of the current through the bilayer capacitor (C_b) and the current flowing through the ion channels (I_i), expressed in the below equation:

$$I_b = I_i + C_b \frac{dV}{dt}$$

Equation 1

During single-channel experiments, I_b is measured using the voltage-clamp technique, first developed by Hodgkin and Huxley (1952) [172]. The artificial bilayer is voltage-clamped which means that dV/dt = 0 therefore eliminating C_b. The current measured across the bilayer is therefore only the current passing through the channel.

2.4.6 Bilayer detection and estimate of the area

The BC-525 amplifier has the ability to measure the capacitance of the membrane using the capacitance test or "CAPTEST" function. The membrane capacitance is used to estimate the size of the membrane area which is a bilayer into which we can fuse vesicles.

The capacitance (C_b) of the bilayer is directly proportional to its surface area (A) and dielectric constant (ε), and is inversely proportional to the thickness of the bilayer (d). Therefore membrane capacitance can be calculated using the following equation:

$$C_b = \varepsilon \frac{A}{d}$$

Equation 2

Where C_b is the membrane capacitance, **ε** is the dielectric constant, ***d*** is the distance between two phospholipid tails and ***A*** is the area. As the current (***I***) through a capacitor is equal to:

$$I = C_b \frac{dV}{dt}$$

Equation 3

Equation 3 can be substituted into Equation 2:

$$I = \varepsilon \frac{A}{d} \frac{dV}{dt}$$

Equation 4

In CAPTEST mode, the amplifier applies a triangular wave to the membrane which means that dV/dt is constant. Additionally, ***ε*** depends on the lipids used and ***d*** depends on the length of the lipid tails and therefore these terms also constant. Equation 4 can thus be simplified as:

$$I = kA$$

Equation 5

Where ***k*** is a constant of proportionality, and ***A*** is the area of the bilayer within the membrane. This was expressed as a capacitance for the membrane in pF.

The desired capacitance for the experiments conducted in this thesis were between 100-120 pF.

2.5 Incorporating liposomes containing native or recombinant protein

After a bilayer of the desired capacitance was formed in symmetrical salt solutions, liposomes containing protein of interest can be incorporated into the bilayer. To achieve this, an osmotic gradient was formed across the membrane by adding a strong salt solution (usually 3 M) to the *cis* chamber. 1-2 µl of the final snap frozen preparation from section 2.1.3 or 2.1.4 which contained liposomes were then also added to the *cis* chamber and the chamber was stirred. The creation of an osmotic gradient is essential for vesicle fusion. It causes the liposomes to move towards the osmotic gradient and adhere to the bilayer where, water flowing down the osmotic gradient across the bilayer from the *trans* to the *cis* chamber results in swelling of the adhered liposomes [173]. Eventually the swollen liposomes burst and fuse with the bilayer [173][174]. After incorporation, the *cis* and *trans* chambers are perfused with the chosen recording solution to remove any un-fused vesicles, preventing further fusion events.

2.5.1 Fusion events

The experiments conducted in thesis incorporated ion channels into the bilayer under gradient conditions where the *cis* chamber held a higher ionic concentration relative to the *trans* chamber. Under these conditions, it is possible to identify whether the vesicle which has incorporated into the bilayer contains predominantly cation or anion channels. Figure 2.5 shows examples of how the fusion of cation selective channels would result in a positive or

upward current fluctuation, and the fusion of anion selective channels would result in a negative or downward current fluctuation. This observation was used when studying Cl^- currents as SR K^+ channels usually incorporated into the bilayer before SR Cl^- channels and therefore it was often important to wait until the first Cl^- incorporation event (a negative current-fluctuation) was observed.

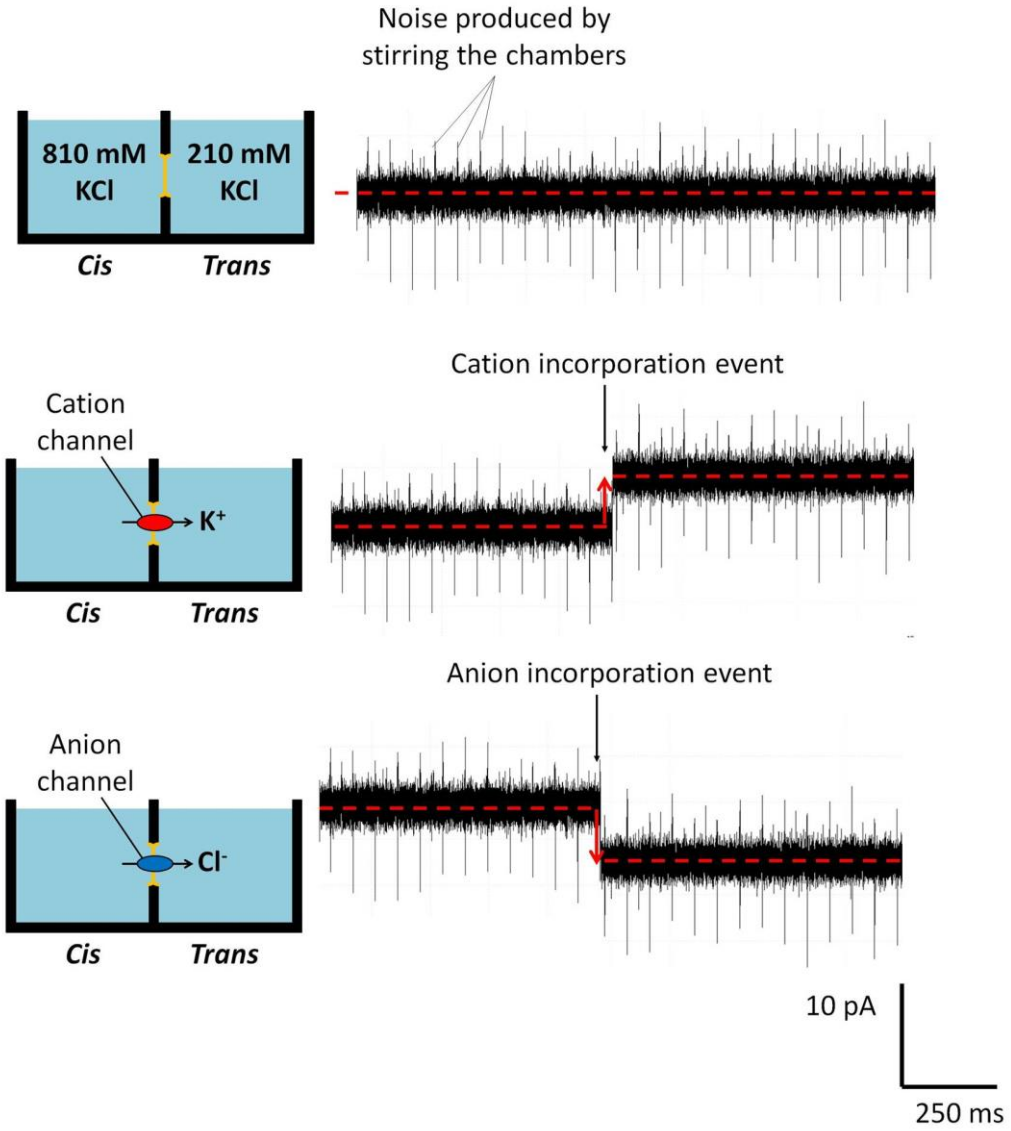


Figure 2.5. Schematic showing examples of current-fluctuations through unfiltered traces when ion channels incorporate into the bilayer

The top trace shows how a bilayer recording during incorporation when no ion channels are present in the bilayer. The spiky events correspond to noise generated by the stir bars in both the *cis* and *trans* chambers used to aid incorporation. The middle traces shows an example of an incorporation event where a vesicle containing a cation selective channel has fused with the bilayer. This fusion event results in a K^+ current from the *cis* to the *trans* chamber (down the gradient slope) and a positive (upward) current-fluctuation being observed. The bottom trace shows an incorporation event where a vesicle containing an anion selective channel has fused with the bilayer. This fusion event results in a Cl^- current from the *cis* to the *trans* chamber, and a negative (downward) current-fluctuation being observed. All recordings were recorded in asymmetric (810 mM *cis*: 210 mM *trans*) KCl solutions and at a holding potential of 0 mV. The average current is shown by a red line.

2.5.2 Incorporation of native SR vesicles

Special note should be taken of the phenomenon of channel orientation when native SR vesicles were incorporated into artificial bilayers. In this thesis, experiments were conducted with either native SR vesicles, or with proteoliposomes which contain purified protein. Ion channels are often not symmetrical and have distinct poles which may have different physiological or pharmacological properties. When studying ion channels in the bilayer system, the orientation of the channel in the bilayer is therefore important. Unfortunately, in purified preparations, this cannot be controlled due to the purification process which usually involved the stripping of the protein from their native membranes with detergent and then reconstituting them into liposomes for bilayer experiments. Under these conditions, ion channels would be unlikely to maintain their original orientation.

This is not the case with native SR membrane preparations however. Vesicles produced from isolated SR membranes leave ion channels in their native lipid environments and have been shown to incorporate into the bilayer in a fixed orientation[64][175][176]. Evidence for this was provided by experiments on SR membranes where tetraethyl ammonium (TEA) block of "native Ca^{2+} release channels" was only observed when the drug was added to the *cis* chamber but never when the drug was added to the *trans* chamber [176]. It was hypothesised that this is due to the "native Ca^{2+} release channels", later identified as the RyR protein, being unable to orientate to the opposite direction during incorporation due to its large size and distinctive mushroom-like shape [176]. We can therefore assume that, when native SR vesicles are incorporated into an artificial bilayer, the *cis* chamber corresponds to the cytosolic side of the membrane and the *trans* chamber corresponds to the luminal side of the membrane [175][176]. We can use this as a marker for the orientation of RyR as well as other SR channels such as the SR K^+ channel and SR Cl^- channels. Further, my own experiments supported this assumption as I observed the voltage sensitivity of the SR K^+ channel to be maintained

throughout my experiments, suggesting that this channel retained its *cis*/cytosolic-*trans*/luminal orientation after incorporation into artificial bilayers (see Chapter 3).

2.6 Solutions used in planar lipid bilayer experiments

2.6.1 Choosing the right ion

In planar lipid bilayer experiments, the choice of permeant ion is important and must be considered in all experiments. Let us consider a basic experimental set-up with 210 mM KCl symmetrically in both the *cis* and *trans* chambers and with an unknown ion channel gating in the bilayer. Under these conditions, the channel conductance can be calculated by performing and IV plot and the channel Po can be measured, pharmacological properties of the channel could also be studied. However, these conditions are limiting if we want to study channel permeability. To find the relative permeability of K^+ relative to Cl^- (P_K/P_{Cl}), a gradient can be formed across the bilayer and the P_K/P_{Cl} calculated from the modified Goldman-Hodgkin-Katz equation (see Equation 15). Ether K^+ or Cl^- can be exchanged for alternative cations or anions, respectively to measure the P_x/P_x. More complications are introduced when we consider native membranes. The SR contains a large number of proteins, many of them ion channels with different properties. This can therefore introduce difficulties if only a cation channel or an anion channel is to be studied. To overcome this, Cl^- could be replaced with a large, impermeable anion such as PIPES or glutamate which would mean that, as most anion channels do not pass these large ions, the cation current can be isolated and studied. Similarly, K^+ can be replaced with NMDG or choline to isolate the anion current.

For each bilayer experiment, therefore, the anion and cation, as well as their *cis* and *trans* concentrations were carefully chosen to fulfil the experimental aims. In this thesis, the bath solutions used in each experiment are detailed in the top right of each figure as described below.

2.6.2 Typical electrophysiological bath solutions used in this thesis

210 mM KCl: 210 mM KCl solution containing contaminant Ca^{2+} at 10 µM, 20 mM HEPES buffered to pH 7.2 with KOH making a final [K^+] of 210 mM. This solution was used to study purified protein.

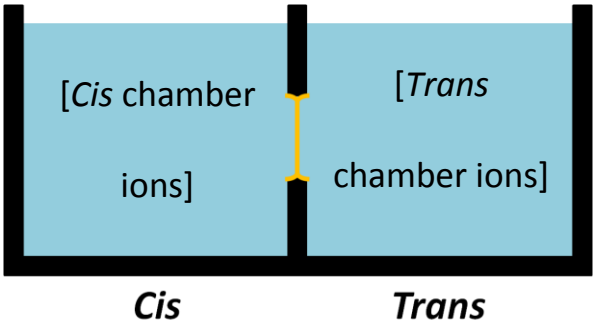
210 mM KPIPES: 210 mM KOH solution containing contaminant Ca^{2+} at 10 µM buffered to pH 7.2 with PIPES salt. This solution was used to study the native SR K^+ channel and RyR.

KCl gradient/asymmetrical KCl: 200 µl of 3 M KCl solution was added to the *cis* chamber in symmetrical conditions to create a gradient. This solution was used for channel incorporation and to study the Sarcoplasmic Reticulum Anion Selective (SRAS) channel (Chapter 4) and TRIC-A and TRIC-B channel P_K/P_{Cl} ratios (Chapter 6).

50 mM choline-chloride: 50 mM choline-Cl solution containing contaminant Ca^{2+} at 10 µM, 10 mM HEPES salt, buffered to pH 7.2 with Tris salt. Higher concentrations of this solution could be added to either the *cis* or *trans* chamber. A KCl gradient was used to incorporate Cl^- channels. This solution as used to study Cl^- currents through native and purified channels.

50 mM NMDG-chloride: 50 mM HCl solution containing contaminant Ca^{2+} at 10 µM buffered to pH 7.2 with NMDG salt. Higher concentrations of this solution could be added to either the *cis* or *trans* chamber. A KCl gradient was used to incorporate Cl^- channels. This solution as also used to study Cl^- currents through native and purified channels.

For the purpose of this thesis, each relevant figure will be accompanied with the schematic below which will describe the ions present in each chamber. The schematic depicts the *cis* and *trans* chambers and the ionic concentrations present in each. Unless otherwise stated, the free [Ca^{2+}] of our solutions is 10 µM, calculated as described below, and the pH is 7.2.



2.6.3 Liquid Junction potentials

When asymmetrical solutions are present in the *cis* and *trans* chamber, a liquid junction potential can form at the junction between the salt bridge and the bath solution [177]. Figure 2.6 shows the components which contribute to the formation of a liquid junction potential.

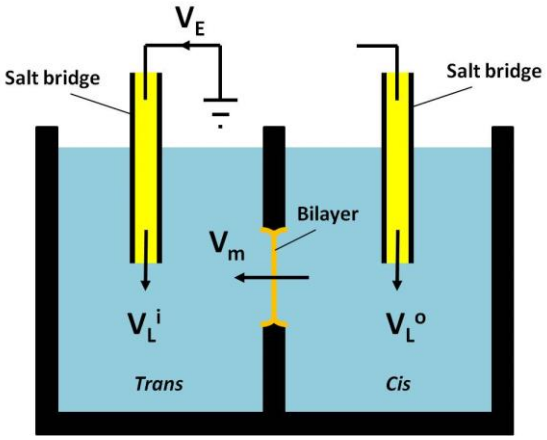


Figure 2.6. A schematic illustration of the cis and trans chambers showing the contributing factors to a liquid junction potential.

The liquid junction potential can thus be calculated using the following equation:

$$V_m = V_E + \left(V_L{}^i - V_L{}^o\right)$$

Equation 6

Where V_m is the calculated E_{rev}, V_E is the holding potential, and $(V_L{}^i - V_L{}^o)$ is the liquid junction potential. In order to accurately calculate an E_{rev} value therefore, the liquid junction potential must be taken into account and added to any observed E_{rev} values.

The liquid junction potentials for common solutions used in this thesis are summarised in the table below.

Cis (mM)	Trans (mM)	Salt bridge (mM)	VLi – VLo (mV)
810 KCl	210 KCl	3000 LiCl	-8.6
210 KPIPES + 600 KCl	210 KPIPES	3000 LiCl	-12.4
350 Choline-Cl	50 Choline-Cl	3000 LiCl	-15.9
350 NMDG-Cl	50 NMDG-Cl	3000 LiCl	-17.1

Table 1. Calculated liquid junction potentials for common solutions used in this thesis
Values were calculated using the Calculate Liquid junction potential function in Clampex 10.3 (Molecular devices, CA, USA).

In order to test the accuracy of the liquid junction potentials calculated using Clampex, the calculated vales were compared with liquid junction potentials measured experimentally. To achieve this, the bilayer system was set up as described in Section 2.3 with symmetrical solutions in both chambers, and the offset of the system was then corrected for. The solutions in the chambers were then adjusted to reflect the conditions for which the liquid junction potential was to be recorded. Over several min, the offset of the system was studied until a no further change in offset was observed. The offset at this point was taken to be the liquid junction potential for the solution.

This was performed for the solutions in Table 1 and the following results were obtained:

Cis (mM)	Trans (mM)	Salt bridge (mM)	Liquid junction potential (mean±SD, mV)
810 KCl	210 KCl	3000 LiCl	-7.8±4.3 (n=4)
210 KPIPES + 600 KCl	210 KPIPES	3000 LiCl	-12.1±3.5 (n=3)
350 Choline-Cl	50 Choline-Cl	3000 LiCl	-11.2±7.1 (n=3)
350 NMDG-Cl	50 NMDG-Cl	3000 LiCl	-18.0±4.9 (n=3)

Table 2. Measured liquid junction potentials for common solutions used in this thesis

Little difference was observed between the calculated (Table 1) and the measured (Table 2) liquid junction potential values and so the calculated values were considered accurate. For the purposes of this thesis, the calculated liquid junction potentials were used when performing planar lipid bilayer experiments.

2.7 Protocol for the study of proteins in the bilayer system

2.7.1 Native membranes

The snap frozen native SR membranes, prepared as described above, were collected at the beginning of the day and stored on ice.

2.7.1.1 The SR K^+ channel and the RyR1 and RyR2 proteins

The c*is* and *trans* chambers were filled with symmetrical 210 mM KPIPES solution. For channel incorporation, a KCl gradient and 1-2 µl of SR membrane was added to the *cis* chamber. The system was voltage clamped at 0 mV and the *cis* chamber was stirred until a fusion event was observed. The *cis* chamber was then perfused with 210 mM KPIPES solution and the experiment begun.

2.7.1.2 The Sarcoplasmic Reticulum Anion Selective (SRAS) channel

The c*is* and *trans* chambers were filled with symmetrical 210 mM KPIPES solution. For channel incorporation, a KCl gradient and 1-2 µl of SR membrane was added to the *cis* chamber. The system was voltage clamped at 0 mV and the *cis* chamber was stirred until a fusion event was observed. The experiment was begun at this point.

2.7.1.3 The Sarcoplasmic Reticulum Anion Leak (SRAL) channel

The c*is* and *trans* chambers were filled with symmetrical 50 mM choline-Cl or NMDG-Cl solution. For channel incorporation, a KCl gradient and 1-2 µl of SR membrane was added to the *cis* chamber. The system was voltage clamped at 0 mV and the *cis* chamber was stirred until a fusion event was observed. The *cis* chamber was then perfused with 50 mM choline-Cl or NMDG-Cl solution and the experiment begun.

2.7.2 Purified TRIC-A and TRIC-B

Recombinant purified TRIC-A and TRIC-B preparations reconstituted into liposomes were obtained directly from our collaborators. Reconstituted human TRIC-A was obtained from the Carpenter laboratory (Structural Genomics Consortium, University of Oxford, Oxford, UK) and reconstituted *C. Elegans* TRIC-B1 was obtained from the Laboratory of Zhenfeng Liu (National Laboratory of Biomacromolecules, CAS Centre for Excellence in Biomacromolecules, Institute of Biophysics, Chinese Academy of Sciences, Beijing 100101, China).

2.7.2.1 KCl experiments

The c*is* and *trans* chambers were filled with symmetrical 210 mM KCl solution. For channel incorporation, a KCl gradient and 1-2 µl of SR membrane was added to the *cis* chamber. The system was voltage clamped at 0 mV and the *cis* chamber was stirred until a fusion event was

observed. The *cis* chamber was then perfused with 210 mM KCl solution and the experiment begun.

2.7.2.2 Choline-Cl experiments

The c*is* and *trans* chambers were filled with symmetrical 50 mM choline-Cl solution. For channel incorporation, a KCl gradient and 1-2 µl of SR membrane was added to the *cis* chamber. The system was voltage clamped at 0 mV and the *cis* chamber was stirred until a fusion event was observed. The *cis* chamber was then perfused with 50 mM choline-Cl solution and the experiment begun.

2.8 Measuring the pH of solutions

The pH of solutions was measured at 20±2°C using a Ross-type pH electrode (Orion 81-55). Unless stated otherwise, the solutions in this thesis were buffered to a pH of 7.2.

2.9 Measurement of free [Ca^{2+}]

The free [Ca^{2+}] of solutions was measured at 20±2°C using a Ca^{2+} electrode (Orion 93-20) following the methods put forward by Bers (1982) [178]. Experiments were performed at 10 µM free [Ca^{2+}] unless stated otherwise. Free [Ca^{2+}] was lowered using EGTA to a calculated free [Ca^{2+}], calculated using MaxChelator software (Stanford University, CA, USA). Free [Ca^{2+}] was increased by adding $CaCl_2$ to either chamber.

2.10 Analysis of single-channel recordings

2.10.1 Data acquisition

As briefly described earlier in this chapter, analogue data was collected by a BC-525 bilayer clamp amplifier (Warner), and converted to a digital format using an InstruTECH ITC-18

Interface (HEKA). The digital data was recorded using WinEDR software (University of Strathclyde) using a computer (Viglen, Microsoft).

When digitising analogue data, there is a danger of aliasing (distorting) the signal if the data unless an optimum sample frequency (f_s) is used when converting the signal. The f_s was calculated according to the Nyquist-Shannon Sampling Theorem which states that the f_s must be a minimum of twice the frequency of the filtering rate (1kHz) see below (*B*) [179][180], thus:

$$f_s = 2(B)$$

Equation 7

In this thesis, I therefore used f_s = 5(*B*) to ensure that aliasing was minimal, but also that recordings were kept to a manageable size on the computer hard drive. The amplifier contained an internal low-pass 4-pole Bessel filter which filtered the data at 10 kHz; therefore by applying the chosen f_s the sampling frequency of the data was 50 kHz.

Once the data had been digitised, it was filtered at 1 kHz using the low-pass filter which is part of the WinEDR software suit. This filtering level removed high frequency noise which could result in erroneous measurements during single-channel analysis.

2.10.2 Single-channel analysis

Ion channel activity can be defined as a function of their single-channel conductance and their open probability (Po). These two parameters were therefore calculated for each channel studied.

2.10.2.1 Single-channel conductance

As described earlier in this chapter, an ion channel gating in the bilayer behaves as a resistor with a resistance (*R*), measured in GΩ. The conductance (*G*) of an ion channel can therefore be calculated as the inverse of the resistance with the units pS according to the following equation:

$$G = \frac{1}{R}$$

Equation 8

In planar bilayer experiments, the system is voltage clamped via the amplifier at a defined voltage (*V*) and the current passing between the chambers (*I*) is measured. Therefore, if the current is measured across a range of voltages, the resistance (*R*) of the ion channel can be calculated via the inverse of Ohm's law.

Ohm's law is defined as the following equation:

$$V = IR$$

Equation 9

Equation 9 can be re-arranged to calculate the resistance of a system:

$$R = \frac{V}{I}$$

Equation 10

By applying Equation 8 to Equation 10, the following equation is reached:

$$G = \frac{I}{V}$$

Equation 11

A current-voltage relationship (Figure 2.7) can therefore be plotted for the data, with *V* forming the *x*-axis and *I* forming the *y*-axis and a linear regression line fitted; the gradient of the line (d*y*/d*x*) would give the conductance of the channel.

For the purposes of our bilayer experiments, the *V* corresponds to the holding potential applied to the *cis* chamber, measured in mV, and *I* corresponds to the current observed passing through the channel at each voltage. The current of individual channel openings was measured by manually positioning cursers on the closed level (baseline), and on an apparent opening to the fully open channel level. The difference between the two levels was recorded as the single-channel conductance. *I* was measured in pA using WinEDRv3.3.1software (University of Strathclyde, UK).

For the purposes of the experiments in this thesis, the potential difference was always calculated as the voltage applied to the *cis* chamber relative to the *trans* chamber, the *trans* chamber being the reference chamber. Likewise, in the case of experiments with native membranes incorporated into the bilayer, and in light of what is discussed earlier in this chapter with respect to native SR channel orientation, the potential difference corresponded to the voltage applied to the cytosolic side of the channels, relative to the luminal side, the luminal side being the reference.

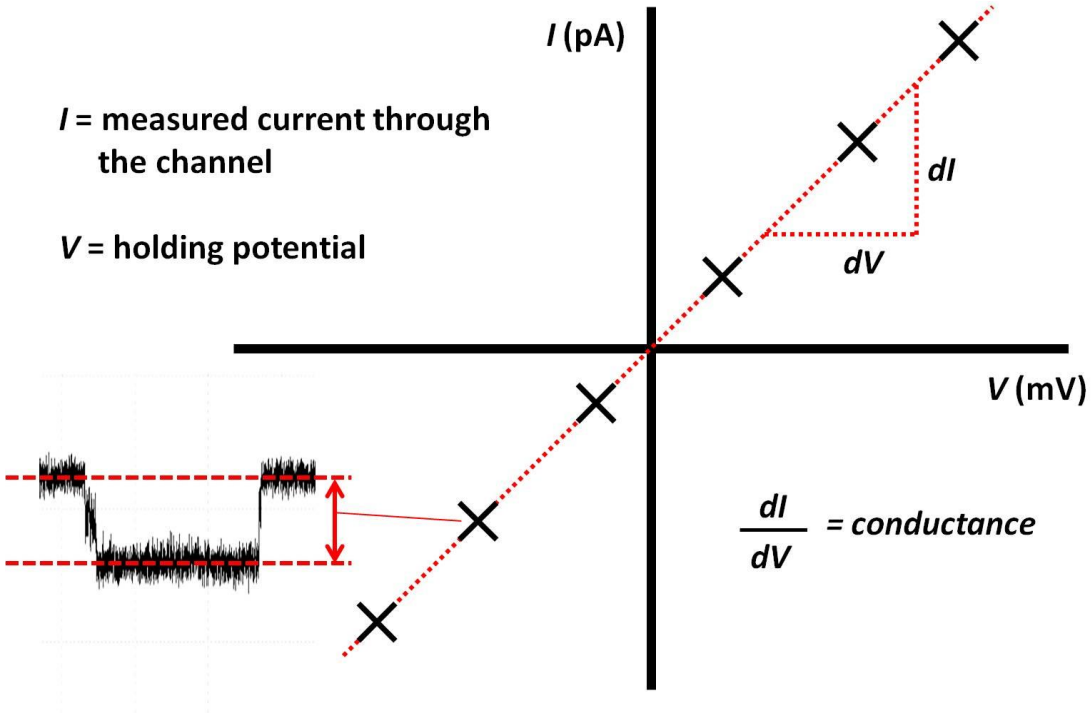


Figure 2.7. A schematic of a current-voltage relationship

2.10.2.1.1 Relative permeability

When current is measured under asymmetrical solutions, such as in a gradient, the point at which the linear regression line, plotted through the data, crosses the *x*-axis is referred to as the E_{rev}. The E_{rev} can be used to calculate the relative permeability of different ions in solution.

When in a KCl gradient (*cis*:810 mM KCl; *trans*: 210 mM KCl), the E_{rev} can be used to calculate the relative permeability of K^+ to Cl^- (P_K/P_{Cl}) through the channel using a modified Goldman-Hodgkin-Katz equation.

The Goldman-Hodgkin-Katz equation is as follows.

$$E_{rev} = \frac{RT}{F} ln\left(\frac{P_{Na}[Na^+]_{out} + P_K[K^+]_{out} + P_{Cl}[Cl^-]_{in}}{P_{Na}[Na^+]_{in} + P_K[K^+]_{in} + P_{Cl}[Cl^-]_{out}}\right)$$

Where E_{rev} is the measured reversal potential of the equation in V; R is the gas constant, 8.31 J/mol/K; T is the temperature in K (295.15 K under experimental conditions); F is the Faraday constant, 96485.33289 C /mol and P_{Na}, P_K and P_{Cl} are the relative permeability values for Na^+, K^+ and Cl^- ions respectively.

If *out* is taken to be represented as the *trans* chamber, and *in* the *cis* chamber:

$$E_{rev} = \frac{RT}{F} ln\left(\frac{P_{Na}[Na^+]_{trans} + P_K[K^+]_{trans} + P_{Cl}[Cl^-]_{cis}}{P_{Na}[Na^+]_{cis} + P_K[K^+]_{cis} + P_{Cl}[Cl^-]_{trans}}\right)$$

Equation 12

Seeing as only K^+ and Cl^- ions are present in the experimental solutions, Na^+ can be discounted.

$$E_{rev} = \frac{RT}{F} ln\left(\frac{P_K[K^+]_{trans} + P_{Cl}[Cl^-]_{cis}}{P_K[K^+]_{cis} + P_{Cl}[Cl^-]_{trans}}\right)$$

Equation 13

To find P_K/P_{Cl}, the equation needs to be re-arranged as follows.

$$Exp\left(\frac{E_{rev}F}{RT}\right) = \frac{P_K[K^+]_{trans} + P_{Cl}[Cl^-]_{cis}}{P_K[K^+]_{cis} + P_{Cl}[Cl^-]_{trans}}$$

Equation 14

$$\frac{P_K}{P_{Cl}} = \frac{[Cl^-]_{cis} - Exp\left(\frac{E_{rev}F}{RT}\right)[Cl^-]_{trans}}{Exp\left(\frac{E_{rev}F}{RT}\right)[K^+]_{cis} - [K^+]_{trans}}$$

Equation 15

P_K and P_{Cl} can be substituted with any monovalent cation or anion, respectively.

2.10.2.2 Open probability calculations for the SR K^+ channel

In order to perform Po measurements, single-channel recordings, collected using WinEDR software, were exported in their unfiltered form as .ABF files to the QuB 2.0.0.29 software suite (University of Buffalo, NY, USA). The recordings were re-sampled in QuB at 10 kHz and a 1 kHz Gaussian digital filter was applied so that the data could be visualised. Each recording was visually inspected for any electrical noise and/or capacitance spikes which were removed from the data before analysis.

At its simplest level, typical single-channel recordings reveal SR K^+ channel gating to consist of two simple conductance states: a closed state and an open channel state. When the channel is closed, no current passes through the channel and the closed state is observed. When the channel is open, ions flow through the channel producing current, and the channel open level is observed. The duration of time that the channel spends in either state is called the 'dwell time'. One measure of channel activity is by measuring the amount of time the channel spends

in the closed or open states. The Po measurement is defined as the fraction of time the channel remained in the open conformation and thus can be a measure of channel activity.

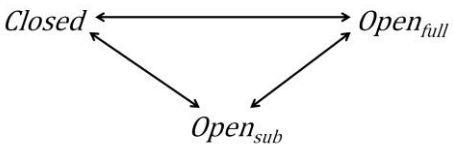
Before calculating the Po of a channel, the recording requires idealisation, assigning each channel event from the recording with an open or a closed state. Typically, when a channel only has two conductance levels, Po is calculated by half-amplitude threshold crossing. The 50 % threshold level is defined as half of the maximum current amplitude observed for the channel. Any opening that reaches the 50 % threshold is counted as an open channel event.

In the case of the SR K^+ channel, this two state model of gating is can be considered too simplistic. The SR K^+ channel has been observed to gate in a sub-conductance state [104], [105], introducing a further open channel level. Some of the sub-conductance level gating observed fell below the 50 % threshold and so would not be considered by the 50 % threshold analysis. It is clear therefore that Po analysis using the 50 % threshold method would not adequately analyse sub-conducting levels. To idealise recordings that contained sub-conductance levels, we instead used the segmental k-means (SKM) algorithm which can be performed using the QuB software suite. The use of a SKM algorithm in single-channel analysis has previously been suggested by Qin in 2004 [181]. The SKM algorithm uses a hidden Markov model to deduce state transitions of a signal such as a single-channel recording. A Markov model was therefore created for each SR K^+ channel and was used to calculate the Po of the channel.

2.10.2.3 Modelling the SR K^+ channel and idealisation

The most appropriate model for the SR K^+ channel has been discussed in number of papers from the Sitsapesan laboratory [104], [105]. The most recent of these papers suggested a three-state Markov model (Model M 1) consisting of the closed, fully open level and a single

'merged' conductance level to accurately idealise the current-fluctuations from SR K^+ channel openings, shown below.



Model M 1

It was also observed however, that the SR K^+ channel rarely gated directly from the closed state to the fully open state or from the fully open state directly to the closed state. Most of events (>97 %) to the fully open or closed states gated through a the sub-conductance level [104]. It was thought that this may indicate that a more accurate model for SR K^+ channel gating would be a linear model as shown below.

$$Closed \leftrightarrow Open_{sub} \leftrightarrow Open_{full}$$

Model M 2

For the purposes of this thesis, the Model M 2 was therefore used to model the SR K^+ channel. The three-state linear Markov model was constructed in QuB with arbitrary rate constants of 10 s^{-1}. The closed and the full conductance levels were highlighted manually on the recording in QuB, and assigned to states on the model as shown in Figure 2.8. The sub-conductance level was assigned at 50 % of the fully open channel level with a large standard deviation to account for the large noise of the state.

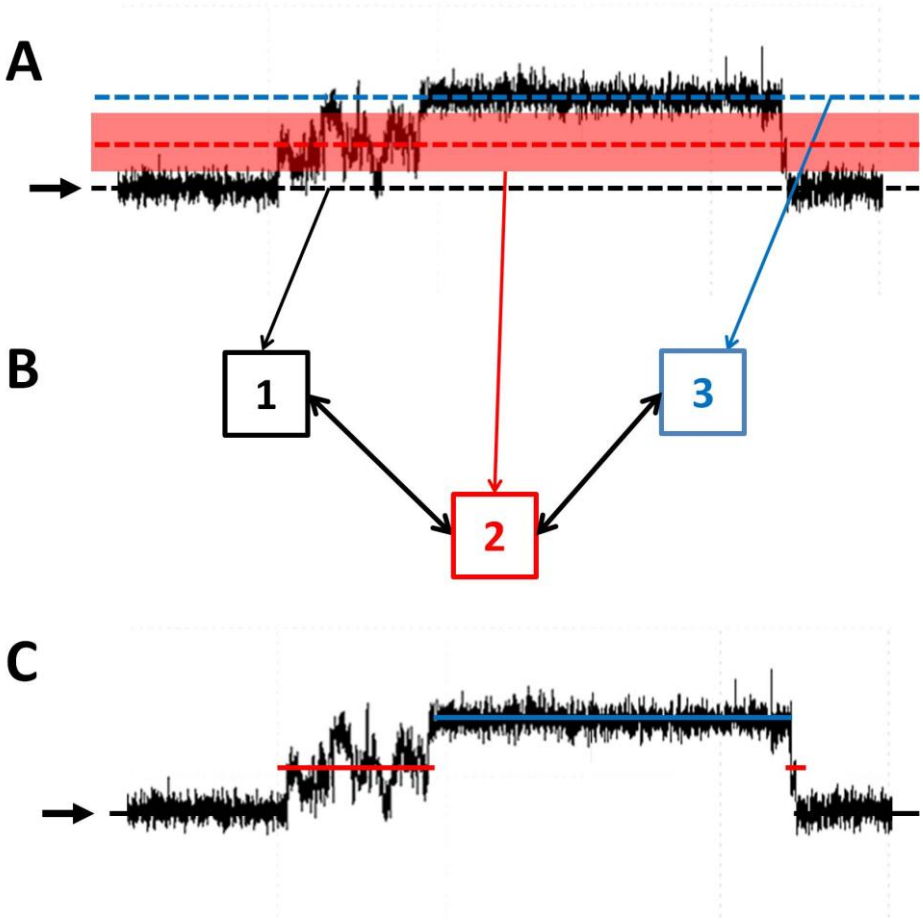


Figure 2.8. Assigning the levels to the model for use in idealisation
(A) Current-fluctuations through a representative SR K^+ channel single-channel event. The channel closed level (black, shown by an arrow) was assigned as state **1**, the sub-conductance level (red) at 50 % of the fully open channel level and with a large standard-deviation (red shaded area) was assigned to state **2**, and the fully open level (blue) was manually assigned as state **3**. **(B)** Model M 2 with each state assigned a number and a colour. Closed is state 1 in place, $Open_{sub}$ is state 2 in red, and $Open_{full}$ is state 3 in blue. **(C)** The idealized trace with each level assigned a state. The Po of each state can now be calculated.

Once the model had been constructed, and the states assigned, the inbuilt idealisation process was begun in QuB. This process performs a number of tasks to aid in analysis of the data. Firstly, the Viterbi algorithm [182][183] was used to find the most likely sequence of hidden states, called the Viterbi path. Secondly, the Viterbi path was used to adjust the model parameters using an iterative procedure that has been termed 'maximum likelihood' fitting

[184] to reach the optimum likelihood, L. Finally, the idealised conductance levels were represented by Gaussian fits to single-channel current amplitude distributions according to the following equation:

$$f(I) = \frac{Po}{\sqrt{2\pi\sigma^2}} exp\left(\frac{-(I-\mu)^2}{2\sigma^2}\right)$$

Equation 16

Where *I* is the current, *Po* is the channel Po in a given state, μ is the mean current amplitude for the given state, and σ is the open channel noise for a given state, defined as the standard deviation of the current.

Once fitted, the Gaussian curves for each state were plotted alongside an amplitude histogram of the recording as shown in Figure 2.9 . The fit could then be visually inspected.

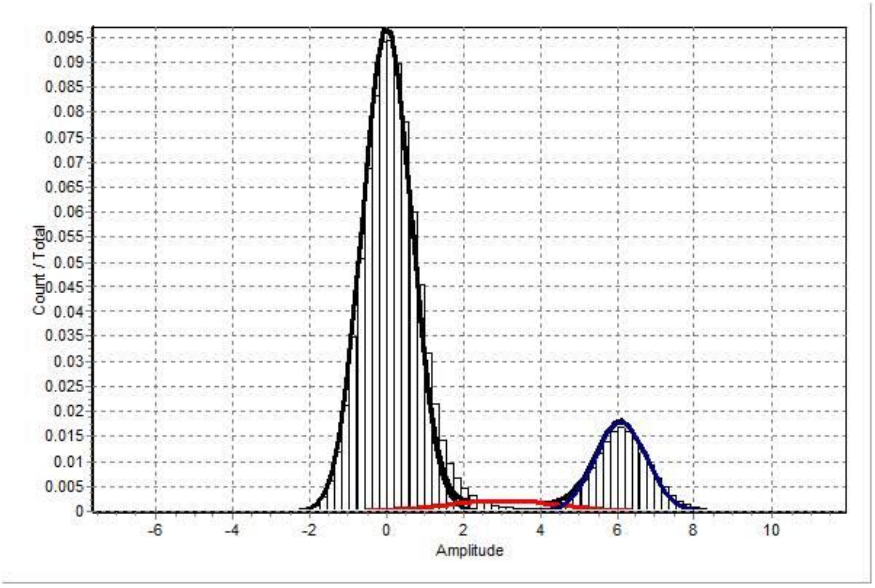


Figure 2.9. Gaussian curves fitted to an amplitude-histogram in QuB
An amplitude histogram generated in QuB from 3 min of recording of a sheep cardiac SR K^+ channel at +30 mV. Each state is plotted with a Gaussian curve, closed in black, the sub-conductance state in red, and the fully open channel level in blue.

2.10.2.4 Open probability

From the idealisation, QuB produced a number of statistics for the recording. These included, the mean dwell time for each state, the number of gating events to each state and the Log-Likelihood (LL) for the model, a measure of goodness of fit to the data. All of these have been used to analyse single-channel data in this thesis. In addition to the above statistics, QuB also calculated the Po for each state using the equation below.

$$Po = \frac{t_{in\ state}}{t_{total}}$$

Equation 17

Where *Po* is the Po of the state, $t_{in\ state}$ is the time spent dwelling in the state, and t_{total} is the total length of the recording.

Data was therefore obtained for Po_{closed}, Po_{sub}, and Po_{full} for the Po values of the closed state, the sub-conductance state, and the fully open channel level, respectively. Often, the Po_{total} was used to express Po of a channel. The Po_{total} was calculated as the sum of the Po_{sub} and Po_{full}. In this thesis, I have also used the '% contribution of Po_{full}' as a measure of how the relative time SR K^+ channels spend in the fully and sub-conductance level changes with different conditions or tissues. This is calculated as the Po_{full} expressed as a percentage of the Po_{total}. It must be noted that these calculations only apply when one SR K^+ channel is gating in the bilayer.

2.10.2.5 Analysis of multiple SR K^+ channels gating in the bilayer

Figure 2.10 shows current-fluctuations through a single SR K^+ channel (Figure 2.10A) and three SR K^+ channels gating in the bilayer (Figure 2.10B). Single SR K^+ channels can be fitted with the models described above and the Po_{full} and Po_{sub} levels are simple to calculate. Multiple SR K^+

channels have to be fitted with the more complex Model M 3 to account for the additional channel open levels.

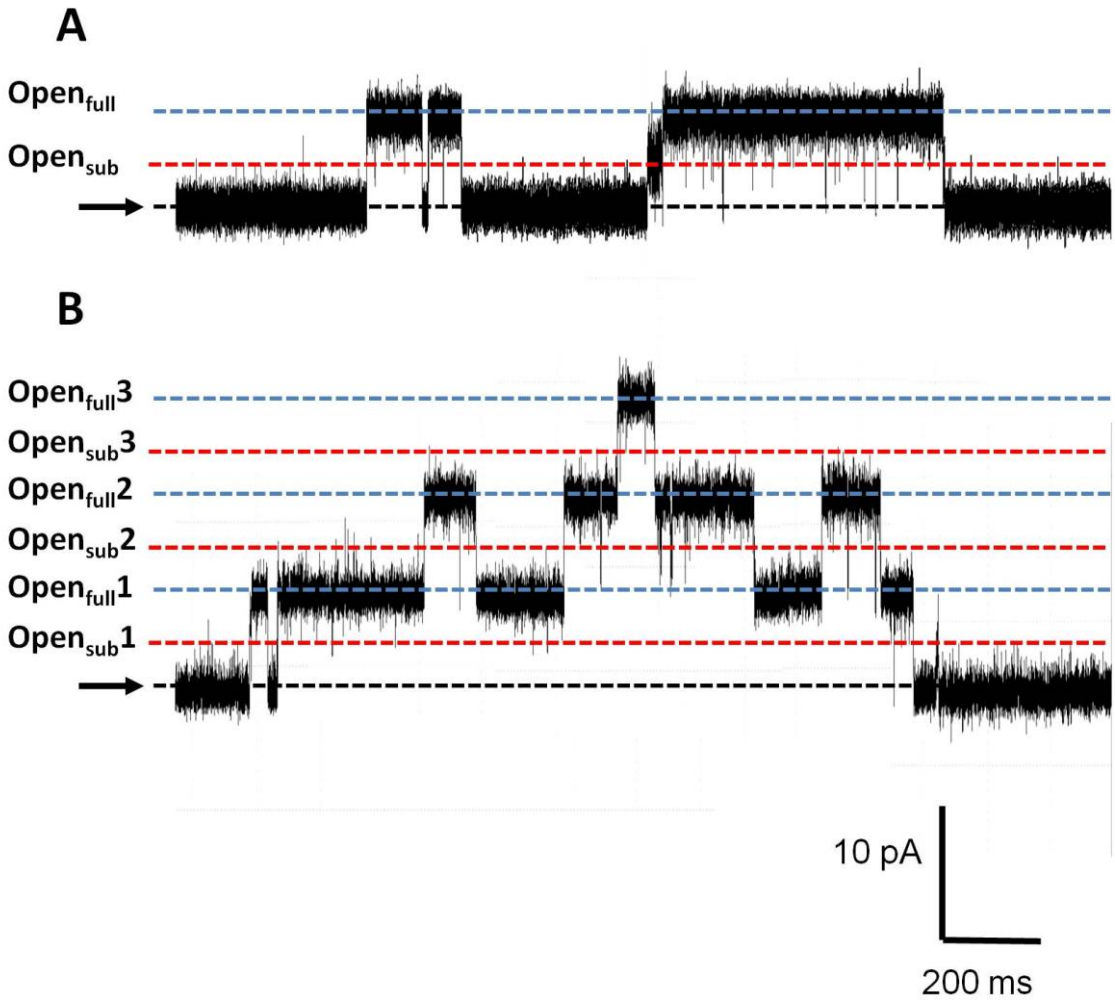


Figure 2.10. Current-fluctuations showing single and multiple SR K^+ channels gating in the bilayer
(A) Current-fluctuations through a single SR K^+ channels gating in the bilayer. **(B)** Current-fluctuations through three SR K^+ channels gating together in the bilayer. Closed channel levels are shown by an arrow, sub-conductance levels by red lines, and fully open channel levels by blue lines.

$$Closed \leftrightarrow Open_{sub}1 \leftrightarrow Open_{full}1 \leftrightarrow Open_{sub}2 \leftrightarrow Open_{full}2 \leftrightarrow Open_{sub}3 \leftrightarrow Open_{full}3$$

Model M 3

The Po values calculated for each state in Model M 3 will not be the actual Po values for the channel level, for example the Po of the *$Open_{sub}2$* state will be the combined Po values for the sub-conductance level for two open SR K^+ channels. This is known as the nPo and is not a true reflection of the Po for each channel. When multiple channels are present it is therefore necessary to calculate the average Po of *n* channels using the following formula.

$$Po = \frac{\sum_1^n nt_{open(n)}}{nt_{total}}$$

Equation 18

2.10.2.6 Noise analysis

When a large current is observed through multiple channels in the bilayer and it is not clear on the number of channels, noise analysis was conducted. Noise analysis was used for multiple SR K^+ channels and multiple SR Cl^- channels gating in the bilayer. Noise analysis is most commonly applied to whole cell currents, and measures the average current across a patch or bilayer. It therefore is a crude measurement of both Po and conductance.

Noise analysis was performed with the WinEDR software. Briefly, the recording was split into a number of segments or 'records', each with a uniform timeframe, e.g. 0.5 ms. The average (mean) current for each sample was calculated using the following formula.

$$I_{mean} = \frac{\sum_{i=1}^{n} I(i)}{N}$$

Equation 19

Where *I(i)* is the amplitude of the *i*th of the N samples in the segment.

The mean was then taken for the average currents for each record at each holding potential and this was plotted against voltage to construct a current-voltage relationship.

2.10.2.7 Log-Likelihood ratio tests

A log-likelihood ratio test was used for comparing the goodness of fit of two models, one which is less complex such as a two-state model (model 0) to one which is more complex such as the three-state model (model 1). The test is based on the likelihood ratio, which expresses how many times more likely the data under model 0 is to be correct compared to the data under model 1. This likelihood ratio, or equivalently its logarithm, can then be used to compute a p-value, or compared to a critical value to decide whether or not to reject model 1. The log-likelihood ratio test was suggested for use in the study of ion channels by Stepanyuk *et al.* in 2011 [185]. Log-liklihood values were calculated for each model using QuB and log-likelihood ratios were calulated using the following equation.

$$LRT = -2log_e\left(\frac{likelihood\ of\ model\ 0}{liklihood\ of\ model\ 1}\right)$$

Equation 20

2.11 Chemical compounds

Chemical compounds used in this thesis, were purchased from Sigma Aldrich Company Ltd (Gillingham, UK) if not otherwise stated.

2.12 Statistics

All statistical analysis was performed using GraphPad Prism 7 software. Microsoft Excel was used for data collation and manipulation.

Data sets with n>6 were tested with the D'Agostino-Pearson Omnibus normality test. If the data was found to be normally distributed then a parametric test for significance was used such as the Student's t-test for two data sets or a One-way ANOVA test for >2 data sets. If the data was not significantly distributed or n≤6 then a non-parametric test for significance was used. For 2 data sets these tests were the Mann-Whitney test for unpaired data and the Wilcoxon matched-pairs signed rank test for paired data. When >2 data sets were compared the tests used were the Kruskal-Wallis test for unpaired data and the Friedman test for paired data. An appropriate multiple comparisons test was performed when data sets were >2.

Error bars are calculated as the Standard error of the mean (SEM) where n>3. For data sets where n=3 the standard deviation (SD) is used.

With respect to data points on graphs, levels of significance were shown with stars, as follows: * = $p<0.05$; ** = $p<0.01$; *** = $P<0.001$.

Chapter 3. Properties of the SR K^+ channel

3.1 Introduction

SR K^+ channels are found at high concentrations in the SR membrane of both skeletal and cardiac muscle cells [72][186] where they are thought to play an important role in EC coupling by providing charge compensation during intracellular Ca^{2+} flux [66], [105], [187]. Whether SR K^+ channels are the sole pathway for countercurrent carrying ions has been disputed however, and the exact physiological function of SR K^+ channels is yet to be established [67][188]. A number of studies have characterised the channels by incorporating them into artificial membranes [64], [72], [98], [99], [186], [189]. The literature suggests that SR K^+ channels from different tissues or species may exhibit different biophysical properties. SR K^+ channels from several species have not been directly compared by one group under identical experimental conditions, however.

SR K^+ channels have been found to be voltage and pH sensitive [104], [105], [186], [189], permeable to K^+, Na^+, Cs^+, Rb^+ and Li^+ [72], [91], [186], and blocked by standard K^+-channel blockers such as decamethonium [102] and TEA [90]. Divalent cations such as Ca^{2+} and Mg^{2+} have been shown to block K^+ current fluxes, but reports in the literature show inconsistent effects [72], [98], [99]. Despite this work, a specific pharmacological tool is yet to be found which could aid in both the study of SR K^+ currents or could form the basis for a potential therapeutic agent.

The aims of this chapter were therefore to investigate differences between SR K^+ channel isoforms found in rabbit skeletal muscle, sheep skeletal muscle, and mouse skeletal and cardiac muscle and to investigate the pharmacological properties of SR K^+ channels to attempt to find a specific pharmacological agent.

Native SR vesicles have been shown to incorporate into the bilayer in a fixed orientation such that the *cis* chamber corresponds to the cytosolic side of the channel and the *trans* chamber to the luminal side of the channel [175][176]. For the purposes of this chapter, therefore, the *cis* chamber will be referred to as the cytosol, and the *trans* chamber as the lumen.

3.2 Results

3.2.1 Species differences in SR K^+ channel gating

The SR K^+ channel was found to display broadly similar gating behaviour across all species and muscle types investigated including voltage-sensitivity, low Po and long open channel bursts which consisted of the channel gating to both fully open and sub-conductance states, as shown in Figure 3.1. Figure 3.2 shows the Po of the various SR K^+ channels at holding potentials of +30 mV and -30 mV. The Po values at negative potentials were consistently lower in all tissues. The Po of SR K^+ channels at -30 mV was lower in channels from mouse cardiac muscle compared to at +30 mV; however this was not found to be significant. The Po of all channels was low (<0.4 at +30 mV) and variable so that although the rabbit skeletal channel appeared to gate with higher Po than those channels from other species; this was only significantly higher than the Po of the mouse cardiac channel. The % of channel open time which was due to openings to the fully open state was also found to be similar between tissue/species types with channels gating for 27-34 % of the open time in the sub-conductance state at +30 mV and for 51-62 % of the time at -30 mV.

Figure 3.3 compares the single-channel conductance of the fully open channel state for the various SR K^+ channels. The conductance of the sheep cardiac SR K^+ channels was significantly lower than the conductance of SR K^+ channels from other tissues.

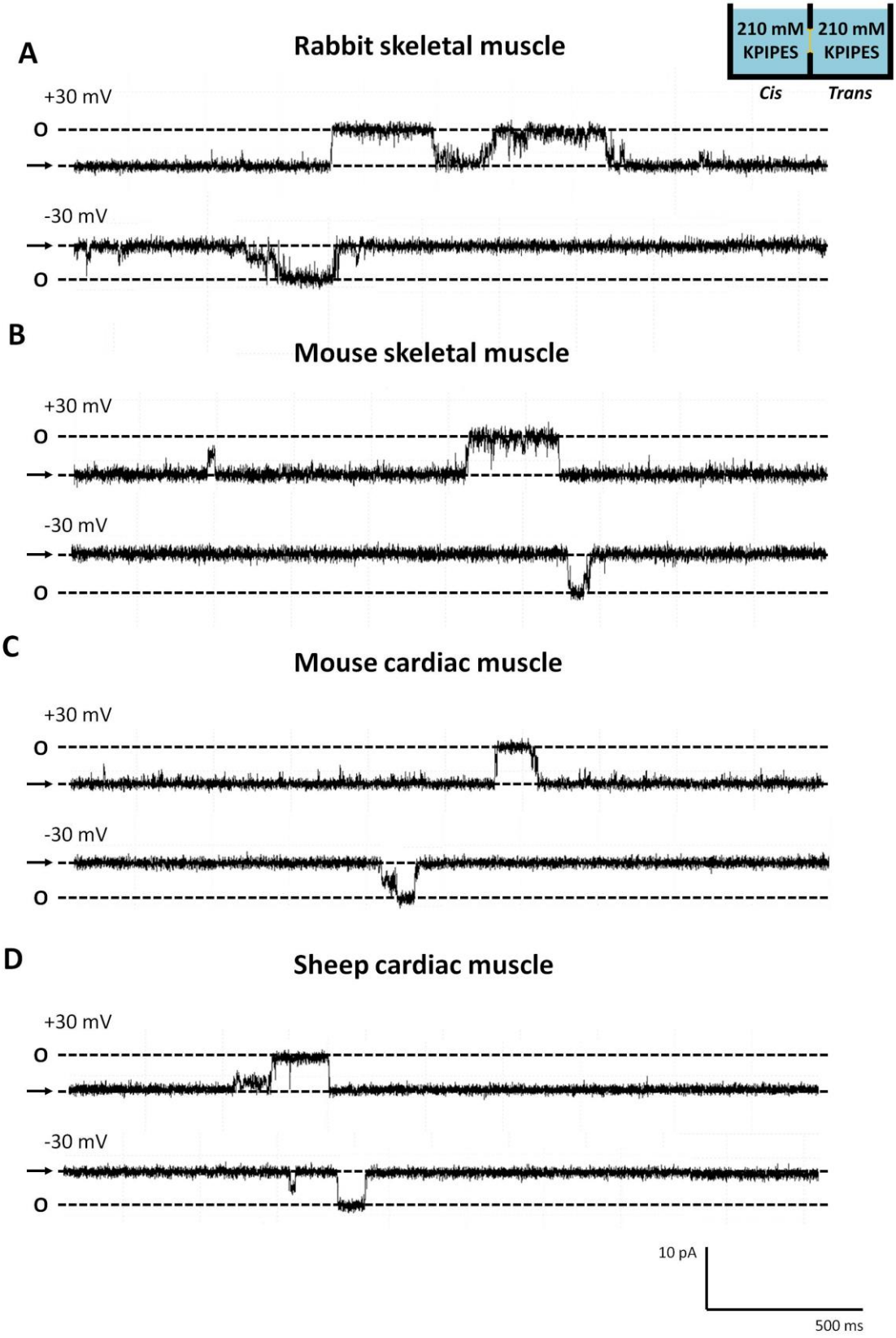
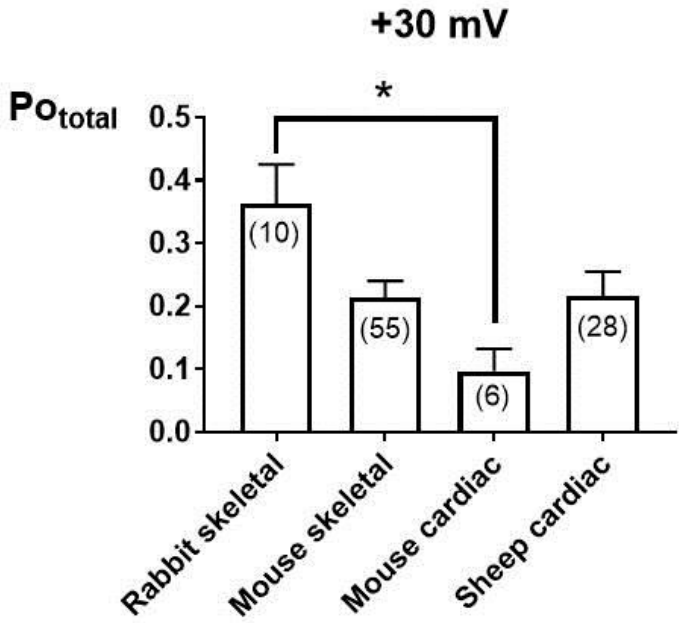
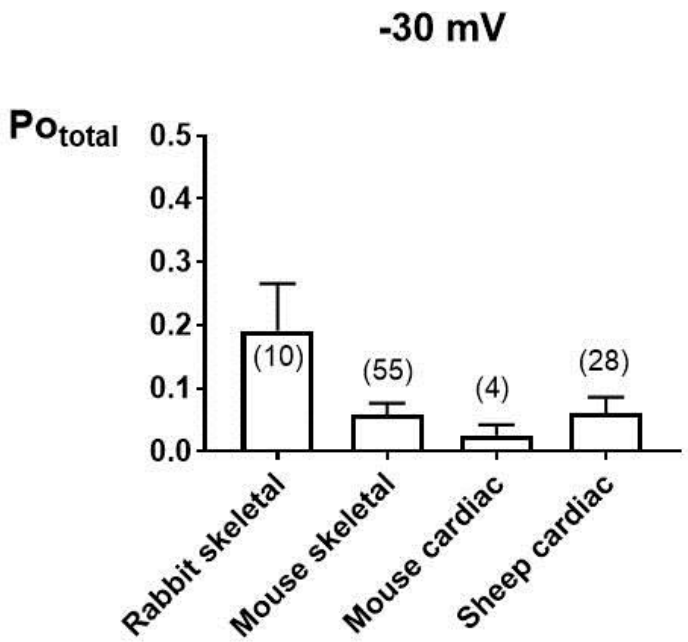

A
Rabbit skeletal muscle
210 mM KPIPES
210 mM KPIPES
Cis
Trans
+30 mV
o
-30 mV
o
B
Mouse skeletal muscle
+30 mV
o
-30 mV
o
C
Mouse cardiac muscle
+30 mV
o
-30 mV
o
D
Sheep cardiac muscle
+30 mV
o
-30 mV
o
10 pA
500 ms

Figure 3.1. Comparison of gating of various mammalian SR K^+ channels
Representative current-fluctuations through native single SR K^+ channels from the SR of rabbit skeletal muscle **(A)**, mouse skeletal muscle **(B)**, mouse cardiac muscle **(C)** and sheep cardiac muscle **(D)**. Recordings were made in symmetrical solutions and at holding potentials of +30 mV and -30 mV. The closed channel level is shown with an arrow and the fully open channel level is shown by O.

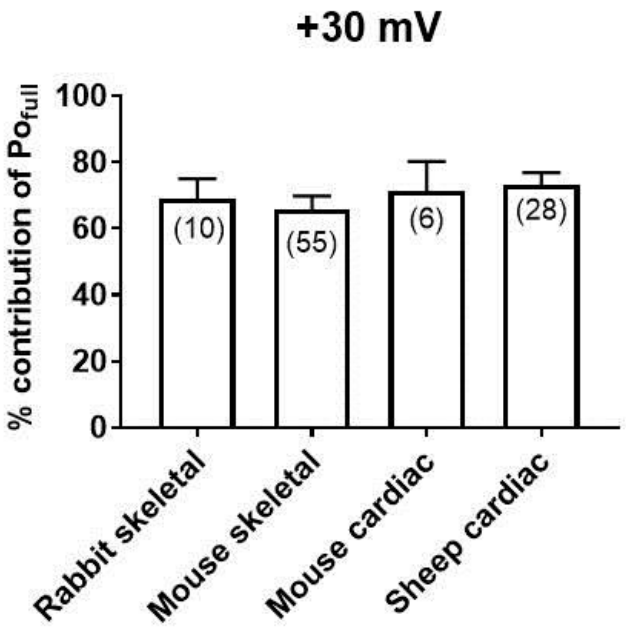
A


+30 mV
*
Po total
0.5
0.4
0.3
0.2
0.1
0.0
(10)
(55)
(6)
(28)
Rabbit skeletal
Mouse skeletal
Mouse cardiac
Sheep cardiac

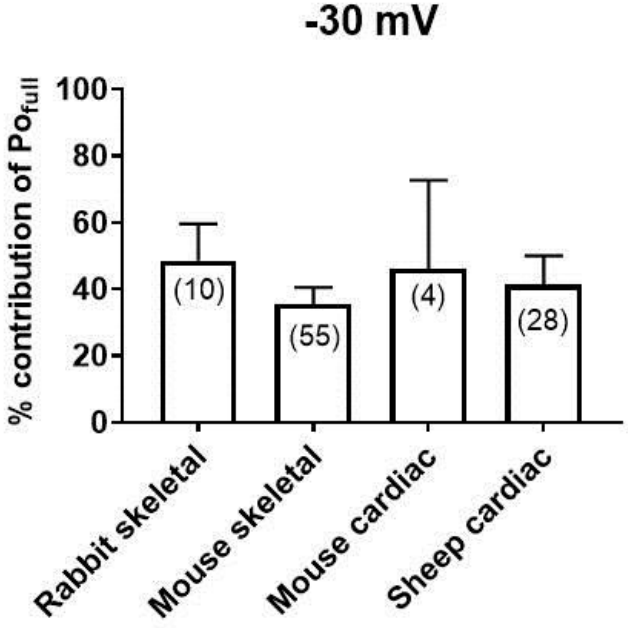
B


-30 mV
Po total
0.5
0.4
0.3
0.2
0.1
0.0
(10)
(55)
(4)
(28)
Rabbit skeletal
Mouse skeletal
Mouse cardiac
Sheep cardiac

C


+30 mV
% contribution of Po full
100
80
60
40
20
0
(10)
(55)
(6)
(28)
Rabbit skeletal
Mouse skeletal
Mouse cardiac
Sheep cardiac

D


-30 mV
% contribution of Po full
100
80
60
40
20
0
(10)
(55)
(4)
(28)
Rabbit skeletal
Mouse skeletal
Mouse cardiac
Sheep cardiac

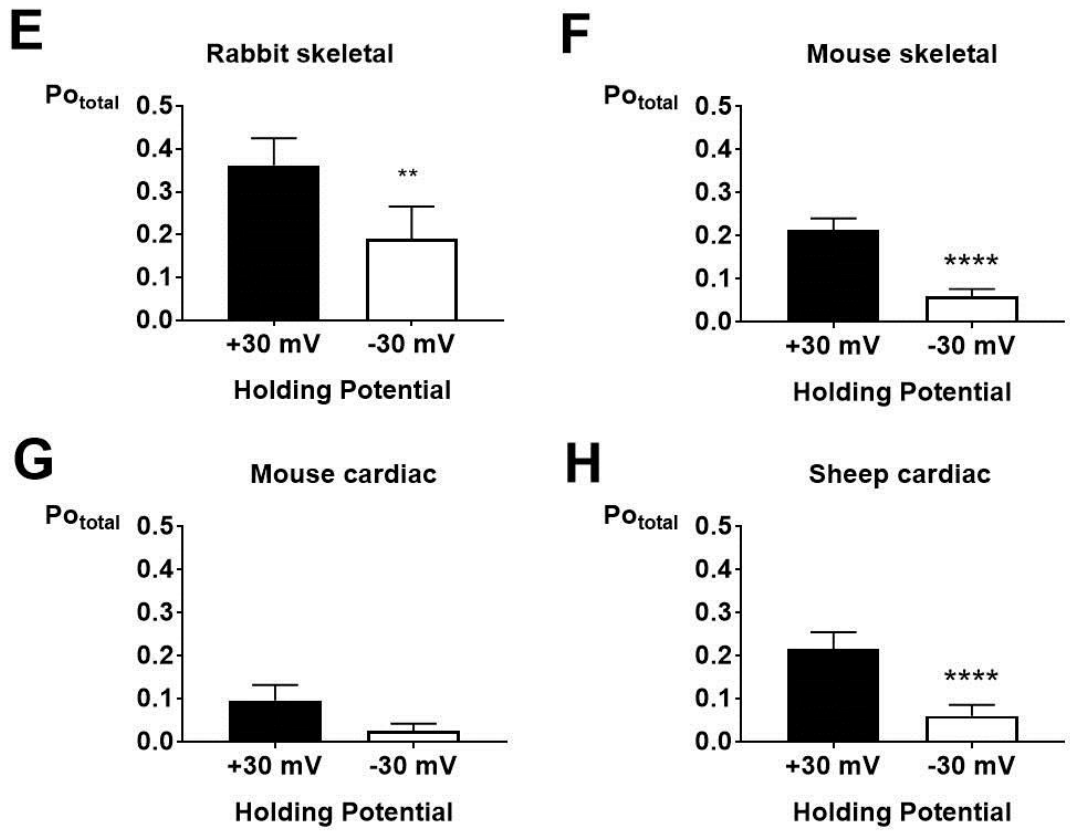


Figure 3.2. Po of the various mammalian SR K^+ channels
(A,B) The Po of various native mammalian SR K^+ channels at +30 mV **(A)** and at -30 mV **(B). (C,D)** The % of channel open time spent in the fully open level for various mammalian SR K^+ channels at +30 mV **(C)** and at -30 mV **(D). (E, F, G, H)** A comparison of the Po at ±30 mV of various mammalian SR K^+ channels. Values are of the mean±SEM. The number of experiments is shown in brackets above or inside the respective bars.

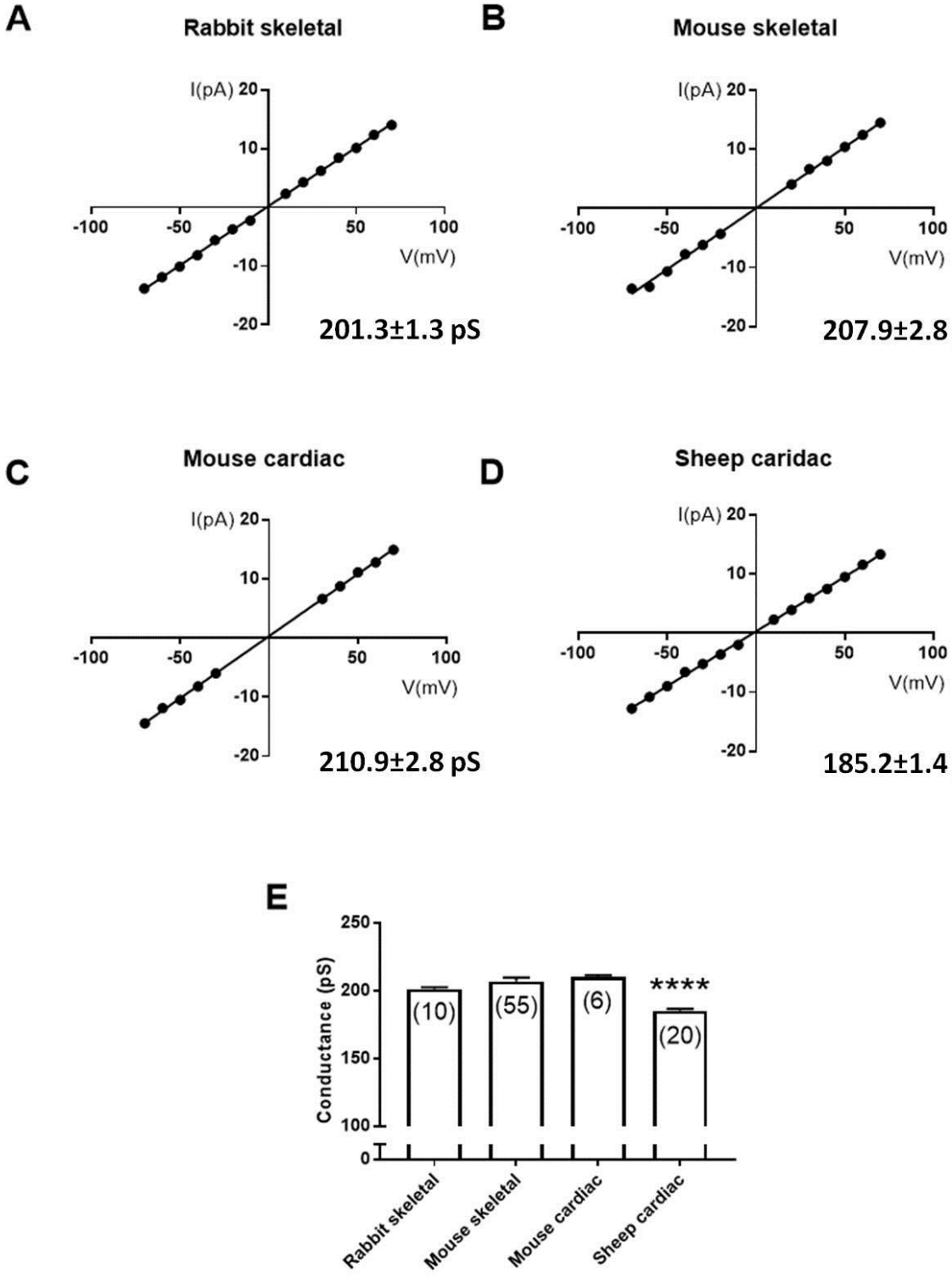

A
Rabbit skeletal
I(pA) 20
10
-10
-20
-100
-50
50
100
V(mV)
201.3±1.3 pS
B
Mouse skeletal
I(pA) 20
10
-10
-20
-100
-50
50
100
V(mV)
207.9±2.8
C
Mouse cardiac
I(pA) 20
10
-10
-20
-100
-50
50
100
V(mV)
210.9±2.8 pS
D
Sheep caridac
I(pA) 20
10
-10
-20
-100
-50
50
100
V(mV)
185.2±1.4
E
Conductance (pS)
250
200
150
100
0
(10)
(55)
(6)
(20)
****
Rabbit skeletal
Mouse skeletal
Mouse cardiac
Sheep cardiac

Figure 3.3. Comparison of the single-channel conductance of various mammalian SR K^+ channels
Current-voltage relationships for native SR K^+ channels from rabbit skeletal **(A)**, mouse skeletal **(B)**, mouse cardiac **(C)** and sheep cardiac **(D)** muscle. Values are of the mean±SEM. Where not shown, error bars are within the symbols. The data are fitted with a linear regression line and the single-channel conductance for the fully open state is detailed on the lower left of each graph. **(E)** Mean data comparing the single-channel conductances for the various mammalian SR K^+ channels. Values are of the mean±SEM.

3.2.2 Finding a ligand for the SR K^+ channel

There is no known specific ligand for the SR K^+ channel. A series of experiments were therefore conducted in an attempt to find a ligand which could be used to activate or inhibit SR K^+ channel currents.

3.2.3 Ca^{2+} as a ligand of the SR K^+ channel

As described earlier in this thesis, the effects of Ca^{2+} on the SR K^+ channel are contentious [72][98][99]. Experiments were therefore performed to observe the effect of Ca^{2+} on SR K^+ channel gating.

3.2.3.1 The SR K^+ channel in low [Ca^{2+}]

Uehara *et al.* (1994) suggested that, as [Ca^{2+}] decreases on either side of the channel, the Po of the SR K^+ channel is diminished [99]. The free [Ca^{2+}] was therefore lowered from 10 µM (control [Ca^{2+}], see methods for details on free Ca^{2+} measurement), to 0.7 nM free Ca^{2+} by the addition of 2.1 mM EGTA to both the cytosolic and the luminal sides of SR K^+ channels from sheep cardiac and rabbit skeletal muscle. Representative SR K^+ channel recordings taken from rabbit skeletal and sheep cardiac SR in both conditions are shown in Figure 3.4. Figure 3.5 compares the single-channel properties of SR K^+ channels in the presence of 10 µM and 0.7 nM Ca^{2+}. The single-channel conductance of the SR K^+ channel from both rabbit skeletal and sheep

cardiac muscle remained unchanged with 0.7 nM free Ca^{2+}. No obvious trends, suggesting differences in the gating of SR K^+ channels, were observed after lowering free [Ca^{2+}] to 0.7 nM in sheep cardiac or rabbit skeletal SR K^+ channels.

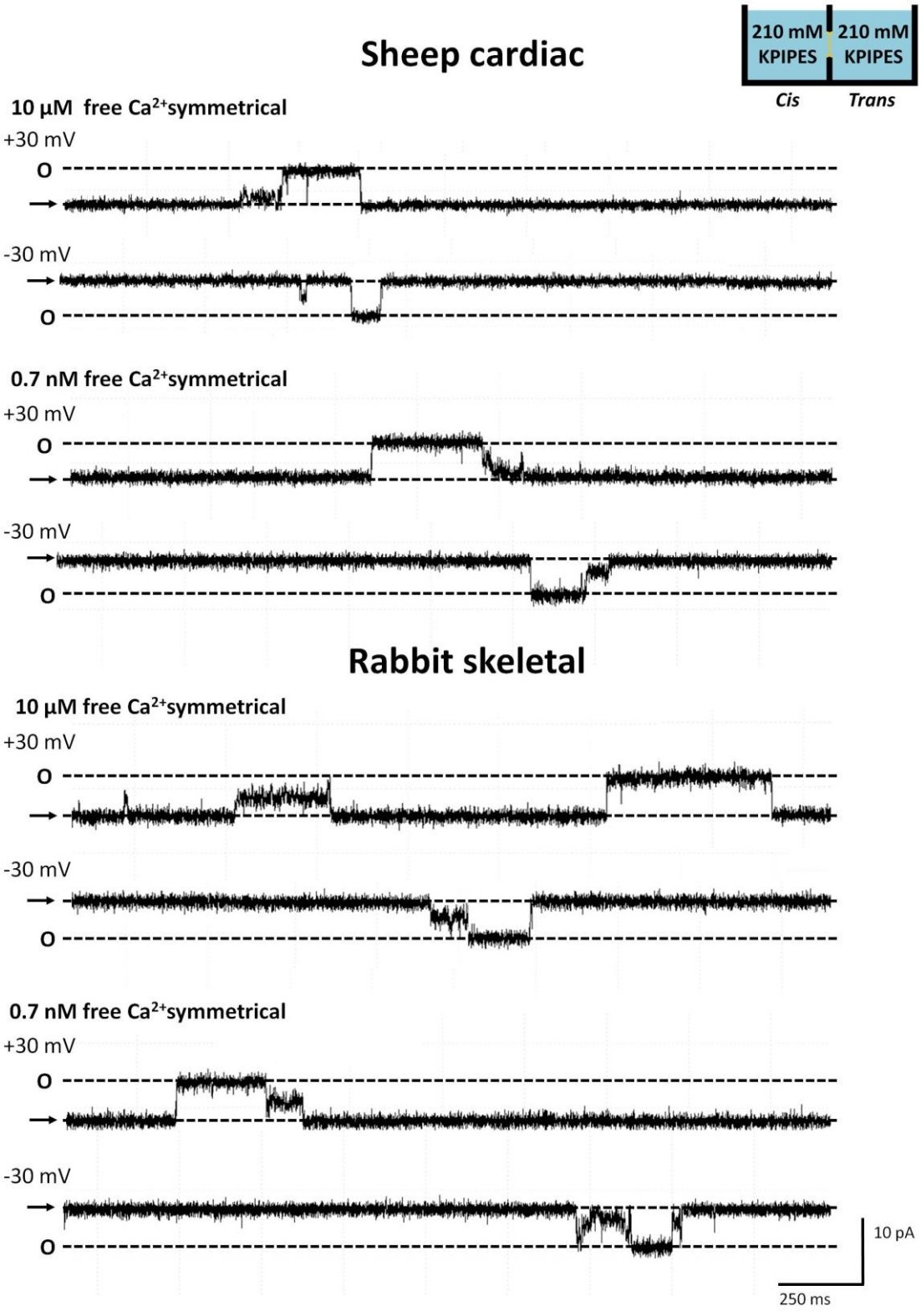
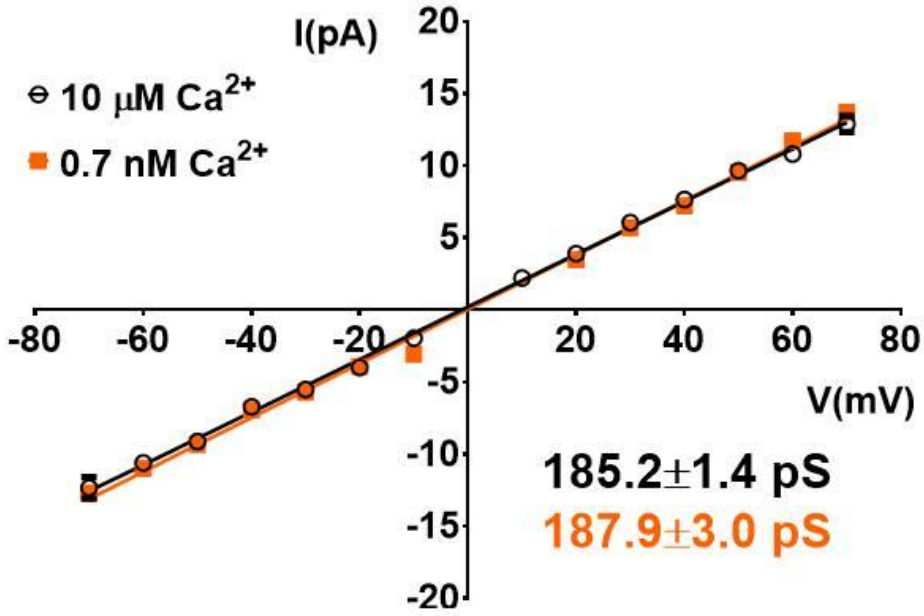

Sheep cardiac
210 mM KPIPES
210 mM KPIPES
Cis
Trans
10 µM free Ca2+symmetrical
+30 mV
O
-30 mV
O
0.7 nM free Ca2+symmetrical
+30 mV
O
-30 mV
O
Rabbit skeletal
10 µM free Ca2+symmetrical
+30 mV
O
-30 mV
O
0.7 nM free Ca2+symmetrical
+30 mV
O
-30 mV
O
10 pA
250 ms

Figure 3.4. The SR K^+ channel from sheep cardiac muscle and rabbit skeletal muscle in low free [Ca^{2+}]

Representative current-fluctuations through the SR K^+ channel from sheep cardiac muscle (top traces) and rabbit skeletal muscle (bottom traces) at the holding potentials of +30 mV and -30 mV in symmetrical 210 mM KPIPES. Free [Ca^{2+}] was lowered from 10 µM to 0.7 nM with the addition of 2.1 mM EGTA to both bath chambers. The zero current level is shown by an arrow and the fully open channel level by an O. Traces are representative of n=4 (sheep) and n=5 (rabbit) recordings and Po values are the mean±SEM.

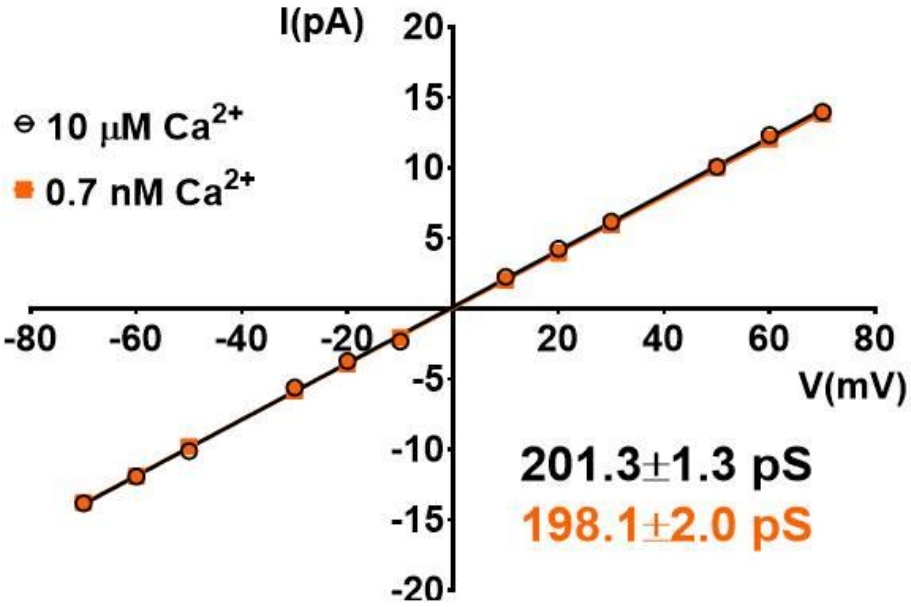
A

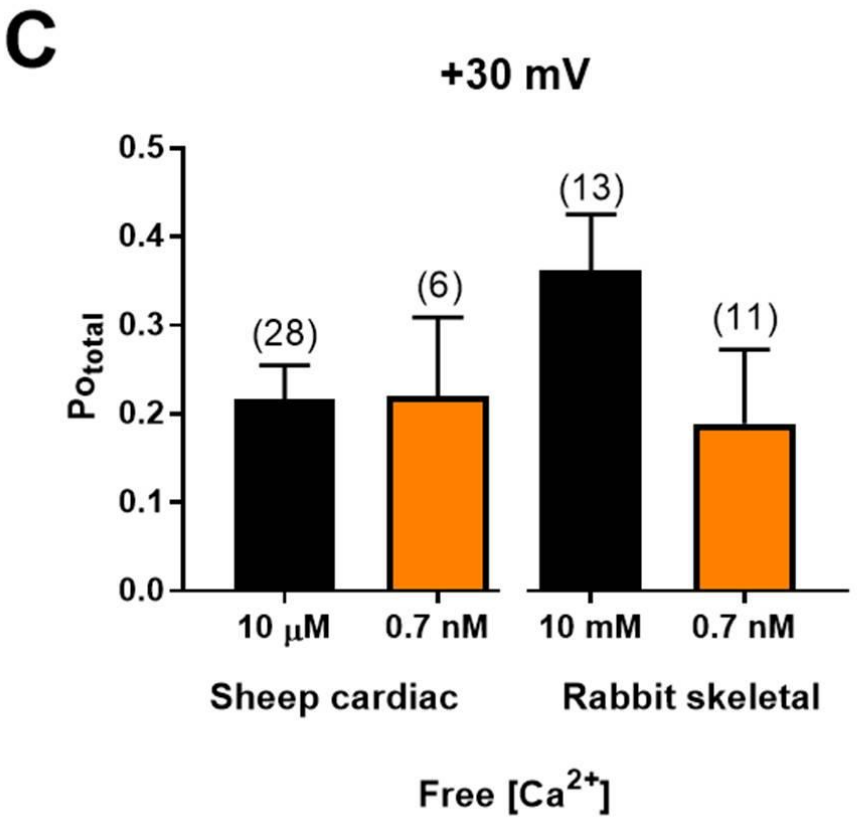
Sheep cardiac muscle

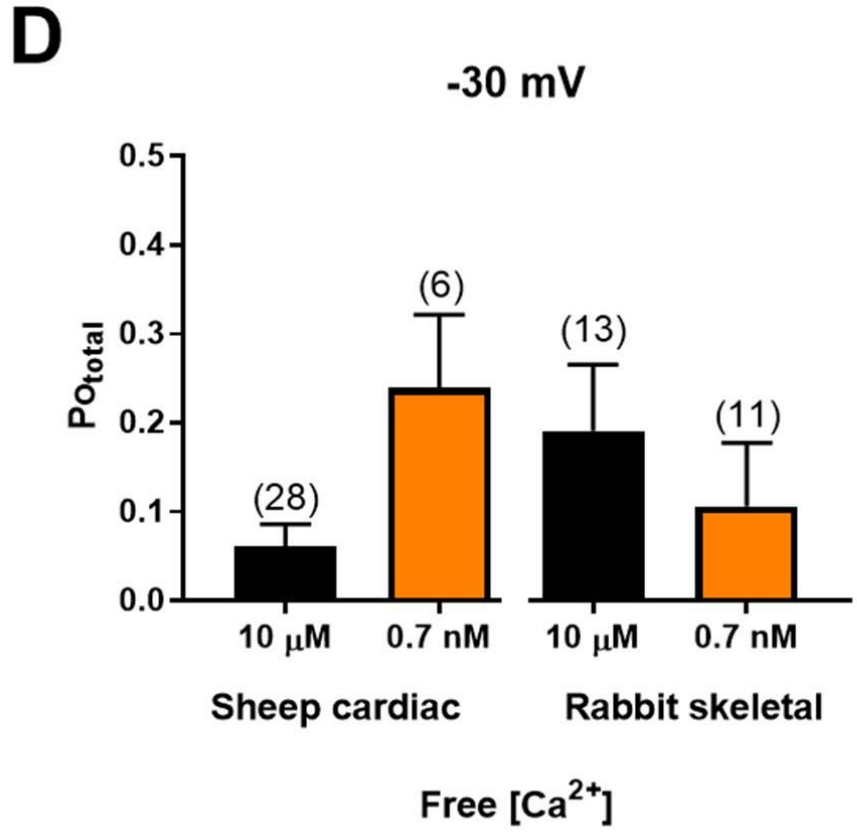


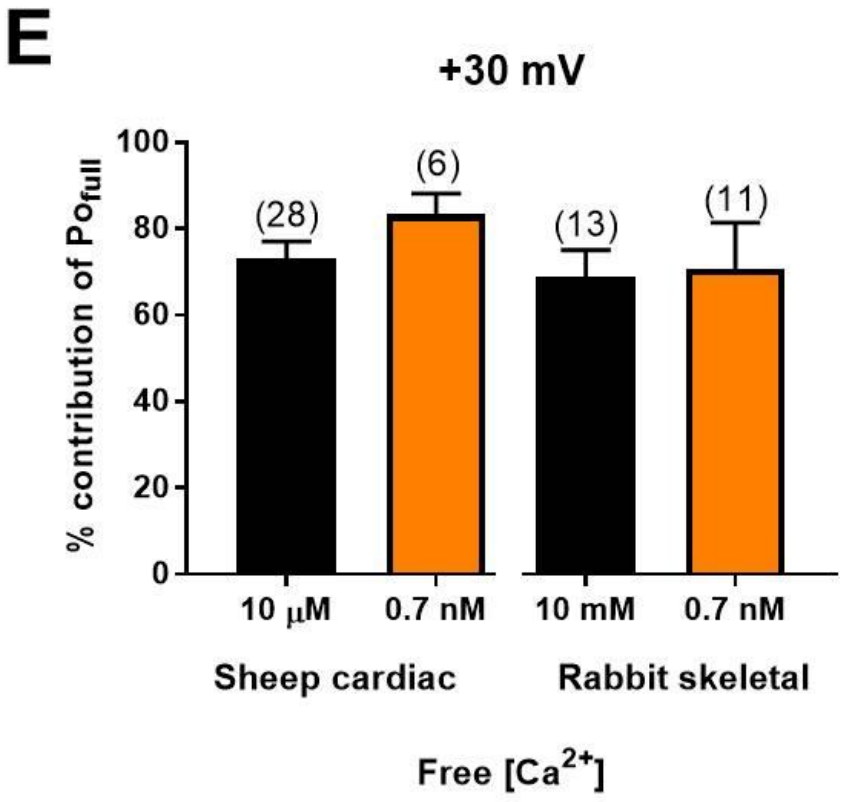
B

Rabbit skeletal muscle




C
+30 mV
0.5
0.4
0.3
0.2
0.1
0.0
$P_{O_{total}}$
(28)
(6)
(13)
(11)
10 μM
0.7 nM
10 mM
0.7 nM
Sheep cardiac
Rabbit skeletal
Free [Ca^{2+}]


D
-30 mV
0.5
0.4
0.3
0.2
0.1
0.0
$P_{O_{total}}$
(28)
(6)
(13)
(11)
10 μM
0.7 nM
10 μM
0.7 nM
Sheep cardiac
Rabbit skeletal
Free [Ca^{2+}]


E
+30 mV
% contribution of Po full
100
80
60
40
20
0
(28)
(6)
(13)
(11)
10 μM
0.7 nM
10 mM
0.7 nM
Sheep cardiac
Rabbit skeletal
Free [Ca2+]

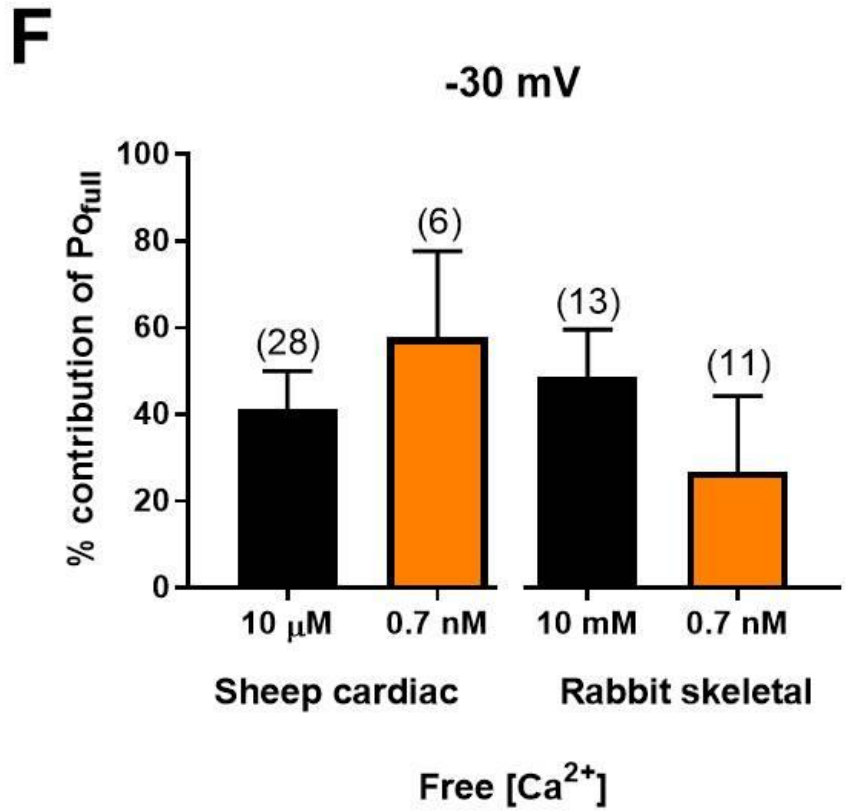

F
-30 mV
% contribution of Po full
100
80
60
40
20
0
(28)
(6)
(13)
(11)
10 μM
0.7 nM
10 mM
0.7 nM
Sheep cardiac
Rabbit skeletal
Free [Ca2+]

Figure 3.5. The effect of lowering Ca^{2+} symmetrically in both chambers on sheep cardiac and rabbit skeletal SR K^+ channel function

(A, B) Current-voltage relationships for native SR K^+ channels from sheep cardiac **(A)** and rabbit skeletal **(B)** muscle in symmetrical 10 μM free Ca^{2+} (black) and symmetrical 0.7 nM free Ca^{2+} (orange). Where not shown, error bars are within the symbols. The data are fitted with a linear regression line and the single-channel conductance for the fully open state is detailed on the lower left of each graph. **(C, D)** A comparison of the Po of SR K^+ channels from sheep cardiac and rabbit skeletal muscle at +30 mV **(C)** and at -30 mV **(D)** in symmetrical 10 μM free Ca^{2+} (black) and symmetrical 0.7 nM free Ca^{2+} (orange). **(E, F)** The % of channel open time spent in the fully open level for SR K^+ channels from each condition. Values are of the mean±SEM. The number of experiments is shown in brackets above the respective bars.

3.2.3.2 The effect of increasing luminal [Ca^{2+}] on SR K^+ channel function

Free luminal [Ca^{2+}] was raised from control levels of 10 µM to 100 µM, 1 mM and 5 mM. Figure 3.6 shows typical recordings of current-fluctuations through mouse skeletal SR K^+ channels at holding potentials of +30 mV and -30 mV. Figure 3.6 shows how the Po of the mouse skeletal SR K^+ channel was altered at +30 mV and -30 mV as luminal [Ca^{2+}] was increased. At +30 mV, the total Po of SR K^+ channels was significantly reduced at millimolar luminal [Ca^{2+}] (Figure 3.7A) which corresponded with a significant increase in channel gating to the sub-conductance level rather than the fully open channel level (Figure 3.7C). There was no apparent change observed when luminal [Ca^{2+}] was raised to 100 µM, nor at negative potentials.

Figure 3.7E to H compares how the voltage sensitivity of the channel changed with higher luminal [Ca^{2+}]. Under control conditions and with luminal [Ca^{2+}] at 100 µM, the channel displayed voltage sensitivity, with the total Po at +30 mV being higher than the total Po at -30 mV (Figure 3.7E and F). When luminal [Ca^{2+}] was raised to 1 mM and 5 mM, however, no voltage sensitivity was observed (Figure 3.7G and H).

Further analysis of the single-channel events was carried out to ascertain a mechanism for the reduced SR K^+ channel Po observed in the presence of millimolar luminal Ca^{2+}. Figure 3.8 shows that, as luminal free [Ca^{2+}] was raised, the mean lifetime of both the fully open and sub-conductance events was reduced at +30 mV (Figure 3.8A and C) with no increase in frequency of events (Figure 3.8E). No change was observed at -30 mV.

It was also found that, with higher luminal [Ca^{2+}], a reduction in single-channel current was observed at negative potentials (Figure 3.9). Figure 3.9A shows how the single-channel openings of the SR K^+ channel displayed reduced channel amplitude at negative potentials when luminal [Ca^{2+}] was increased to 5 mM. This effect became more exaggerated as the holding potential became more negative (Figure 3.9B).

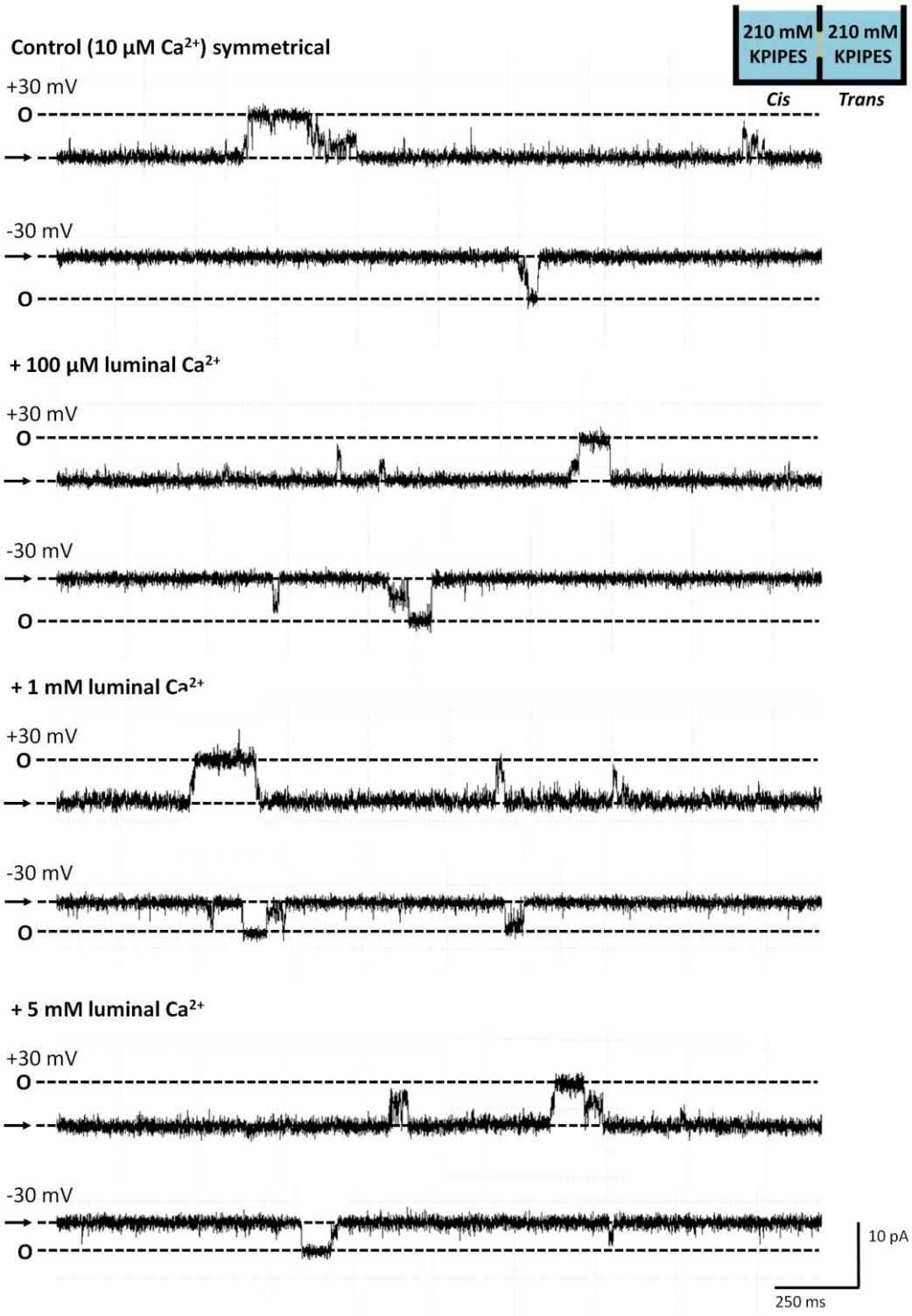
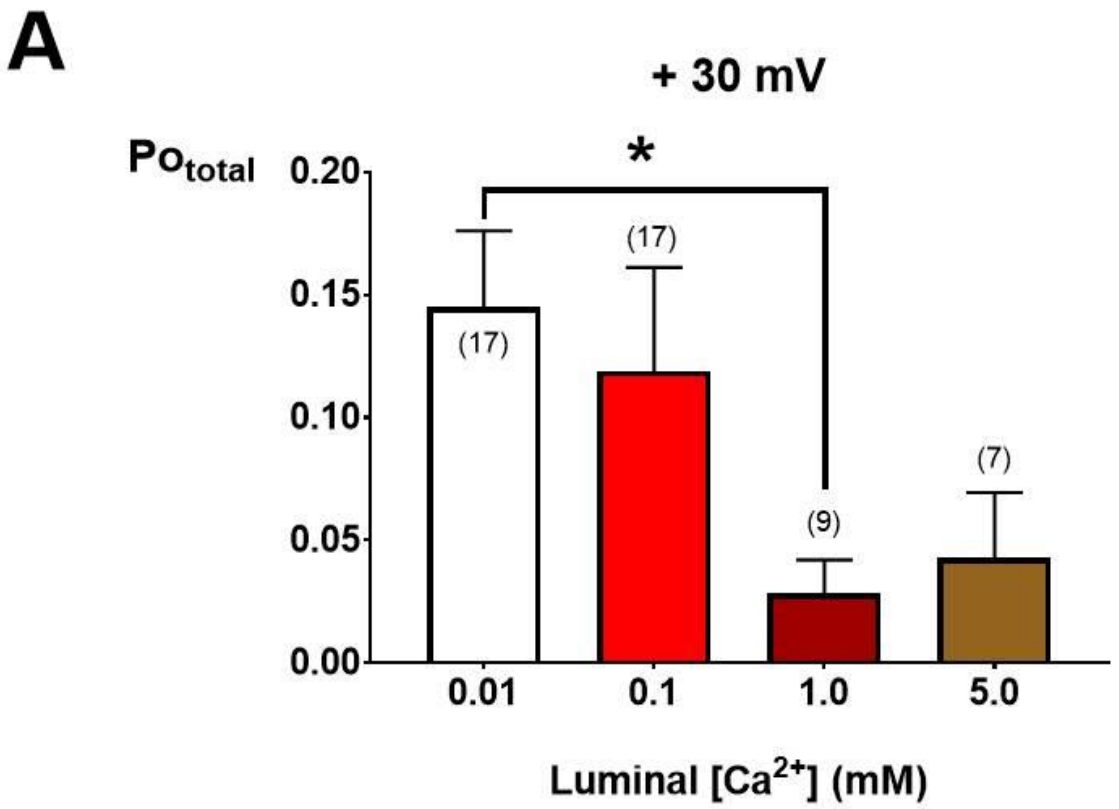
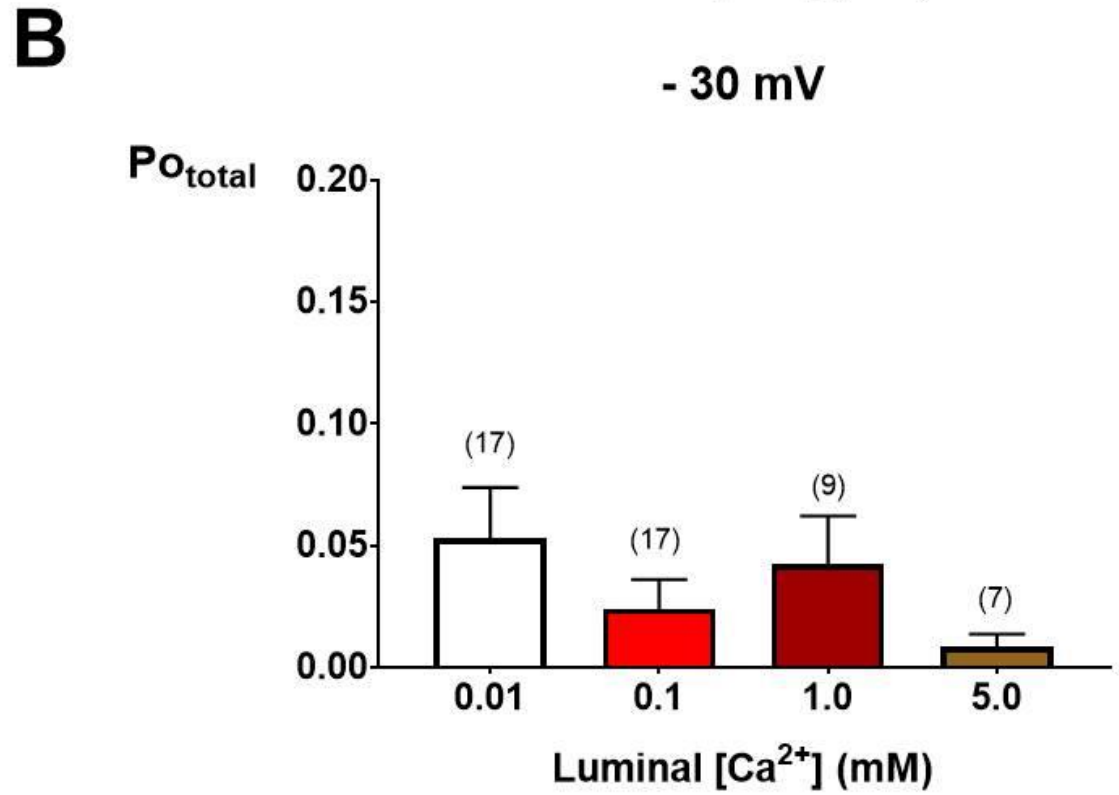
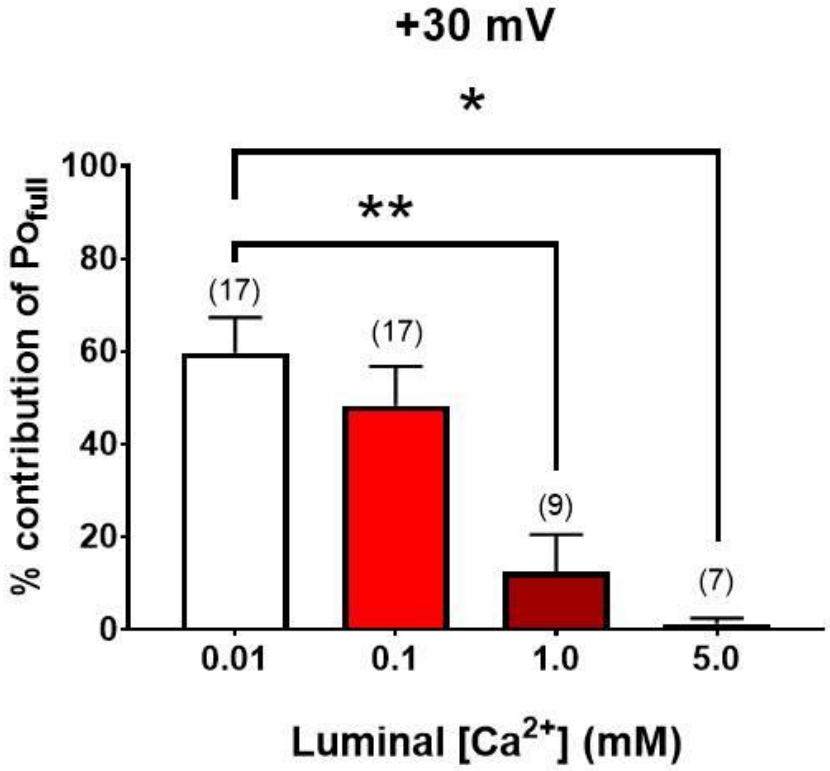


Figure 3.6. The mouse skeletal SR K^+ channel in the presence of increasing luminal [Ca^{2+}]
Representative current-fluctuations through the SR K^+ channel from mouse skeletal muscle at the holding potentials of +30 mV and -30 mV in symmetrical 210 mM KPIPES. Increasing concentrations of Ca^{2+} were added to the luminal side of the channel to the concentrations indicated. The zero current level is shown by an arrow and the fully open channel level by an O.

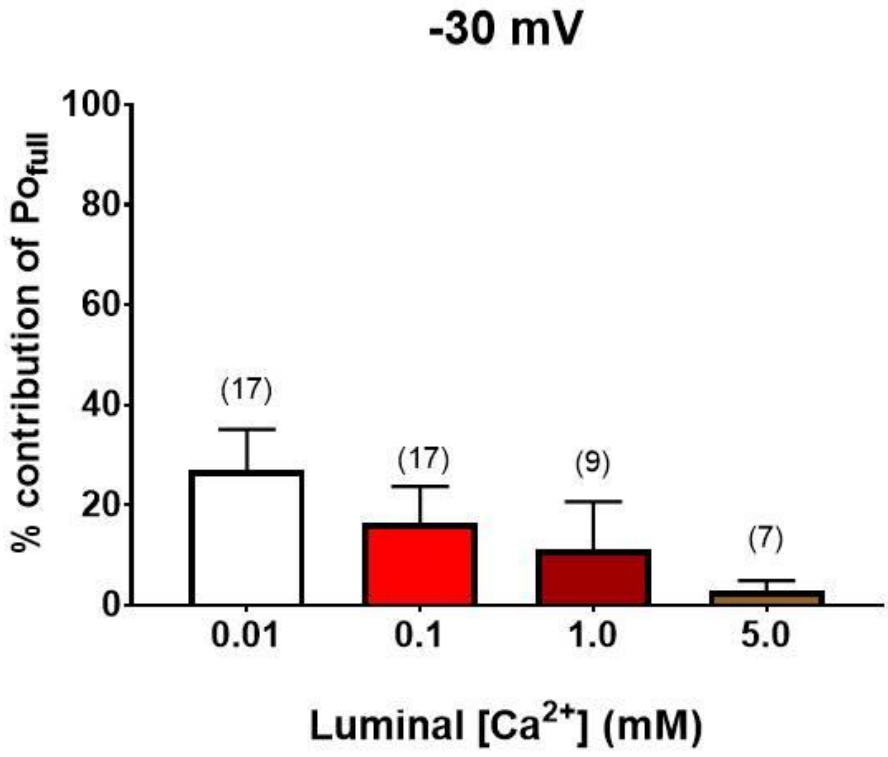

A
+ 30 mV
Po total
0.20
0.15
0.10
0.05
0.00
*
(17)
(17)
(9)
(7)
0.01
0.1
1.0
5.0
Luminal [Ca2+] (mM)


B
- 30 mV
Po total
0.20
0.15
0.10
0.05
0.00
(17)
(17)
(9)
(7)
0.01
0.1
1.0
5.0
Luminal [Ca2+] (mM)

C


+30 mV
*
**
100
80
60
40
20
0
% contribution of Po full
(17)
(17)
(9)
(7)
0.01
0.1
1.0
5.0
Luminal [Ca2+] (mM)

D


-30 mV
100
80
60
40
20
0
% contribution of Po full
(17)
(17)
(9)
(7)
0.01
0.1
1.0
5.0
Luminal [Ca2+] (mM)

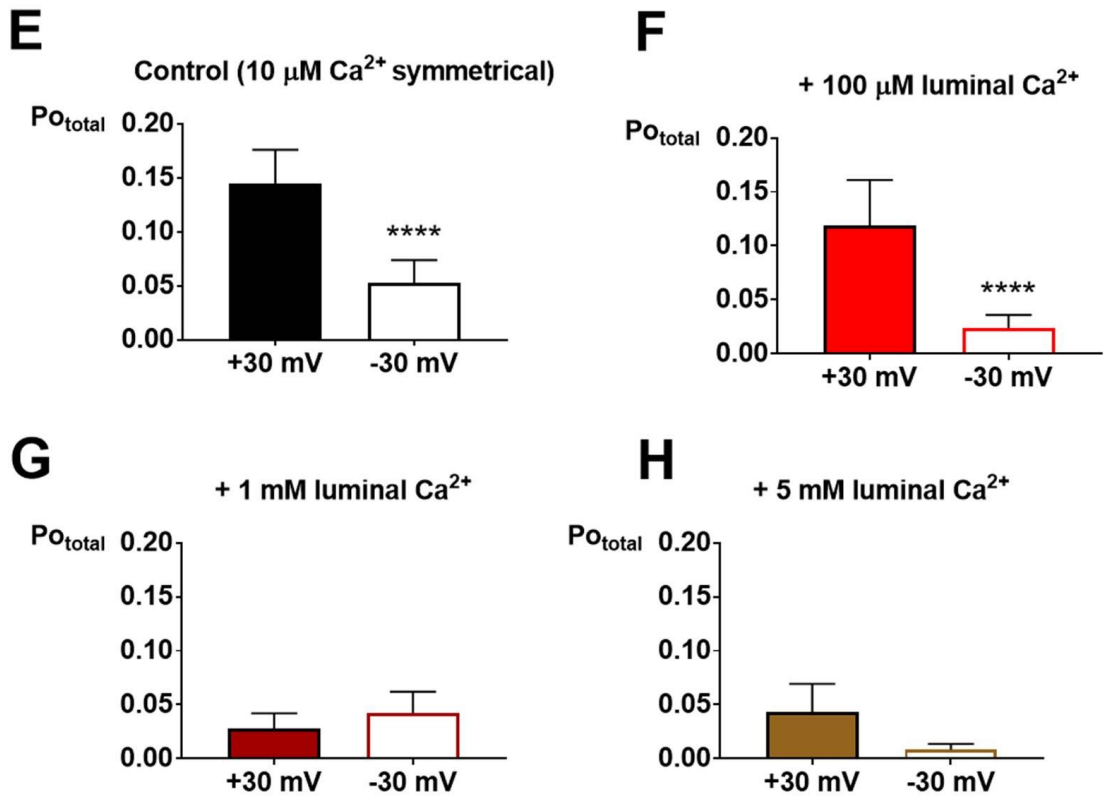
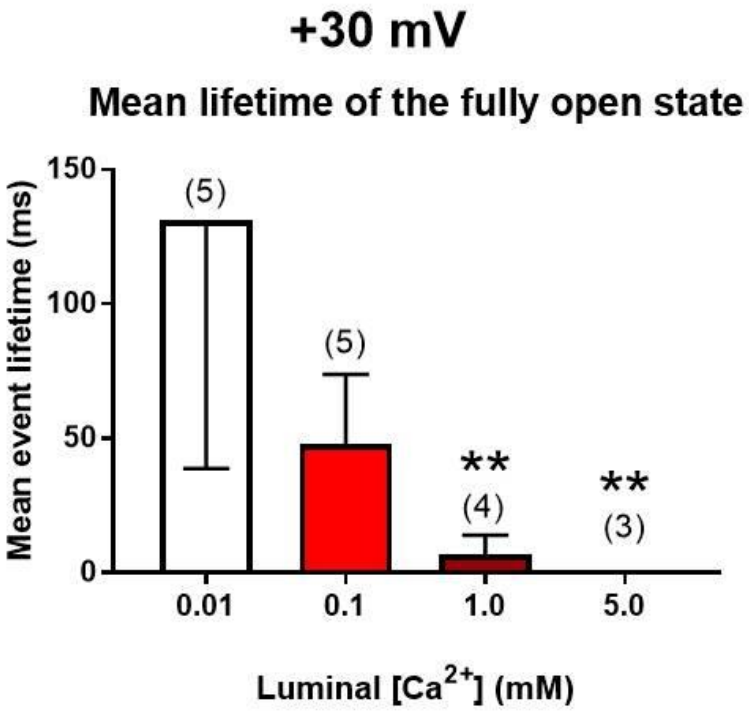
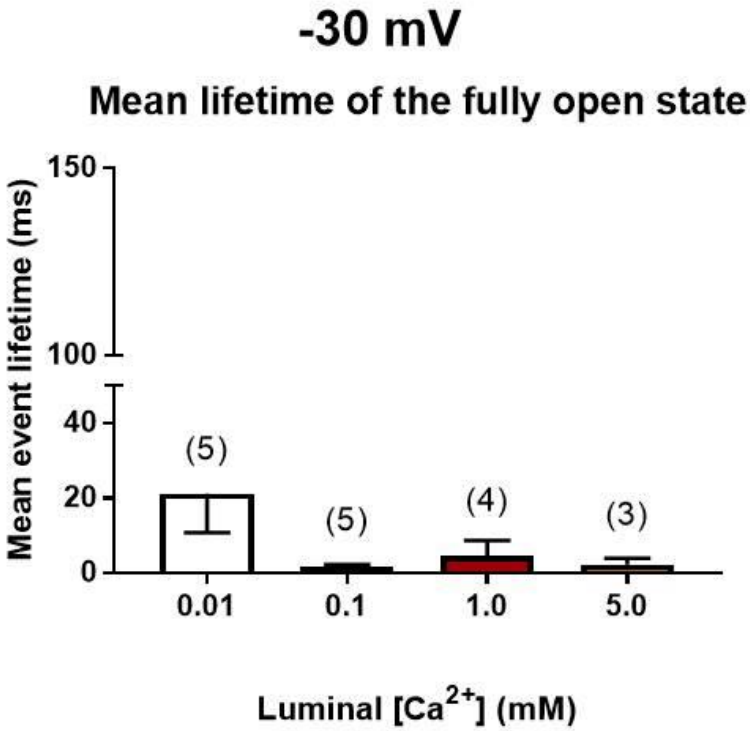


Figure 3.7. The effect of increasing luminal [Ca^{2+}] on the Po of mouse skeletal SR K^+ channels
(A, B) The total Po of the SR K^+ channel from mouse skeletal muscle with increasing luminal [Ca^{2+}] at +30 mV **(A)** and at -30 mV **(B)**. **(C, D)** The percentage of channel open time which was spent in the fully open state with increasing luminal [Ca^{2+}] at +30 mV **(C)** and at -30 mV **(D)**. **(E, F, G, H)** Comparisons of the total Po of the mouse skeletal SR K^+ channel at +30 mV and -30 mV holding potentials at each luminal Ca^{2+} concentration. Values are of the mean±SEM. The number of experiments is shown in brackets and the degree of significance relative to control is shown by stars above the respective bars.

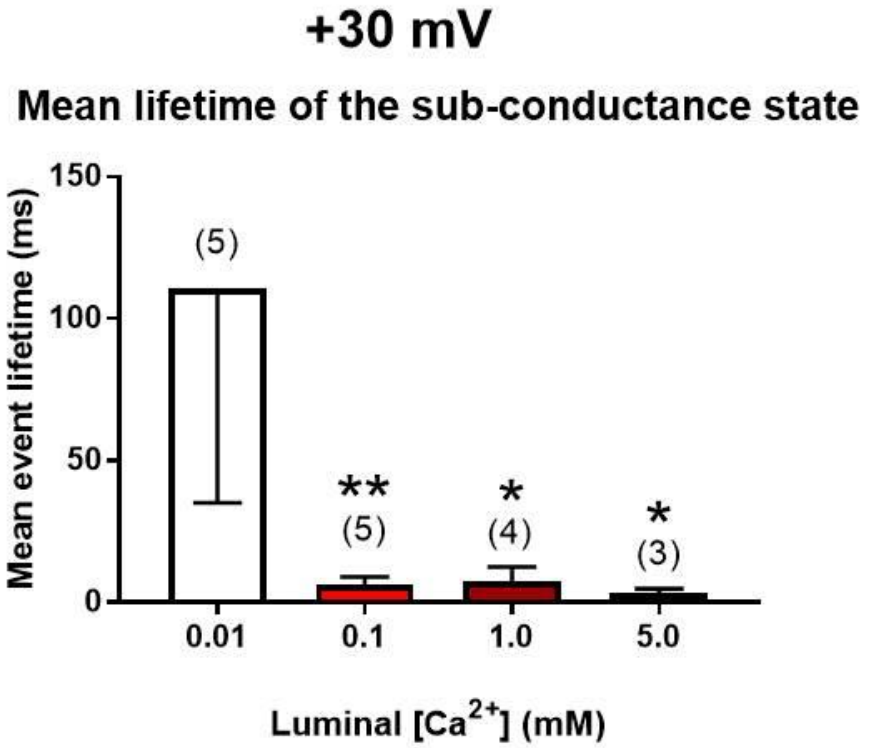
A


+30 mV
Mean lifetime of the fully open state
Mean event lifetime (ms)
150
100
50
0
(5)
(5)
**
(4)
**
(3)
0.01
0.1
1.0
5.0
Luminal [Ca2+] (mM)

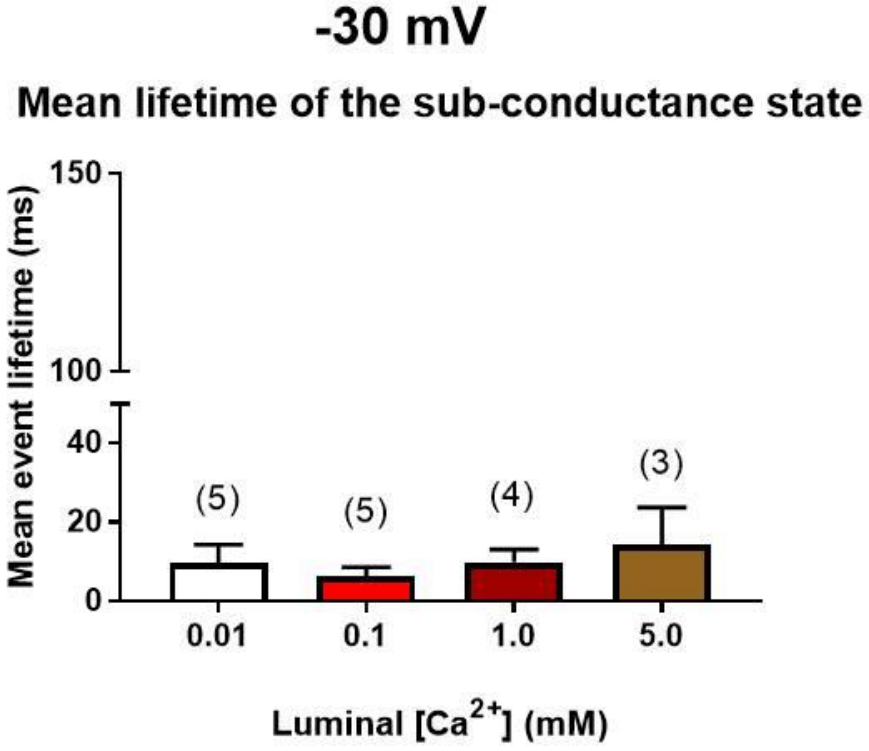
B


-30 mV
Mean lifetime of the fully open state
Mean event lifetime (ms)
150
100
40
20
0
(5)
(5)
(4)
(3)
0.01
0.1
1.0
5.0
Luminal [Ca2+] (mM)

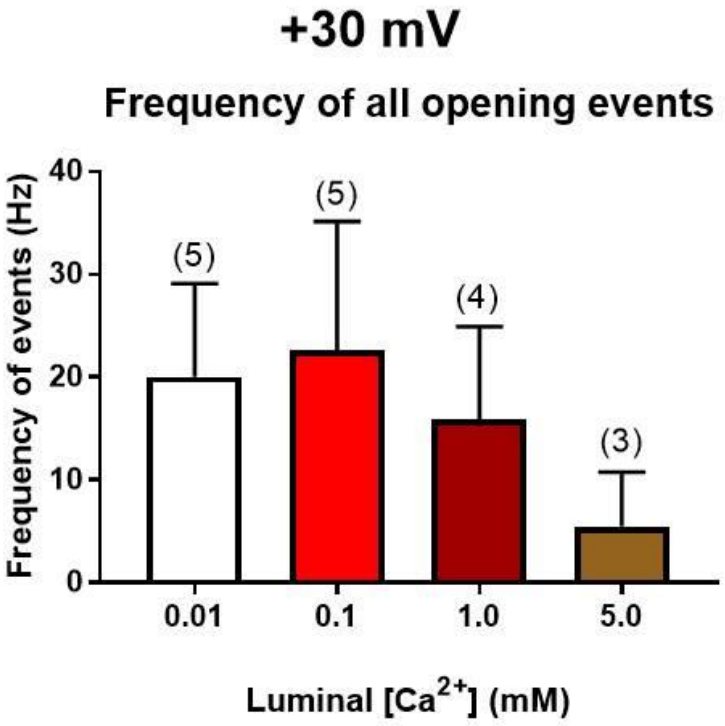
C


+30 mV
Mean lifetime of the sub-conductance state
Mean event lifetime (ms)
150
100
50
0
(5)
**
(5)
*
(4)
*
(3)
0.01
0.1
1.0
5.0
Luminal [Ca2+] (mM)

D


-30 mV
Mean lifetime of the sub-conductance state
Mean event lifetime (ms)
150
100
40
20
0
(5)
(5)
(4)
(3)
0.01
0.1
1.0
5.0
Luminal [Ca2+] (mM)

E


+30 mV
Frequency of all opening events
Frequency of events (Hz)
40
30
20
10
0
(5)
(5)
(4)
(3)
0.01
0.1
1.0
5.0
Luminal [Ca2+] (mM)

F

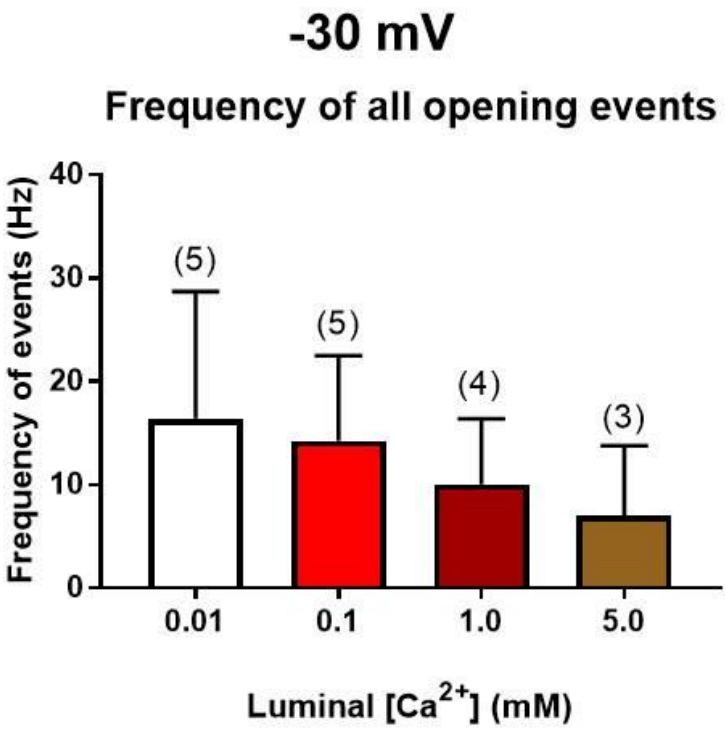

-30 mV
Frequency of all opening events
Frequency of events (Hz)
40
30
20
10
0
(5)
(5)
(4)
(3)
0.01
0.1
1.0
5.0
Luminal [Ca2+] (mM)

Figure 3.8. Single-channel event analysis of mouse skeletal SR K^+ channels with increasing luminal [Ca^{2+}]

(A, B) The mean lifetime of events which gate to the fully open state in the presence of increasing luminal [Ca^{2+}] at +30 mV **(A)** and at -30 mV **(B)**. **(C, D)** The mean lifetime of events which gate to the sub-conductance state in the presence of increasing luminal [Ca^{2+}] at +30 mV **(C)** and at -30 mV **(D)**. **(E, F)** The frequency of single-channel events (both to the full and the sub-conductance level) at +30 mV **(E)** and -30 mV **(F)** holding potentials with increasing luminal [Ca^{2+}]. Values are of the mean±SEM or mean±SD. The number of experiments is shown in brackets and the degree of significance relative to control is shown by stars above the respective bars.

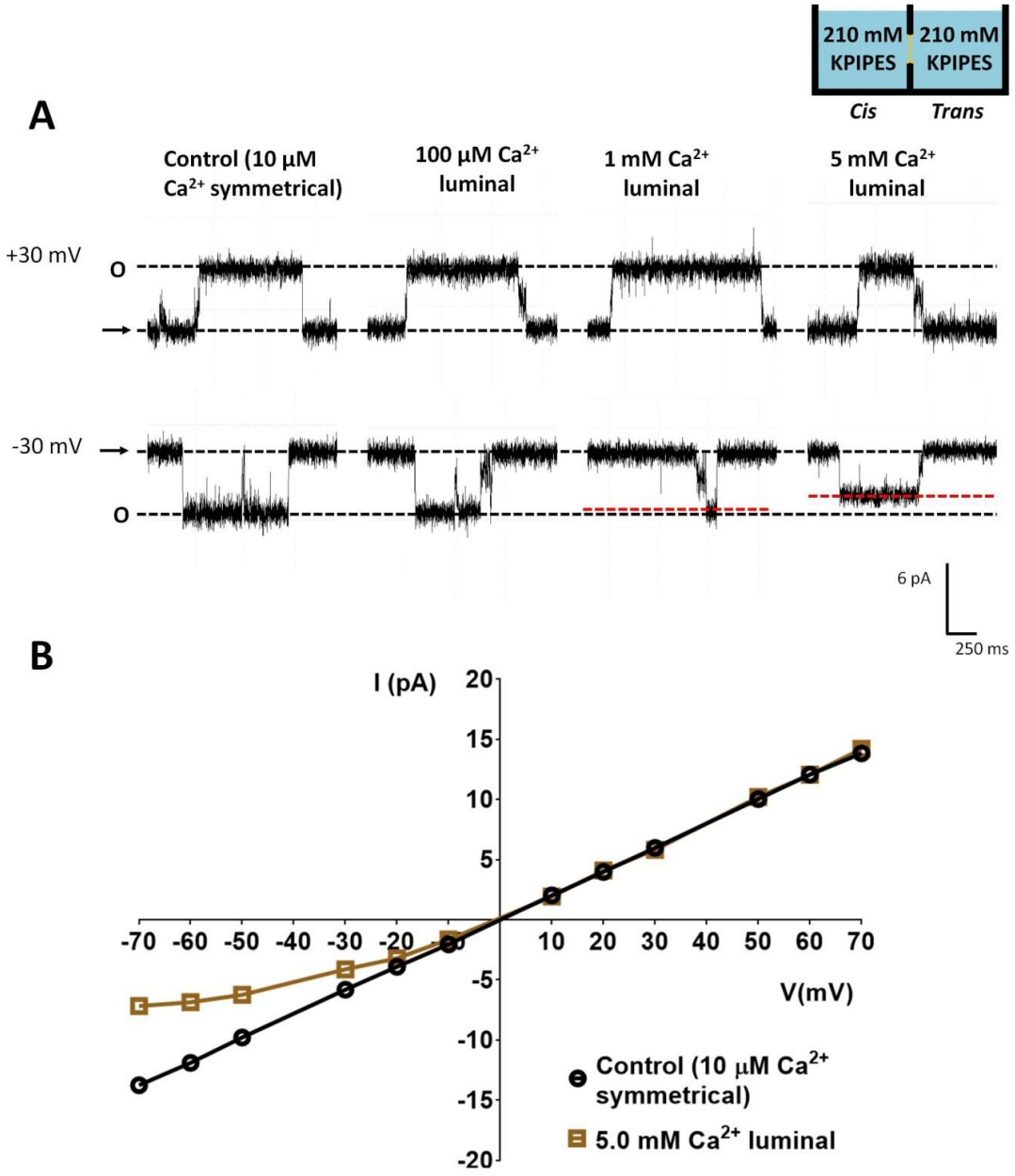


Figure 3.9. Block of the mouse skeletal SR K^+ channel by 5 mM luminal Ca^{2+}.
(A) Current-fluctuations representing mouse skeletal SR K^+ channel single-channel opening events at +30 mV and at -30 mV holding potentials with 10 µM, 100 µM, 1 mM and 5 mM luminal Ca^{2+}. The closed channel level is shown with an arrow and the fully open level with an O. The reduced fully open channel level due to a high luminal free [Ca^{2+}] is shown by a red line. **(B)** The current-voltage relationship for mouse skeletal SR K^+ channels in symmetrical 210 mM KPIPES under control conditions (black, n=25) and with 5 mM Ca^{2+} on the luminal side of the channel (brown, n=4). Values are mean±SEM. Where not shown, error bars are within the symbols.

3.2.3.3 The effect of increasing cytosolic [Ca^{2+}] on SR K^+ channel function

As well as the effect of luminal Ca^{2+} on the SR K^+ channel, the effect of cytosolic Ca^{2+} was studied. Figure 3.10 shows current-fluctuations through a mouse skeletal SR K^+ channel at +30 mV and -30 mV holding potentials as [Ca^{2+}] was increased from control levels of 10 µM, to 100 µM, 1 mM, and 5 mM concentrations on the cytosolic side of the channel. No obvious change was observed in SR K^+ channel gating when cytosolic [Ca^{2+}] was raised (Figure 3.11A-D). A reduction in current was observed at positive potentials with 5 mM cytosolic Ca^{2+} (Figure 3.11E). The reduction of current observed at positive potentials when 5 mM Ca^{2+} was present on the cytosolic side of the channel was observed to be smaller than the corresponding current reduction at negative potentials when 5 mM Ca^{2+} was present on the luminal side of the channel.

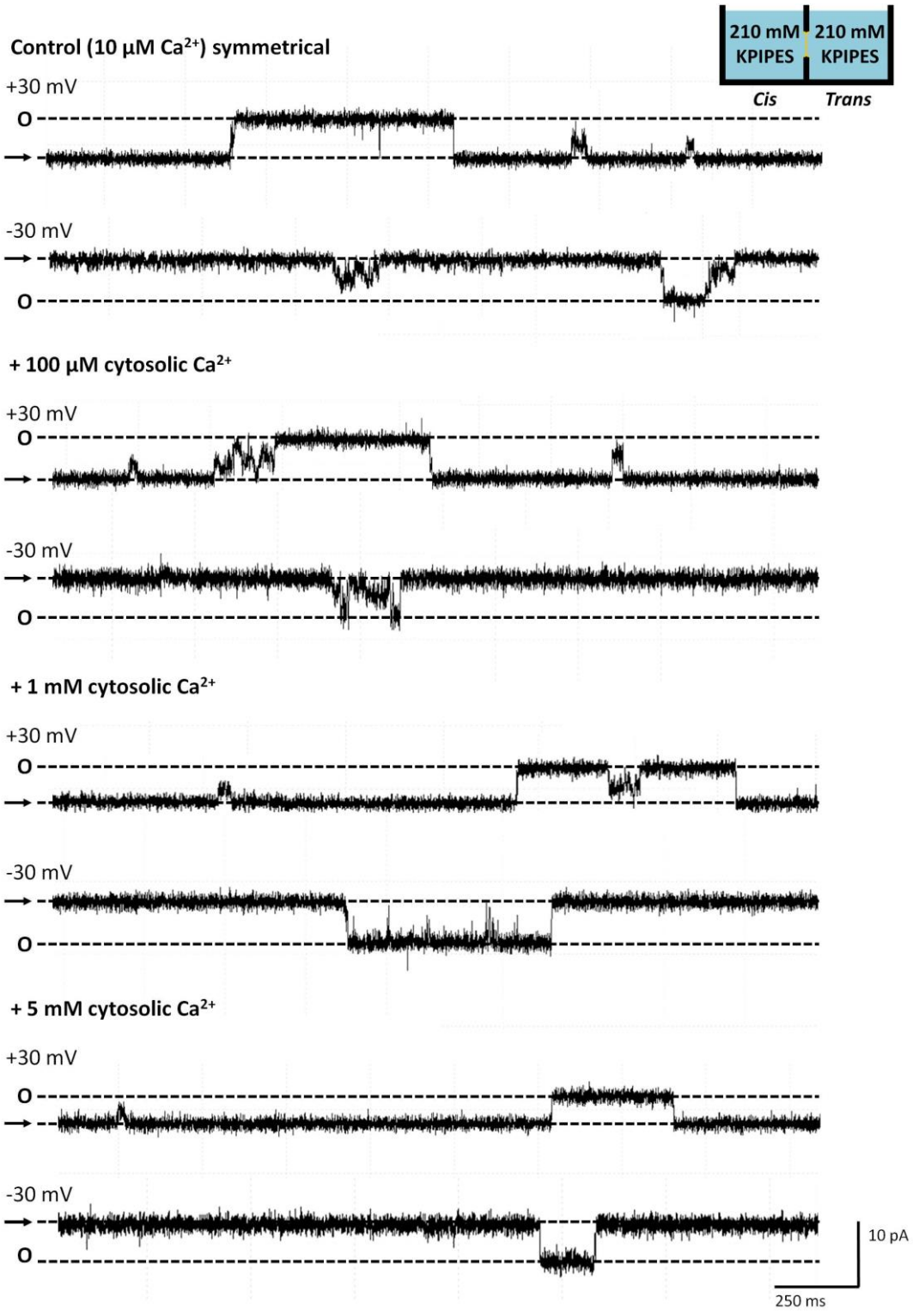
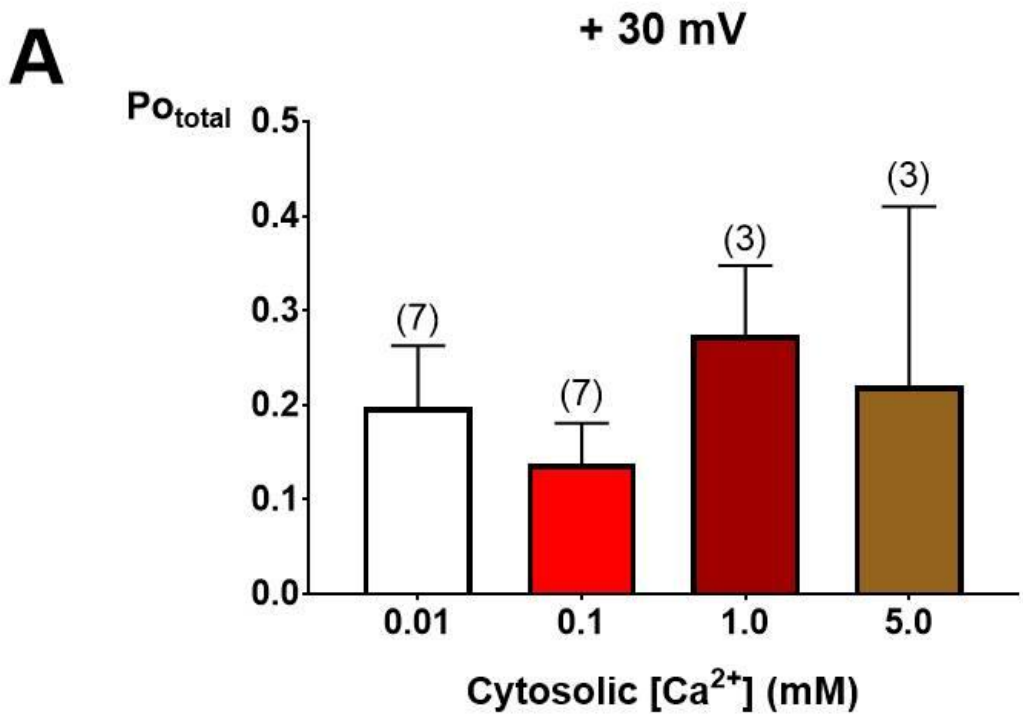
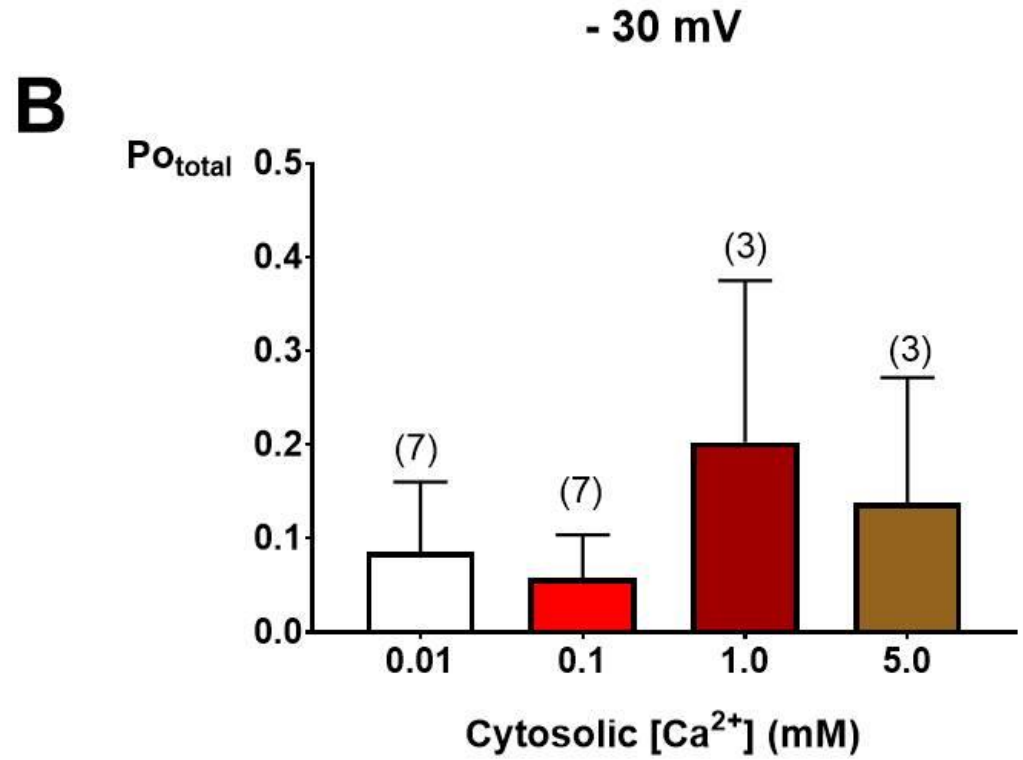
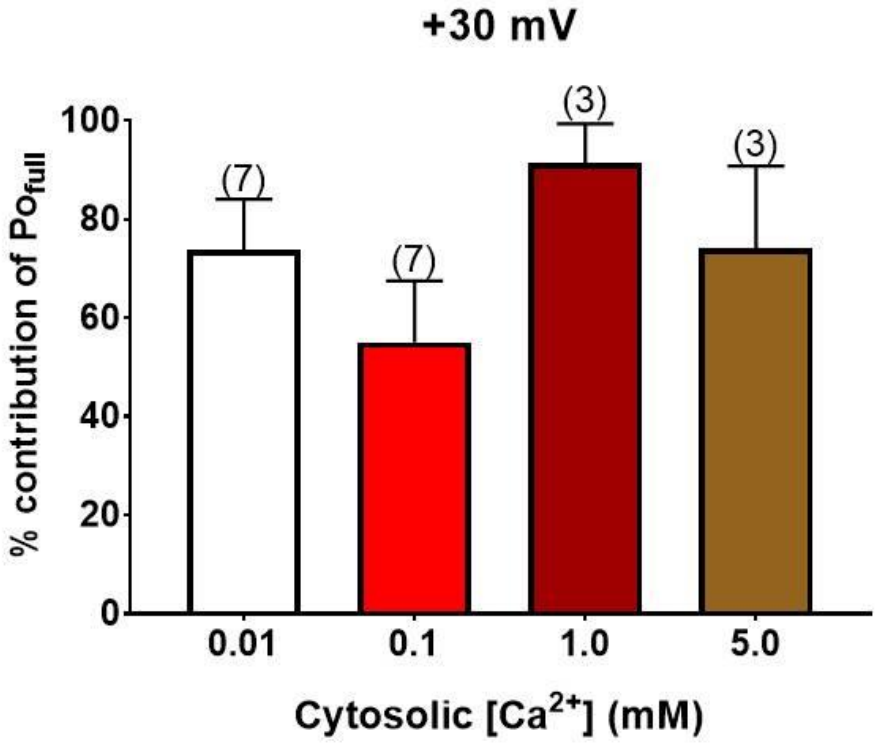


Figure 3.10. The mouse skeletal SR K^+ channel in the presence of increasing cytosolic [Ca^{2+}] Representative current-fluctuations through the SR K^+ channel from mouse skeletal muscle at the holding potentials of +30 mV and -30 mV in symmetrical 210 mM KPIPES. Increasing concentrations of Ca^{2+} were added to the cytosolic side of the channel to the concentrations indicated. The zero current level is shown by an arrow and the fully open channel level by an O.

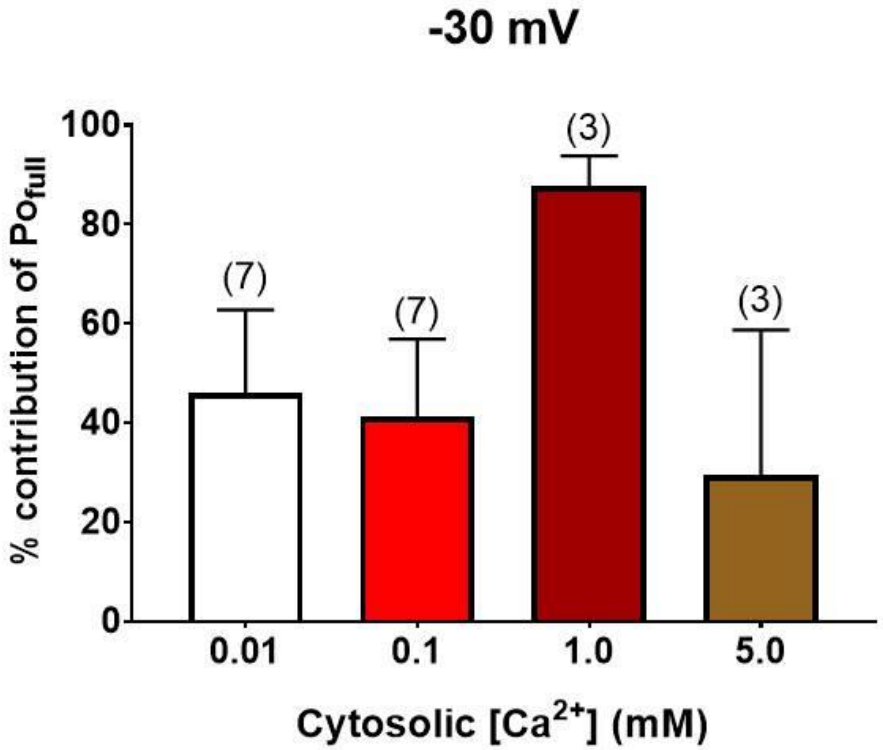

A
+ 30 mV
Po total
0.5
0.4
0.3
0.2
0.1
0.0
(7)
(7)
(3)
(3)
0.01
0.1
1.0
5.0
Cytosolic [Ca2+] (mM)


B
- 30 mV
Po total
0.5
0.4
0.3
0.2
0.1
0.0
(7)
(7)
(3)
(3)
0.01
0.1
1.0
5.0
Cytosolic [Ca2+] (mM)

C


+30 mV
% contribution of Po full
100
80
60
40
20
0
(7)
(7)
(3)
(3)
0.01
0.1
1.0
5.0
Cytosolic [Ca2+] (mM)

D


-30 mV
% contribution of Po full
100
80
60
40
20
0
(7)
(7)
(3)
(3)
0.01
0.1
1.0
5.0
Cytosolic [Ca2+] (mM)

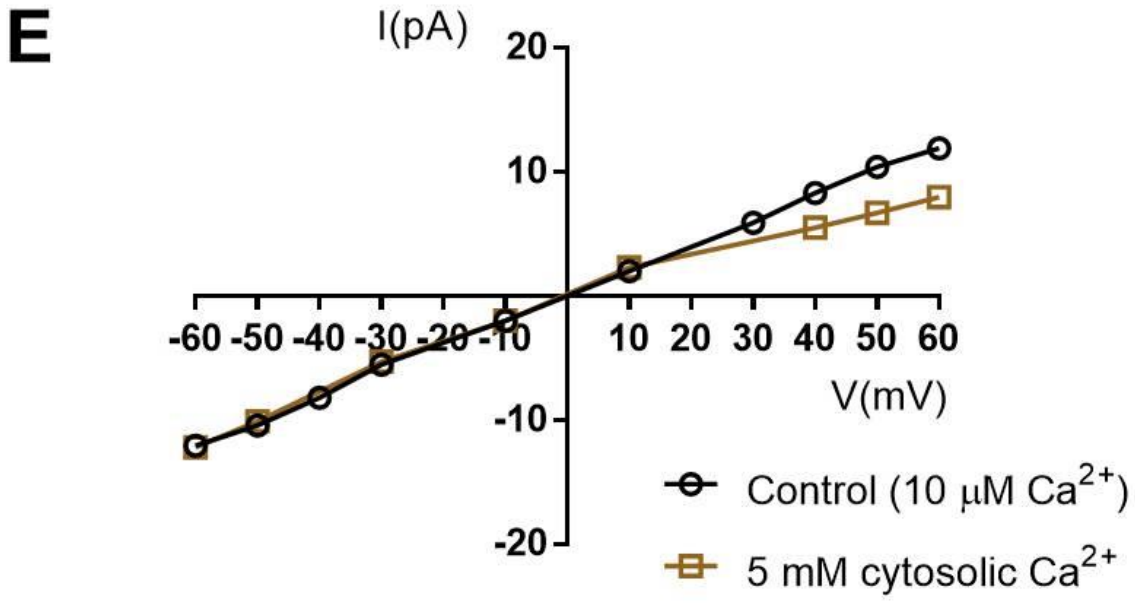


Figure 3.11. The effect of increasing cytosolic [Ca^{2+}] on the single-channel properties of mouse skeletal SR K^+ channels

(A, B) The total Po of the SR K^+ channel from mouse skeletal muscle with increasing cytosolic [Ca^{2+}] at +30 mV **(A)** and at -30 mV **(B)**. **(C, D)** The percentage of channel open time which was spent in the fully open state with increasing cytosolic [Ca^{2+}] at +30 mV **(C)** and at -30 mV **(D)**. Values are of the mean±SEM. The number of experiments is shown in brackets above the respective bars. **(E)** The current-voltage relationship for mouse skeletal SR K^+ channels in symmetrical 210 mM KPIPES under control conditions (black, n=25) and with 5 mM Ca^{2+} on the cytosolic side of the channel (brown, n=3). Values are mean±SEM or mean±SD. Where not shown, error bars are within the symbols.

3.2.3.4 The effect of increasing symmetrical [Ca^{2+}] on SR K^+ channel function

[Ca^{2+}] was increased symmetrically on both sides of SR K^+ channels from mouse skeletal muscle. Figure 3.12 shows current-fluctuations through an SR K^+ channel from mouse skeletal muscle with symmetrical [Ca^{2+}] increased from control levels of 10 µM to 100 µM and 5 mM. The Po of the SR K^+ channel was observed to decrease at both +30 mV and -30 mV holding potentials as symmetrical [Ca^{2+}] was increased (Figure 3.13A and B). The channel was also observed to spend more channel open time dwelling in the sub-conductance level (Figure 3.14C and D). This effect was observed at both +30 mV and -30 mV holding potentials.

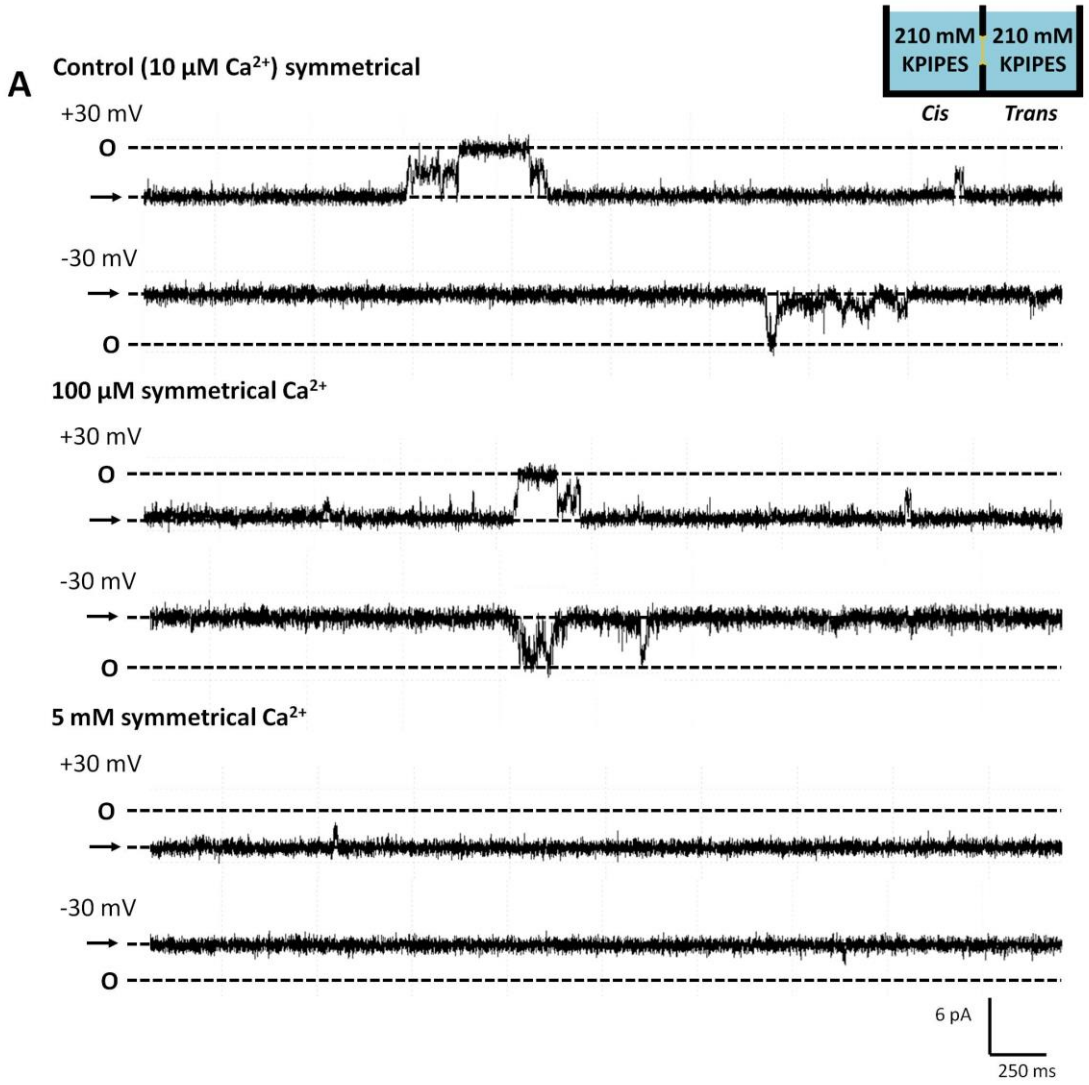
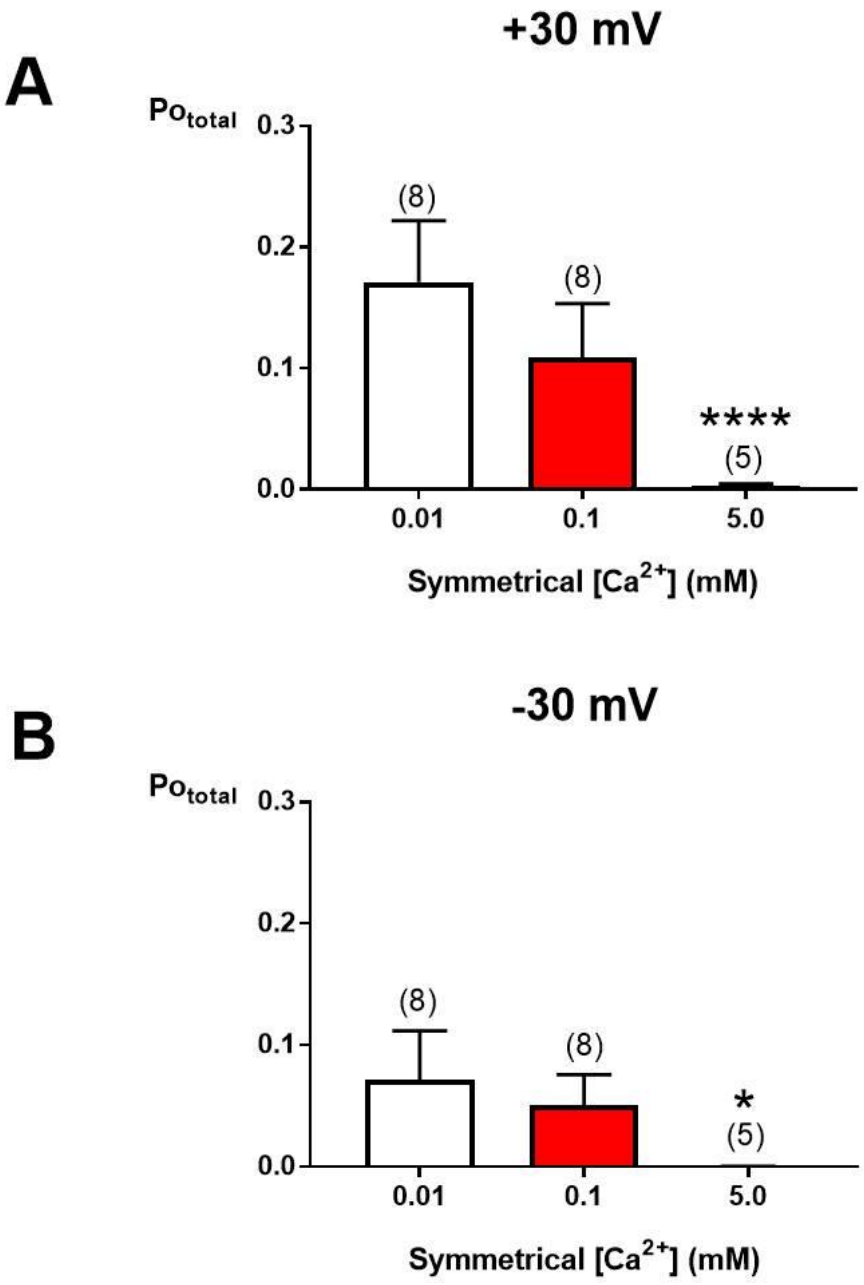


Figure 3.12. The mouse skeletal SR K^+ channel in the presence of increasing symmetrical [Ca^{2+}]

Representative current-fluctuations through the SR K^+ channel from mouse skeletal muscle at the holding potentials of +30 mV and -30 mV in symmetrical 210 mM KPIPES. Increasing concentrations of Ca^{2+} were added symmetrically to both the cytosolic and luminal sides of the channel to the concentrations indicated. The zero current level is shown by an arrow and the fully open channel level by an O.


A
+30 mV
Po total
0.3
0.2
0.1
0.0
(8)
(8)
****
(5)
0.01
0.1
5.0
Symmetrical [Ca2+] (mM)
B
-30 mV
Po total
0.3
0.2
0.1
0.0
(8)
(8)
*
(5)
0.01
0.1
5.0
Symmetrical [Ca2+] (mM)

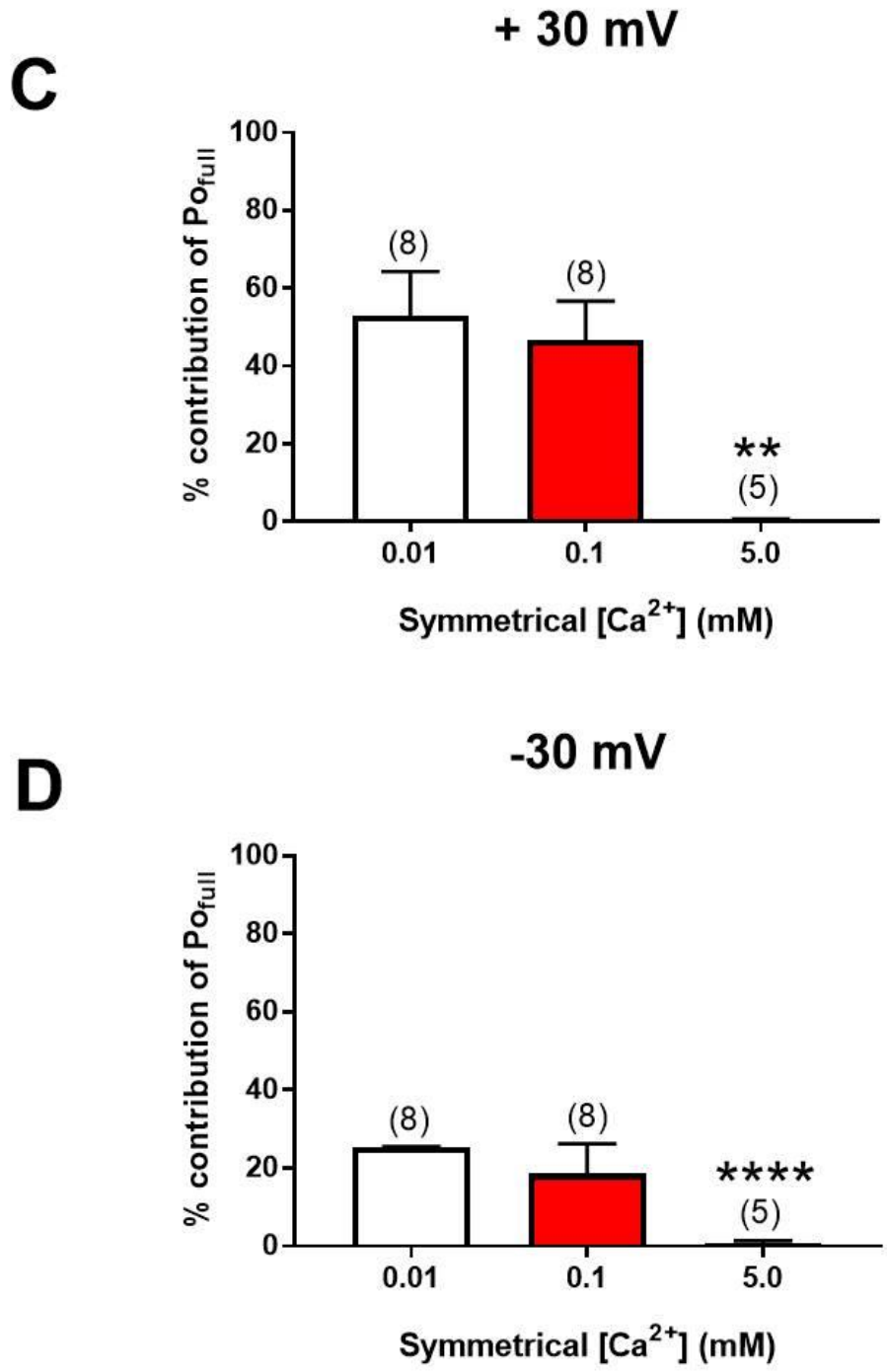


Figure 3.13. The effect of increasing symmetrical [Ca^{2+}] on the Po of mouse skeletal SR K^+ channels

(A, B) The total Po of the SR K^+ channel from mouse skeletal muscle with increasing symmetrical [Ca^{2+}] at +30 mV **(A)** and at -30 mV **(B)**. **(C, D)** The percentage of channel open time which was spent in the fully open state with increasing symmetrical [Ca^{2+}] at +30 mV **(C)** and at -30 mV **(D)**. Values are of the mean±SEM. The number of experiments is shown in brackets and the degree of significance relative to control is shown by stars above the respective bars.

3.2.4 Mg^{2+} as a ligand of the SR K^+ channel

The effect of Ca^{2+} on SR K^+ channels led to the study of other divalent cation channels such as Mg^{2+}. [Mg^{2+}] was raised from control levels (contaminant Mg^{2+}) to 1 mM and 5 mM on the luminal side of the channel, the cytosolic side of the channel, and symmetrically, on both sides of the channel via the addition of Mg-glutamate solution. Representative current-fluctuations through mouse skeletal SR K^+ channels with elevated luminal, cytosolic and symmetrical [Mg^{2+}] are shown in Figure 3.14, Figure 3.16 and Figure 3.18, respectively.

Unlike the effects of Ca^{2+} on the SR K^+ channel, both the Po and the % of open time spent in the fully open state of mouse skeletal SR K^+ channels were observed not to be altered with millimolar Mg^{2+} on the luminal side of the channel (Figure 3.15), the cytosolic side of the channel (Figure 3.17) or symmetrically (Figure 3.19). This was observed at both +30 mV and -30 mV holding potentials.

Figure 3.20 shows how K^+ currents through SR K^+ channels were altered in the presence of millimolar Mg^{2+}. Mg^{2+}, present on the luminal side of mouse skeletal SR K^+ channels, was observed to reduce the single-channel conductance at negative potentials at concentrations of 1 mM. Increasing the luminal [Mg^{2+}] to 5 mM further reduced single-channel conductance (Figure 3.20A). Mg^{2+} was also added to the cytosolic side of the channel and was observed to reduce single-channel conductance at positive potentials at concentrations of 5 mM. At a cytosolic concentration of 1 mM Mg^{2+}, only a limited reduction in single-channel current at positive potentials was observed (Figure 3.20B). Interestingly, when 5 mM Mg^{2+} was present on the cytosolic side of the channel, a reduction in single-channel conductance was also observed at negative potentials. 5 mM Mg^{2+}, added symmetrically to both sides of the channel,

was found to reduce the single-channel conductance of the SR K^+ channel at both positive and negative potentials (Figure 3.20C).

Figure 3.21 compares the pore block of the mouse skeletal SR K^+ channel by 5 mM Mg^{2+} and 5 mM Ca^{2+}. 5 mM Ca^{2+} was observed to reduce the K^+ current passing through mouse skeletal SR K^+ channels to a greater extent than 5 mM Mg^{2+} when present on either the cytosolic or luminal side of the channel.

Figure 3.22 provides evidence of the inability of mouse skeletal SR K^+ channels to pass Mg^{2+}. Experiments were conducted which exchanged 210 mM KPIPES with 100 mM Mg-glutamate on either the cytosolic or the luminal side of the channel. When 100 mM Mg-glutamate was present on the cytosolic side of the channel, no current was observed at positive potentials. When 100 mM Mg-glutamate was present on the luminal side of the channel, no current was observed at negative potentials. This demonstrates that the mouse skeletal SR K^+ channel is impermeable to Mg^{2+} as was previously shown to be the case for Ca^{2+} [98].

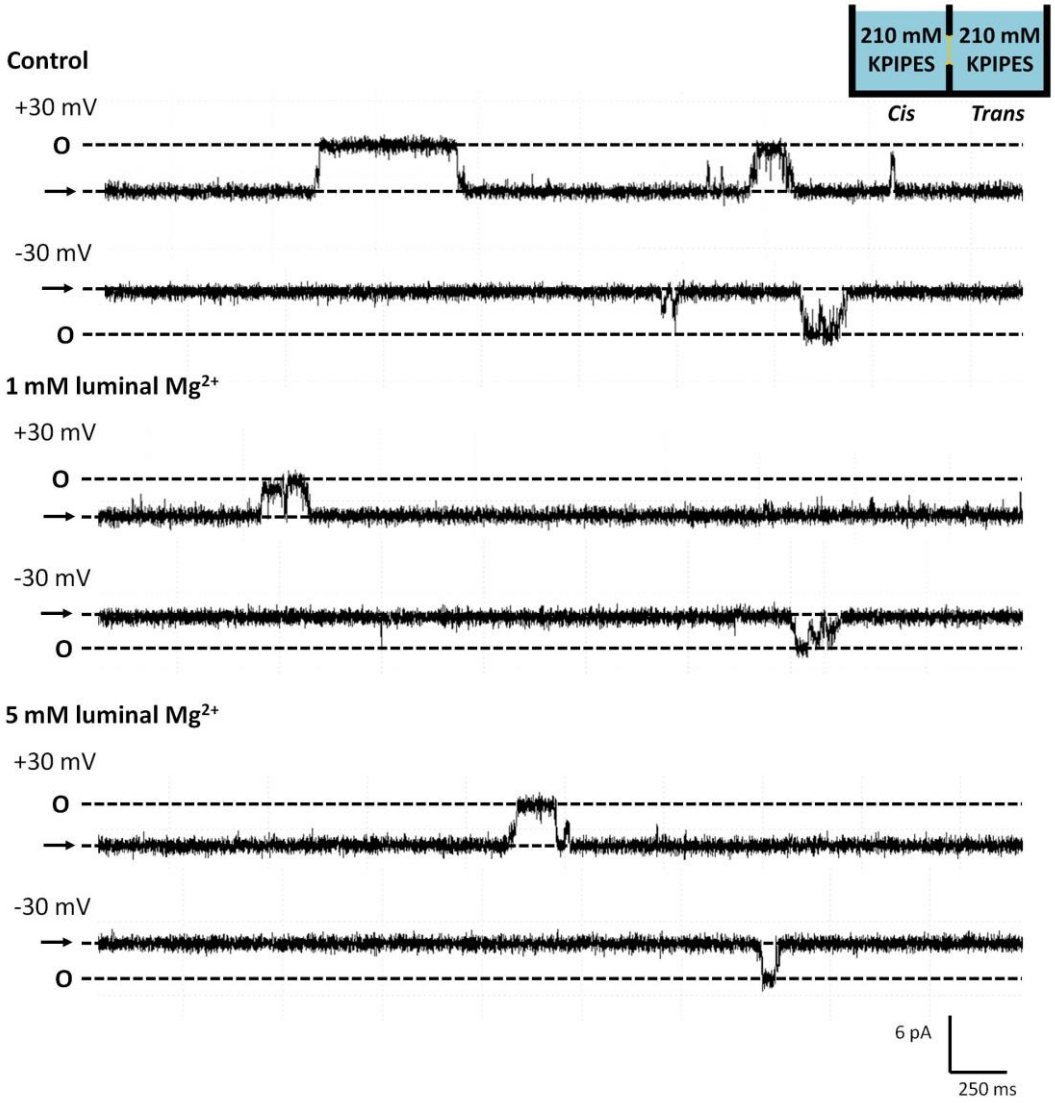
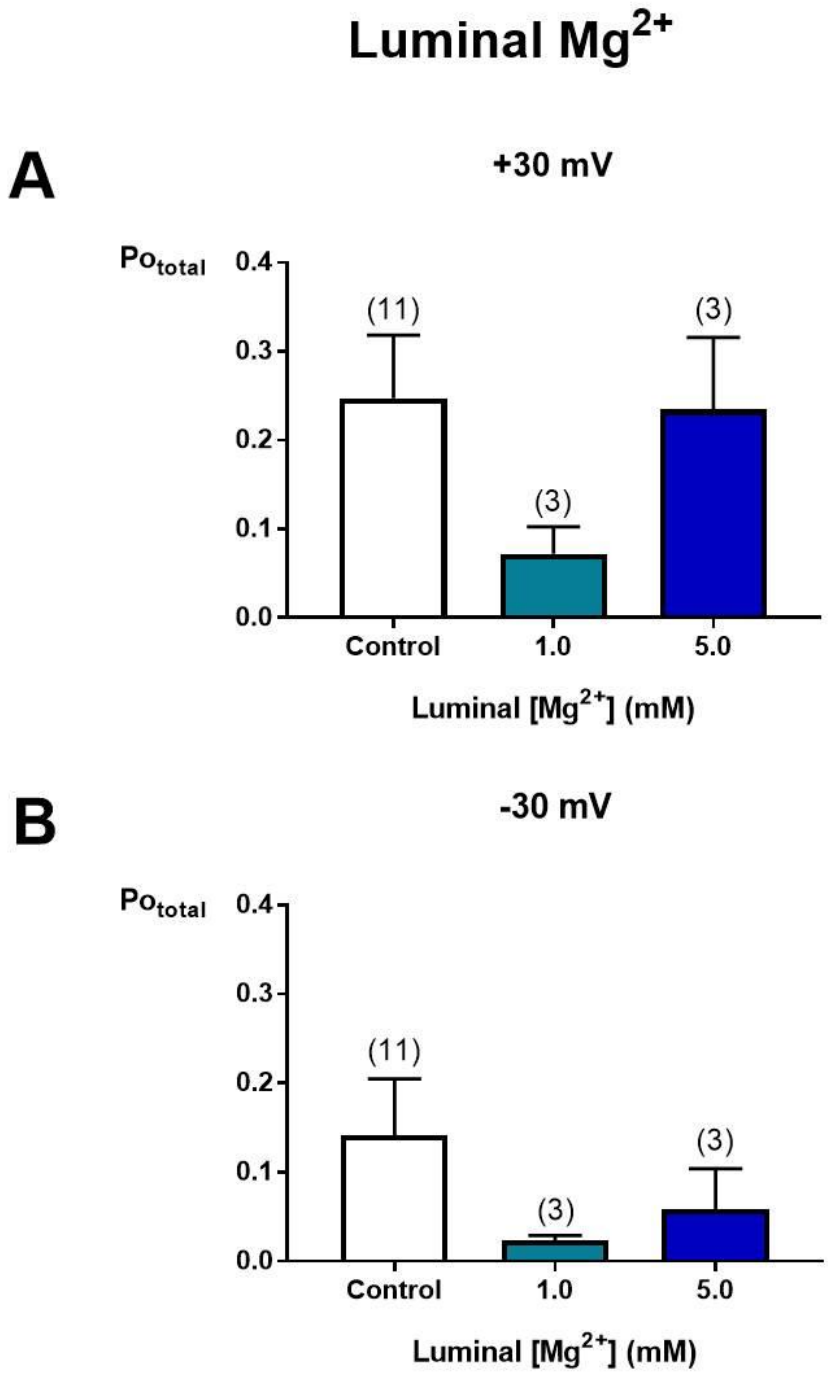


Figure 3.14. The mouse skeletal SR K^+ channel in the presence of increasing luminal [Mg^{2+}]
Representative current-fluctuations through the SR K^+ channel from mouse skeletal muscle at the holding potentials of +30 mV and -30 mV in symmetrical 210 mM KPIPES. Increasing concentrations of Mg^{2+} were added to the luminal side of the channel to the concentrations indicated. The zero current level is shown by an arrow and the fully open channel level by an O.


Luminal Mg2+
A
+30 mV
Pototal
0.4
0.3
0.2
0.1
0.0
(11)
(3)
(3)
Control
1.0
5.0
Luminal [Mg2+] (mM)
B
-30 mV
Pototal
0.4
0.3
0.2
0.1
0.0
(11)
(3)
(3)
Control
1.0
5.0
Luminal [Mg2+] (mM)

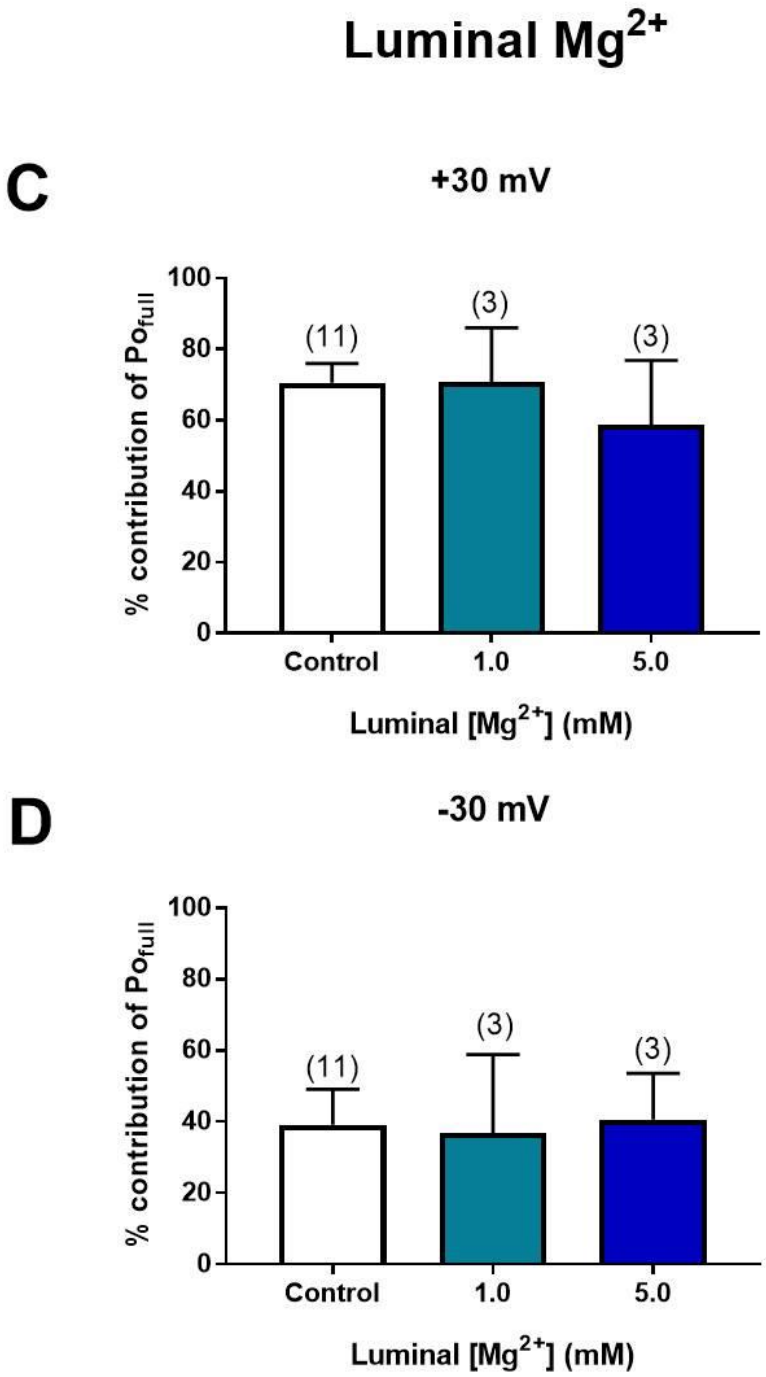


Figure 3.15. The effect of increasing luminal [Mg^{2+}] on the Po of mouse skeletal SR K^+ channels

(A, B) The total Po of the SR K^+ channel from mouse skeletal muscle with increasing luminal [Mg^{2+}] at +30 mV **(A)** and at -30 mV **(B)**. **(C, D)** The percentage of channel open time which was spent in the fully open state with increasing luminal [Mg^{2+}] at +30 mV **(C)** and at -30 mV **(D)**. Values are of the mean±SEM. The number of experiments is shown in brackets above the respective bars.

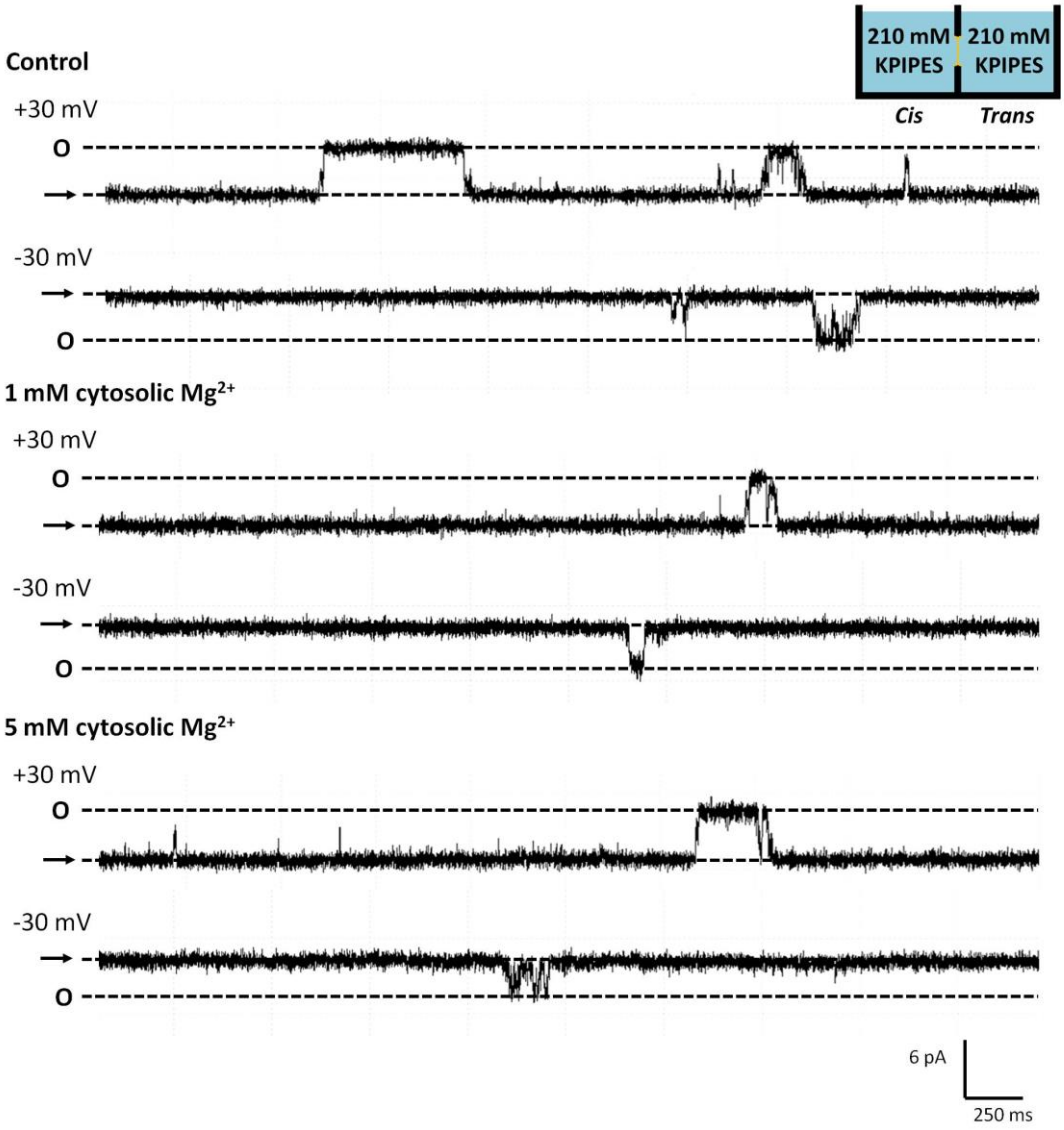
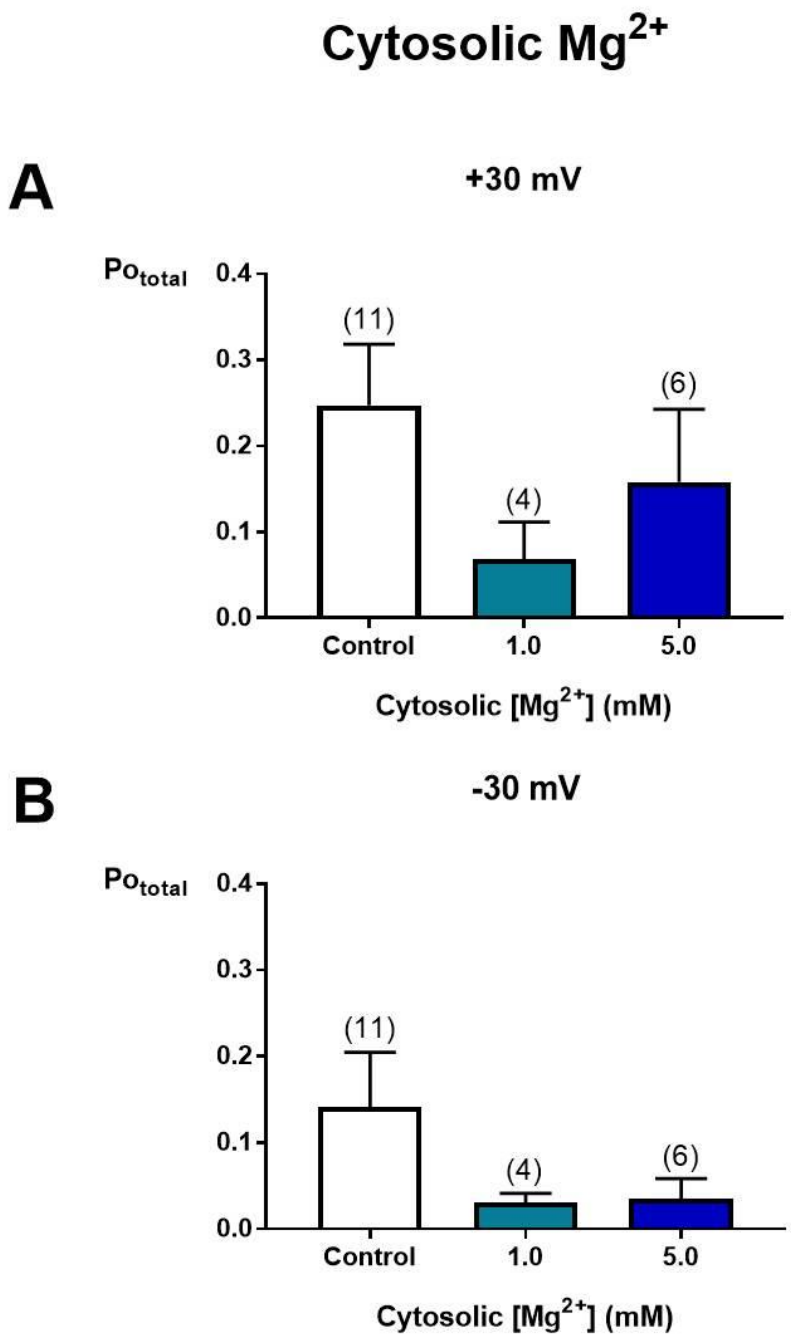


Figure 3.16. The mouse skeletal SR K^+ channel in the presence of increasing cytosolic [Mg^{2+}]
Representative current-fluctuations through the SR K^+ channel from mouse skeletal muscle at the holding potentials of +30 mV and -30 mV in symmetrical 210 mM KPIPES. Increasing concentrations of Mg^{2+} were added to the cytosolic side of the channel to the concentrations indicated. The zero current level is shown by an arrow and the fully open channel level by an O.


Cytosolic Mg2+
A
+30 mV
Pototal
0.4
0.3
0.2
0.1
0.0
(11)
(4)
(6)
Control
1.0
5.0
Cytosolic [Mg2+] (mM)
B
-30 mV
Pototal
0.4
0.3
0.2
0.1
0.0
(11)
(4)
(6)
Control
1.0
5.0
Cytosolic [Mg2+] (mM)

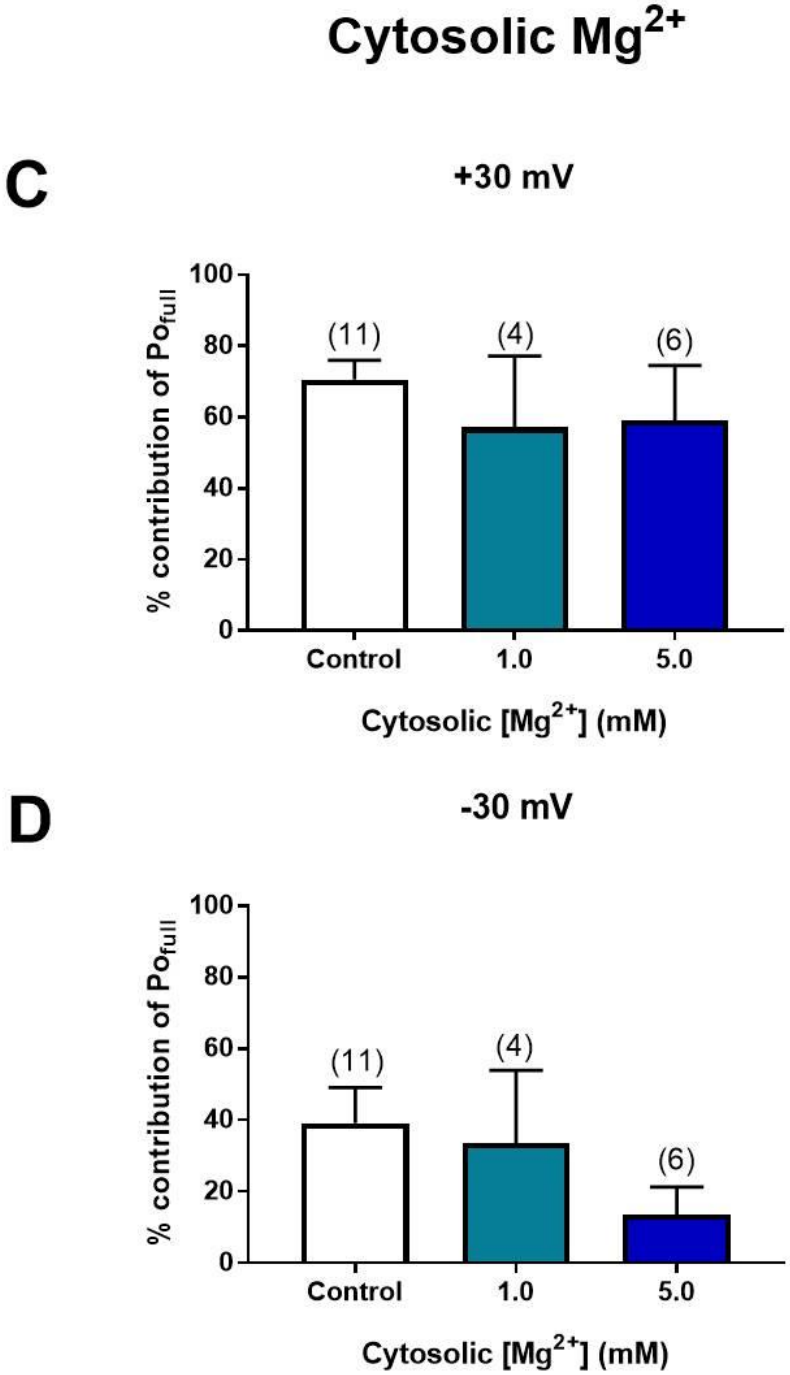


Figure 3.17. The effect of increasing cytosolic [Mg^{2+}] on the Po of mouse skeletal SR K^+ channels

(A, B) The total Po of the SR K^+ channel from mouse skeletal muscle with increasing cytosolic [Mg^{2+}] at +30 mV **(A)** and at -30 mV **(B)**. **(C, D)** The percentage of channel open time which was spent in the fully open state with increasing cytosolic [Mg^{2+}] at +30 mV **(C)** and at -30 mV **(D)**. Values are of the mean±SEM. The number of experiments is shown in brackets above the respective bars.

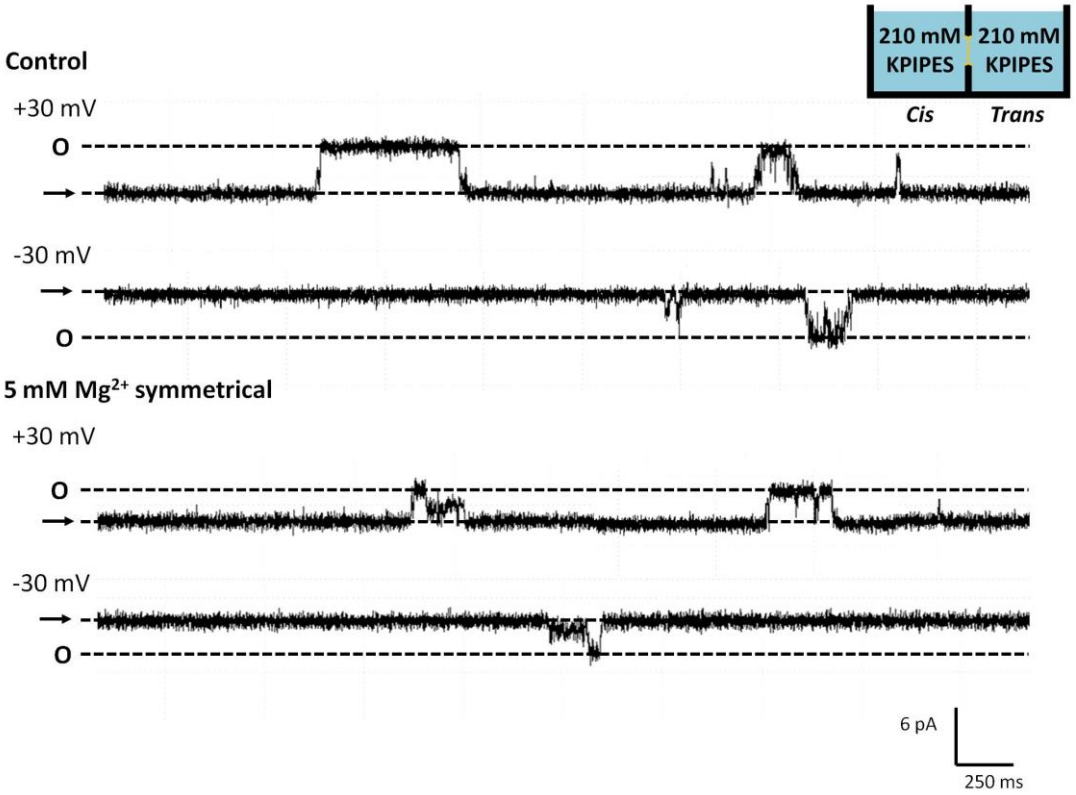
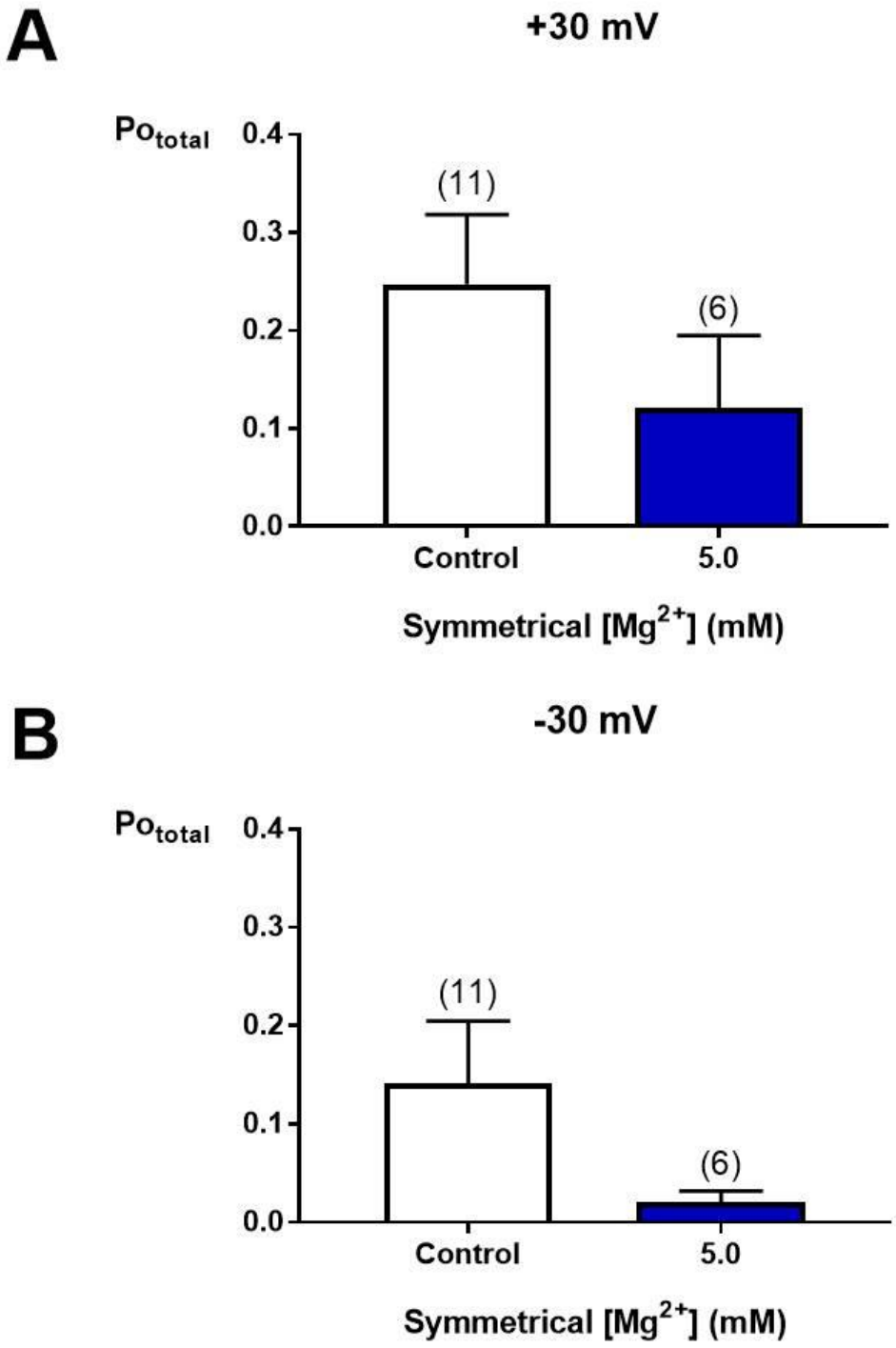


Figure 3.18. The mouse skeletal SR K^+ channel in the presence of increasing symmetrical [Mg^{2+}]

Representative current-fluctuations through the SR K^+ channel from mouse skeletal muscle at the holding potentials of +30 mV and -30 mV in symmetrical 210 mM KPIPES. Increasing concentrations of Mg^{2+} were added symmetrically, to both the luminal and cytosolic sides if the channel, to the concentrations indicated. The zero current level is shown by an arrow and the fully open channel level by an O.

Symmetrical Mg^{2+}



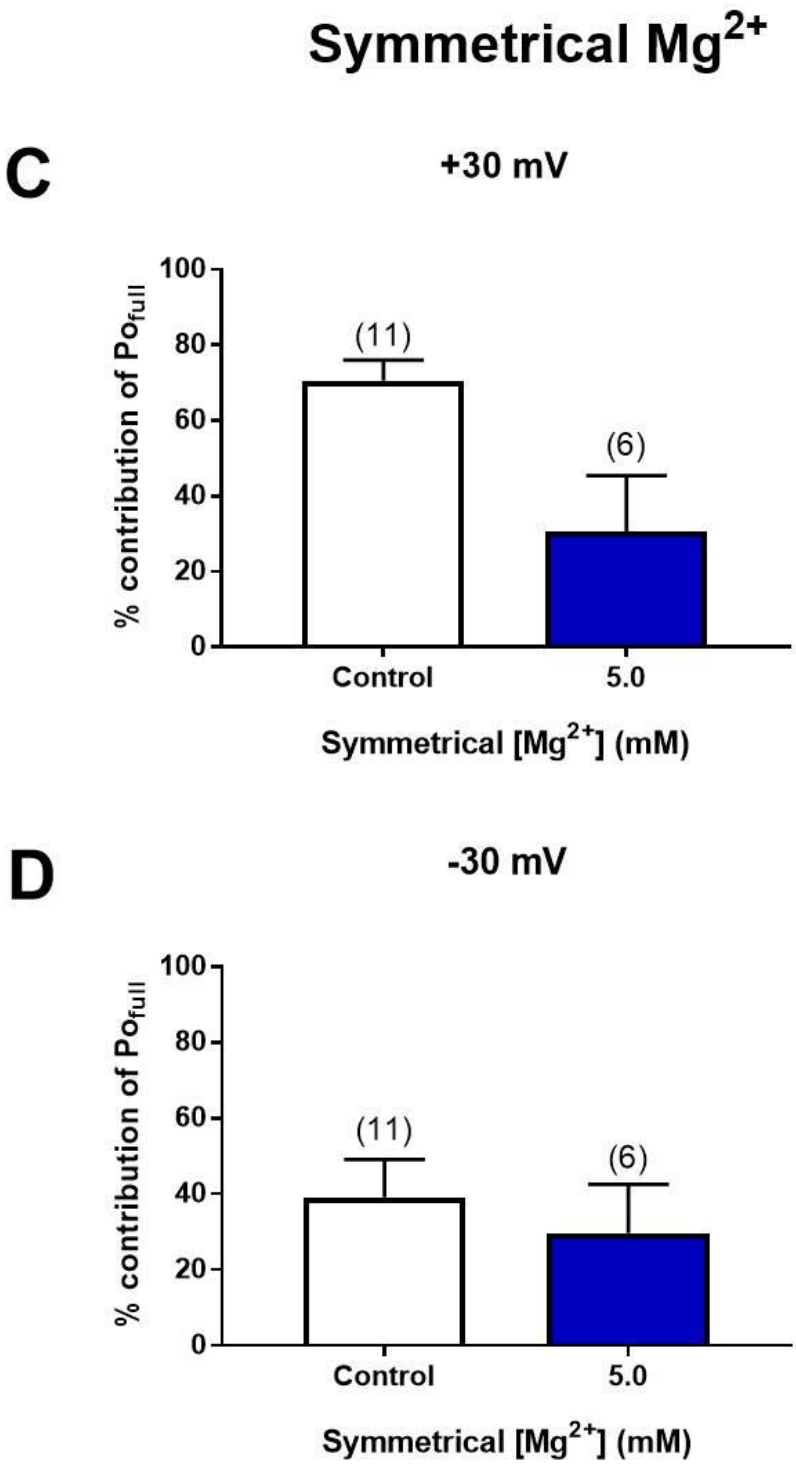


Figure 3.19. The effect of increasing symmetrical [Mg^{2+}] on the Po of mouse skeletal SR K^+ channels

(A, B) The total Po of the SR K^+ channel from mouse skeletal muscle with increasing symmetrical [Mg^{2+}] at +30 mV **(A)** and at -30 mV **(B)**. **(C, D)** The percentage of channel open time which was spent in the fully open state with increasing symmetrical [Mg^{2+}] at +30 mV **(C)** and at -30 mV **(D)**. Values are of the mean±SEM. The number of experiments is shown in brackets above the respective bars.

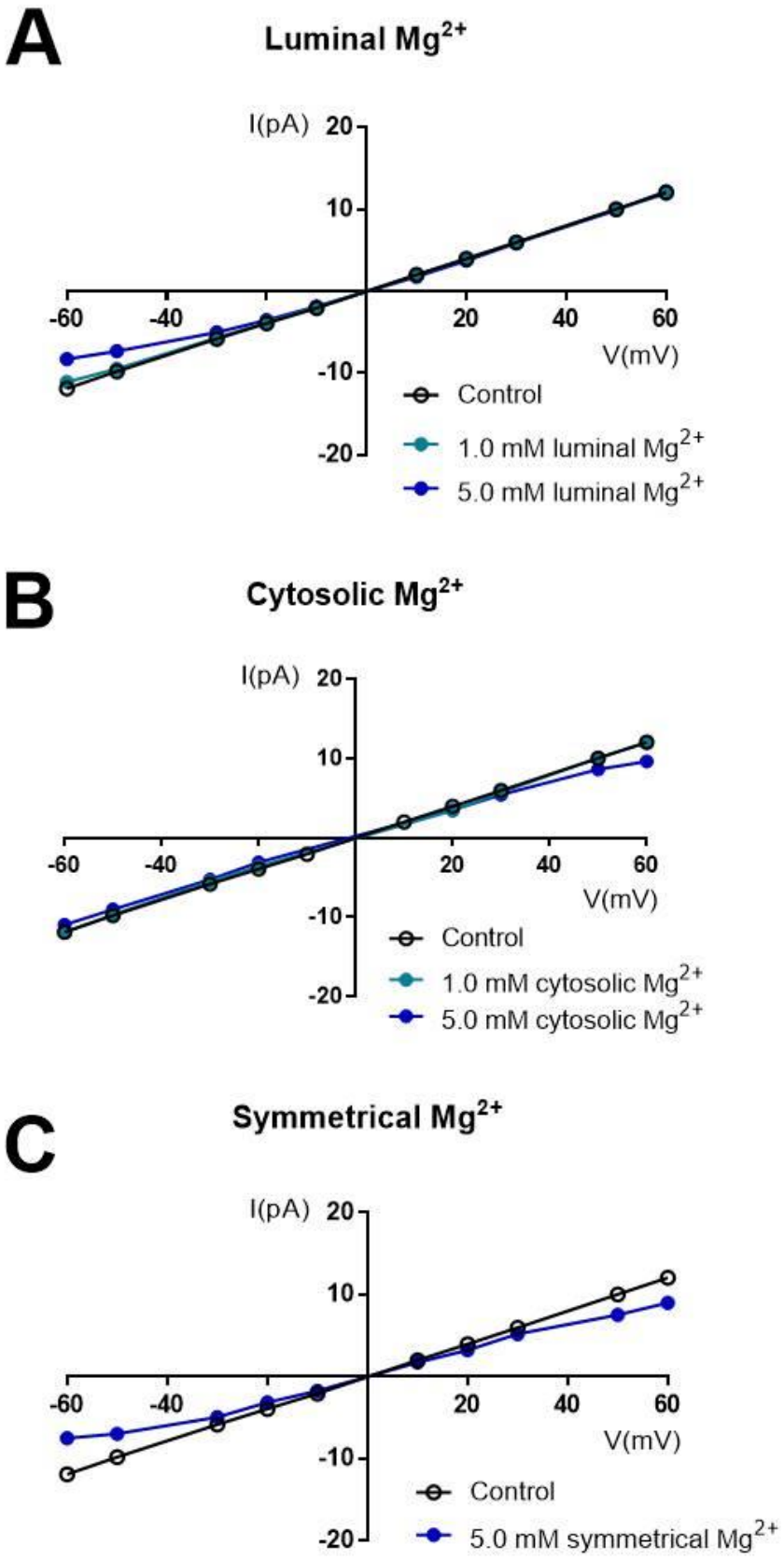

A
Luminal Mg2+
I(pA)
20
10
-10
-20
-60
-40
20
40
60
V(mV)
Control
1.0 mM luminal Mg2+
5.0 mM luminal Mg2+
B
Cytosolic Mg2+
I(pA)
20
10
-10
-20
-60
-40
20
40
60
V(mV)
Control
1.0 mM cytosolic Mg2+
5.0 mM cytosolic Mg2+
C
Symmetrical Mg2+
I(pA)
20
10
-10
-20
-60
-40
20
40
60
V(mV)
Control
5.0 mM symmetrical Mg2+

Figure 3.20. The effect of Mg^{2+} on the current-voltage relationships of mouse skeletal muscle SR K^+ channels

Current-voltage relationships of the SR K^+ channel from mouse skeletal muscle in symmetrical 210 mM KPIPES. [Mg^{2+}] was increased to 1 mM (light blue) and then to 5 mM (dark blue) on the luminal side of the channel (control, n=11; 1 mM Mg^{2+}, n=5; 5 mM Mg^{2+}, n=4) **(A)**, the cytosolic side of the channel (control, n=11; 1 mM Mg^{2+}, n=5; 5 mM Mg^{2+}, n=6) **(B),** and symmetrically (control, n=11; 5 mM Mg^{2+}, n=8) **(C).** Values are of the mean±SEM. Where not shown, error bars are within the symbols.

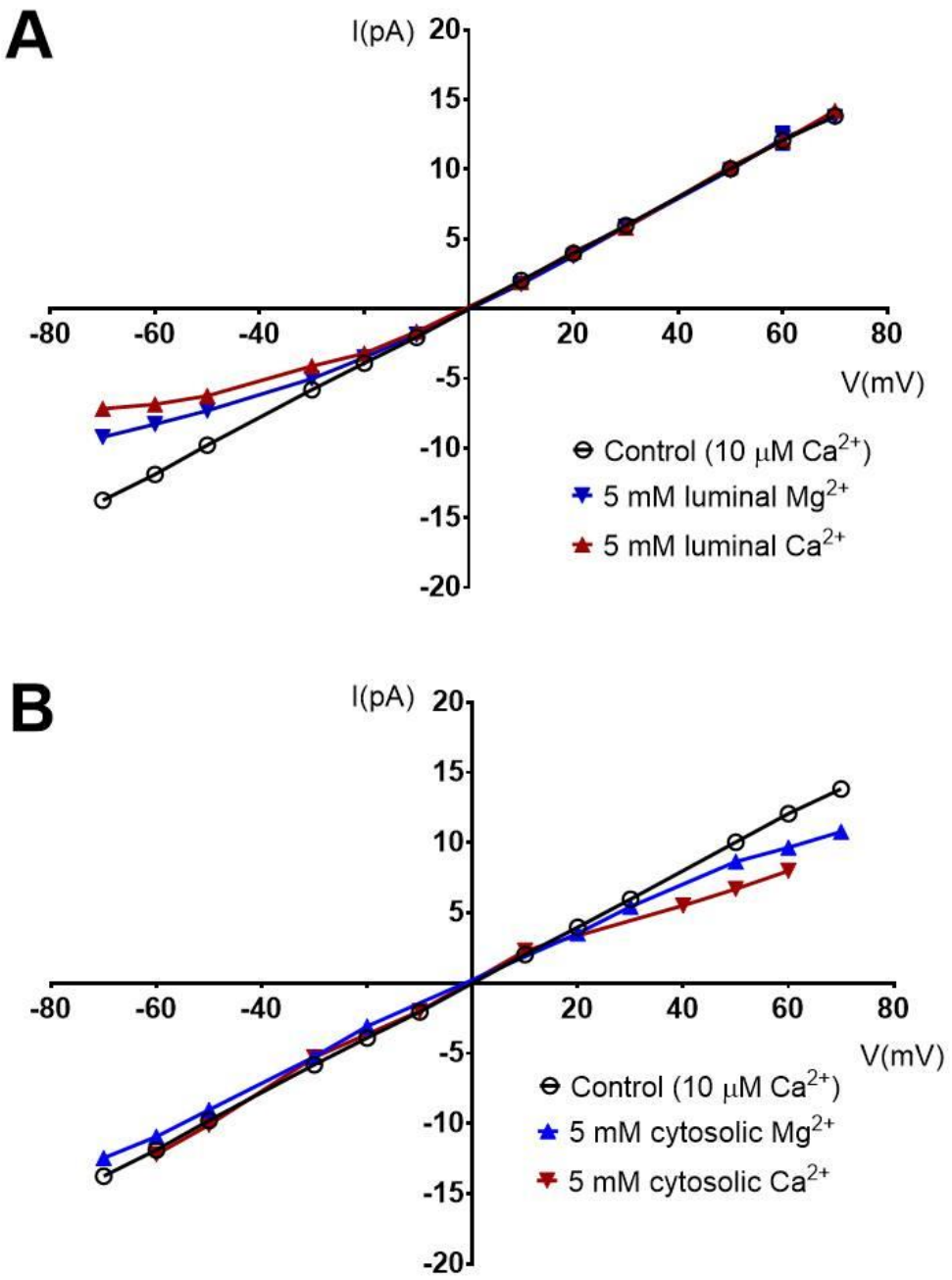


Figure 3.21. A comparison of the current-voltage relationships for mouse skeletal SR K^+ channels in the presence of 5 mM Ca^{2+} and 5 mM Mg^{2+}

Current-voltage relationships of the SR K^+ channel from mouse skeletal muscle under control conditions and in the presence of 5 mM Ca^{2+} (red) and 5 mM Mg^{2+} (blue). Divalent cations were added to the luminal **(A)** and the cytosolic **(B)** sides of the channel. Values are of the mean±SEM. Where not shown, error bars are within the symbols.

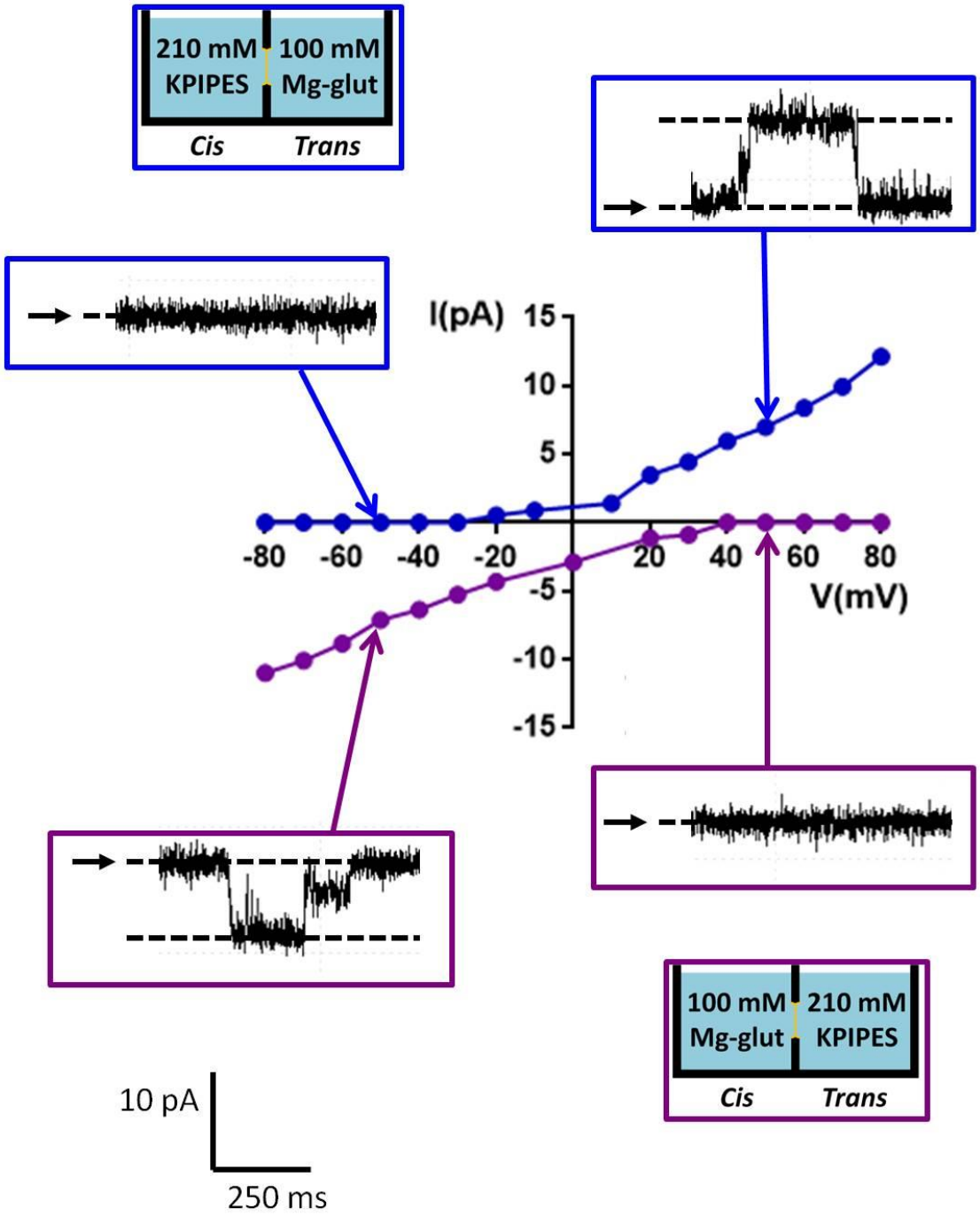


Figure 3.22. The pore of the mouse skeletal muscle SK K^+ channel is impermeable to Mg^{2+}
Current voltage relationships of the SR K^+ channel from mouse skeletal muscle in bionic conditions. 100 mM Mg-glutamate (Mg-glut) solution was perfused onto either the luminal (blue, n=3) or the cytosolic (purple, n=3) chambers. The chamber opposite to the Mg-glutamate contained 210 mM KPIPES solution. Values are of the mean±SD. Where not shown, error bars are within the symbols.

3.2.5 Ni^{2+} as a ligand of the SR K^+ channel

The effect of Ni^{2+} was also tested on the SR K^+ channel. It has previously been suggested that certain transition metals could activate the SR K^+ channel from the luminal side [64]. 0.5 mM $NiSO_4$ (the K_d previously stated for Ni^{2+}) was therefore added to the luminal side of SR K^+ channels from mouse skeletal muscle.

Figure 3.23 shows current-fluctuations through an SR K^+ channel from mouse skeletal muscle under control conditions and when 0.5 mM Ni^{2+} was present on the luminal side of the channel. A visual comparison of the channel gating under control conditions and in the presence of 0.5 mM luminal Ni^{2+} suggests that, when Ni^{2+} is present on the luminal side of the channel, the channel gates predominantly into the sub-conductance state. This is shown in Figure 3.24. The total Po of the channel is unchanged; however the % of channel open time spent in the fully open state is significantly reduced in the presence of 0.5 mM luminal Ni^{2+} at both +30 mV and -30 mV holding potentials. Additionally, contrary to previous findings, 0.5 mM Ni^{2+} on the luminal side of the SR K^+ channel did not result in channel activation.

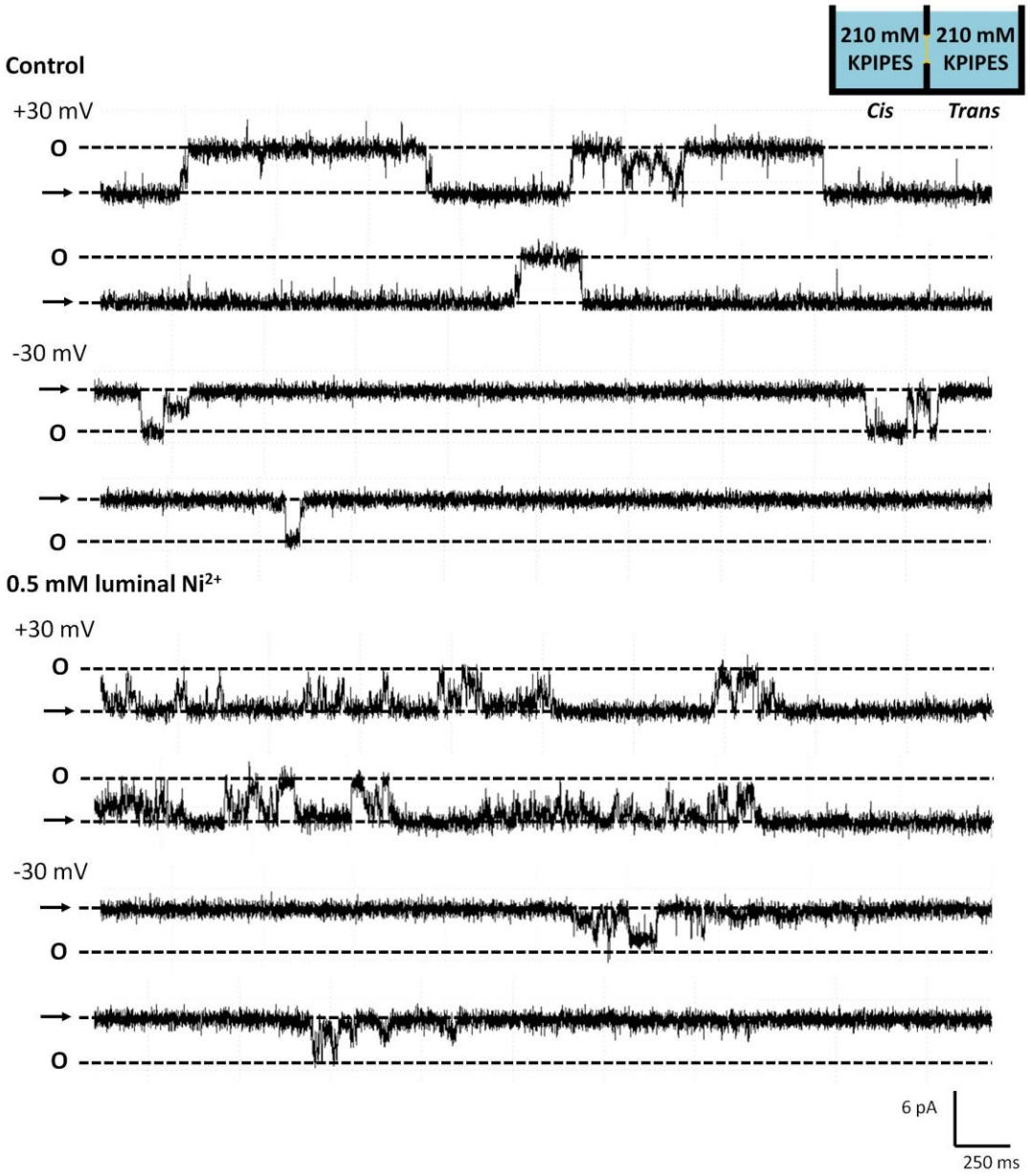
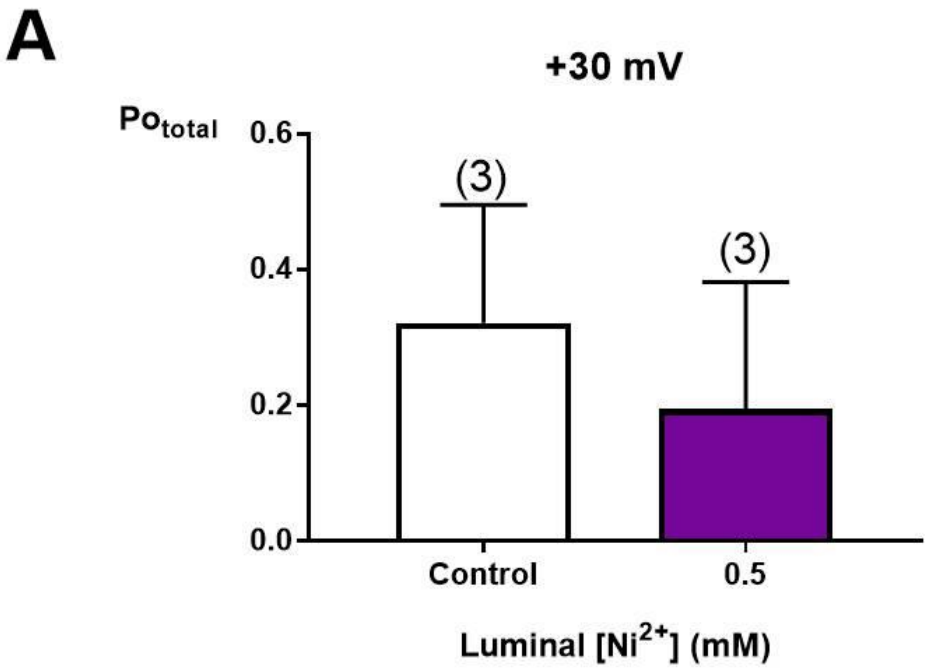
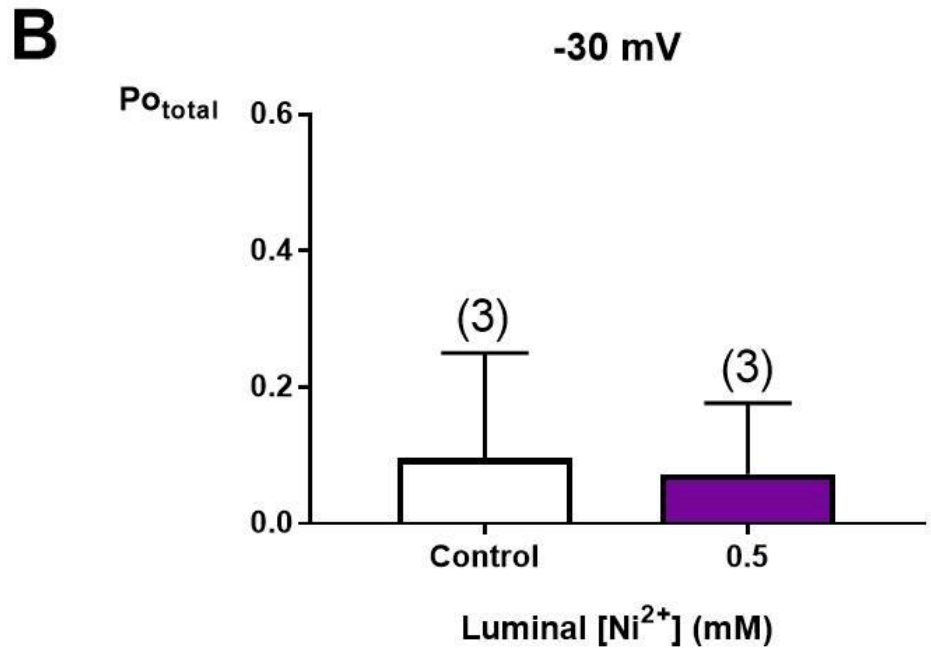


Figure 3.23. The mouse skeletal SR K^+ channel in the presence of 0.5 mM luminal [Ni^{2+}]
Representative current-fluctuations through the SR K^+ channel from mouse skeletal muscle at the holding potentials of +30 mV and -30 mV in symmetrical 210 mM KPIPES. 0.5 mM Ni^{2+} was added to the luminal side of the channel. The zero current level is shown by an arrow and the fully open channel level by an O.


A
+30 mV
Po total
0.6
0.4
0.2
0.0
(3)
(3)
Control
0.5
Luminal [Ni2+] (mM)


B
-30 mV
Po total
0.6
0.4
0.2
0.0
(3)
(3)
Control
0.5
Luminal [Ni2+] (mM)

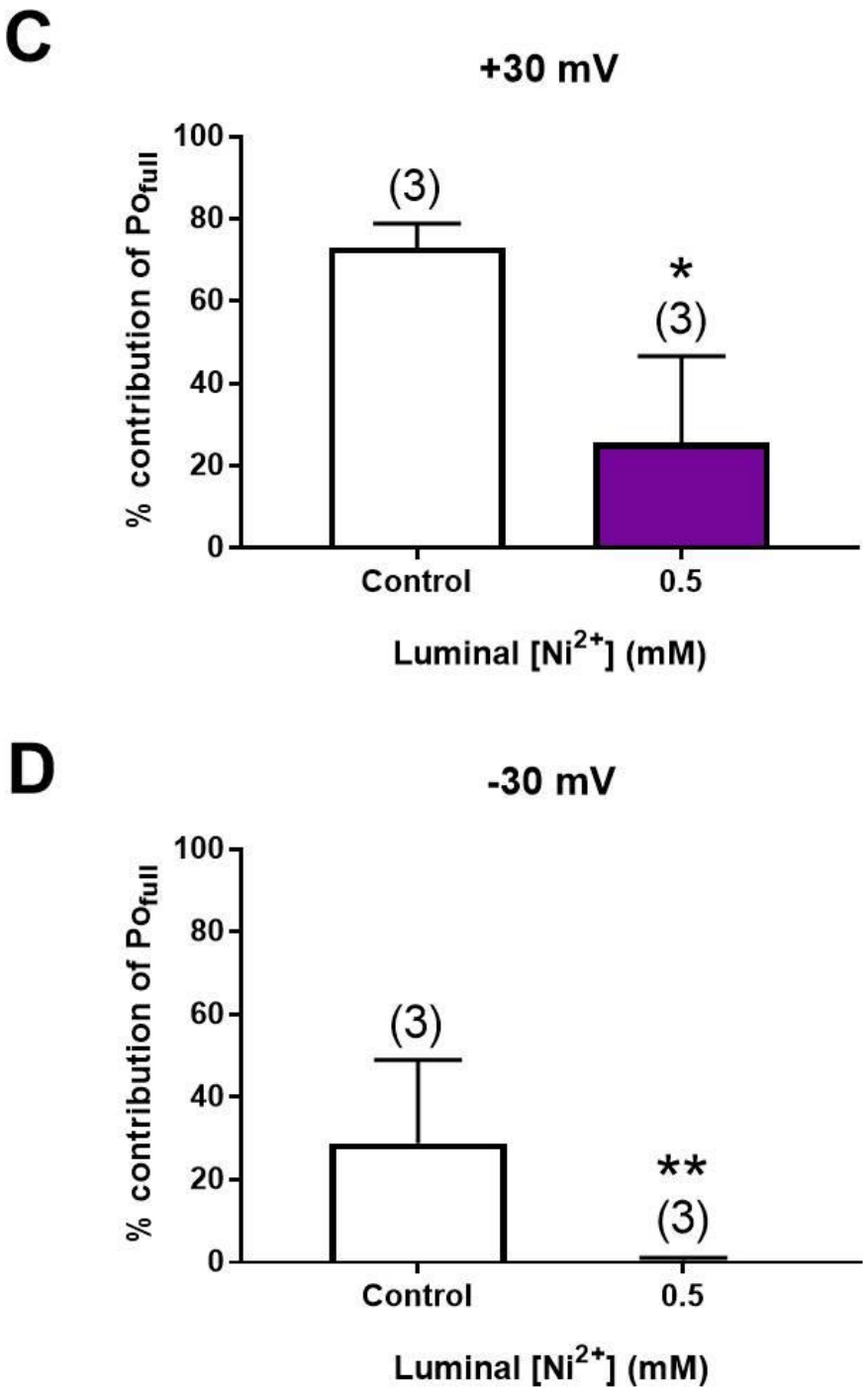


Figure 3.24. The effect of 0.5 mM luminal [Ni^{2+}] on the Po of mouse skeletal SR K^+ channels
(A, B) The total Po of the SR K^+ channel from mouse skeletal muscle under control conditions (white) with 0.5 mM luminal [Ni^{2+}] (purple) at +30 mV **(A)** and at -30 mV **(B)**. **(C, D)** The percentage of channel open time which was spent in the fully open state with 0.5 mM luminal [Ni^{2+}] at +30 mV **(C)** and at -30 mV **(D)**. Values are of the mean±SEM. The number of experiments is shown in brackets and the degree of significance relative to control is shown by stars above the respective bars.

3.2.6 ATP as a ligand of the SR K^+ channel

In attempting to find a ligand for the SR K^+ channel, the effect of cytosolic ATP on the SR K^+ channel was studied. 1 mM Na-ATP was added to the cytosolic side of sheep cardiac SR K^+ channels.

Figure 3.25 shows current-fluctuations through a sheep cardiac SR K^+ channel under control conditions and with 1 mM Na-ATP on the cytosolic side of the channel. There was found to be no apparent visual change in gating of sheep cardiac SR K^+ channels when 1 mM Na-ATP was present on the cytosolic side of the channel. The total Po and % of channel open time spent in the full open channel level were also observed not to change with cytosolic Na-ATP (Figure 3.26).

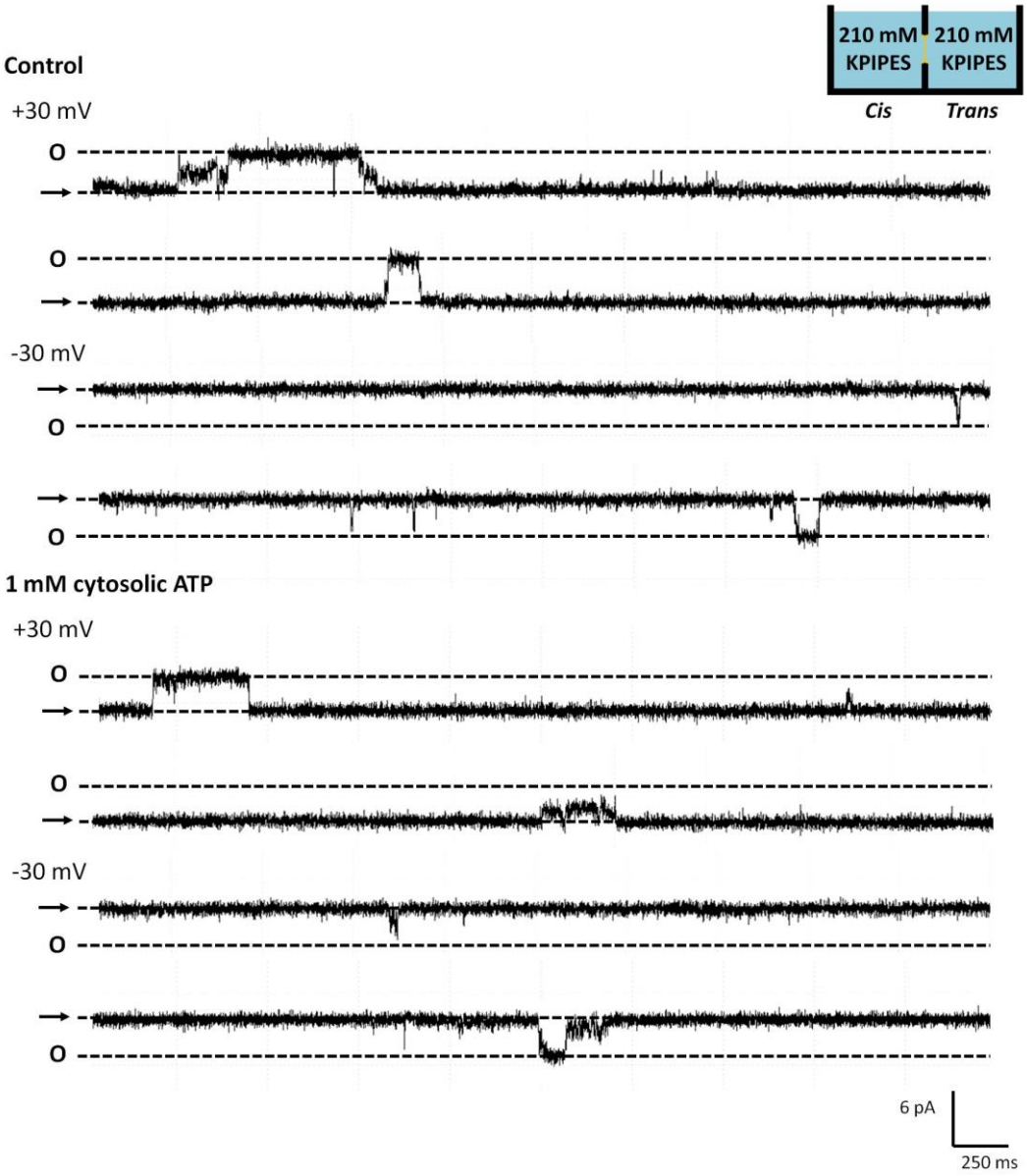
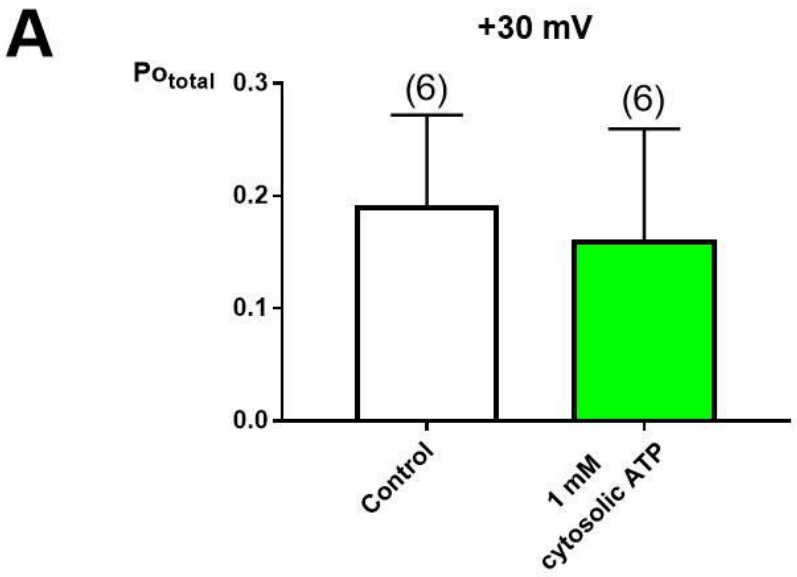
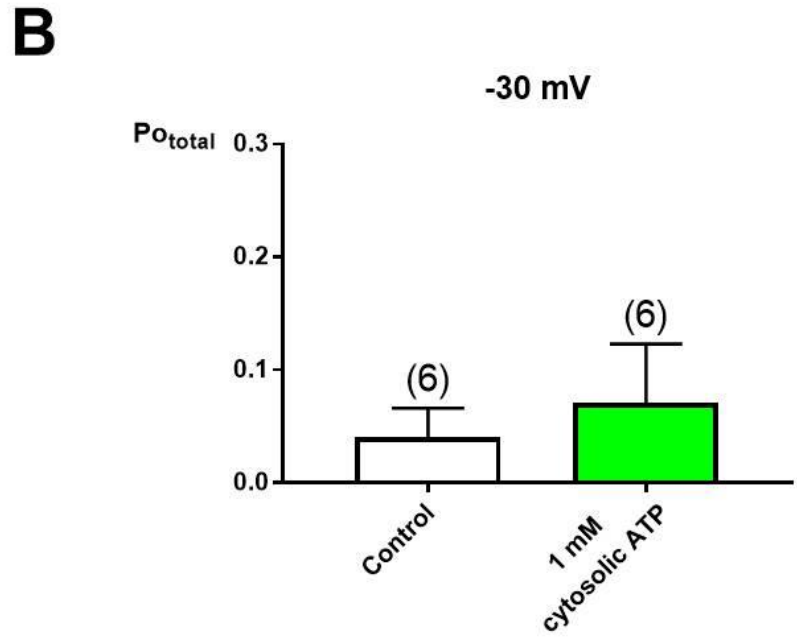


Figure 3.25. The sheep cardiac SR K^+ channel in the presence of 1 mM cytosolic Na-ATP
Representative current-fluctuations through the SR K^+ channel from sheep cardiac muscle at the holding potentials of +30 mV and -30 mV in symmetrical 210 mM KPIPES. 1 mM Na-ATP was added to the cytosolic side of the channel. The zero current level is shown by an arrow and the fully open channel level by an O.


A
+30 mV
Po total
0.3
0.2
0.1
0.0
(6)
(6)
Control
1 mM
cytosolic ATP


B
-30 mV
Po total
0.3
0.2
0.1
0.0
(6)
(6)
Control
1 mM
cytosolic ATP

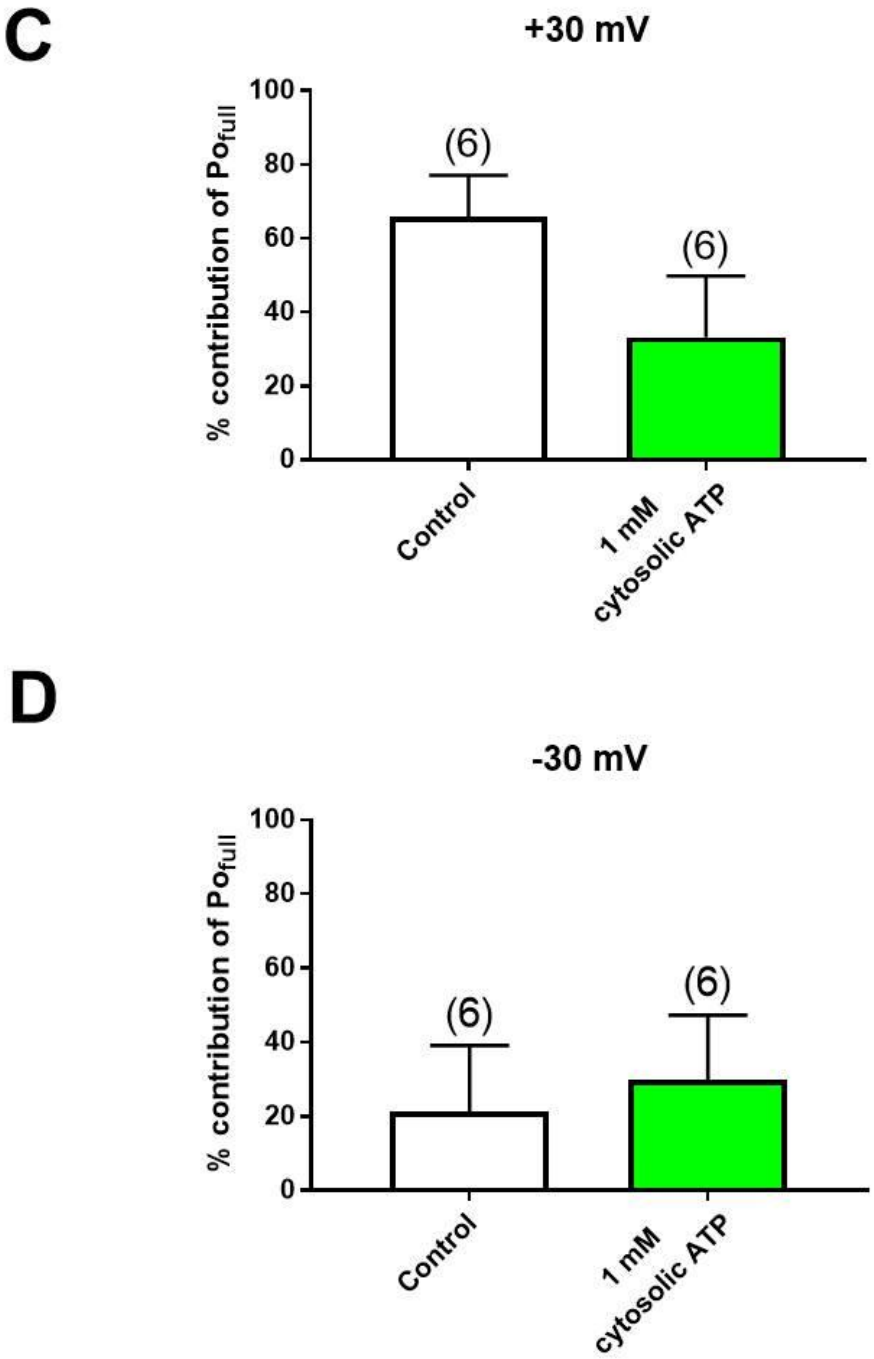


Figure 3.26. The effect of 1 mM cytosolic Na-ATP on the single-channel properties of sheep cardiac SR K^+ channels

(A, B) The total Po of the SR K^+ channel from sheep cardiac muscle under control conditions (white) and with 1 mM cytosolic Na-ATP (green) at +30 mV **(A)** and at -30 mV **(B)**. **(C, D)** The percentage of channel open time which was spent in the fully open state with 1 mM cytosolic Na-ATP at +30 mV **(C)** and at -30 mV **(D)**. Values are of the mean±SEM. The number of experiments is shown in brackets above the respective bars.

3.2.7 Effect of high pH on the SR K^+ channel

It has been suggested that during EC-coupling, the pH of the SR lumen may become more acidic relative to the rest of the cell cytosol [88]. Previous work within the Sitsapesan group has also found that an acidic cytosol or lumen can alter the gating of the SR K^+ channel [190] as has also been previously demonstrated by Miller in 1978 [72]. The effect of alkaline pH on the gating of the SR K^+ channel has not been studied however. Experiments were therefore carried out to study the effect of changing the pH of the solution on the cytosolic side of mouse skeletal SR K^+ channels from pH of 7.2 to a pH of 9.2. These data were collected using SR K^+ channels from mouse skeletal muscle taken from mice lacking the MG23 protein. MG23 KO mice were used as the bilayers were found to be more stable when bathed in solution at pH 9.2. Detailed comparison of the SR K^+ channel from MG23 KO mice is discussed in Chapter 7 of this thesis.

Figure 3.27 shows the gating if the SR K^+ channel under control conditions (symmetrical 210 mM KPIPES at pH 7.2) and when the cytosolic side of the channel was perfused with 210 mM KPIPES buffered to pH 9.2. At +30 mV, the change in pH caused a significant reduction in Po which was not repeated at -30 mV (Figure 3.28A and B). When the cytosolic side of the channel was perfused with solution at pH 9.2, a significant increase in the % of channel open time which is spent in the sub-conductance state was observed (Figure 3.28C and D). Observational data of the current-fluctuations shown in Figure 3.27 confirms the reduced gating to the fully open state and suggests that the mouse skeletal SR K^+ channel may gate with more events with a high pH on the cytosolic side of the channel. Figure 3.29 shows that perfusing the cytosolic side of the channel with solution at pH 9.2 removes the voltage-dependant Po effect seen in control.

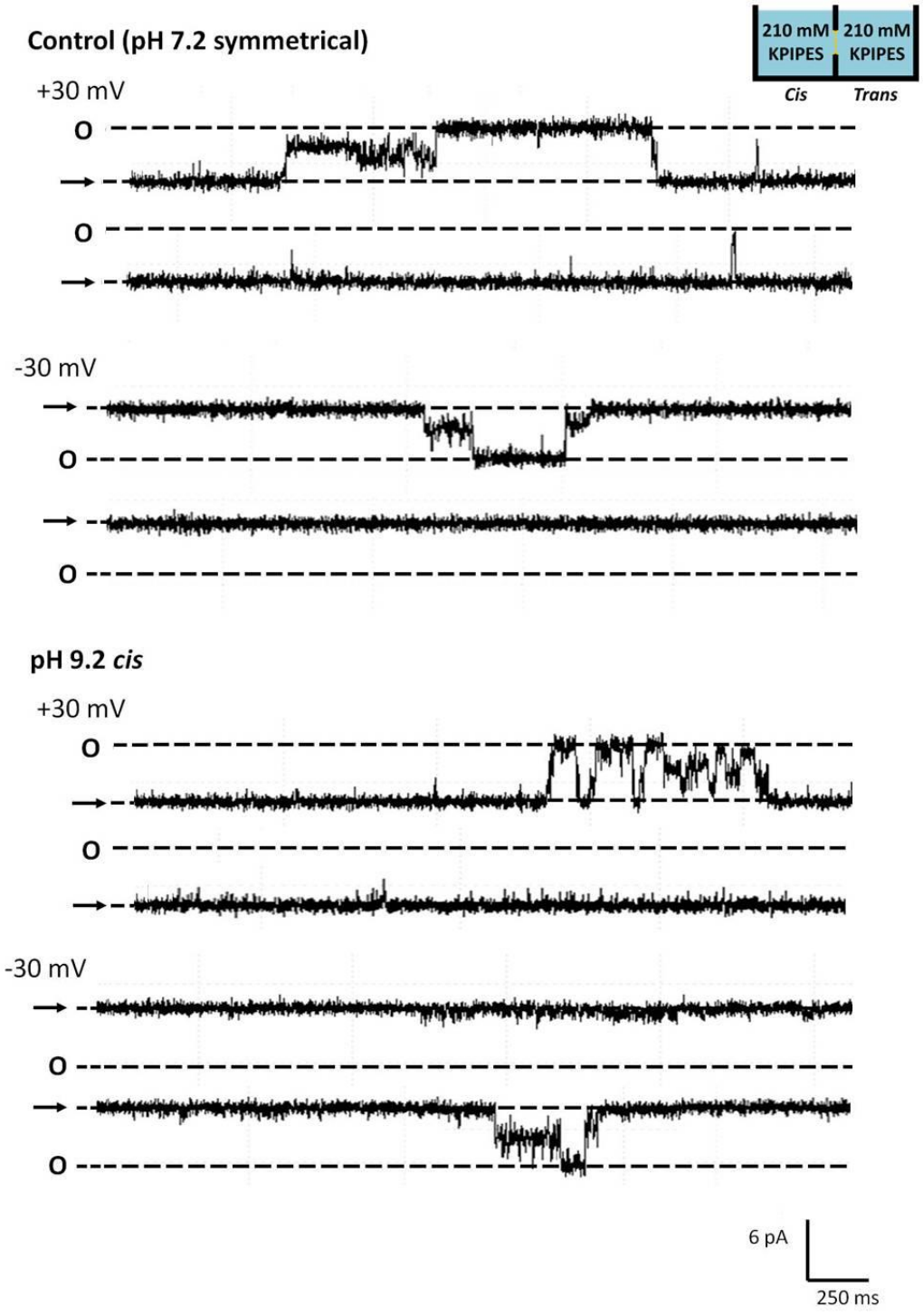
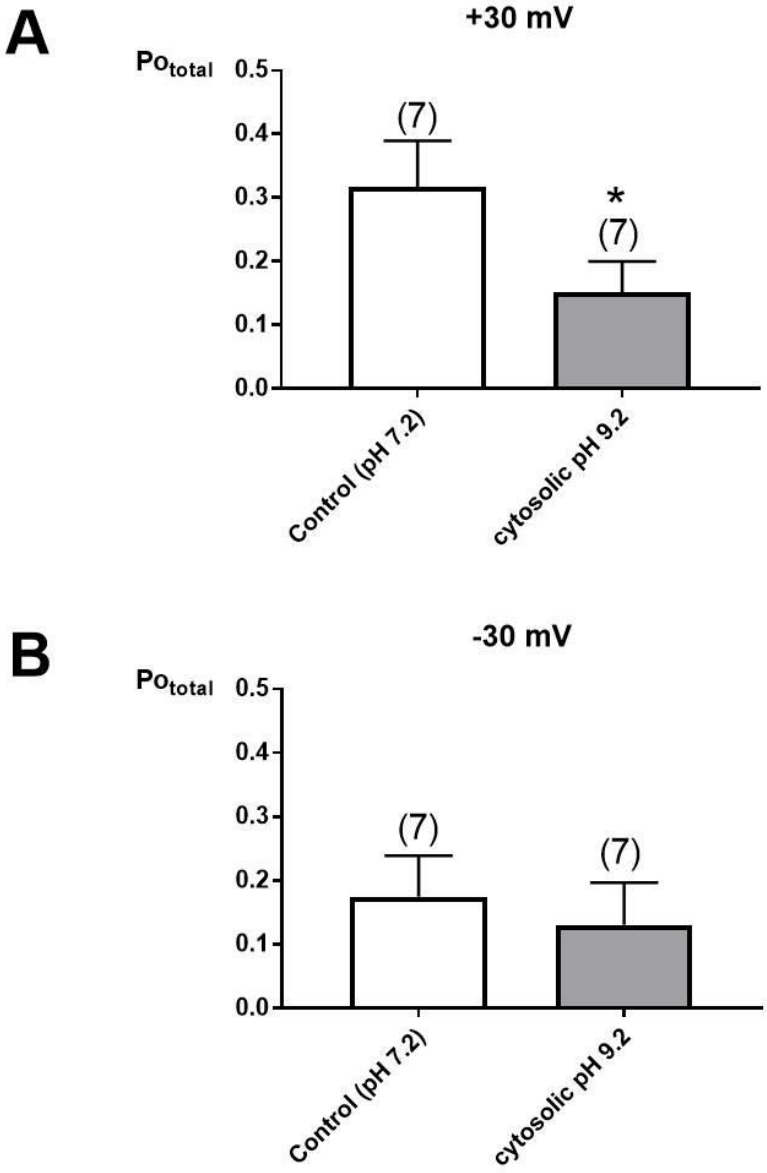


Figure 3.27. The mouse skeletal SR K^+ channel in the presence cytosolic pH 9.2
Representative current-fluctuations through the SR K^+ channel from mouse skeletal muscle at the holding potentials of +30 mV and -30 mV in symmetrical 210 mM KPIPES at pH 7.2 (top traces) and then the cytosolic side of the channel is perfused with 210 mM KPIPES at pH 9.2 (bottom traces). The zero current level is shown by an arrow and the fully open channel level by an O.


A
+30 mV
Po total
0.5
0.4
0.3
0.2
0.1
0.0
(7)
*
(7)
Control (pH 7.2)
cytosolic pH 9.2
B
-30 mV
Po total
0.5
0.4
0.3
0.2
0.1
0.0
(7)
(7)
Control (pH 7.2)
cytosolic pH 9.2

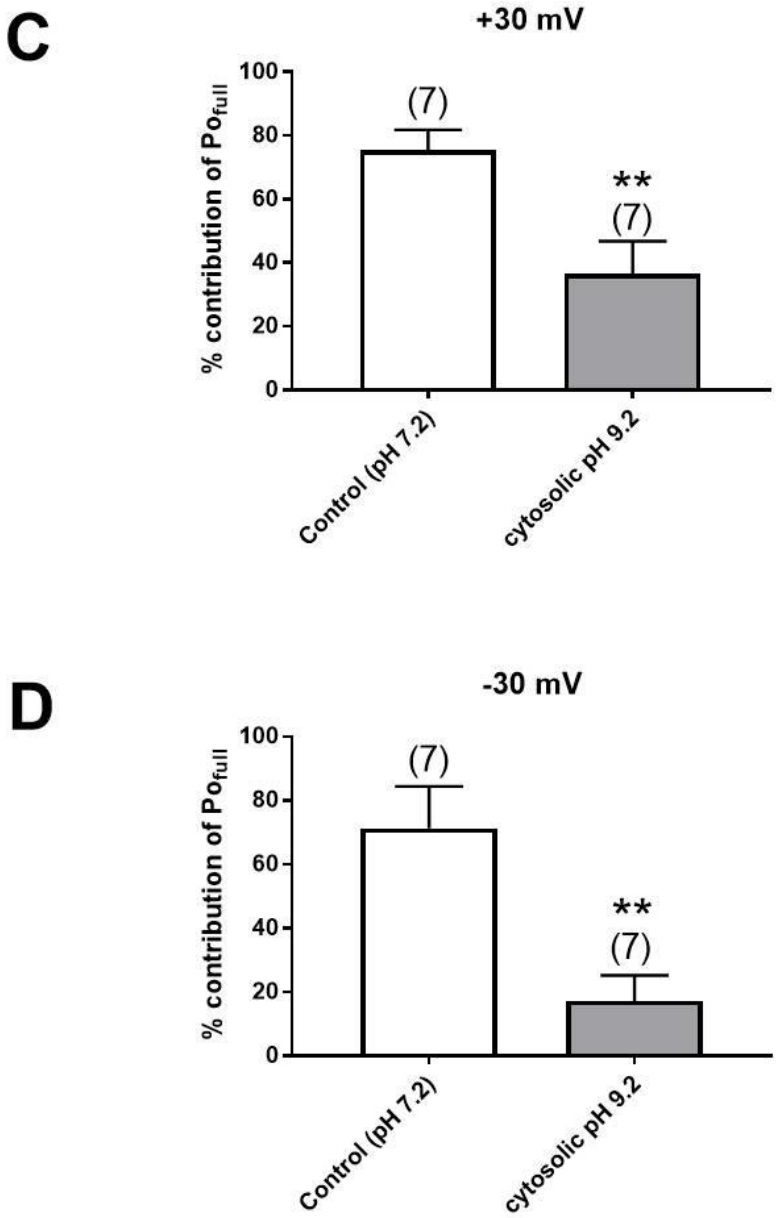


Figure 3.28. The effect of cytosolic pH 9.2 on the single-channel properties of mouse skeletal SR K^+ channels

(A, B) The total Po of the SR K^+ channel from mouse skeletal muscle symmetrical 210 mM KPIPES at pH 7.2 (white) and then the cytosolic side of the channel is perfused with 210 mM KPIPES at pH 9.2 (grey) at +30 mV **(A)** and at -30 mV **(B)**. **(C, D)** The percentage of channel open time which was spent in the fully open state in symmetrical 210 mM KPIPES at pH 7.2 (white) and then the cytosolic side of the channel is perfused with 210 mM KPIPES at pH 9.2 (grey) at +30 mV **(C)** and at -30 mV **(D)**. Values are of the mean±SEM. The number of experiments is shown in brackets and the degree of significance relative to control is shown by stars above the respective bars.

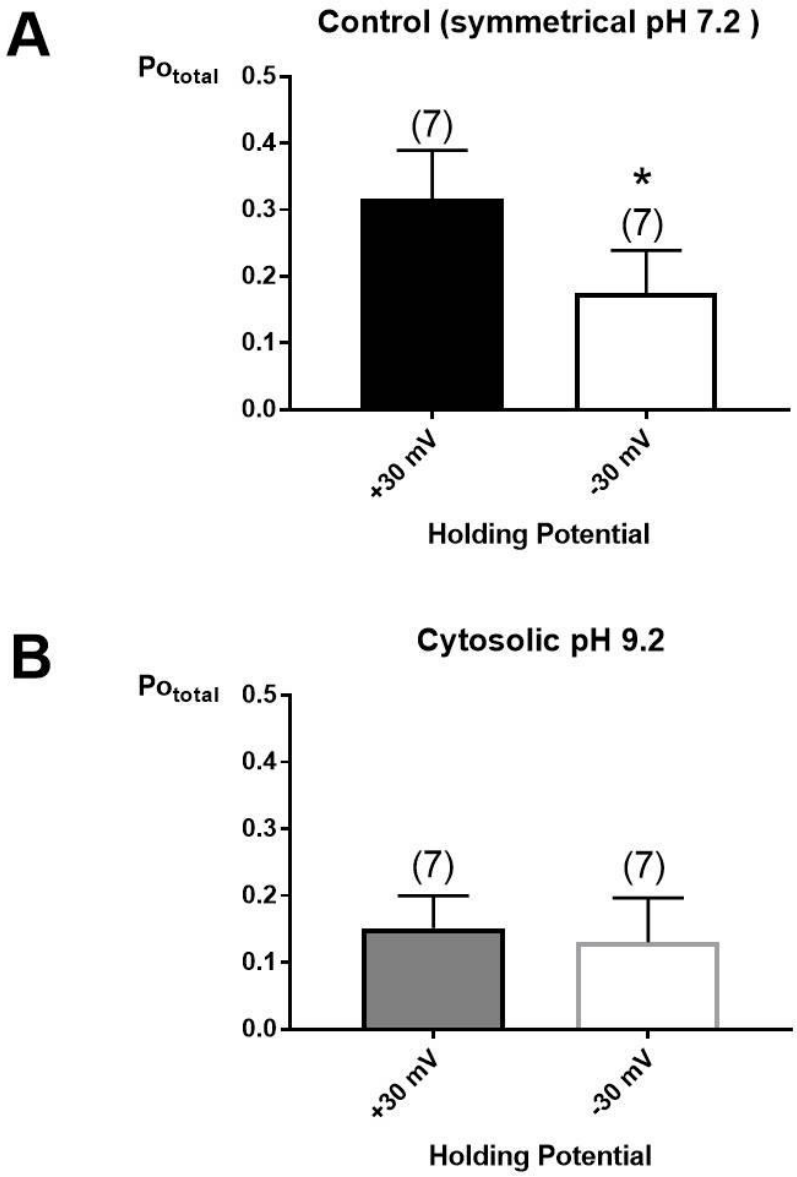


Figure 3.29. The effect of cytosolic pH 9.2 on voltage sensitivity of mouse skeletal SR K^+ channels

The total Po of the SR K^+ channel from mouse skeletal muscle symmetrical at +30 mV and -30 mV holding potentials in KPIPES at pH 7.2 **(A)** and then the cytosolic side of the channel is perfused with 210 mM KPIPES at pH 9.2 **(B)**. Values are of the mean±SEM. The number of experiments is shown in brackets and the degree of significance relative to control is shown by stars above the respective bars.

3.3 Discussion

The aims of this chapter were twofold; firstly, to establish any differences in the gating of SR K^+ channels from mouse skeletal, mouse cardiac, rabbit skeletal and sheep cardiac muscle and, secondly, to attempt to find a specific ligand for the SR K^+ channel.

3.3.1 Gating differences between mammalian SR K^+ channel isoforms

The work presented in this chapter found the gating pattern of the SR K^+ channels to be broadly similar between the various mammalian channel isoforms studied (exceptions are discussed below). All channel isoforms gated with long open bursts which contained a fully open channel level and sub-conductance levels. All channels also displayed voltage sensitivity which may highlight the importance of this characteristic to SR K^+ channel function. The voltage sensitivity of the SR K^+ channel in our bilayer set-up may indicate that the channel passes K^+ ions more easily from the cytosol to the lumen, rather than in the opposite direction.

The Po of mouse cardiac SR K^+ channels was found to be significantly lower than those from rabbit skeletal SR K^+ channels. It is unclear why this is the case. The effect may be due to a difference between species, or due to inaccuracies caused by the low number of mouse cardiac experiments. Additionally, sheep cardiac SR K^+ channels exhibited a smaller single-channel conductance compared to the other isoforms studied (Figure 3.3). It is likely that this is due to a species difference as mouse cardiac and skeletal SR K^+ channel isoforms displayed no difference in conductance values. The physiological relevance of this finding is unclear however.

Although the SR K^+ channel is yet to be identified, I speculate that SR K^+ channels from mouse, sheep and rabbit share a high degree of sequence homology, especially in the pore region. It

would be interesting to further this study and examine differences between other species, especially non-mammalian and human SR K^+ channels isoforms.

3.3.2 Pharmacological properties of the SR K^+ channel

The data presented in this chapter suggests Ca^{2+} to be a ligand for the SR K^+ channel from the luminal side at concentrations >100 µM, but not the cytosolic side of the channel. This finding supports what has been suggested in previous studies [72][98]. The Po of the channel was reduced at positive potentials (Figure 3.7A) and more detailed analysis of the channel events revealed that this is due to a reduction in the lifetimes of events (Figure 3.8, although the lifetimes of the sub-conductance state reported in this thesis are higher than those reported elsewhere [104]) and a decrease in the channel open time which was spent in the fully open channel level (Figure 3.7C). No change in event frequency was observed, which suggests that the change in Po was not due to 'flickery' block of the channel as with decamethonium [100], but was instead due to a modulation of the gating which may suggest ligand binding. It is possible that Ca^{2+} binding to the luminal side of the channel causes the channel to be less stable in the fully open state, thus reducing the lifetime of events, especially to the fully open state. Interestingly, Mg^{2+} does not have a similar effect on Po as Ca^{2+}. This could indicate that, if a Ca^{2+} binding site exists on the luminal side of the channel which triggers the effects described above, it does not bind Mg^{2+}. It is possible that the site binds Ni^{2+} however as Ni^{2+} causes SR K^+ channel currents to exhibit similar effects as Ca^{2+}.

The reduction in channel Po occurred when luminal [Ca^{2+}] was increased from 100 µM to 1 mM (the approximate change during loading of the SR in diastole [191]). I speculate that when the SR luminal [Ca^{2+}] is high, the SR K^+ channel is less active, gating with shorter events and predominantly to the sub-conductance level. During systole, as SR luminal [Ca^{2+}] drops, the SR

K^+ channel becomes more active with longer events to the higher conductance fully open state, allowing the channel to provide counter ion currents. This is summarised in Figure 3.30.

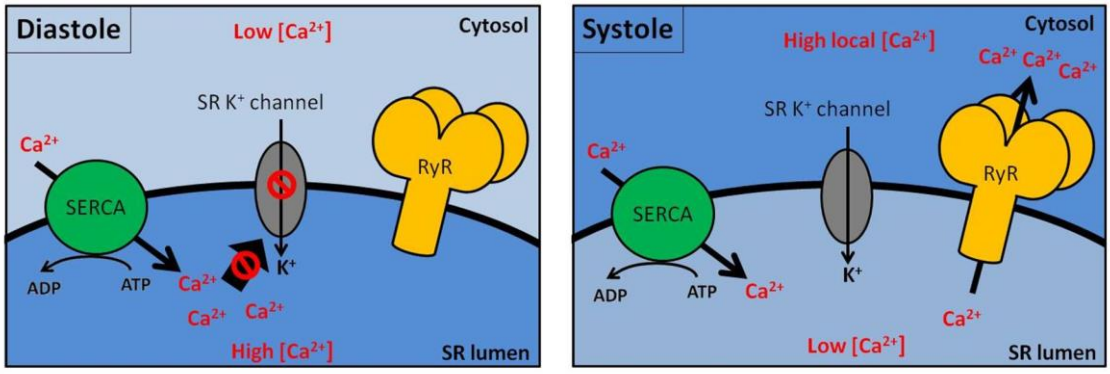


Figure 3.30. A schematic of the proposed Ca^{2+} inhibition of the SR K^+ channel during diastole (left) and systole (right)

A reduction in single-channel current of mouse skeletal SR K^+ channels was observed at positive and negative holding potentials when Mg^{2+} and Ca^{2+} were present on the cytosolic and luminal sides of the channel, respectively. The voltage sensitivity of the effect is indicative of pore block of the SR K^+ channel by Ca^{2+} and Mg^{2+} [192]; this has been previously described with Ca^{2+} block [193] and hexamethonium block [100] of the SR K^+ channel.

This blocking effect can be explained as follows; if we consider the example of millimolar [Mg^{2+}] on the cytosolic side of the channel, at more positive potentials Mg^{2+} ions are driven into the pore, repulsed by the positive holding potential, but cannot permeate the channel (as shown in Figure 3.22). Mg^{2+} therefore blocks the pore, preventing K^+ current flow. Mg^{2+} then quickly dissociates away from the pore allowing K^+ flow to be restored. This happens at such a fast rate that individual blocking events cannot be resolved by the recording equipment. Instead, a reduced single-channel current is observed. This phenomenon has been referred to as 'smooth block' of SR K^+ channel currents [100]. Ca^{2+} appears to block the pore of the SR K^+

channel more effectively and may dissociate away from the pore at a slower rate than Mg^{2+} as it results in a larger decrease in current compared with Mg^{2+} (Figure 3.21).

The data presented and discussed thus far in this chapter suggest a dual effect of Ca^{2+} on the SR K^+ channel. It appears that Ca^{2+} can behave as a ligand on the luminal side of the channel, reducing channel Po, but also that Ca^{2+} blocks the pore of the SR K^+ channel. These effects are distinct as evidenced by Mg^{2+} blocking, but not modulating the channel.

ATP was found not to affect the gating of the SR K^+ channel and it is possible that the molecule is not a ligand for the SR K^+ channel. The channel was found to be sensitive to high cytosolic pH which supports the theory of pH sensitivity of the SR K^+ channel [72][190]. It is possible that acidification of the lumen relative to the cytosol, which is thought to occur during EC-coupling [88], could act to regulate the SR K^+ channel during diastole.

Chapter 4. SR Cl^- channels

4.1 Introduction

As discussed in the introduction to this thesis, a number of different Cl^- channels are thought to be present in the SR with distinct physiological and pharmacological properties [79], [115]–[121]. Broadly, these fell into two groups which included a Cl^--selective channel with defined sub-conductance states [86], [116], [118], [119], [122], [123], and a larger non-selective channel [117], [124]–[126] .

More recently, a number of SR Cl^- channels have been identified. These include the CFTR Cl^- channel, which is a PKA-sensitive small conductance (6-10 pS) channel (the small conductance of the CFTR channel means that it is too small to view in bilayer experiments under the conditions used in this thesis) [133], VDAC, a large conductance, porin-like channel [134], [135], [139], and CLIC proteins, a novel class of membrane-bound proteins, some of which are thought to from Cl^- channels [142]–[145] [146]. CLIC2 is thought to associate with RyR2 proteins [147].

This chapter aimed to identify and characterise Cl^- currents which are observed after the fusion of native SR vesicles with an artificial bilayer to better understand the Cl^- channels in the SR.

4.2 Results

4.2.1 The different flavours of SR Cl- channels

Figure 4.1 shows a continuous current recording showing the types of Cl^- currents which were typically observed in the SR of all tissue types (sheep cardiac muscle, rabbit skeletal muscle, mouse cardiac muscle and mouse skeletal muscle) studied. These channels were often observed to incorporate together with RyR channels, which may suggest association or co-localisation. The recordings appeared to contain multiple types of channels permeable to Cl^-.

A series of experiments was therefore conducted, in view of the very different types of gating observed, to characterise the Cl^- channels in the SR and to ascertain whether TRIC could behave as one of the SR Cl^- channels. At least two distinct types of SR Cl^- channel were observed which I have termed the 'SR anion-selective' (SRAS) channel and the 'SR anion leak' (SRAL) channel. A third SR Cl^- channel type was also observed; however this channel rarely incorporated into the bilayer and was not observed in the absence of other types of Cl^- channel, so analysis of the channel was not possible.

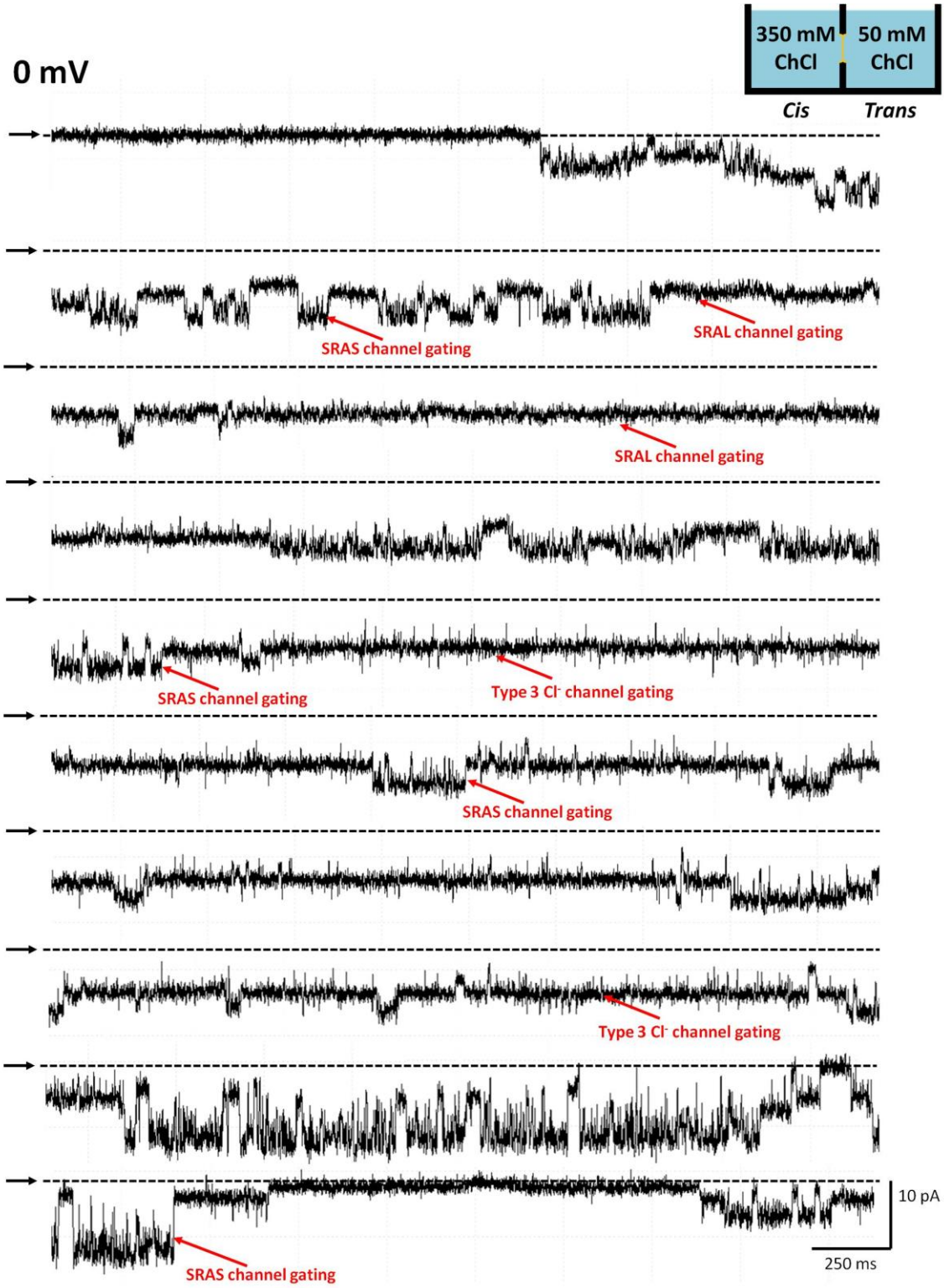

0 mV
350 mM ChCl
50 mM ChCl
Cis
Trans
SRAS channel gating
SRAL channel gating
SRAL channel gating
SRAS channel gating
Type 3 Cl- channel gating
SRAS channel gating
Type 3 Cl- channel gating
SRAS channel gating
10 pA
250 ms

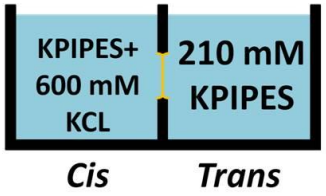
Figure 4.1. Cl^- channel currents observed in the rabbit HSR
Representative current-fluctuations over 25 s of continuous recording through SR chloride channels from rabbit skeletal muscle at the holding potential of 0 mV in asymmetrical choline-chloride solutions. The zero current level is shown by an arrow. Arrows indicate different types of channel gating which might indicate distinct types of ion channel.

4.2.2 The SR anion-selective (SRAS) channel

Representative single-channel data from SRAS channels observed from sheep cardiac muscle (Figure 4.2 and Figure 4.3) and mouse skeletal muscle (Figure 4.4 and Figure 4.4) fractions under voltage clamp conditions show that the gating behaviour of SRAS channels is characterised by high Po with long full open and closed states plus frequent sojourns in two distinct sub-conductance levels. The sub-conductance levels are observed at 50 % and 70% of the channel fully open level (sheep cardiac isoform) and at 20% and 60% (mouse skeletal isoform). The Po of the SRAS channel increased at more negative holding potentials for channels from both sheep cardiac muscle and mouse skeletal muscle

The sheep cardiac SRAS channel exhibited a single-channel conductance of 138.0 pS (mean, n=2) compared to the mouse skeletal isoform which exhibited a single-channel conductance of 177.9±15.0 pS (mean±SEM, n=6) as shown in Figure 4.8. Figure 4.8 also illustrates that the current-voltage relationship is not linear but curves towards the *x*-axis as would be expected if the channel was impermeable to K^+. As there are only contaminant levels of Cl^- in the *trans* chamber, if the channel is impermeable to K^+, no current will pass from the *trans* to the *cis* chamber and therefore no positive channel openings will be observed (as was the case). The channel was thus named the SR anion-selective (SRAS) channel due to its apparent impermeability to cations.

Sheep cardiac SRAS channel



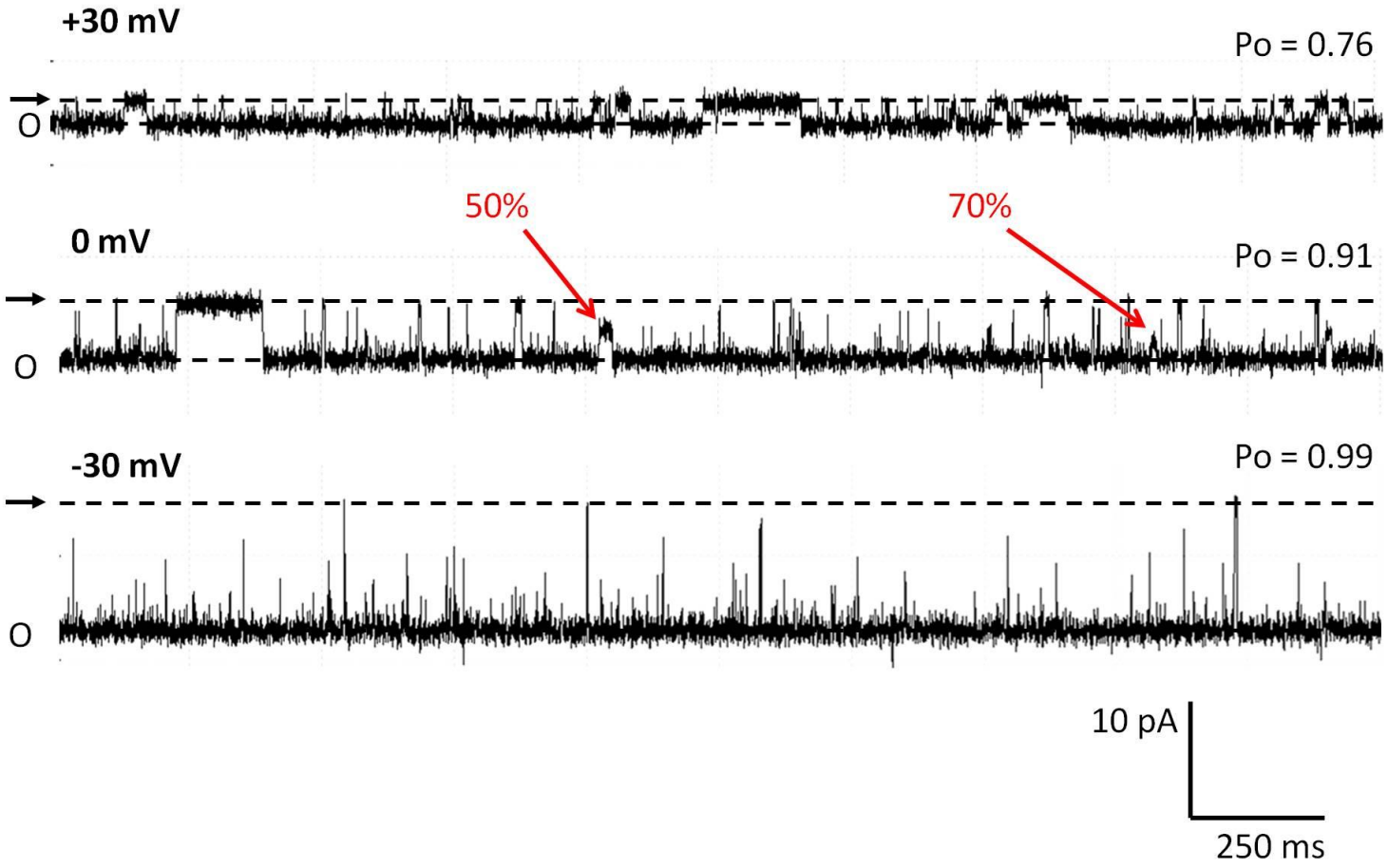


Figure 4.2. The SRAS channel from sheep cardiac muscle
Representative current-fluctuations through a sheep cardiac SRAS channel at the holding potentials +30 mV, 0 mV and -30 mV in asymmetrical conditions. The fully open state is shown by O and the closed level is shown by an arrow. Examples of channel gating to the sub-conductance levels are shown by red arrows. The traces are representative of n=10 experiments.

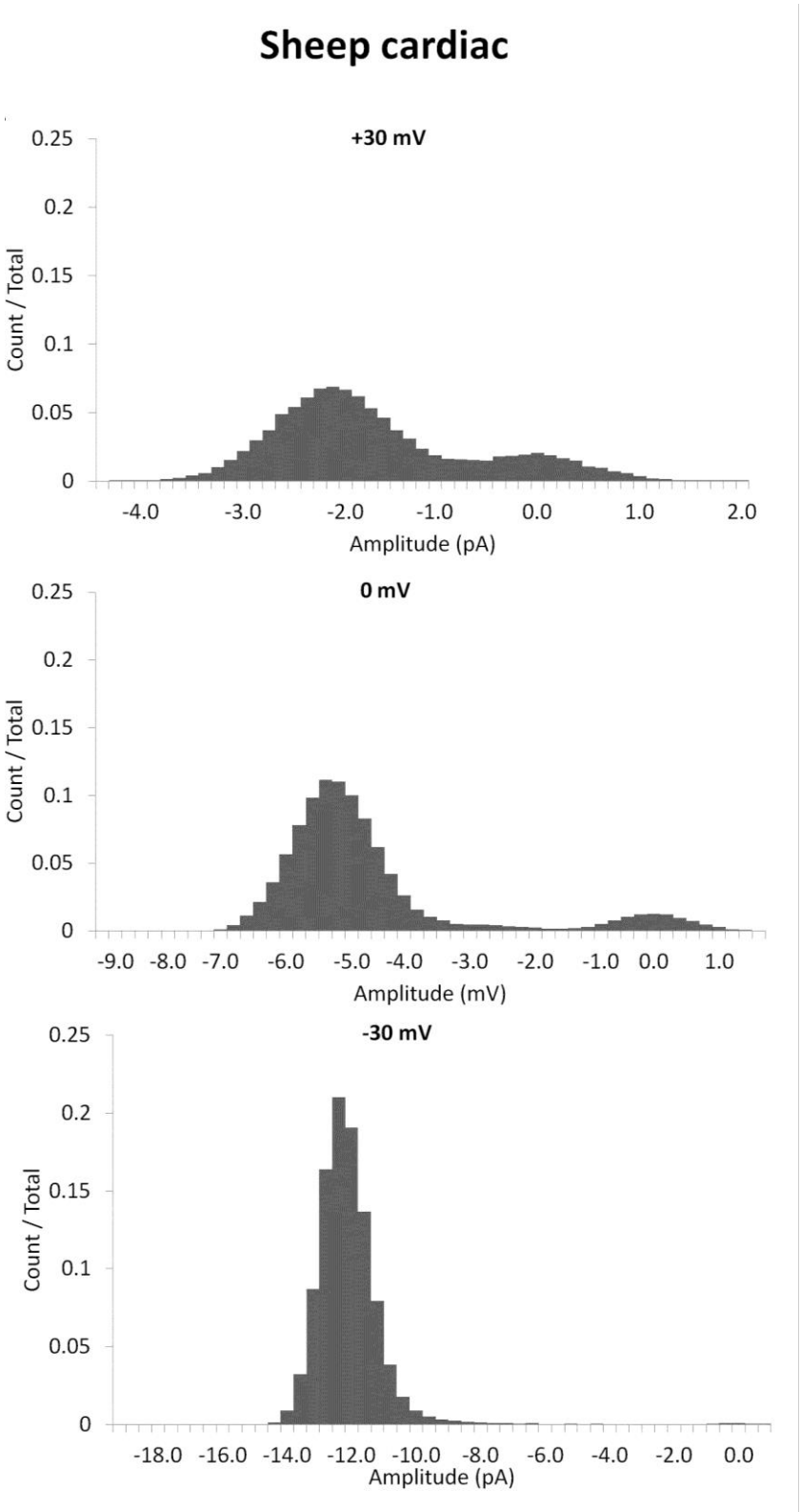


Figure 4.3. Sheep cardiac SRAS channel amplitude-histograms
Amplitude-histograms were obtained from 10 s of recording for SRAS channels from sheep cardiac muscle at the indicated holding potentials.

Mouse skeletal SRAS channel

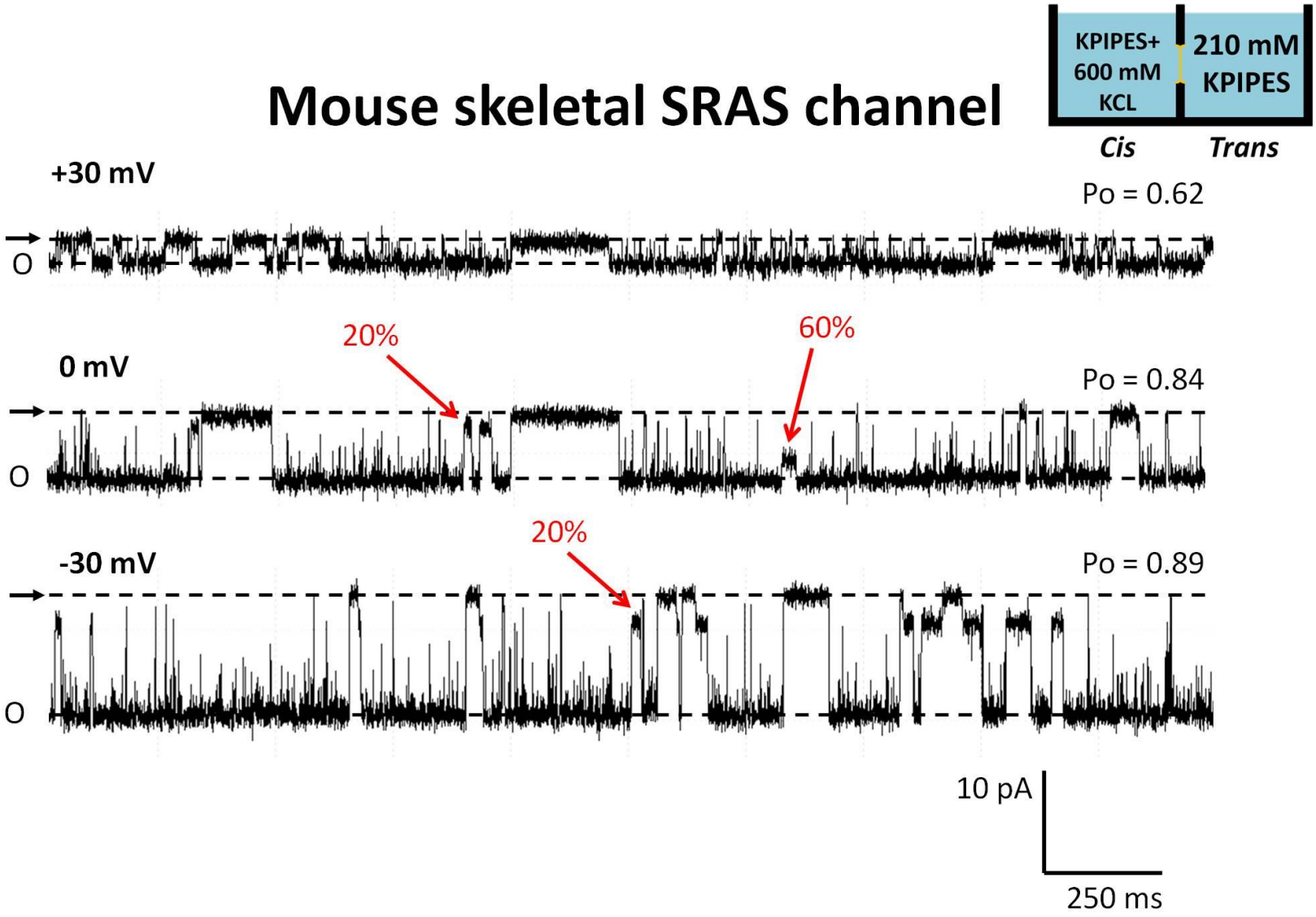


Figure 4.4. The SRAS channel from mouse skeletal muscle
Representative current-fluctuations through a mouse skeletal SRAS channel at the holding potentials +30 mV, 0 mV and -30 mV in asymmetrical conditions. The fully open state is shown by O and the closed level is shown by an arrow. Examples of the channel gating to the sub-conductance levels are shown by red arrows. The traces are representative of n=6 experiments.

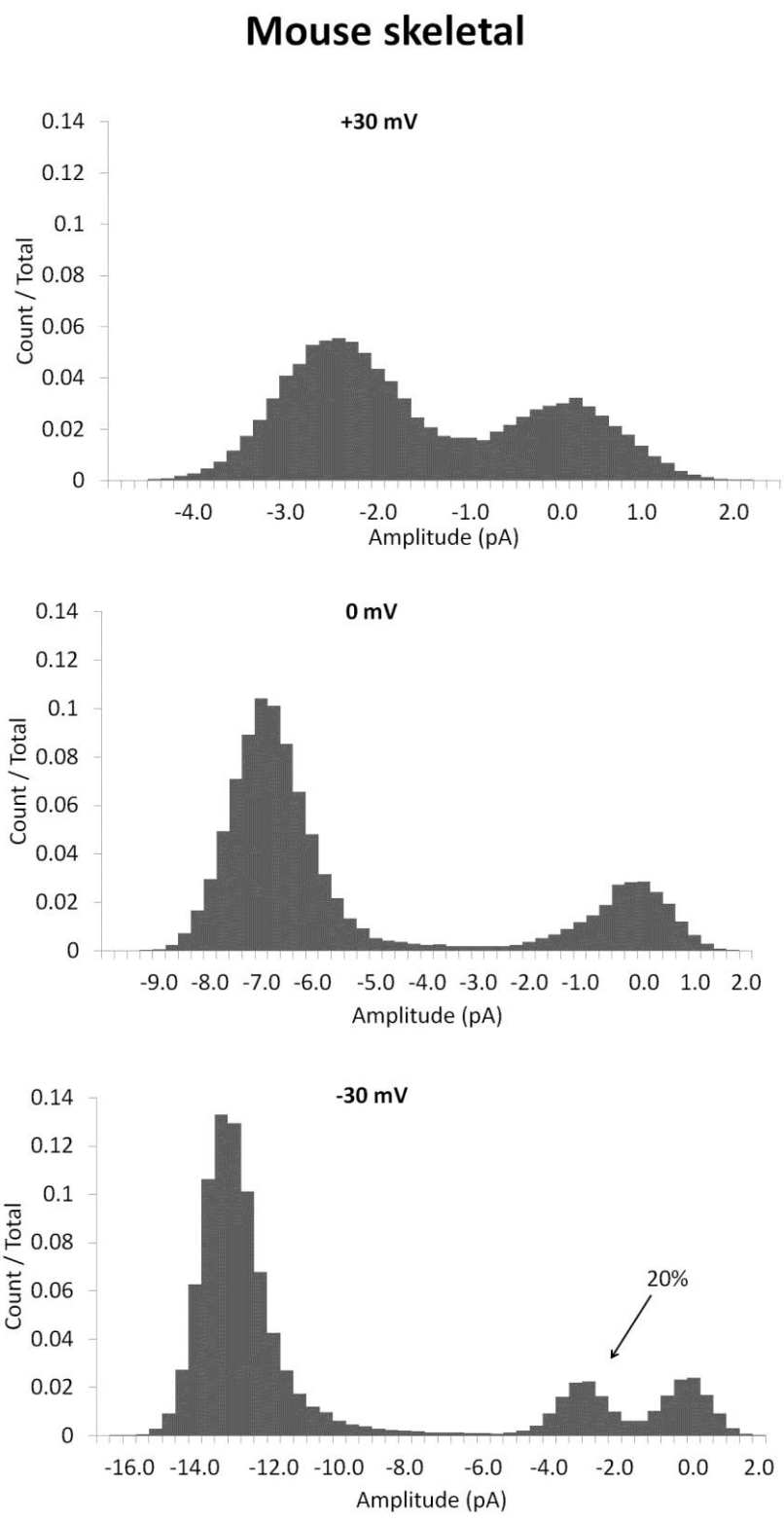


Figure 4.5. Mouse skeletal SRAS channel amplitude-histograms
Amplitude-histograms were obtained from 10 s of recording for SRAS channels from mouse skeletal at the indicated holding potentials.

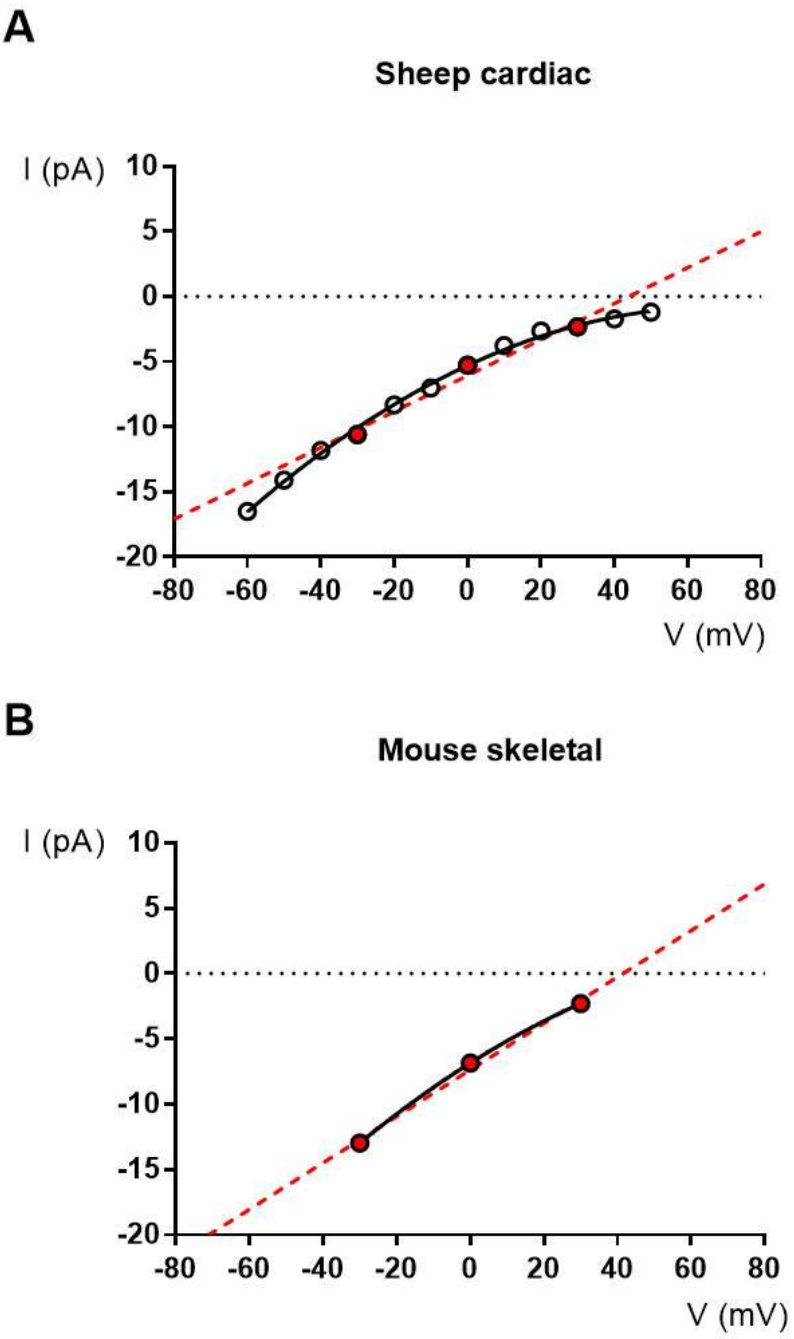


Figure 4.6. Current-voltage relationships for the SRAS channel
Current-voltage relationships for the SRAS channel from sheep cardiac muscle **(A)** and from mouse skeletal muscle **(B)**. The red broken line is the calculated linear regression for the data points at +30 mV, 0 mV, and -30 mV (coloured red for clarity), resulting in a single-channel conductance of 138.0 pS (mean, n=2) for sheep cardiac SRAS channels and 177.9±15.0 (mean±SEM, n=6) for mouse skeletal SRAS channels. Mean values are shown in **(A)**; mean±SEM are shown in **(B)**. Where not shown, error bars are within the symbols.

4.2.3 The SR anion leak (SRAL) channel

A second type of SR Cl^- channel was observed from mouse skeletal muscle. Representative examples of these currents in choline-chloride are shown in Figure 4.7A. The channels were observed to gate with high Po and with few resolved closings, causing the current-fluctuations through multiple channels to appear similar to a leak current. I therefore termed this the 'SR anion leak' (SRAL) channel. Apparent unitary single-channel events were observed as shown by red arrows. An expanded portion of the trace at -40 mV is shown with predicted single-channel levels. Although SR vesicles were removed from the *cis* chamber after one fusion event with the bilayer to prevent further fusions, single SRAL channels were never observed.

Figure 4.7B shows the current-voltage relationship of apparent unitary SRAL channel currents under the same experimental conditions as the current-fluctuations illustrated in Figure 4.7A. An E_{rev} of 6.9 mV and an apparent unitary conductance of 91.5±7.3 pS were calculated for the mouse skeletal SRAL channel. The E_{rev} for a Cl^- selective channel would be +49.2 mV, thus the SRAL channel is permeable to both choline and Cl^- with a $P_{choline}/P_{Cl}$ of 0.5±1.0 (mean±SEM, n=5), calculated using a modified version of the Goldman-Hodgkin-Katz equation (see methods).

Since single-channel events were small and difficult to resolve, the SRAL E_{rev} was also measured using noise analysis of the leak currents at various potentials. Figure 4.8 and Figure 4.9 show the current-voltage relationships for SRAL channels where the average currents were measured using noise analysis in choline-chloride and NMDG-chloride respectively. Like the relationship for single-channel events, the E_{rev}, calculated from noise analysis of the SRAL channel, does not pass through the calculated E_{rev} for Cl^- in either choline-chloride or NMDG-chloride, confirming that the channel is non-selective and passes Cl^-, choline, and NMDG. This

gives a calculated $P_{choline}/P_{Cl}$ = 0.6±0.2 (Mean ±SEM, n=6) and P_{NMDG}/P_{Cl} of 0.77±0.2 (mean±SD, n=3) indicating that SRAL channels are more permeable to Cl^- than choline and NMDG.

Figure 4.8 and Figure 4.9 show that the current-voltage relationship for the SRAL channel in gradient conditions is non-linear, becoming larger at negative potentials. This was the case in all experiments including for the unitary channel events shown in Figure 4.7. However, in symmetrical conditions, no rectification was observed (Figure 4.10), even at molar ionic concentrations.

From the data shown in Figure 4.10, conductance-activity relationships were plotted in NMDG-chloride and choline-chloride solutions using by means of a Michaelis–Menten equation (Figure 4.11). The half maximal conductance for choline-chloride and NMDG-chloride was obtained at 568 mM and 216 mM, respectively. Maximal conductance was obtained at 1396 mM and 593 mM in choline-chloride and NMDG-chloride respectively.

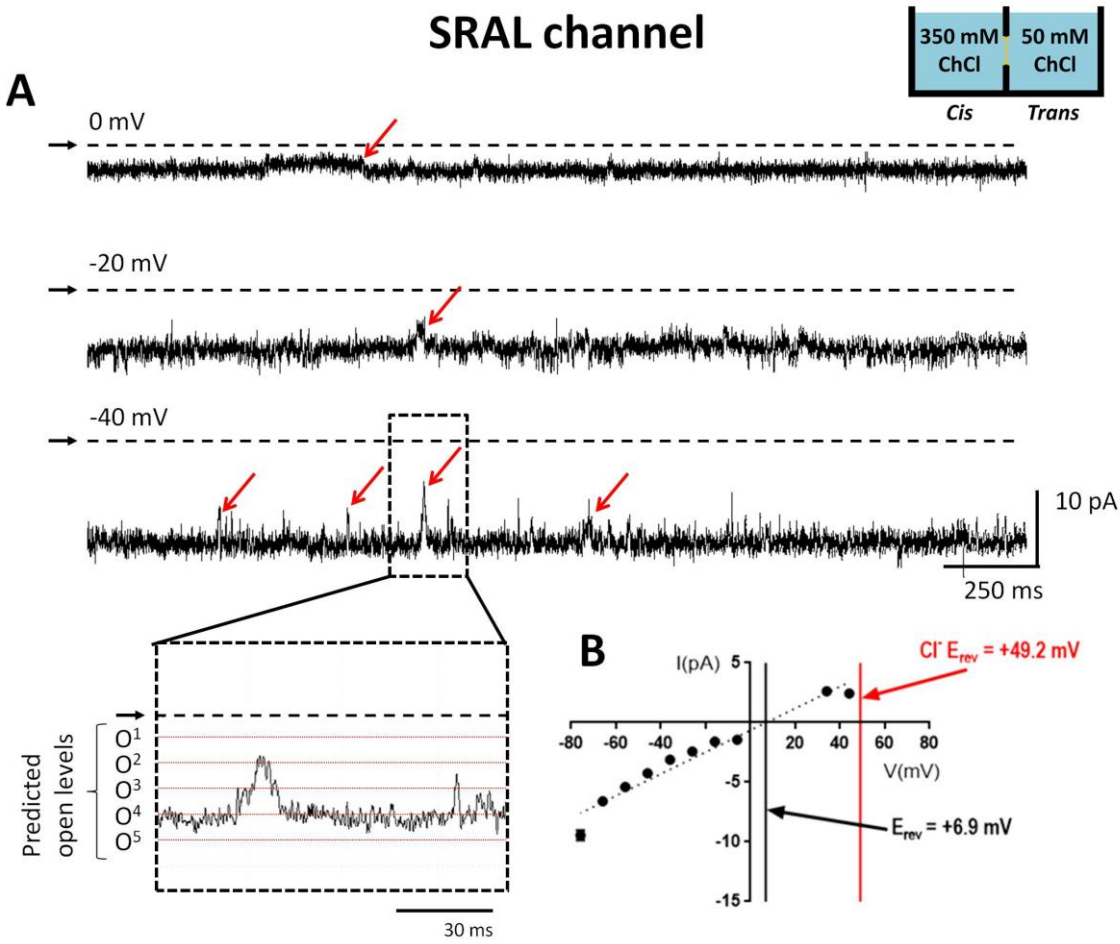


Figure 4.7. Current-fluctuations through the mouse skeletal SRAL channel.
(A) Representative current-fluctuations through multiple mouse skeletal SRAL channels derived from SR vesicles and obtained after a single vesicle fusion event with the bilayer. Recordings were obtained in asymmetric ionic conditions. The zero current level is shown by black arrows. Examples of possible unitary SRAL channel events are illustrated by the red arrows. The traces are representative of 6 experiments. The expanded section illustrates the possible individual channel events. The red lines represent the predicted single-channel open levels and are labelled with the estimated number of channels thought to be opening. **(B)** The current-voltage relationship of possible single SRAL channel events. The E_{rev} for the data, calculated by fitting with a linear regression line is shown by a black vertical line and the Cl^- E_{rev} is shown by a red vertical line. Values are of the mean±SEM (n=6). Where not shown, error bars are within the symbols.

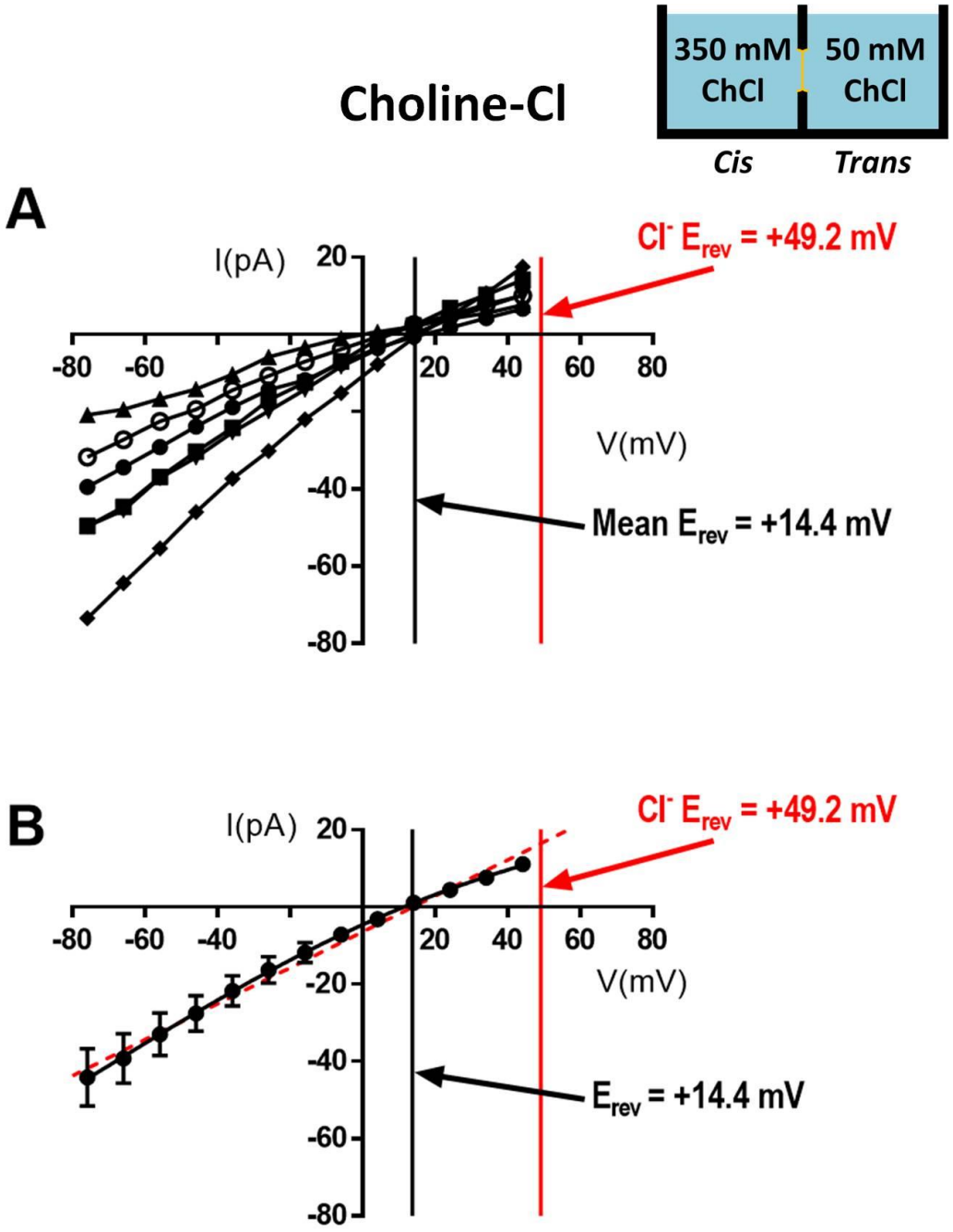


Figure 4.8. Current-voltage relationships for the SRAL channel in choline-chloride
Noise analysis was used to obtain the current-voltage relationships in asymmetric choline-chloride (choline-Cl). **(A)** shows the relationships for 6 individual experiments while **(B)** shows the mean of these experiments (±SEM, n=6). The calculated reversal potential for Cl^- is shown by a red vertical line, and the mean E_{rev} for the SRAL channel is shown by a black vertical line for comparison. Where not shown, error bars are within the symbols.

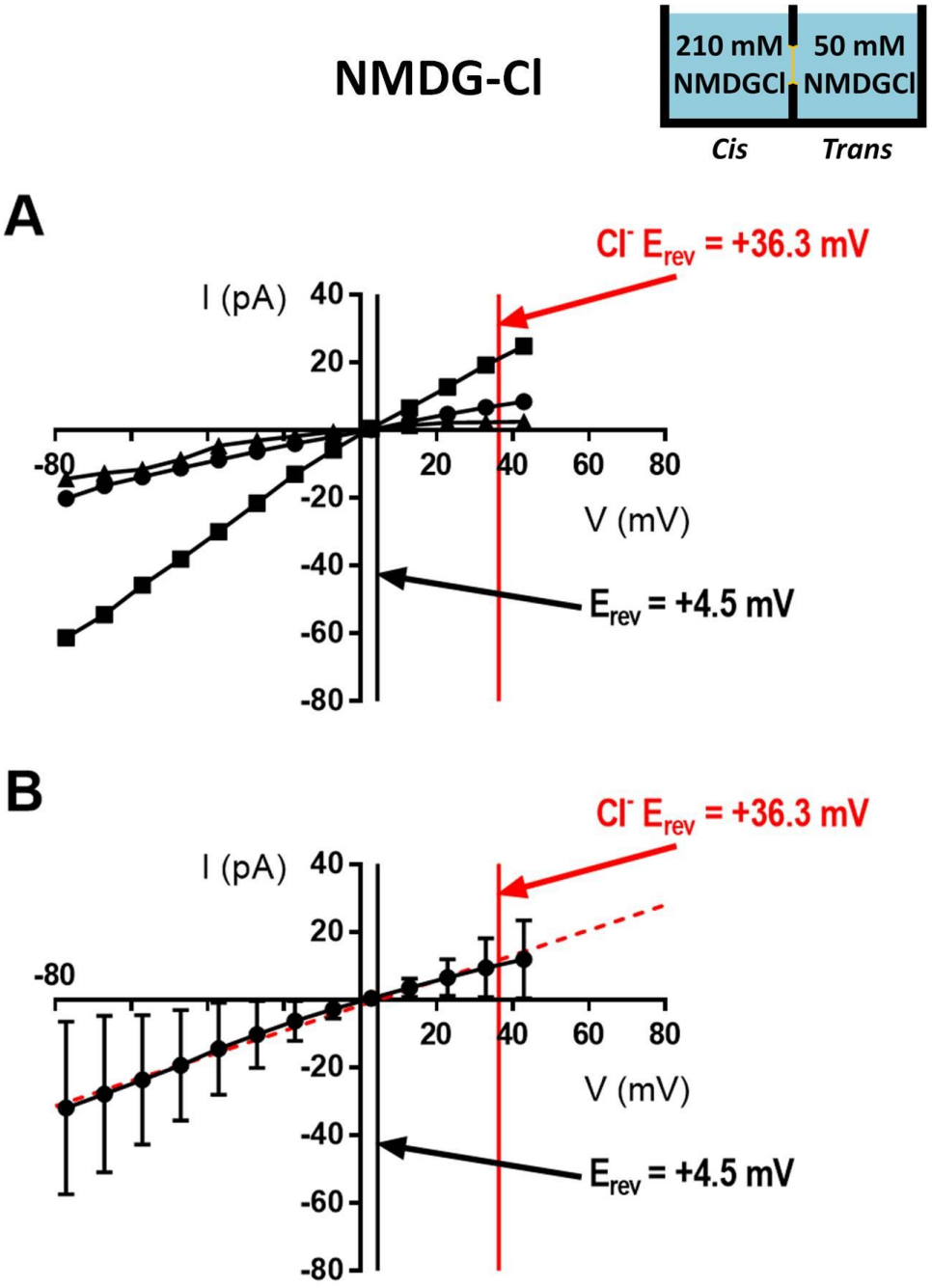


Figure 4.9. Current-voltage relationships for the SRAL channel in NMDG-Chloride
Noise analysis was used to obtain the current-voltage relationships in asymmetric NMDG-chloride (NMDG-Cl). **(A)** shows the relationships for 3 individual experiments while **(B)** shows the mean of these experiments (SEM, n=3). The calculated reversal potential for Cl^- is shown by a red vertical line, and the mean E_{rev} for the SRAL channel is shown by a black vertical line for comparison. Where not shown, error bars are within the symbols.

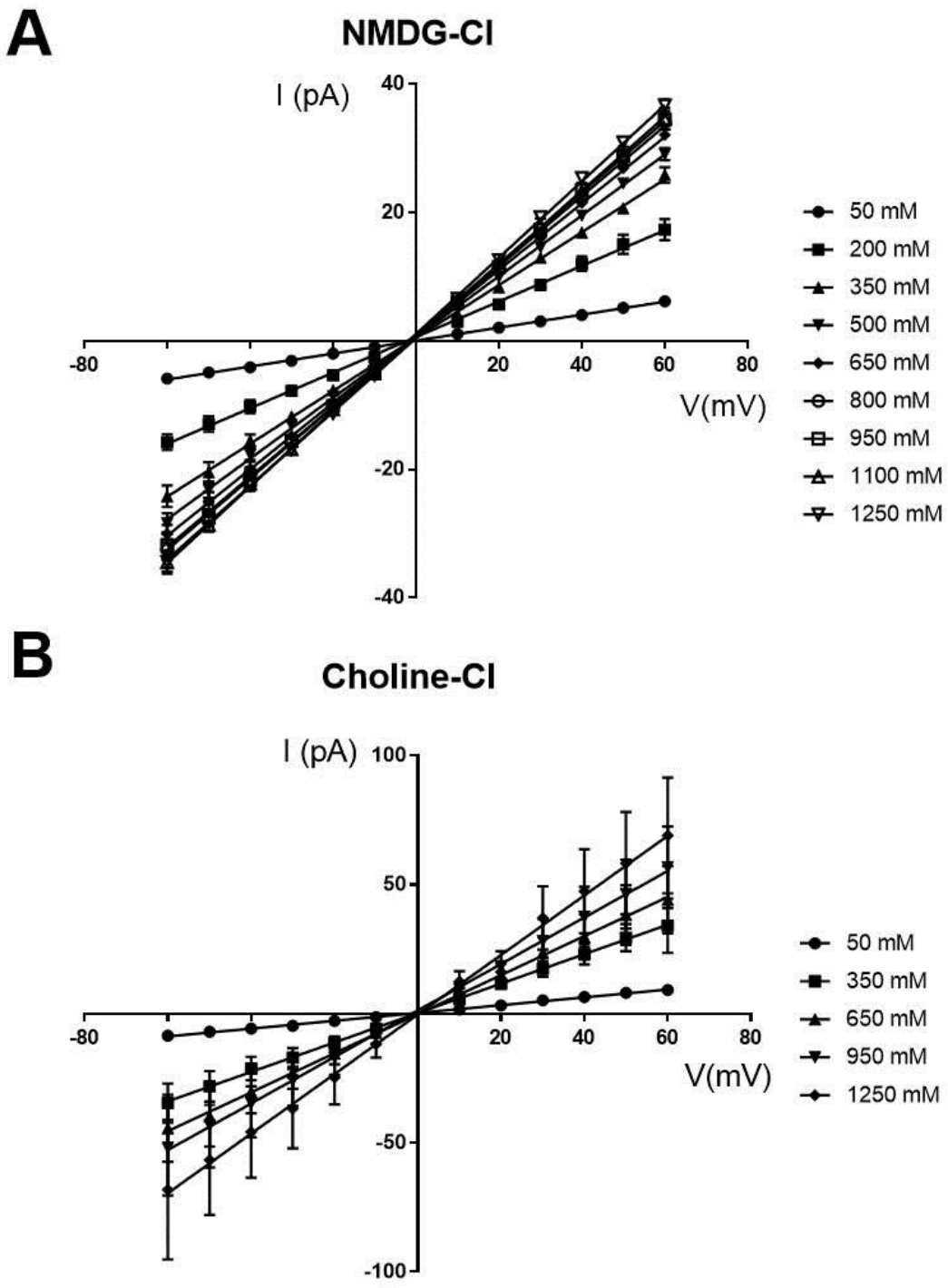
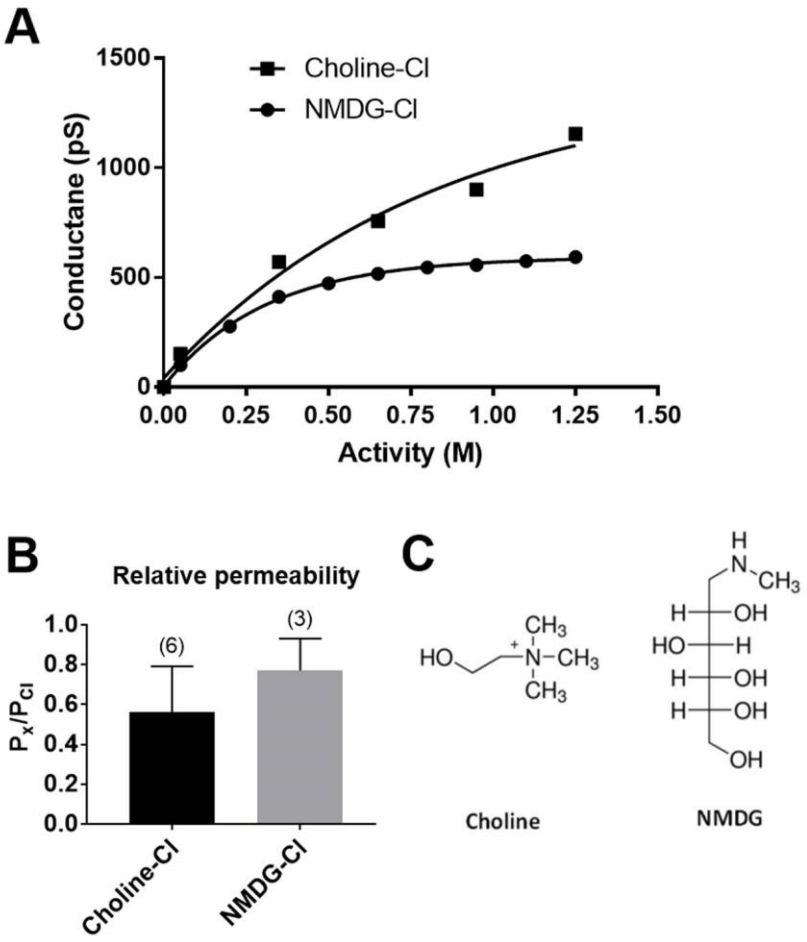


Figure 4.10. Current-voltage relationships of the SRAL channel with increasing ionic concentrations

Current-voltage relationships from noise analysis of the SRAL channel in the presence of symmetrical solutions of NMDG-chloride (n=5) **(A)** and choline-chloride (n=3) **(B)**. For each experiment, a current-voltage relationship was plotted in solutions of increasing ionic strength (50 mM – 1250 mM). Values are of the mean±SEM or mean±SD. Where not shown, error bars are within the symbols.



D

Ion	Length (Å)	Width (Å)	Depth (Å)
Choline	7.49	5.02	4.49
NMDG	13.06	5.58	5.33
Cl^-	3.62	3.62	3.62

Figure 4.11. Conductance-concentration relationships of the SRAL channel
(A) The conductance-activity relationship for the SRAL channel in NMDG-chloride and choline-chloride. Half maximal conductance values of 568.4 mM (choline-chloride) and 216.0 mM (NMDG-chloride), and maximal conductance values of 1396.0 mM (choline-chloride) and 592.9 mM (NMDG-chloride) are calculated. Values are of the mean±SEM. Where not shown, error bars are within the symbols. **(B)** A comparison of the $P_{choline}/P_{Cl}$ and P_{NMDG}/P_{Cl} values for the SRAL channel. Mean±SD. **(C)** The molecular structure of NMDG and choline molecules shown for comparison of size (https://www.sigmaaldrich.com). **(D)** The approximate dimensions of the choline and NMDG molecules [194] as well as the dehydrated Cl^- ion (the fully hydrated diameter of Cl^- is 6.96 Å) [209].

4.2.4 The Type 3 SR Cl^- channel

A third type of Cl^- channel, termed the 'Type 3 SR Cl^- channel' was observed in the SR. The channel was observed in only 2 SR Cl^- experiments and was not recorded in isolation from the other two Cl^- channels. As such, it was not possible to study the properties of this channel in detail. Figure 4.12 demonstrates typical gating of the Type 3 SR Cl^- channel. The channel gates with a high Po and mainly to a high-noise sub-conductance level with occasional current-fluctuations to higher and lower conductance states.

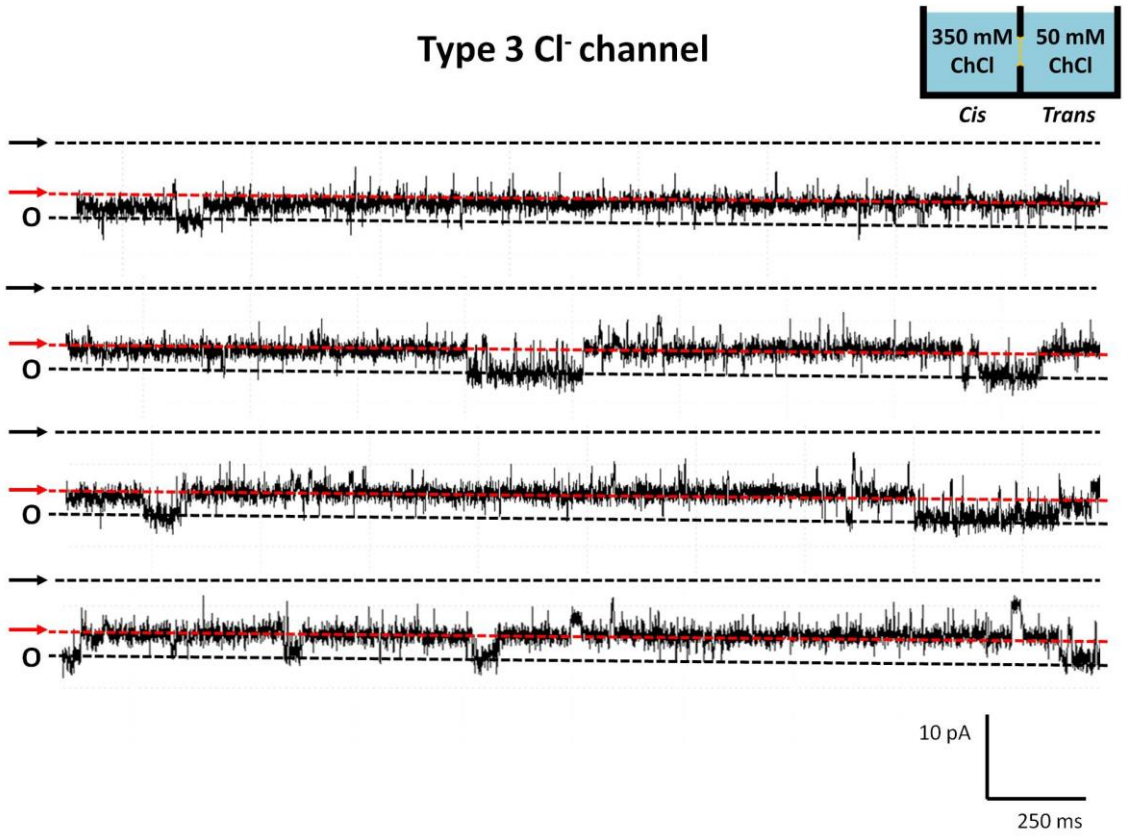


Figure 4.12. Current-fluctuations through the Type 3 SR Cl^- channel observed in the rabbit skeletal SR

Representative current-fluctuations through the Type 3 SR Cl^- channel from rabbit skeletal muscle at a 0 mV holding potential in asymmetrical choline-chloride. The zero current level is shown by a black arrow, the apparent fully open channel level is shown by O and the high noise sub-conductance level is shown by a red arrow.

4.3 Discussion

The aim of this chapter was to identify and characterise the Cl^- channels observed when native SR vesicles were incorporated into the bilayer. I identified three channels which I have termed the SRAS channel, the SRAL channel, and the Type 3 SR Cl^- channel.

4.3.1 SRAS channels

The SRAS channel was only observed in solutions where Cl^- was present in the *cis* chamber, but not in the *trans* chamber. The channel was entirely selective for Cl^- as is demonstrated in Figure 4.6 where the current-voltage relationships for the channel from both sheep cardiac and mouse skeletal muscle do not follow a linear relationship. Instead, the line curves away from the *x*-axis and can be extrapolated never to meet it. This is evidence for SRAS channel impermeabiltiy to K^+ ions. Under the experimental conditions used therefore, positive current-fluctuations were impossible. This is summarised in Figure 4.13.

The mouse skeletal SRAS channel displays similarities with the Cl^--selective ion channel observed previously in the literature [86], [116], [118], [119], [122], [123]. A comparison of the gating between these channels and the SRAS channel is shown in Figure 4.14. It is possible that these studies are describing various different SRAS channel isoforms.

The SRAS channel is also comparable with the rabbit skeletal SCl channel described by Kourie *et al.* in 1996 [121] (Figure 4.15). Although the channel conductances cannot be compared due to the different ionic conditions used, both channels gated in both fully open and sub-conductance levels (Figure 4.15A and B). The SCl channel was predicted to gate with 5 sub-conductance states at 7 %, 24 %, 39 %, 67 % and 86 % [120], a major peak is observed in the amplitude histogram for the channel at 24 % of the fully open state which is similar to the major peak in the mouse skeletal SRAS channel amplitude-histogram (Figure 4.15C and D). It

can be argued, therefore, that the SRAS channel and SCl channel display similar gating patterns. With the limited data available, however, it is difficult to speculate whether the SRAS channel is the SCl channel or any of the other SR Cl^- channels observed previously. The SCl channel was shown to be sensitive to Ca^{2+} [120] and ATP [128], and other published SR Cl^--selective channels have been reported to be modulated by DIDS, NPPB, CaM, and Zn^{2+} [116] [118][123]. Future experiments which test these compounds on the SRAS channel could provide further evidence for similarities/differences between the SRAS and other SR Cl channels.

Another channel which displays similar properties to the SRAS channel is the CLIC1 channel. As with the SRAS and SCl channels, the CLIC1 channel gates with defined sub-conductance states [146]. A study of the single-channel properties of purified human CLIC1 proteins in planar lipid bilayers found the channels to dwell in sub-conductance levels at 45 % and 22 % of the fully open channel level [146]. This is not dissimilar to the SRAS channels from mouse skeletal and sheep cardiac muscle. The CLIC1 channel exhibited a small conductance (38±3 pS in 500/50 mM *cis*/*trans* Cl^-) compared with the SRAS channel (138-178 pS in 600/0 mM *cis*/*trans* Cl^-), however, and was permeable to both cations and anions (P_{Cl}/P_K = 1.4) [146], which indicate that CLIC1 is unlikely to be the SRAS channel. The CLIC2 channel shares sequence homology with the CLIC1 channel and has been shown to modulate RyR2 activity [147][148]. It is possible that the SRAS channel could be CLIC2. The CLIC2 channel is yet to be studied on a single-channel level, however.

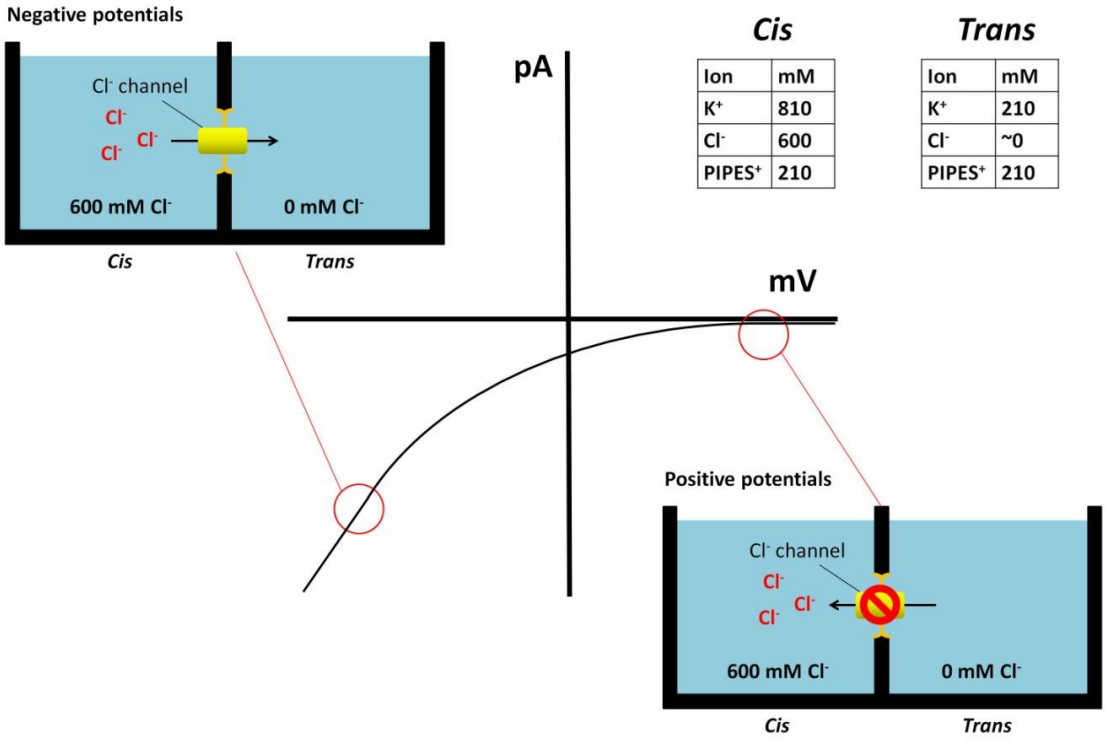


Figure 4.13. A schematic showing a current-voltage relationship of a Cl^--selective channel in asymmetrical solutions with 600 mM Cl^- in the *cis* chamber and 0 mM Cl^- in the *trans* chamber

At negative potentials (left side of the graph), Cl^- passes through the channel from the *cis* chamber to the *trans* chamber due to the abundance of Cl^- in the *cis* chamber. At positive potentials (right side of the graph), current cannot pass through the channel from the *trans* chamber to the *cis* chamber as no Cl^- is present in the *trans* chamber. The tables show the ionic conditions with which recordings of the SRAS channel were made.

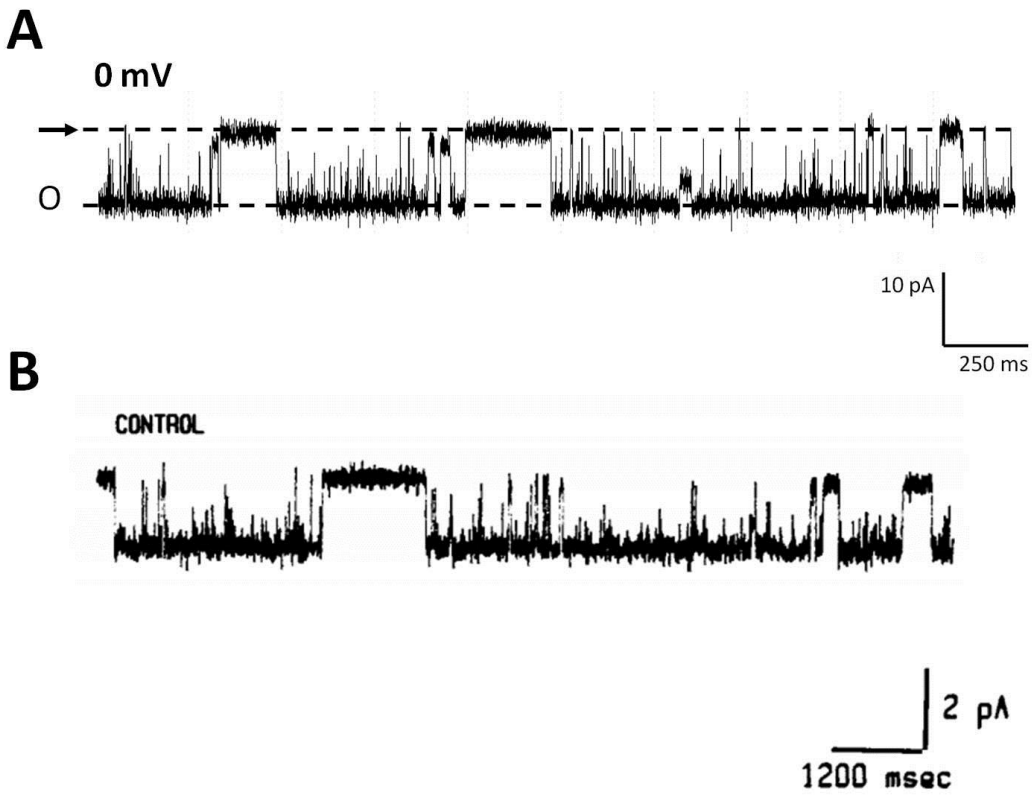


Figure 4.14. Examples of gating of the SRAS channel and a Cl^--selective channel observed in previous studies
(A) Currents through the SRAS channel in KPIPES with a KCl gradient at 0 mV. **(B)** An example of the small Cl^--selective channels observed in bilayer experiments at 0 mV. The channel was recorded in 260/60 mM *cis*/*trans* choline-chloride solutions and reversed at +31 mV, close to the Cl^- E_{rev} of 36.7 mV. The figure is adapted from Rousseau, 1989 [116].

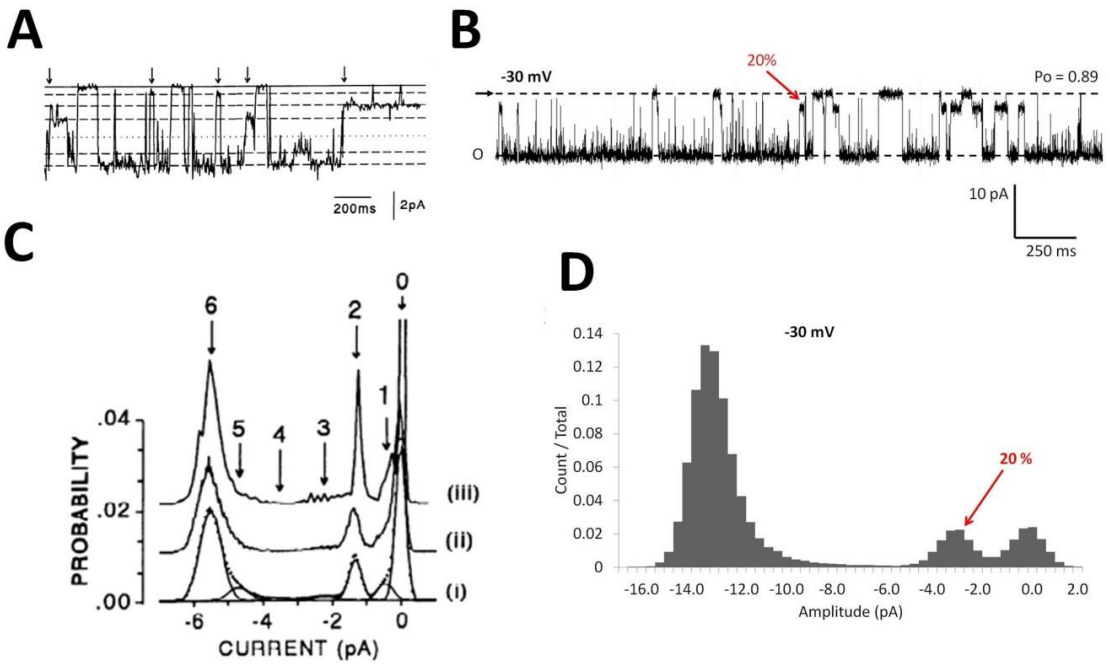


Figure 4.15. A comparison of the SCl and SRAS channels adapted from by Kourie *et al.* in 1996 [120]
(A) Current-fluctuations through the SCl channel from rabbit skeletal SR at -40 mV in 250/50 mM *cis*/*trans* CsCl [120]. **(B)** Current-fluctuations through the SRAS channel from mouse skeletal SR at -30 mV in *cis*: 210 mM KPIPES + 600 mM KCl and *trans*: 210 mM KPIPES. **(C)** Amplitude-histogram for an SCl channel showing the major peaks. Peak 2 is equivalent to 24 % of the apparent fully open channel state. (i), (ii), and (iii) correspond to different filtering levels [120] **(D)** Amplitude-histogram for the SRAS channel with the major peak representing the 20 % sub-conductance state labeled with a red arrow.

4.3.2 SRAL channels

SRAL channels were observed in choline-chloride solution and appeared similar to leak currents. The SRAL channel displays similarities to non-selective Cl^- channels described in the SR previously [117], [124]–[126], and the BCl channel described by Kourie *et al.* in 1996 [121]. The BCl channel exhibited a large conductance (210-250 pS in 250/50 mM *cis*/*trans* CsCl) and >13 sub-conductance states were observed which may be equivalent to the unitary currents observed in SRAL channels Figure 4.16.

The SRAL channel was found to exhibit porin-like selectivity. The channel was found to be permeable to both anions (Cl^-) and large cations (choline and NMDG). These permeability properties are not shared with the BCl channel. The SRAL channel permeability properties are more similar to those of VDAC which is thought to pass ATP molecules through its pore. The VDAC channel is voltage sensitive, however, which the SRAL channel has not been shown to be [134], [135], [139].

I speculate that the large currents exhibited after SRAL channel incorporation are due to channel clusters which contain many individual SRAL channels. Evidence for this lies in the large range of channel conductance values for the SRAL channel (250 pS to 754 pS in 350/50 mM *cis*/*trans* choline-chloride) and the existence of apparent unitary channel events within the SRAL channel current.

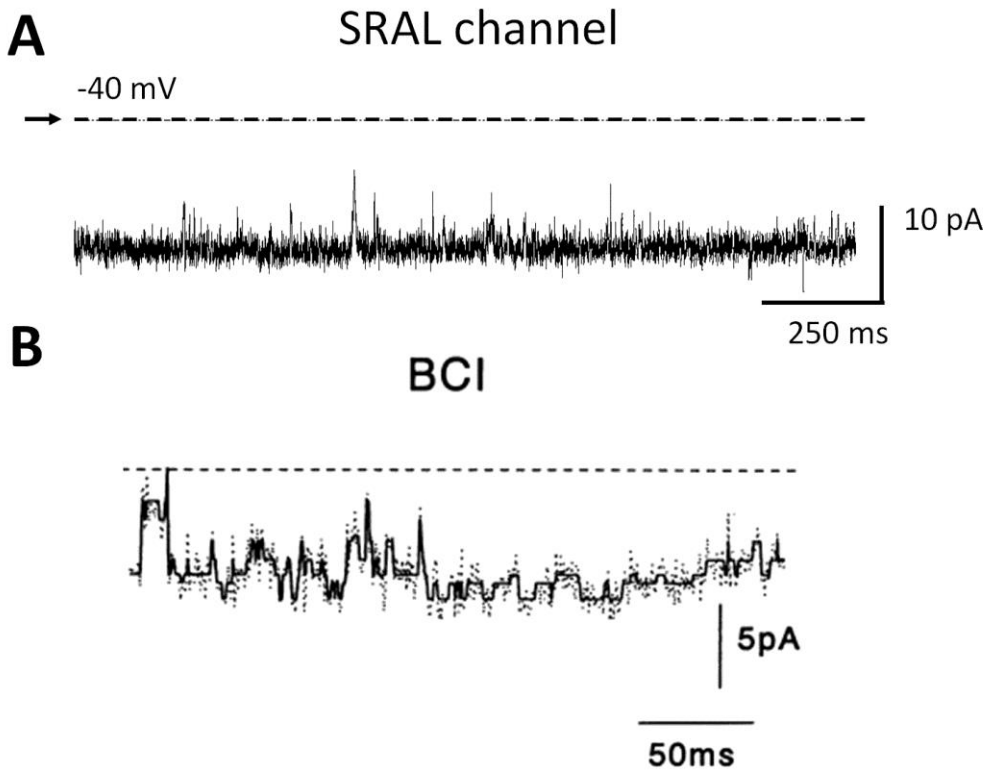


Figure 4.16. Current-fluctuations through the SRAL channel and the BCl channel adapted from Kourie *et al.* 1996 [121]
(A) Current-fluctuations through the mouse skeletal SRAL channel at -40 mV in 350/50 mM *cis*/*trans* choline-chloride. **(B)** Current-fluctuations through the BCl channel rabbit skeletal SR at 0 mV in 250/50 mM *cis*/*trans* CsCl [121].

Figure 4.11A compares conductance-activity relationships between the SRAL channels conducting choline-chloride and NMDG-chloride. In NMDG-chloride, the channel reaches its saturation point (where the maximum conductance possible was reached) at a lower concentration (592.9 mM) compared to choline-chloride (1396.0 mM). It is unclear why this is the case; however, I speculate that this could occur because the large size of the NMDG ions, compared with choline Figure 4.11D, limits the rate at which they can pass through the SRAL channel pore. It is possible that ions which are larger than NMDG may not permeate the SRAL channel pore.

4.3.3 The Type 3 SR Cl^- channel

The Type 3 SR Cl^- channel was rarely recorded gating in the bilayer, and exhibited a gating pattern which has not been observed with other Cl^- channels in the literature. The channel gates with a high Po and mainly to a high-noise sub-conductance level with occasional current-fluctuations to higher and lower conductance states. The Type 3 SR Cl^- channel gating pattern is comparable to that of the TRIC channel discussed in later chapters in this thesis.

Chapter 5. TRIC-A proteins from native membranes

5.1 Introduction

In mammalian tissue TRIC channel exists in two subtypes, TRIC-A and TRIC-B and are found in the ER/SR and nuclear membranes of most cell types [81]. TRIC-A and TRIC-B are not identically expressed, however. TRIC-A is expressed at high levels in excitable cells such as in cardiac and skeletal muscle cells [81] where they are estimated to be present at levels as high as 5:1 with the RyR channel [85]. TRIC-B is ubiquitously expressed, but at much lower levels than TRIC-A [81]. It has been suggested that the identity of the TRIC proteins could SR K^+ channels [97].

Physiological roles for the channels are yet to be established, however, mice lacking either one or both of the TRIC proteins have been developed and their phenotypes studied by the Takeshima laboratory (Department of Biological Chemistry, Kyoto University, Kyoto, Japan). The Takeshima group developed three mouse phenotypes, a TRIC double knock-out (TRIC-DKO) mouse model which lacked both TRIC-A and TRIC-B proteins [81], a *Tric-a* KO mouse model, lacking the TRIC-A protein [85], and a *Tric-b* KO mouse, lacking the TRIC-B protein [83].

TRIC-DKO mice were observed to die of pre-natal cardiac failure at around day E9.5 [81]. The SR of the TRIC-DKO mice was found to be swollen and overloaded with Ca^{2+}, suggesting that the TRIC-A and TRIC-B isoforms play a complementary role in allowing effective Ca^{2+} release during EC-coupling [81].

The *Tric-b* KO mouse was found to die immediately after birth due to respiratory failure [83]. Alveolar epithelial cells of the *Tric*-b KO mouse displayed markedly reduced IP3R-mediated Ca^{2+} release and intracellular stores showed evidence of Ca^{2+} overload [83].

The *Tric-a* KO mouse survives until adulthood. Mice were found to develop hypertension due to insufficient RyR-mediated Ca^{2+} sparks, which are responsible for inducing hyperpolarisation,

resulting in vascular hypertonicity [84]. In addition, dysregulations in Ca^{2+} signalling and release were reported in the skeletal muscle of *Tric-a* KO mice where, again, the mice exhibited overloaded intracellular stores [85]. It has also shown that TRIC-A functions as an excitatory modulator of RyR1 channels [195].

In the light of this research, we formed a collaboration with the Takeshima laboratory group to study TRIC proteins in the bilayer system. We were supplied with CHO cells stably expressing TRIC-A proteins tagged with a PA tag on either the C or N terminus (named PA-TRIC-A or TRIC-A-PA, respectively), and with *Tric-a* KO mouse skeletal and cardiac muscle samples. The ER/SR membranes from the cells and muscle were isolated and reconstituted into artificial bilayers. The aims of these experiments were therefore to identify TRIC-A in the reconstituted membranes of CHO cells over- expressing TRIC-A and to characterise the ion channel function, and to compare the gating of the SR channels from WT and *Tric-a* KO mice, since in *Tric-a* KO mice, only TRIC-B will be present.

5.2 Results

5.2.1 The study of CHO cell membranes over-expressing human TRIC-A

Isolated ER mixed membrane vesicles from CHO cells over-expressing TRIC-A proteins were studied in the bilayer system. These membranes were difficult to characterise due to the apparent large variation in ion channel types which incorporated into the bilayer. Only one type of channel was observed in over-expressing CHO cells which was not observed in WT cells. Figure 5.1 shows an example of current-fluctuations through this channel. The channels exhibited a high Po and gated mainly to a flickery sub-conductance state at around 70 % of the apparent fully open state. The single-channel conductance of the apparent fully open state was 118.9±9.5 pS and the channel was selective for K^+ as the E_{rev} was equal to the E_{rev} for K^+ under the same experimental conditions (Figure 5.1B).

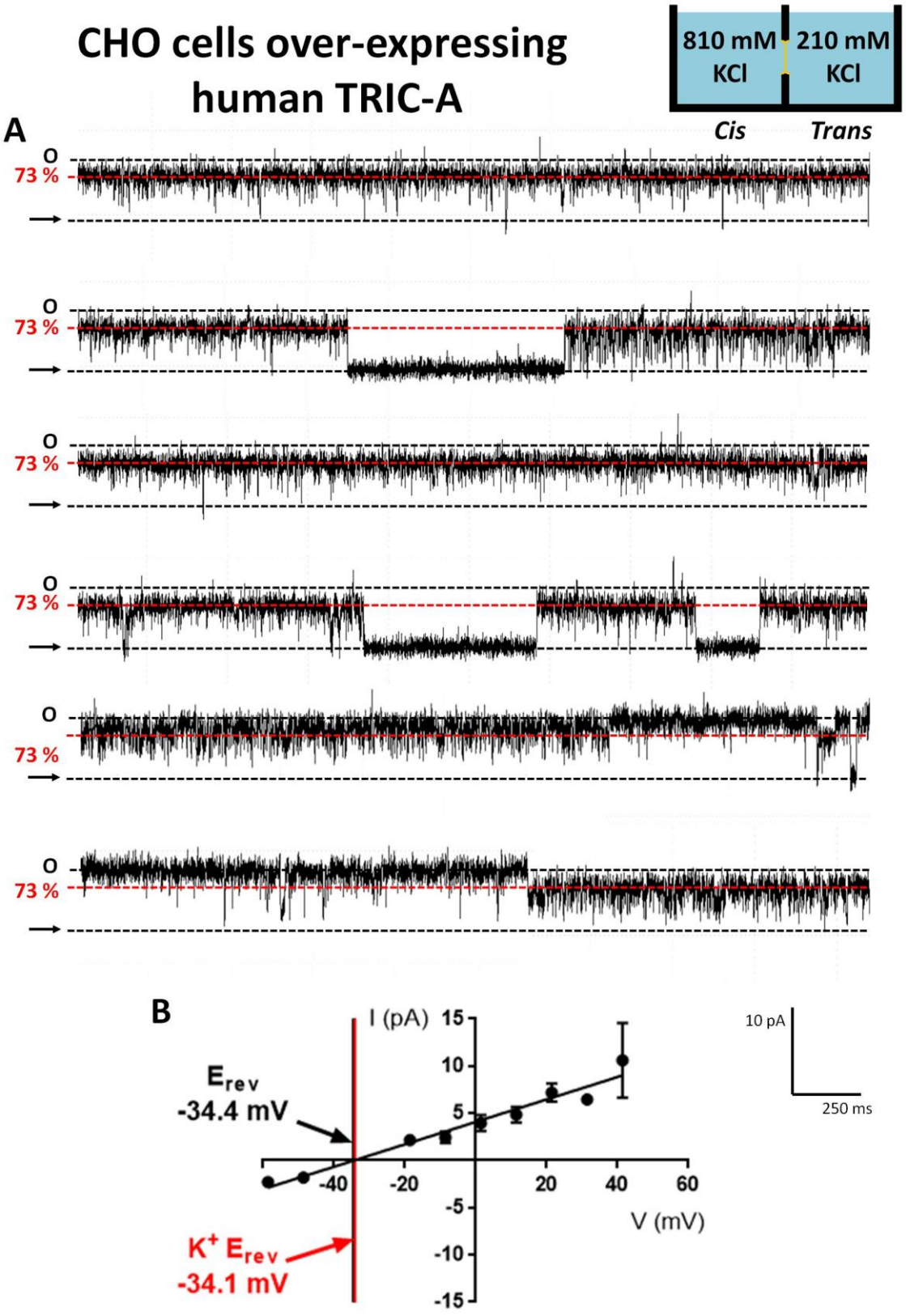

CHO cells over-expressing human TRIC-A
810 mM KCl
210 mM KCl
Cis
Trans
A
o
73 %
B
I (pA)
15
10
5
-5
-10
-15
-40
-20
20
40
60
V (mV)
E rev
-34.4 mV
K+ E rev
-34.1 mV
10 pA
250 ms

Figure 5.1. Current-fluctuations through a possible TRIC-A channel
(A) Current-fluctuations through a possible TRIC-A channel from the mixed membranes of CHO cells over-expressing human TRIC-A at +30 mV. The recording is representative of 4 experiments and was conducted using asymmetric solutions. The closed channel level is shown by an arrow and the channel fully open level is shown by O. The 73% sub –conductance level is shown with a red broken line. **(B)** Current-voltage relationship for the channel. The single-channel conductance is 118.9±9.5 pS (mean±SEM, n=4). The K^+ E_{rev} is shown by means of a vertical red line and the channel E_{rev} by a vertical black line. Values are of the mean ±SD, n=4.

5.2.2 SR ion channels in *Tric-a* KO tissue

Our collaborator, Hiroshi Takashema, produced *Tric-a* KO [85], *tric-b* KO [83] and DKO [81] mice. Only the *Tric-a* KO mice survived to adulthood and therefore the hearts and skeletal muscle from these animals was used for single-channel experiments. The SR ion channels in the *Tric-a* KO tissue were studied and compared with those from WT mice.

5.2.3 SR K^+ channels from *Tric-a* KO tissue

In initial studies we only used experiments where single-channels had incorporated into the bilayer because the sub-conductance state of SR K^+ channels made the study of multiple channels difficult. Current-fluctuations through SR K^+ channels from WT and *Tric-a* KO mice are shown in Figure 5.2 (mouse skeletal) and Figure 5.3 (mouse cardiac). A visual comparison of the recordings suggests that no obvious difference exists in the typical gating pattern of SR K^+ channels is similar in both WT and *Tric-a* KO muscle. Figure 5.4 compares the single-channel properties of SR K^+ channels from WT and *Tric-a* KO skeletal and cardiac muscle. The single-channel conductance and voltage sensitivity of SR K^+ channels from WT and *Tric-a* KO mice are similar in both skeletal and cardiac muscle. The total Po of SR K^+ channels at +30 mV was significantly lower in *Tric-a* KO skeletal muscle when compared with WT however. More detailed analysis was therefore carried out to compare the single-channel gating of SR K^+ channels from WT and *Tric-a* KO mouse muscle tissue. Due to the small number of

experiments available with mouse cardiac tissue, this analysis was carried out using SR K^+ channels from mouse skeletal muscle only.

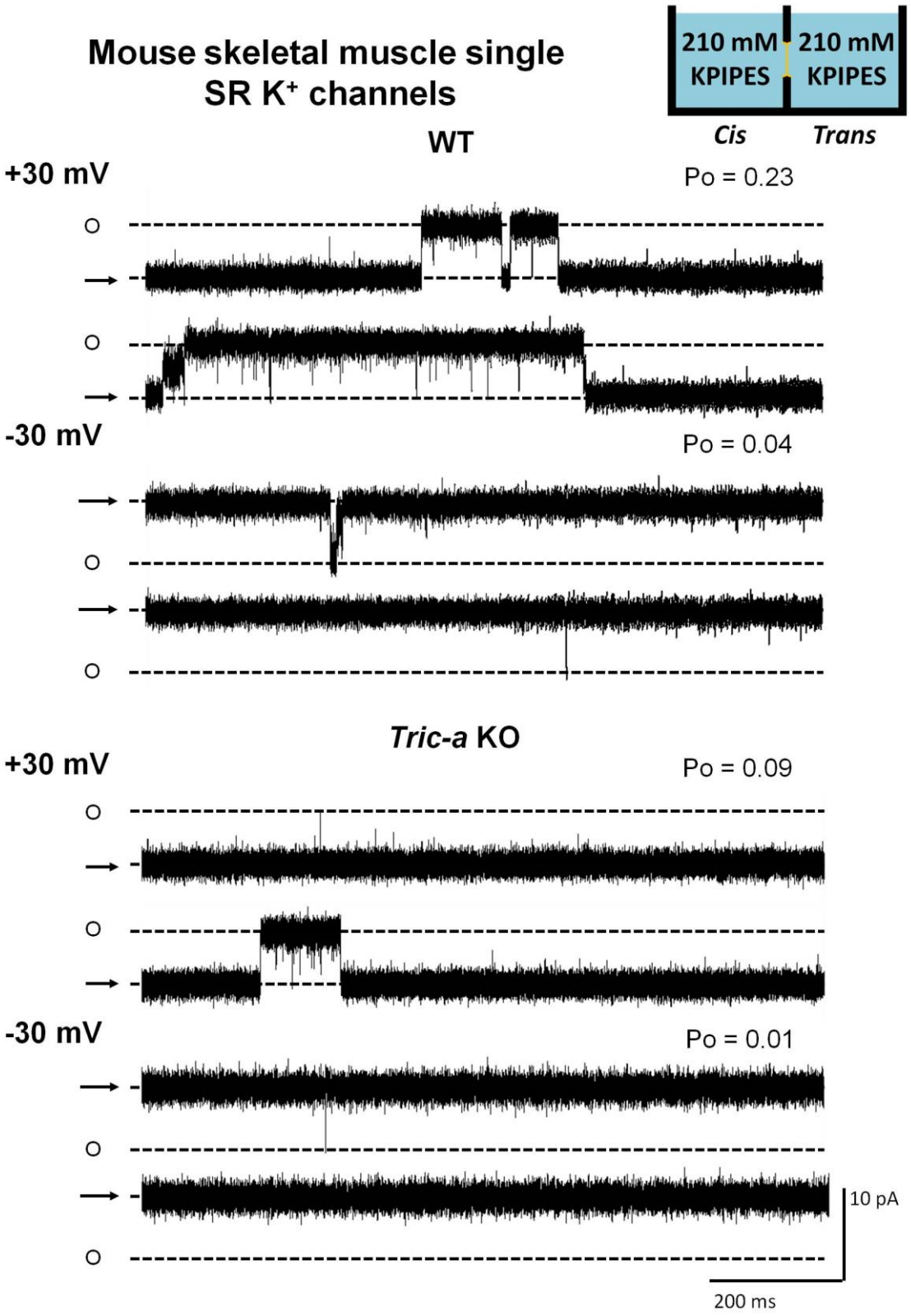

Mouse skeletal muscle single SR K+ channels
210 mM KPIPES
210 mM KPIPES
Cis
Trans
WT
+30 mV
Po = 0.23
-30 mV
Po = 0.04
Tric-a KO
+30 mV
Po = 0.09
-30 mV
Po = 0.01
10 pA
200 ms

Figure 5.2. Current-fluctuations through SR K^+ channels from WT and *Tric-a* KO mouse skeletal muscle

Representative single-channel recordings showing current-fluctuations through mouse skeletal SR K^+ channels from WT (top traces) and *Tric-a* KO (bottom traces) mice at holding potentials of ±30 mV. The channels were recorded in symmetrical 210 mM K^+, 10 µM Ca^{2+}, buffered to pH 7.2 with PIPES and are representative of 19 (WT) and 23 (*Tric-a* KO) experiments. The fully open level is shown by O and the closed level by an arrow.

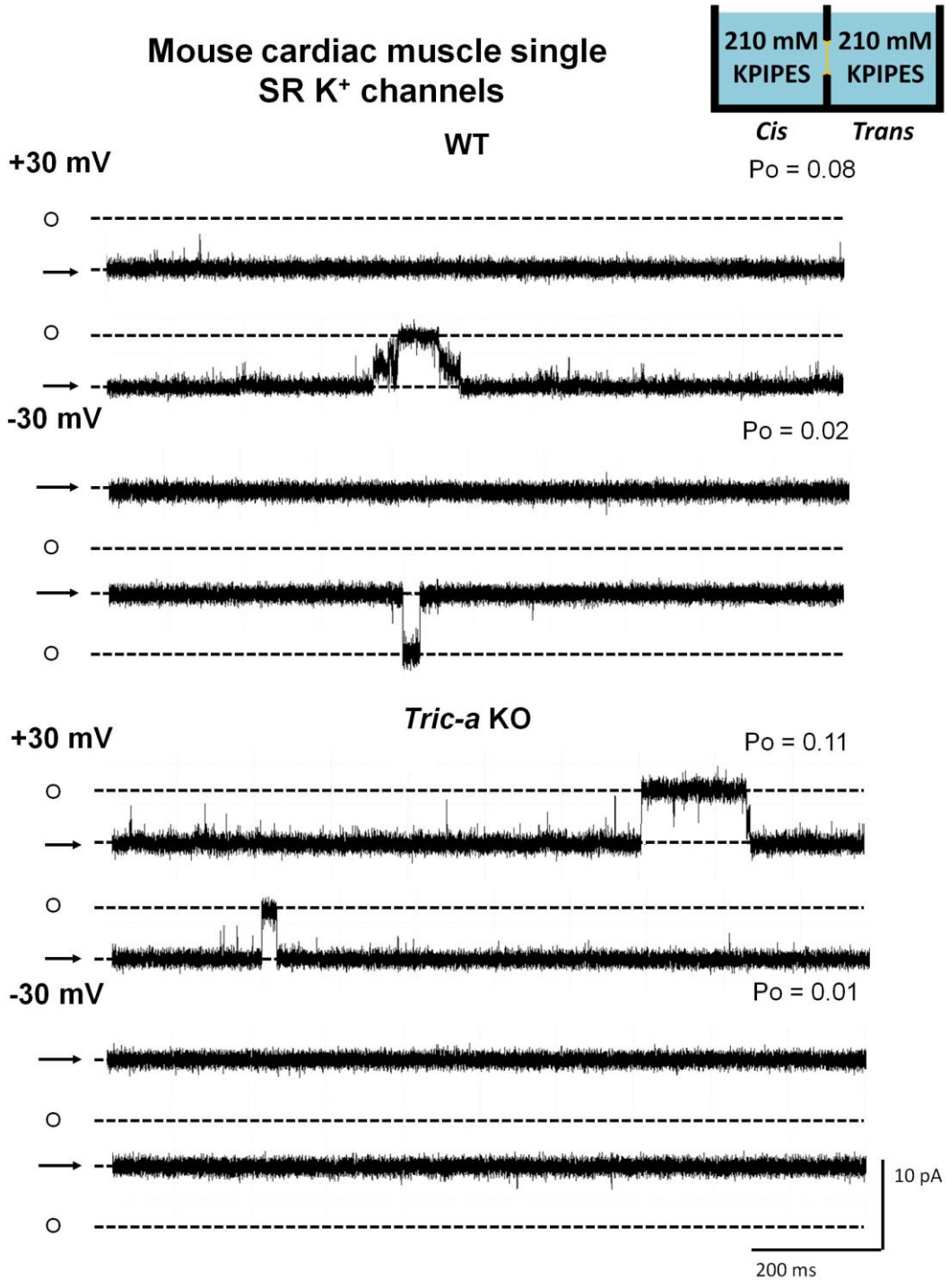
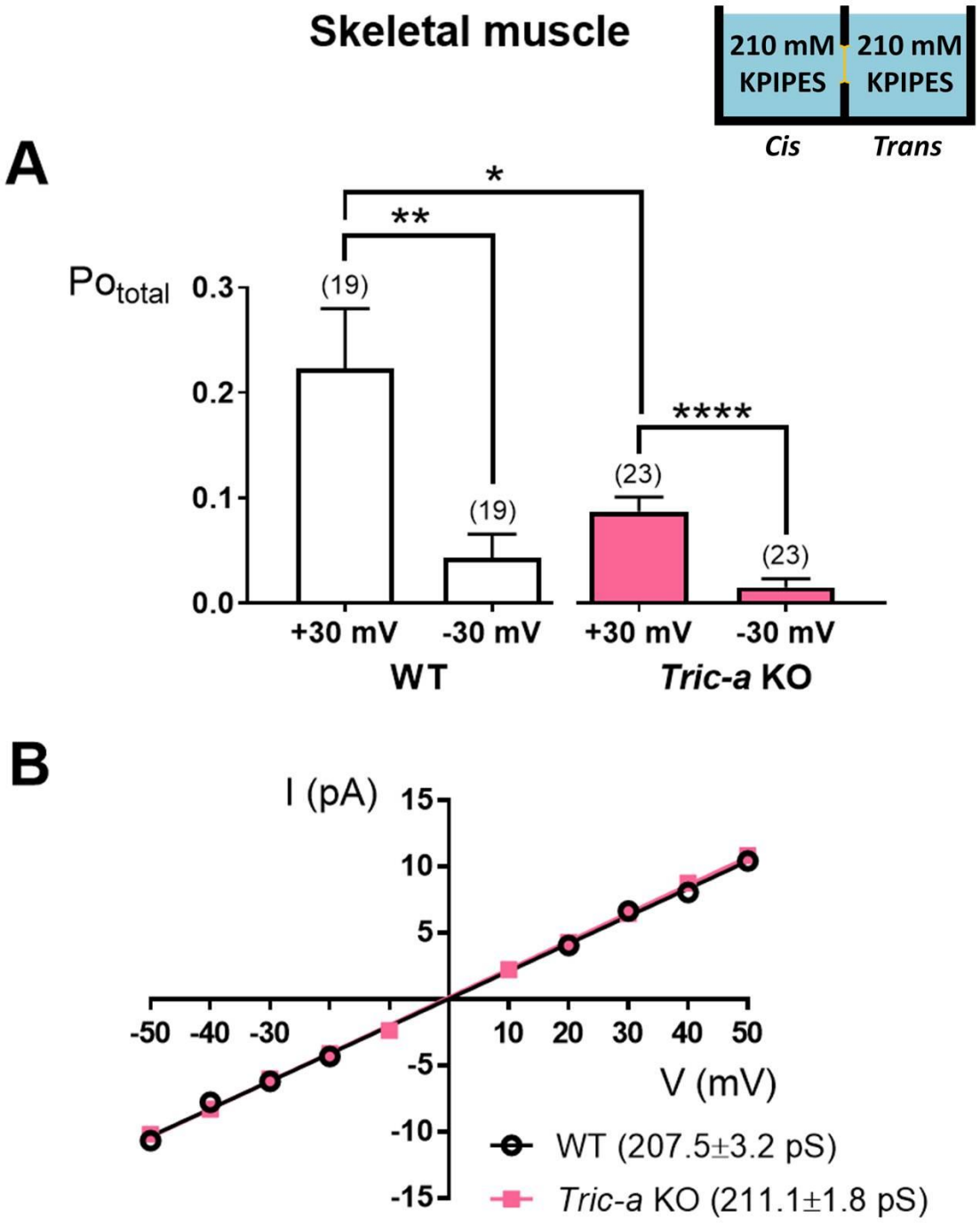


Figure 5.3. Current-fluctuations through SR K^+ channels from WT and *Tric-a* KO mouse cardiac muscle

Representative single-channel recordings showing current-fluctuations through mouse cardiac SR K^+ channels from WT (top traces) and *Tric-a* KO (bottom traces) mice at holding potentials of ±30 mV. The channels were recorded in symmetrical 210 mM K^+, 10 µM Ca^{2+}, buffered to pH 7.2 with PIPES and are representative of 6 (WT) and 4 (*Tric-a* KO) experiments. The fully open channel level is shown by O and the closed levels by an arrow.


Skeletal muscle
210 mM KPIPES
210 mM KPIPES
Cis
Trans
A
*
**
****
Po total
0.3
0.2
0.1
0.0
(19)
(19)
(23)
(23)
+30 mV
-30 mV
+30 mV
-30 mV
WT
Tric-a KO
B
I (pA)
15
10
5
-5
-10
-15
-50 -40 -30
10 20 30 40 50
V (mV)
WT (207.5±3.2 pS)
Tric-a KO (211.1±1.8 pS)

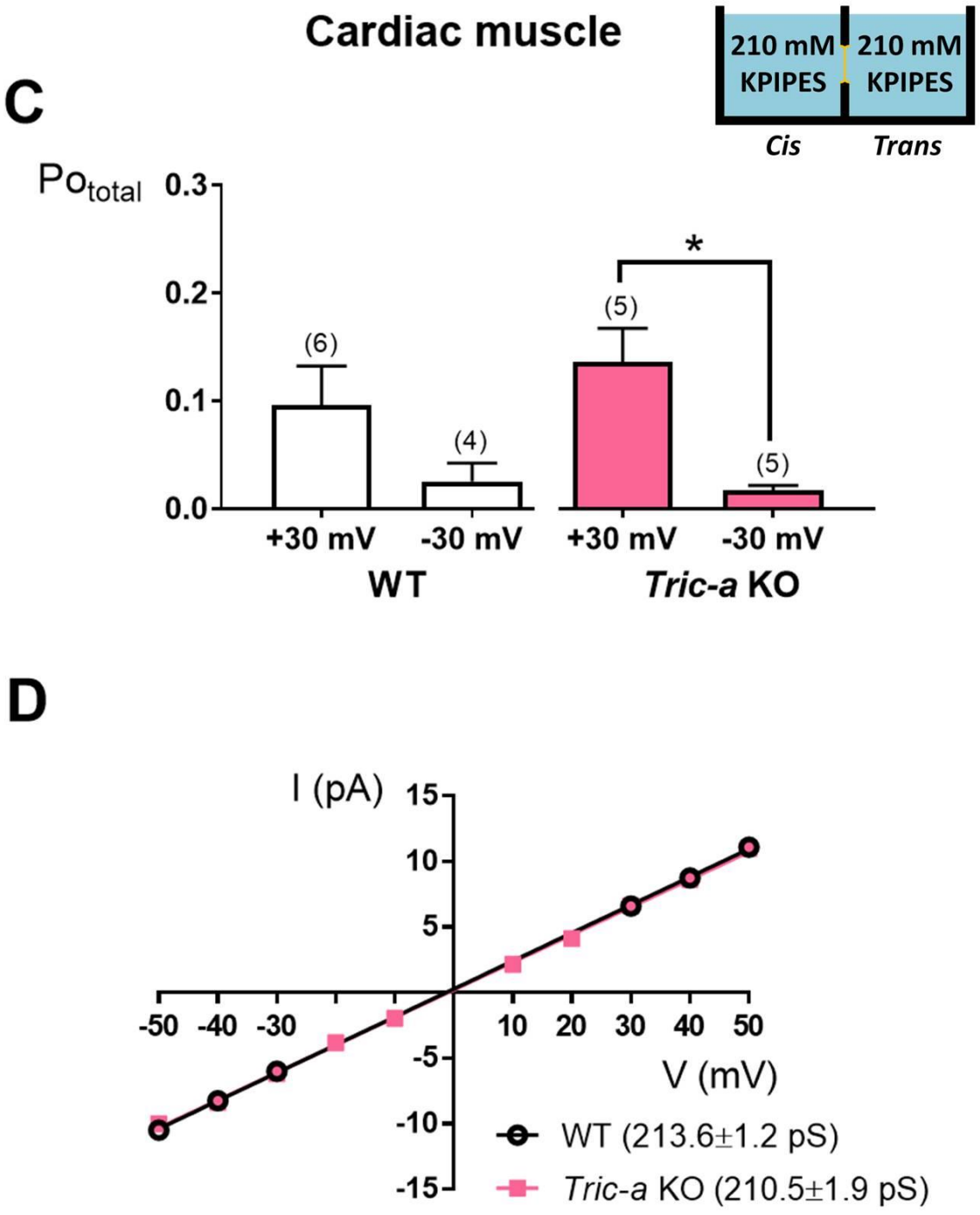


Figure 5.4. Single-channel properties of SR K^+ channels from WT and *Tric-a* KO mouse skeletal and cardiac muscle

(A, C) The Po of SR K^+ channels from WT (white) and *Tric-a* KO (pink) mouse skeletal muscle **(A)** and cardiac muscle **(C)** at ±30 mV. Values are of the mean±SEM. Experiment numbers are shown in brackets above the respective bar. **(B, D)** Current-voltage relationship for SR K^+ channels from WT (black circles) and *Tric-a* KO (pink squares) mouse skeletal muscle **(B)** and cardiac muscle **(D)** Values are of the mean±SEM. Where not shown, error bars are within the symbols. The single-channel conductance values±SEM are shown in the figure legends.

More detailed analysis of the single-channel events of SR K^+ channels from WT and *Tric-a* KO tissue was therefore conducted to try to find a mechanism for the lower Po observed in SR K^+ channels from *Tric-a* KO mice. Figure 5.5 demonstrates that that the Po difference between WT and *Tric-a* KO channels at +30 mV was due to a lower Po of the fully open state (Figure 5.5E) and less of the channel open time spent in the fully open level at both +30 mV (Figure 5.5G) and at -30 mV (Figure 5.5H). The Po of the sub-conductance level remained unchanged however (Figure 5.5C and D).

Figure 5.6 shows representative single-channel openings of SR K^+ channels from WT and *Tric*-a KO mouse skeletal muscle. SR K^+ channels from *Tric-a* KO tissue was observed to gate with shorter opening bursts which contain more events to the sub-conductance level when compared with the opening of SR K^+ channels from WT tissue. This visual comparison is supported by the data in Figure 5.7. SR K^+ channels from *Tric*-a KO mice gate with a greater frequency of events, especially to the sub-conductance state compared with channels from WT tissue (Figure 5.7A, B and C). The channel from *Tric-a* KO tissue was also observed to dwell for shorter durations in both the fully open and sub-conductance levels (Figure 5.7E and F).

Figure 5.8 demonstrates the spread of Po_{total} data from recordings of SR K^+ channels from WT and *Tric-a* KO mice. SR K^+ channels from WT mouse tissue exhibited a number of high-Po channels which are not observed in *Tric-a* KO mouse tissue.

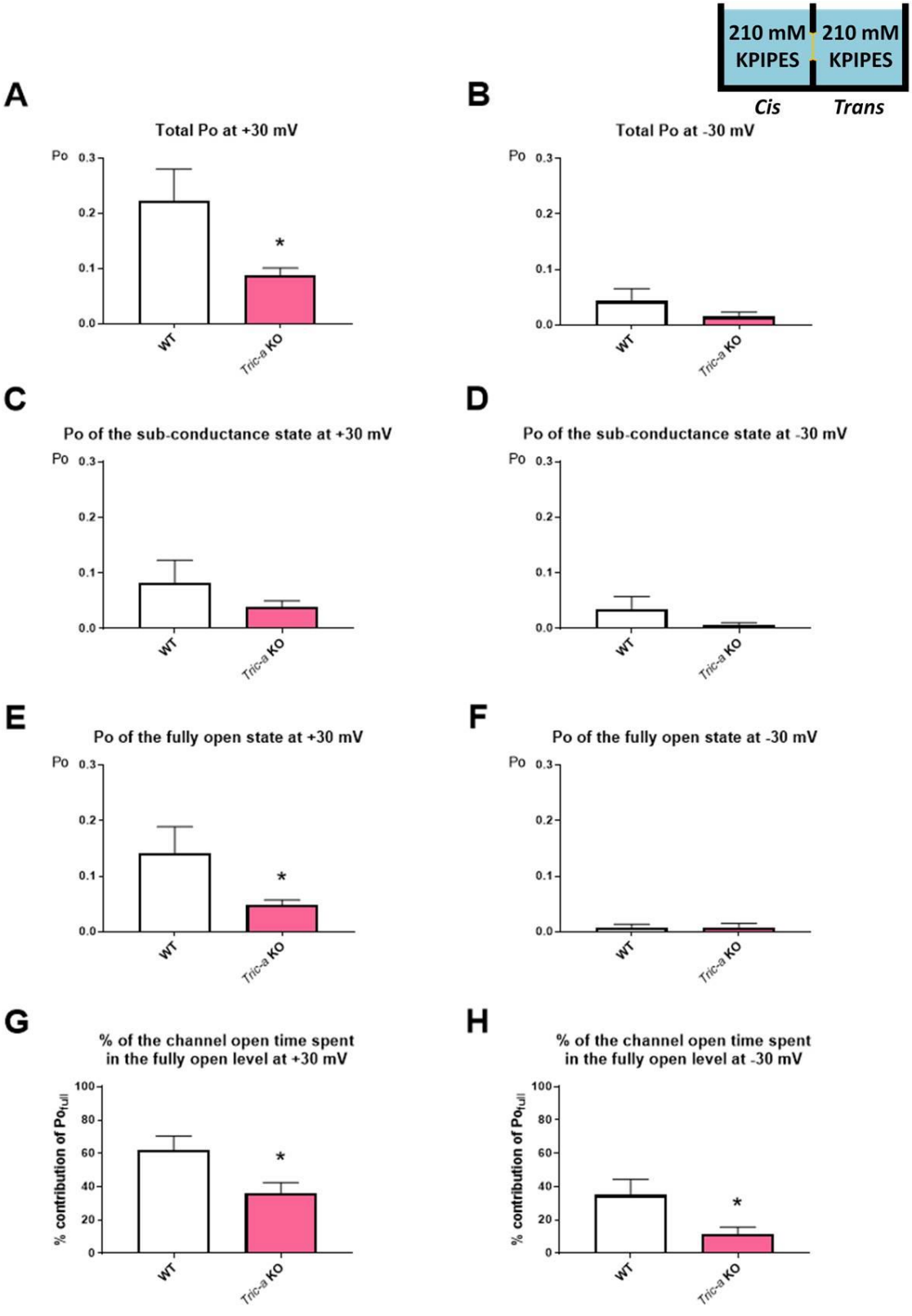

210 mM KPIPES
210 mM KPIPES
Cis
Trans
A
Total Po at +30 mV
Po
0.3
0.2
0.1
0.0
*
WT
Tric-a KO
B
Total Po at -30 mV
Po
0.3
0.2
0.1
0.0
WT
Tric-a KO
C
Po of the sub-conductance state at +30 mV
Po
0.3
0.2
0.1
0.0
WT
Tric-a KO
D
Po of the sub-conductance state at -30 mV
Po
0.3
0.2
0.1
0.0
WT
Tric-a KO
E
Po of the fully open state at +30 mV
Po
0.3
0.2
0.1
0.0
*
WT
Tric-a KO
F
Po of the fully open state at -30 mV
Po
0.3
0.2
0.1
0.0
WT
Tric-a KO
G
% of the channel open time spent in the fully open level at +30 mV
% contribution of Po full
100
80
60
40
20
0
*
WT
Tric-a KO
H
% of the channel open time spent in the fully open level at -30 mV
% contribution of Po full
100
80
60
40
20
0
*
WT
Tric-a KO

Figure 5.5. A comparison of the single-channel properties of the SR K^+ channel from WT and *Tric-a* KO mouse skeletal muscle

WT data is shown in white (n=19) and *Tric-a* KO data is shown in pink (n=23) **(A, B)** The total Po of the SR K^+ channel at +30 mV **(A)** and at -30 mV **(B)**. **(C, D)** The Po of the sub-conductance state of the SR K^+ channel at +30 mV **(C)** and at -30 mV **(D)**. **(E, F)** The Po of the fully open channel level of the SR K^+ channel at +30 mV **(E)** and at -30 mV **(F)**. **(G, H)** The % of channel open time spent in the fully open level at +30 mV **(G)** and at -30 mV **(H)**. Values are of the mean±SEM.

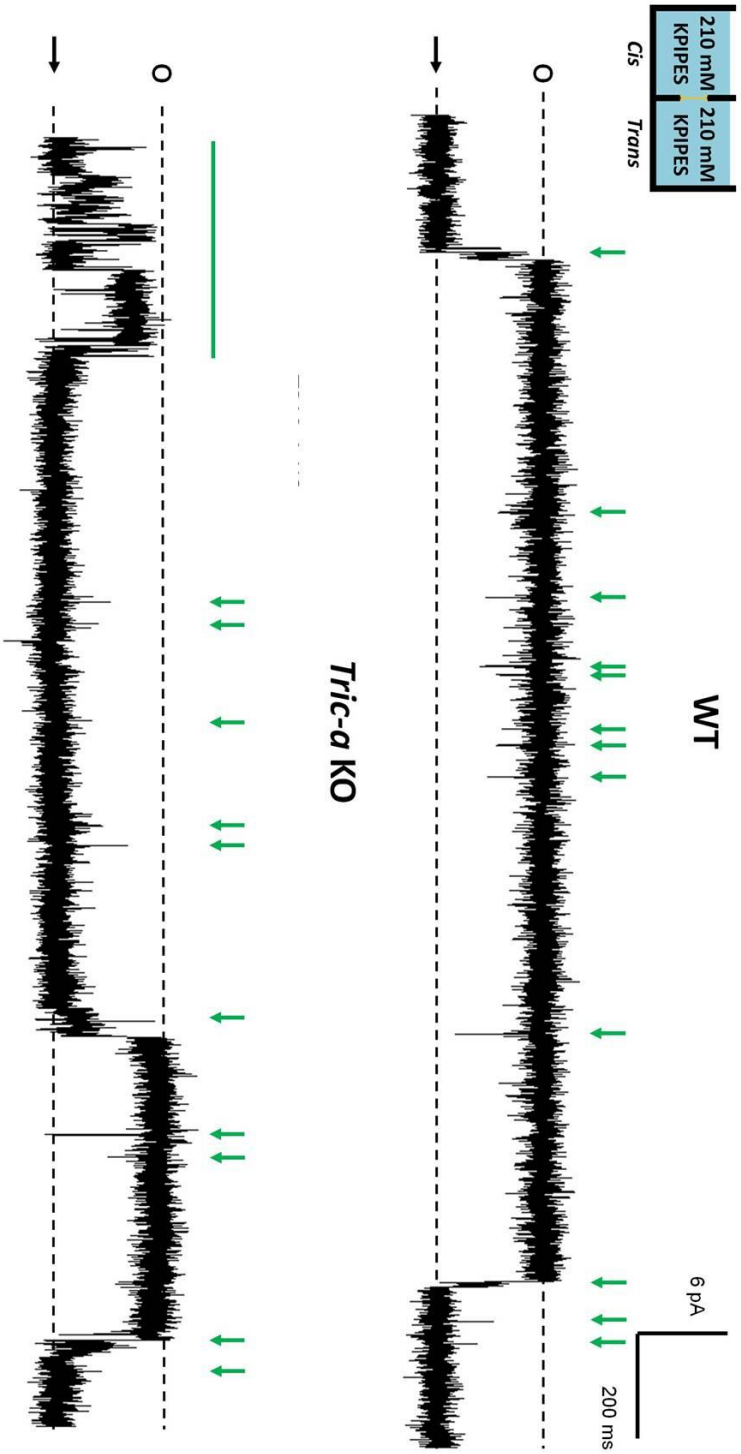


Figure 5.6. Examples of current-fluctuations through SR K^+ channels from WT and *Tric-a* KO mouse skeletal muscle

The zero current level is shown by an arrow and the channel fully open level by an O. Gating to the sub-conductance level is shown by green arrows.

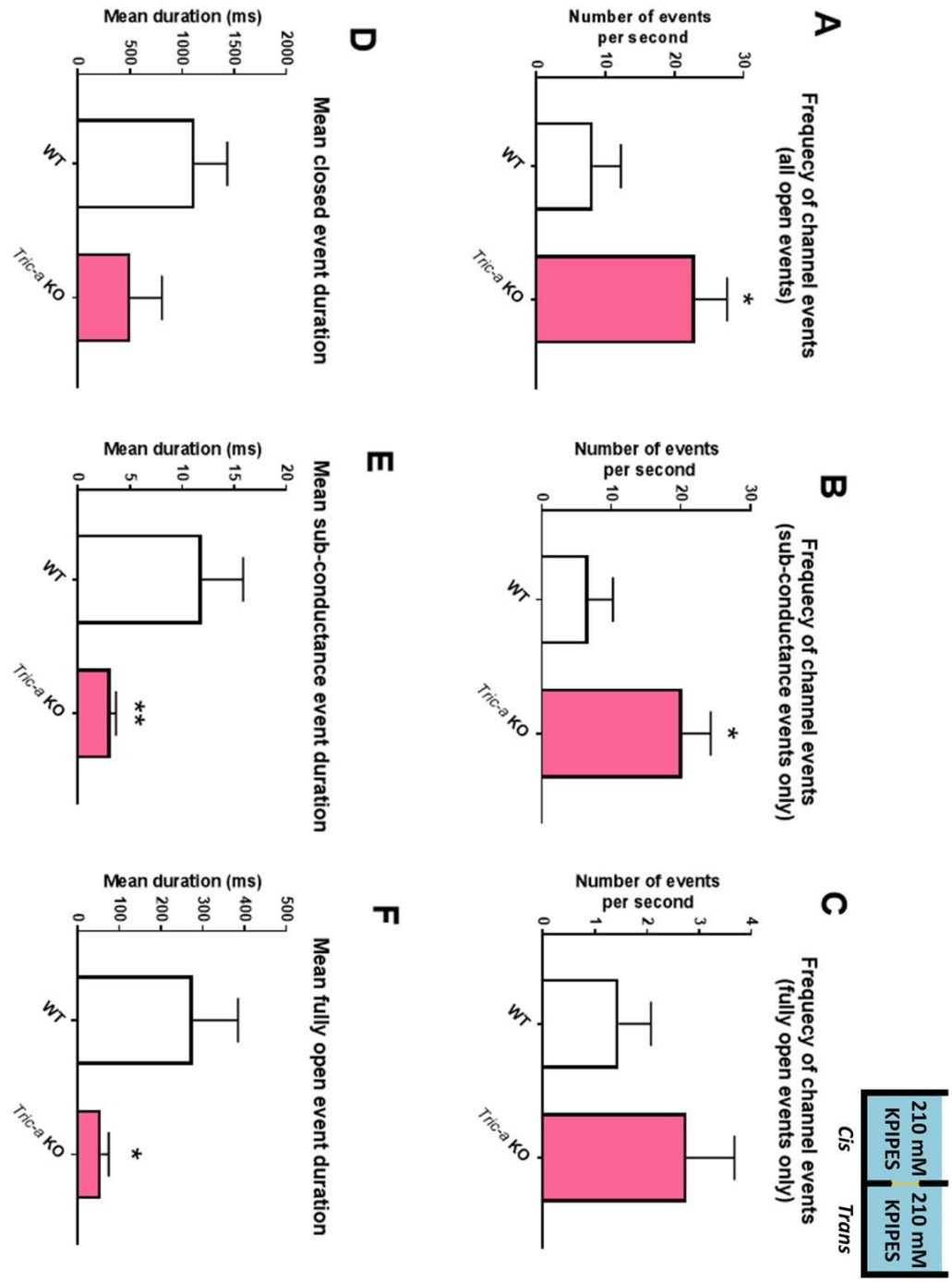


Figure 5.7. Event analysis of SR K^+ channels from WT and *Tric-a* KO mouse skeletal muscle
WT data is shown in white (n=19) and *Tric-a* KO data is shown in pink (n=23). Data was recorded at +30 mV. **(A)** The frequency of all channel events. **(B)** The frequency of channel events to the sub-conductance level. **(C)** The frequency of channel events to the fully open channel level. **(D, E, F)** the mean event duration for closed events **(D)**, sub-conductance events **(E)** and fully open events **(F)**. Values are the mean±SEM.

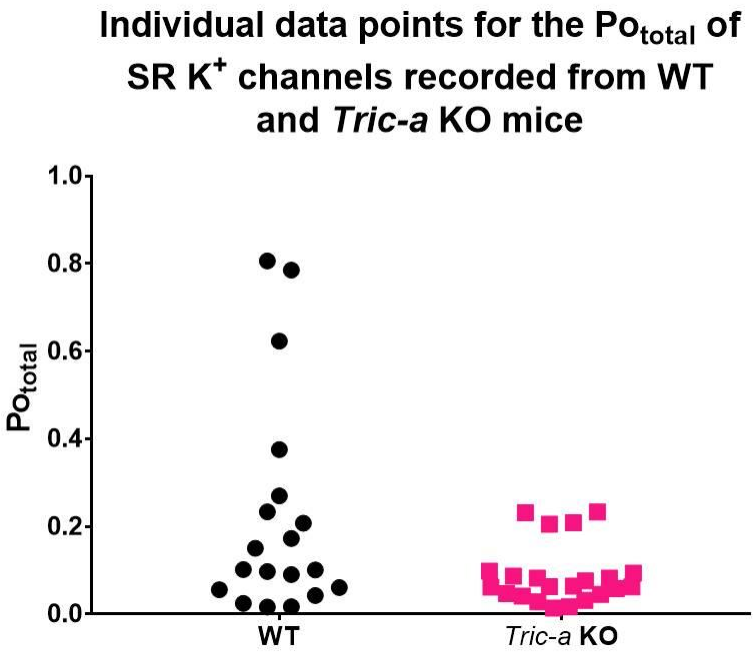


Figure 5.8. The spread of data for the Po_{total} of SR K^+ channels from WT and *Tric-a* KO mice
Individual data points for the Po_{total} of single SR K^+ channels recorded from WT (black) and *Tric-a* KO (pink) mice.

5.2.3.1 Studying the gating of multiple SR K^+ channels gating in bilayers

Often SR incorporations with the bilayer contained multiple ion channels as shown in Figure 5.9. SR K^+ channels from *Tric-a* KO skeletal muscle, studied when multiple channels were gating in the bilayer, were found to have a significantly higher Po than multiple SR K^+ channels from WT tissue (Figure 5.10). The Po values of SR K^+ channels from WT and *Tric-a* KO tissue, where two or three channels were gating in the bilayer, were therefore compared. In WT tissue, Po of the SR K^+ channel was found to be consistent regardless of the number of channels observed in the bilayer (Figure 5.11A). Conversely, in *Tric-a* KO tissue, the average Po of SR K^+ channels was found to become significantly larger with increasing numbers of channels (Figure

5.11B). This could be an indication that SR K^+ channels may be gating in a cooperative manner in *Tric-a* KO tissue, but not in WT tissue.

Binomial analyse can be used to ascertain whether channels gate cooperatively in the bilayer; such an approach was suggested by Patlak and Horn in 1982 [196]. The analysis rests on binomial theory for independent statistical events. As Po is a probability measurement, this can be applied to ion channel gating. In a patch containing N number of channels, all of which are gating independently, the Po of channel n can be predicted by the following equation.

$$P_{(n\ channels\ opening)} = \binom{N}{n} Po^n (1 - Po)^{N-n}$$

Equation 21

Where N is the total number of channels in the bilayer, n the number of channels gating (e.g. 2, if finding the probability of 2 channels gating out of a total of 4), and Po is the probability measured for a single-channel gating alone in the bilayer (i.e. the Po_{total} from single-channel recordings).The predicted Po for each channel gating in the bilayer when multiple channels are observed can therefore be calculated.

Shown in white in Figure 5.12 are the predicted Po values for SR K^+ channels from WT and *Tric-a* KO tissue when three channels were observed gating in the bilayer, assuming that each channel is gating independently. Plotted in blue next to each predicted value is the actual Po_{total} value for each channel. The Po of SR K^+ channels from WT tissue were observed to follow the binomial prediction more closely than those from *Tric-a* KO tissue, suggesting that channels from WT gate independently, where as those from *Tric-a* KO do not. This was further illustrated by Figure 5.13 which compares the ratio of the predicted/experimental values between channels from WT and *Tric-a* KO tissue. The closer the predicted/experimental value

is to 1, the more likely the Po values are to follow a binomial statistical pattern of independent gating. Following this logic, it is clear from Figure 5.13 that SR K^+ channels from *Tric-a* KO tissue do not follow a binomial statistical prediction for independent channel gating and thus it is likely that SR K^+ channels in *Tric-a* KO tissue gate in a cooperative manner. This seems not to be the case for SR K^+ channels from WT tissue.

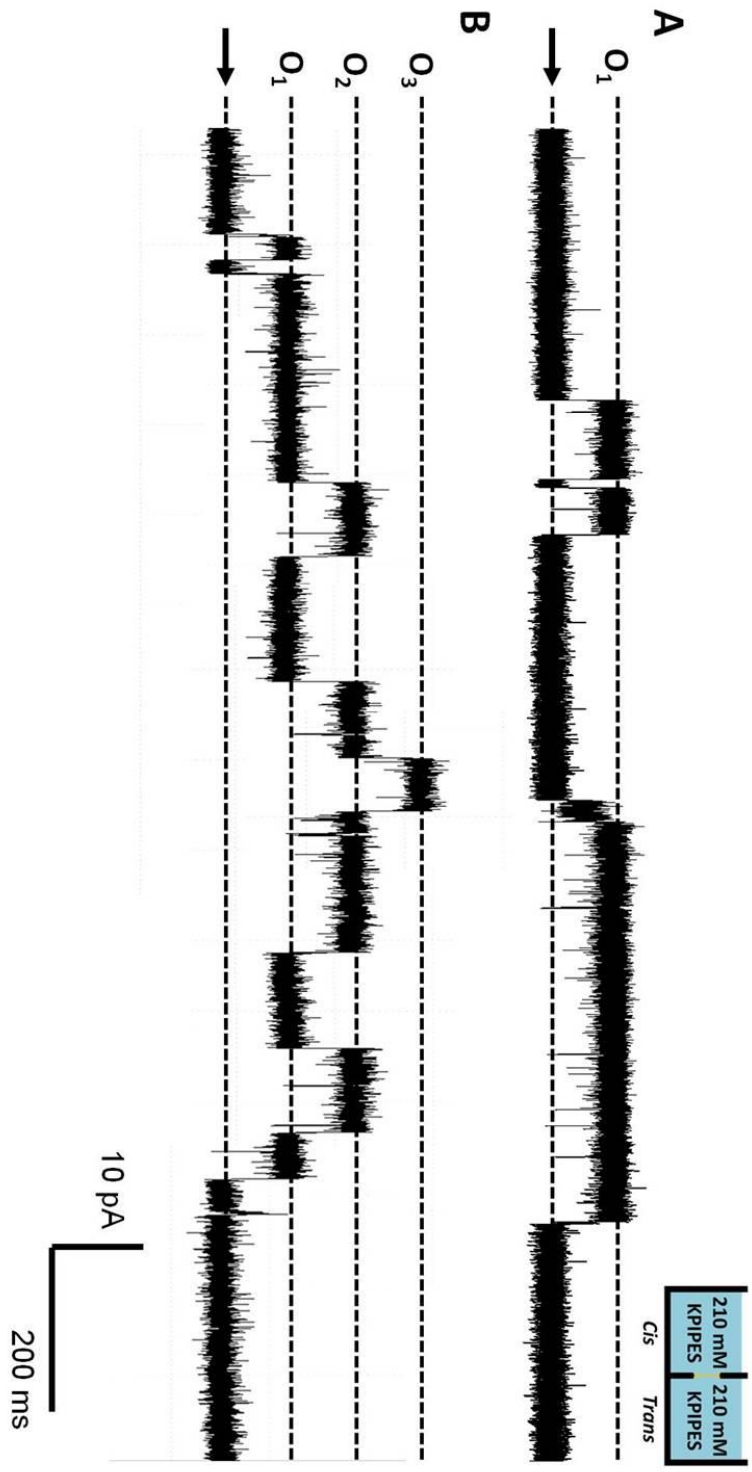


Figure 5.9. Representative channel recordings showing a single SR K^+ channel gating in the bilayer (A) and multiple channels gating in the bilayer (B)

The closed channel level is shown by an arrow and the fully open level of each channel with O_{1-3}

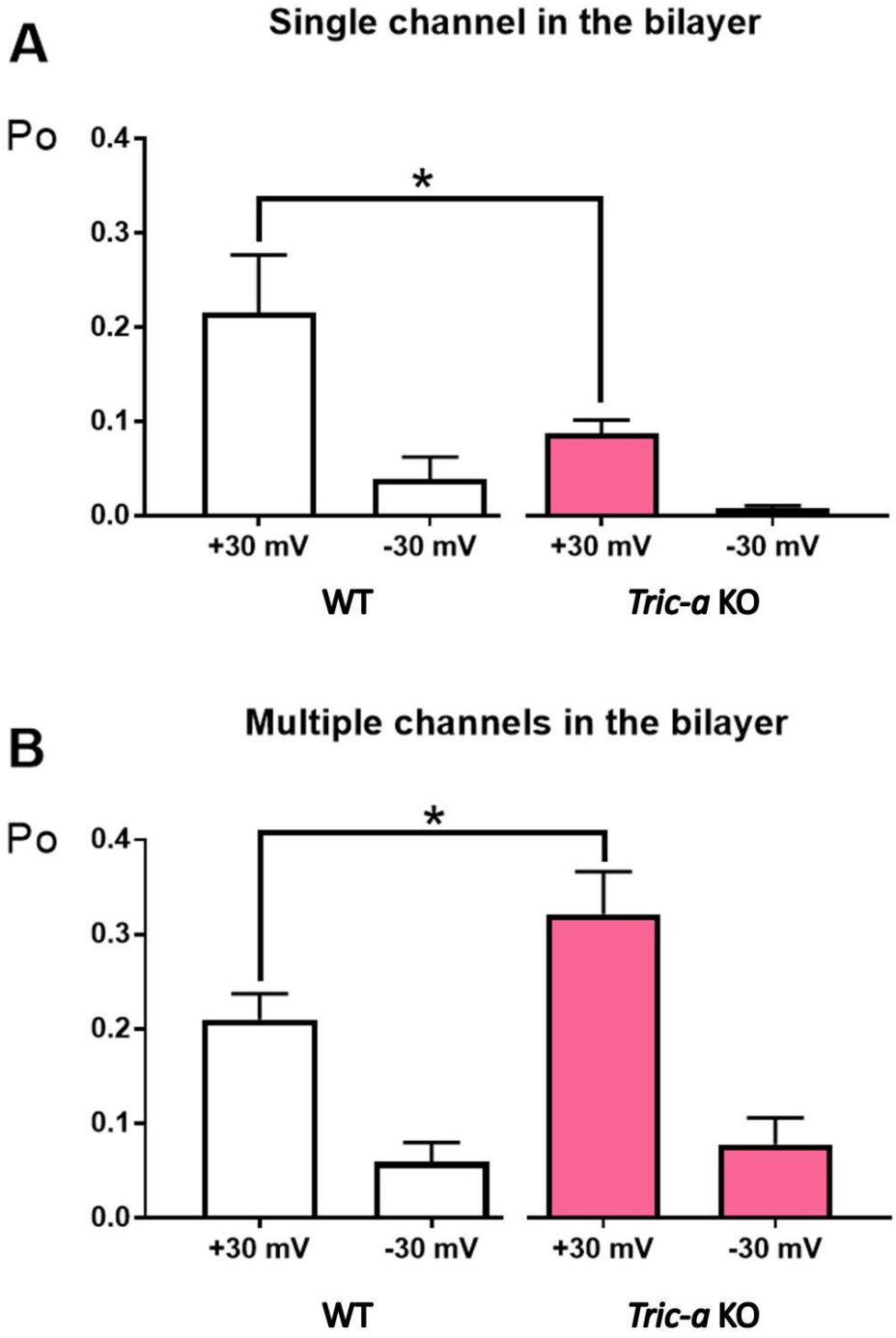


Figure 5.10. The Po of single and multiple SR K^+ channels from WT and *Tric-a* KO skeletal muscle

(A) The Po of single SR K^+ channel experiments at ±30 mV from WT (white, n=19) and *Tric-a* KO tissue (pink, n=23). **(B)** The Po of the SR K^+ channel when >1 channels are gating in the bilayer at ±30 mV from WT (white, n=39) and *Tric-a* KO tissue (pink, n=23). Values are the mean±SEM.

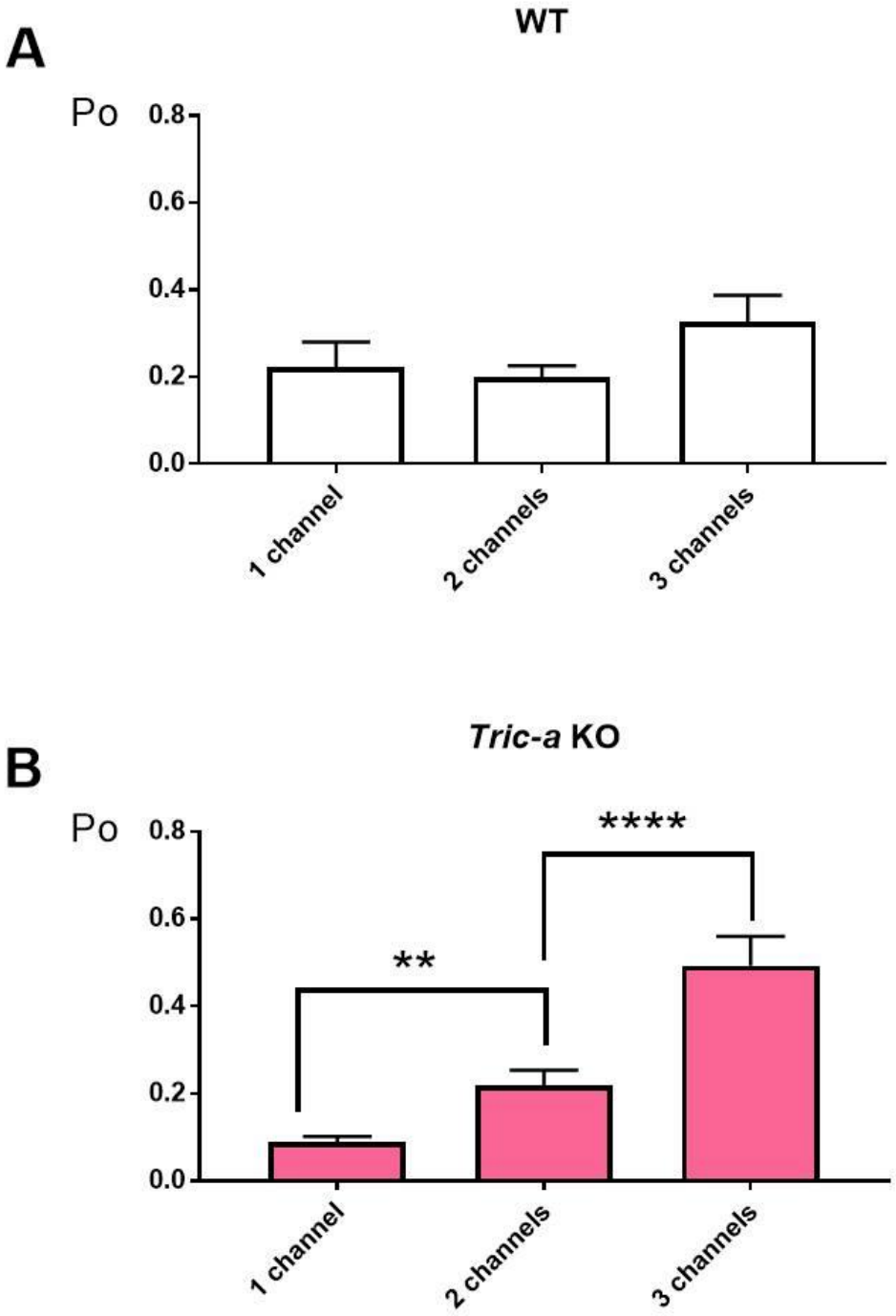


Figure 5.11. The Po of SR K^+ channels as a function of the number of channels gating in the bilayer

(A) The Po of WT SR K^+ channels when 1 channel (n=19), 2 channels (n=31) or 3 channels (n=8) were gating in the bilayer. **(B)** The Po of SR K^+ channels from *Tric-a* KO tissue when 1 channel (n=23), 2 channels (n=17) or 3 channels (n=6) were gating in the bilayer. Data was recorded at +30 mV. Values are the mean±SEM.

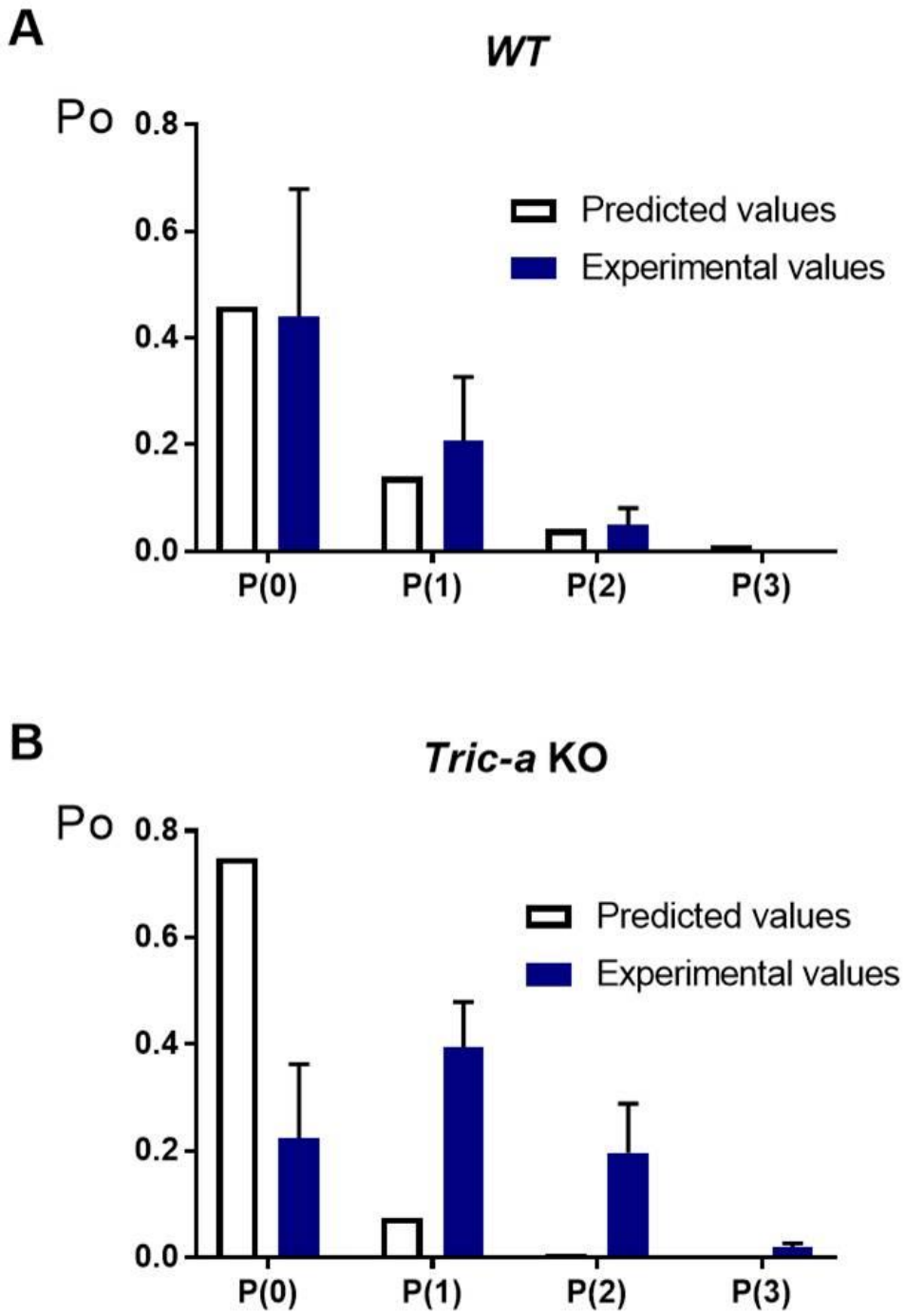


Figure 5.12. The binomial statistical prediction for three SR K^+ channels gating in the bilayer **(A)** WT, n=5. **(B)** *Tric-a* KO, n=4. The white bars show the binomial statistical prediction of the Po of the closed channel level (P(0)) and of each open channel level (P(1), P(2), P(3)) if three SR K^+ channels are gating together in the bilayer at +30 mV. Predicted values were calculated using the Po from single SR K^+ channel experiments (WT = 0.23, *Tric-a* KO = 0.09). Blue bars represent the equivalent experimental data. Values are of the mean±SEM.

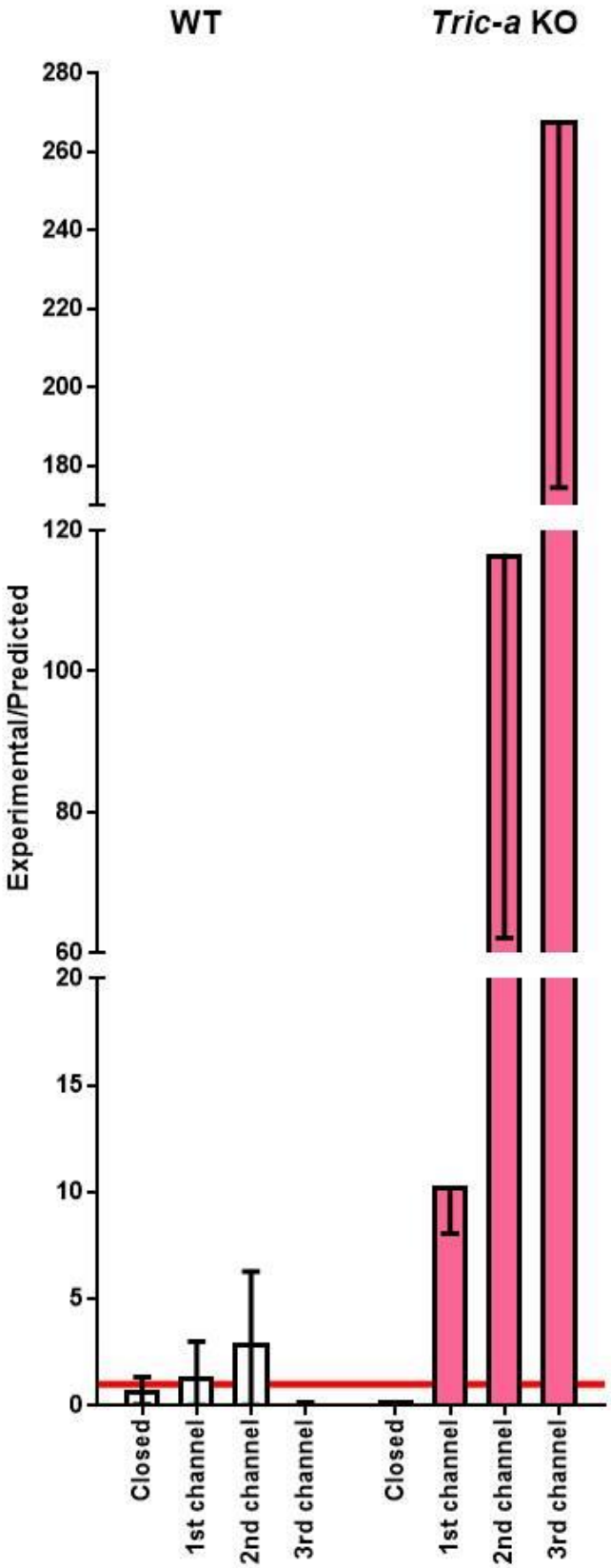

WT
Tric-a KO
Experimental/Predicted
280
260
240
220
200
180
120
100
80
60
20
15
10
5
0
Closed
1st channel
2nd channel
3rd channel
Closed
1st channel
2nd channel
3rd channel

Figure 5.13. A comparison of experimental data to the binomial statistical prediction
The ratio of experimental Po to the Po predicted through the binomial equation is plotted for SR K^+ channel experiments from WT (white bars) and *Tric-a* KO (pink bars) where three channels are gating together in the bilayer at +30 mV. The red line represents the point where Experimental/predicted Po values are equal to one and thus follows a binomial distribution.

5.2.4 The RyR1 channel in *Tric-a* KO tissue

We recently published a paper describing differences in RyR1 channel properties in *Tric-a* KO tissue compared to that of WT [195]. The paper found no change in the activation of the RyR1 channels from *Tric-a* KO and WT tissue by activators such as caffeine or ATP. However, RyR1 channels were found to be significantly more sensitive to inhibition by Mg^{2+} in *Tric-a* KO tissue compared with WT tissue (Figure 5.14). It was also found that the channel was not activated by PKA (Figure 5.15), this was despite the channel phosphorylation being equal between WT and *Tric-a* KO tissue. It was concluded that TRIC-A functions as an excitatory modulator of RyR1 channels.

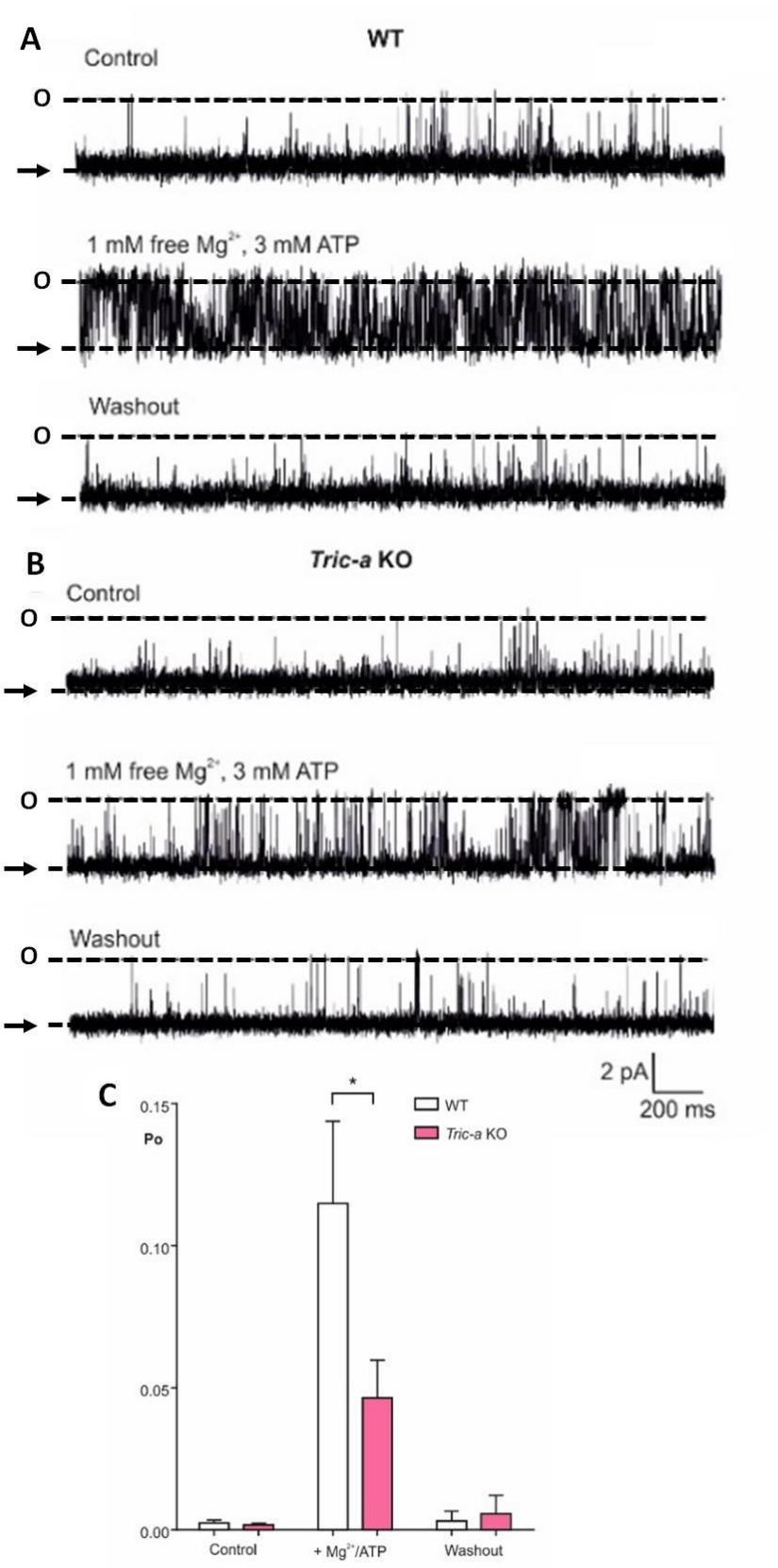

A
WT
Control
O
1 mM free Mg2+, 3 mM ATP
O
Washout
O
B
Tric-a KO
Control
O
1 mM free Mg2+, 3 mM ATP
O
Washout
O
2 pA
200 ms
C
*
WT
Tric-a KO
Po
0.15
0.10
0.05
0.00
Control
+ Mg2+/ATP
Washout

Figure 5.14. Mg^{2+} inhibition of RyR1 channels from WT and *Tric-a* KO tissue
(A, B) Representative RyR1 single-channel recordings obtained from WT **(A)** and *Tric-a* KO **(B)** mice under control conditions (top traces, 10 µM cytosolic Ca^{2+}), in the presence of 1 mM free Mg^{2+}/3 mM ATP/10 µM cytosolic Ca^{2+} (middle traces), and after washout of the Mg^{2+}/ATP, returning to control conditions (bottom traces). The holding potential was 0 mV. Closed channel levels are shown by an arrow and open channel levels by O. **(C)** Mean Po values for RyR1 derived from WT (white) and *Tric-a* KO mice (pink) under control conditions and in the presence of and after washout of Mg^{2+}/ATP (n = 14 for WT; n = 22 for KO). Values are the mean±SEM. This figure has been adapted from El-Ajouz *et al.* (2017) [197].

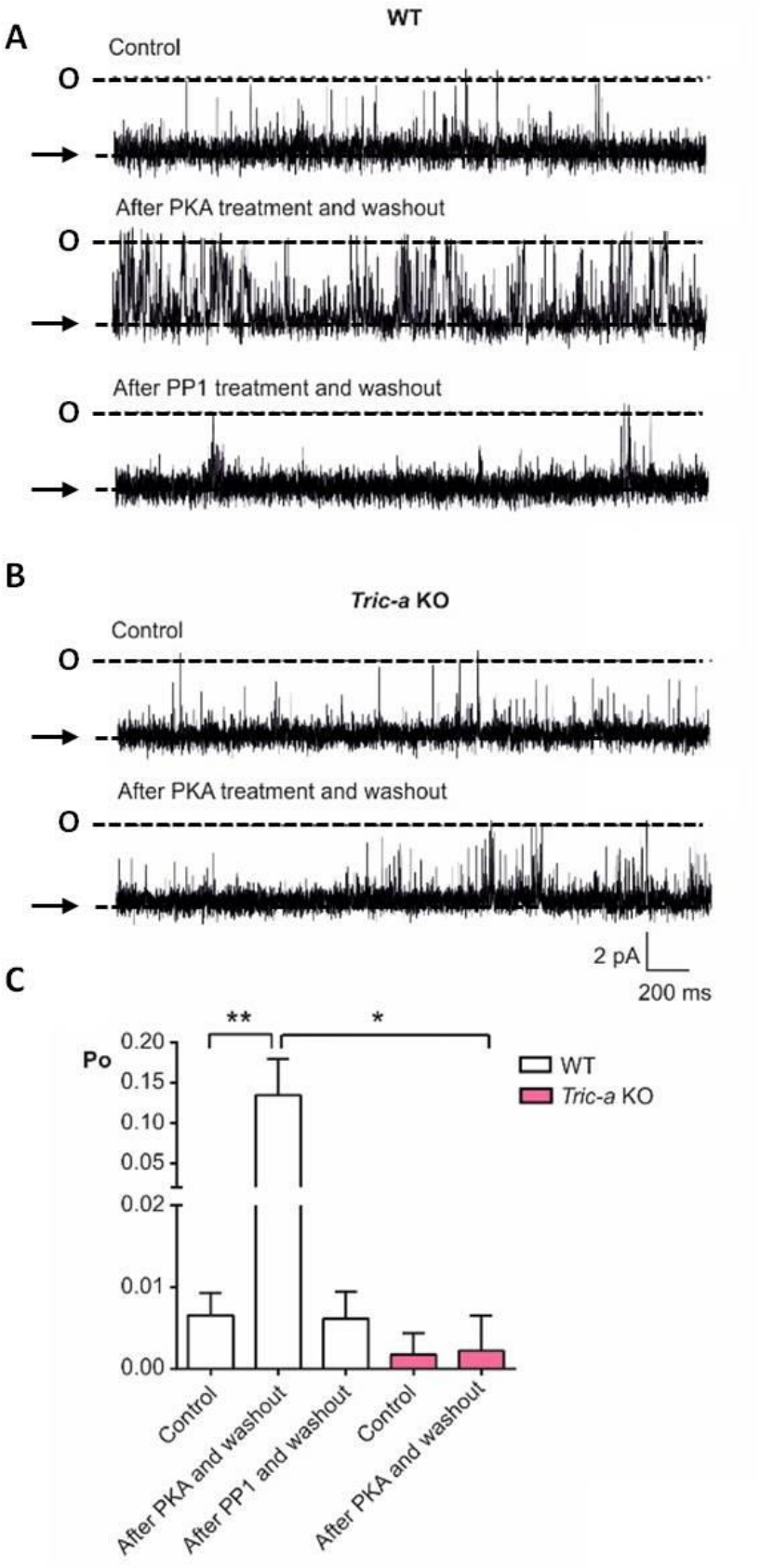

A
WT
Control
O
After PKA treatment and washout
O
After PP1 treatment and washout
O
B
Tric-a KO
Control
O
After PKA treatment and washout
O
2 pA
200 ms
C
**
*
Po
0.20
0.15
0.10
0.05
0.02
0.01
0.00
WT
Tric-a KO
Control
After PKA and washout
After PP1 and washout
Control
After PKA and washout

Figure 5.15. Effect of PKA-dependent phosphorylation on the Ca^{2+}-dependence of gating of RyR1 from WT and *Tric-a* KO mice
(A, B) RyR1 channel activity from WT **(A)** and *Tric-a* KO **(B)** mice in the presence of 10 µM cytosolic Ca^{2+} (Control, top traces), after washout of a 10 min treatment of 10 units of PKA, 3 mM ATP and 1 mM free Mg^{2+} (after PKA treatment and washout, second traces), and after washout of a 10 min treatment with 5 units of PP1 added to the cytosolic chamber in the buffer from New England Biolabs (after PP1 treatment and washout). Holding potential was 0 mV. The holding potential was 0 mV. Closed channel levels are shown by an arrow and open channel levels by O. **(C)** Mean Po of the RyR1 channels from WT (white) and *Tric-a* KO mice (pink) under control conditions (control), after washout of PKA (after PKA and washout) and after washout of PP1 (after PP1 and washout) (n = 10-15). Values are the mean±SEM. This figure has been adapted from El-Ajouz *et al.* (2017) [197].

5.2.5 +SR Cl^- currents *Tric-a* KO mice

To investigate if there were any gross changes in the behaviour or types of SR ion channels that could be observed after the knock-out of TRIC-A, I incorporated SR vesicles into bilayers and waited for the first fusion that had chloride channels present so that I could observe if there were any alteration to Cl^- channel function. In order to compare WT with *Tric-a* KO SR in an identical manner, I always perfused out the vesicles after the first incorporation of Cl^- channels irrespective of whether a cation channel had incorporated.

SRAL channels, as described in Chapter 4, were observed and studied in *Tric-a* KO mouse skeletal muscle. An example of SRAL channels recorded from *Tric-a* KO SR is shown in Figure 5.16. Figure 5.17A shows the average current, calculated by noise analysis, through SRAL channels from WT and *Tric-a* KO mouse skeletal muscle. There was no obvious change to the average current observed with a first fusion event with the bilayer, indicating that SRAL channel activity is unaffected by knocking-out TRIC-A. Figure 5.17B shows the permeability ratio of choline to Cl^- ($P_{choline}/P_{Cl}$) for all first Cl^- fusion events/SRAL channel currents from WT and *Tric-a* KO mouse skeletal SR K^+ channels. While there was no significant difference observed in the mean $P_{choline}/P_{Cl}$ values, Figure 5.17B shows that the permeability values for the *Tric-a* KO channels are clustered around a lower $P_{choline}/P_{Cl}$, indicating that overall, there could

be a loss in choline/cation current after the knockout of TRIC-A. This data also suggest that that TRIC-A contributes towards the SRAL channel current in WT tissue.

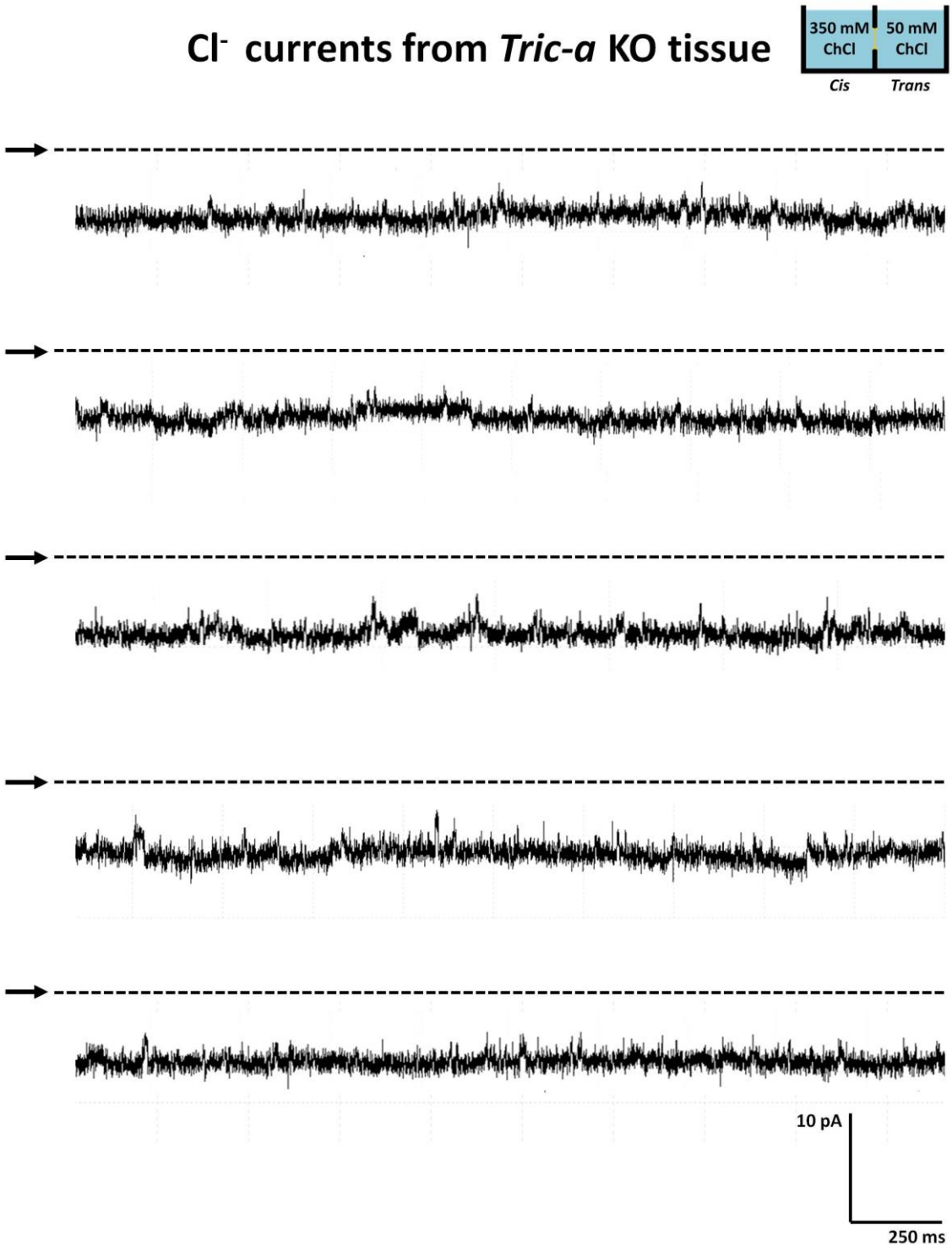


Figure 5.16 Representative recordings of SR Cl^-/SRAL channel currents observed in *Tric-a* KO tissue
Channel closed levels are shown by an arrow.

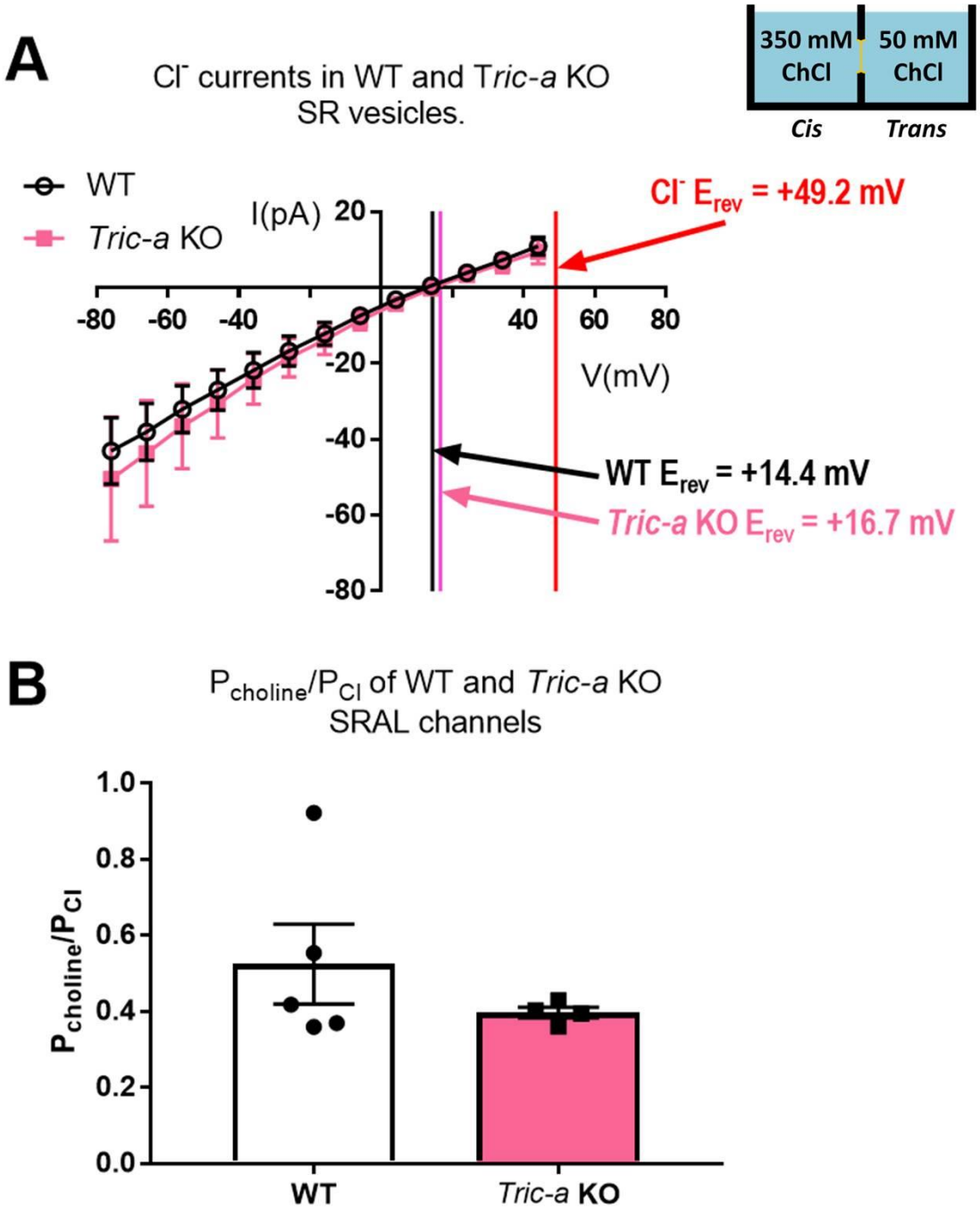


Figure 5.17. Permeability properties of SRAL channels from WT and *Tric-a* KO mouse skeletal muscle

(A) The current-voltage relationship for average currents through SRAL channels calculated by noise analysis from WT (black, n=6) and *Tric-a* KO (pink, n=4) mouse skeletal muscle. Experiments were conducted in asymmetrical solutions. The E_{rev} values for Cl^-, SRAL channels from WT tissue and SRAL channels from *Tric-a* KO tissue are shown by vertical lines on the graph. **(B)** The relative permeability of choline to Cl^- ($P_{choline}/P_{Cl}$) between WT and *Tric-a* KO tissue. Values are of the mean±SEM.

5.3 Discussion

The aim of this chapter was to use the bilayer technique to study TRIC-A from native membranes. Initial experiments used mixed membrane preparations from CHO cells over-expressing the human TRIC-A protein. No ion channels were observed in these preparations which shared exactly the same gating pattern as an SR K^+ channel. On 4 occasions however, I did observe particular types of current-fluctuations in the bilayers that were not observed after fusion of control CHO cell mixed membrane preparations. Analysis of the events suggested that these channels were ideally selective for K^+ over Cl^- and that they gated predominantly in high noise sub-conductance states. This was often at approximately 70% of what I would estimate for the full open channel level. As has been suggested and studied at length for SR K^+ channels [104], it is possible that the sub-conductance state is an artefact of rapid channel gating; this is discussed in more detail in the next chapter. The permeability properties of the channel and the existence of the noisy sub-conductance gating suggest that these channels could be equivalent to SR K^+ channels observed in lipid bilayers [105][104].

Although the apparent single-channel conductance of the potential TRIC-A channel observed in CHO cells was around 118 pS, the channel rarely opened to the fully open level and as such the apparent fully open channel level was found to be variable. It is possible that the actual single conductance value is more similar to that of native SR K^+ channels observed in the bilayer (210 pS, Chapter 3) [105][104] and that TRIC-A proteins are miss-folded or lack native auxiliary proteins or lipids which allow correct protein gating.

SR membrane preparations were also studied from *Tric-a* KO mice and compared with WT tissue. SR K^+ channels from *Tric-a* KO tissue exhibited a lower Po and the channels gated in shorter bursts with a larger number of sub-conductance events. TRIC-A and TRIC-B may be SR K^+ channels that possess very similar biophysical properties since both channel subtypes have

highly homologous amino acid sequences in the pore regions (Figure 5.18). In *Tric-a* KO tissue, only TRIC-B would be present. It is therefore possible that SR K^+ channels currents observed from *Tric-a* KO tissue are due to TRIC-B channels gating. If this is the case, then TRIC-B exhibits similar channel properties to TRIC-A (a similar permeability and gating pattern), but is a lower Po channel which gates with shorter channel bursts and spends less time in the fully open channel level. Evidence for this is demonstrated in Figure 5.8 where some SR K^+ channel experiments from WT mouse skeletal muscle exhibit high Po values whereas in *Tric-a* KO tissue, similar channels are not observed. It is possible that these high-Po channels are TRIC-A and that they are observed less often in the bilayer. It is unclear why this should be the case; however it is possible that TRIC-A channels require activation by a trigger such as a soluble ligand, phosphorylation or the binding of an accessory protein and so is usually silent in bilayer experiments.

A second theory could be that TRIC-A not only contributes to a counter-current by passing K^+ ions itself, but that it also stimulates other SR K^+ channels to gate. When TRIC-A is absent, as in *Tric-a* KO tissue, the remaining SR K^+ channels, such as TRIC-B, gate with a lower Po due to a lack of stimulation from TRIC-A proteins. If this is the case then it is possible that channel-channel interactions exist between TRIC-A and other SR K^+ channels.

Figure 5.18. Sequence alignment of mouse TRIC-A and TRIC-B showing sequence similarities
The amino acid sequences alignment of mouse TRIC-A (TM38A) and TRIC-B (TM38B) proteins. Sequence similarity is shown shaded in grey. The red shaded areas are the amino acids thought to form part of the *c. elegans* TRIC-B1 pore [112]. This figure was produced using the database and the online tools provided by Uniprot (http://www.uniprot.org/).

Another difference between SR K^+ channels from *Tric-a* KO tissue and those from WT is that SR K^+ channels from *Tric-a* KO tissue exhibit cooperative gating which is not observed in WT channels. It is possible that, in WT tissue, the high concentration of TRIC-A present in the SR membrane (there is around 5 times more TRIC-A than TRIC-B or RyR [85]) prevents the TRIC-B SR K^+ channels from interacting and gating cooperatively. Figure 5.19 demonstrates that in *Tric-a* KO tissue, other SR K^+ channels such as TRIC-B can associate and interact leading to cooperative gating. Membrane crowding has previously been described in the ER [198] and prokaryotic membranes [199]. A schematic of an example of SR membrane crowding is shown in Figure 5.20. This figure includes the MG23 protein which is discussed in Chapter 7 of this thesis.

The knockout of TRIC-A has also been shown to affect RyR function as described in a recent paper from the Sitsapesan laboratory where I am a contributing author [195]. RyR modulation was found to be altered in *Tric-a* KO mice as is also summarised in Figure 5.19. The findings of this paper are described in the results section of this chapter.

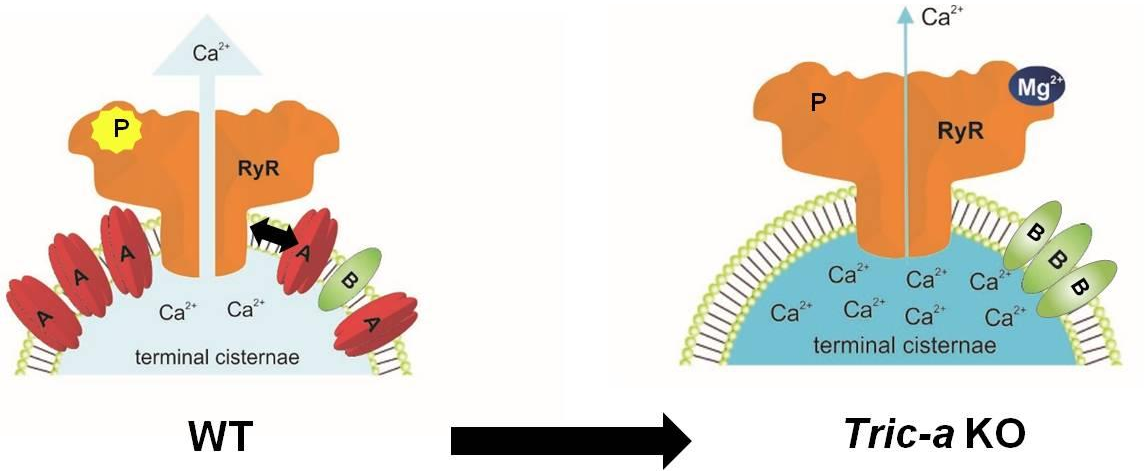


Figure 5.19. The SR membrane in WT and *Tric-a* KO tissue adapted from El-Ajouz *et al.* (2017)[197]

A schematic of the proposed channel-channel interactions in WT (left) and *Tric-a* KO (right) muscle. In WT SR, TRIC-A proteins are present in large numbers and so prevent TRIC-B proteins from interacting. TRIC-A may also interact directly with RyR1, allowing increased Po. In *Tric-a* KO SR, TRIC-B channels can interact and gate cooperatively. TRIC-A is shown in red and TRIC-B in green. The highlighted 'P' represents a phosphorylates site on the RyR protein [197].

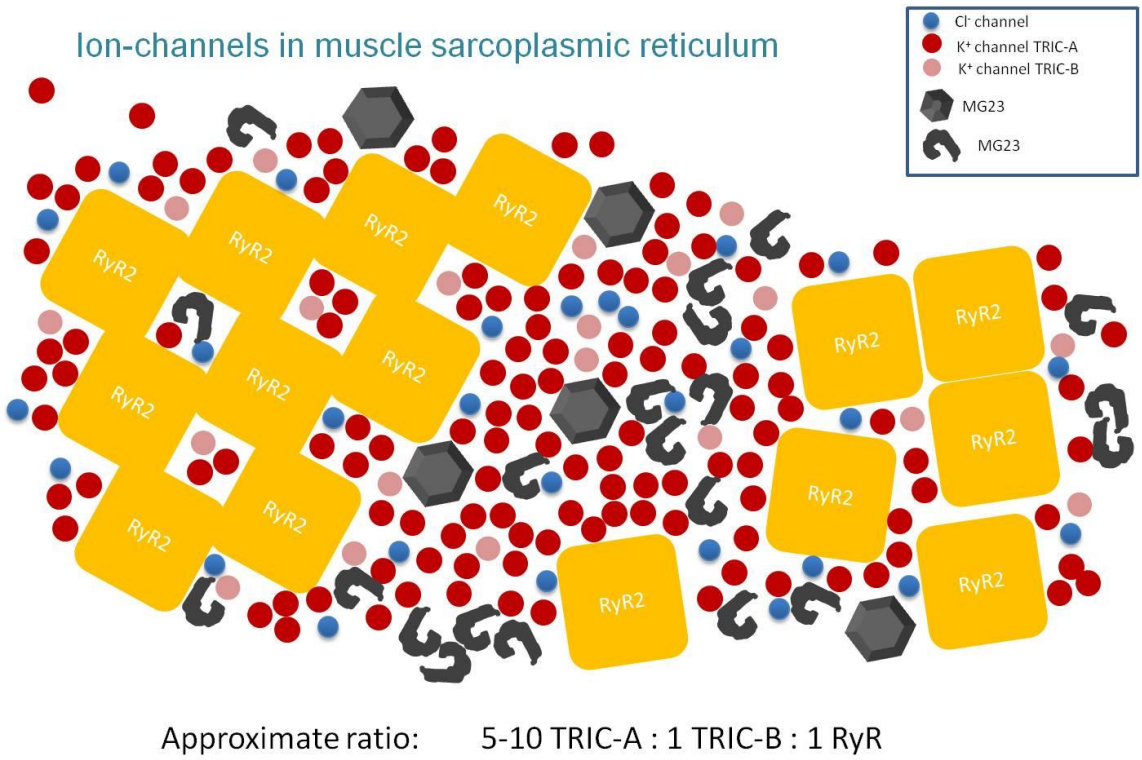


Figure 5.20. A schematic of proposed crowding of ion channels in the WT SR membrane
A schematic of how ion channels may crowd in the SR membrane. For simplicity, only the ion channels discussed in this thesis are included, however it should be noted that the SR contains many more proteins which may also contribute to the effect of SR membrane crowding Channels are not shown to scale.

In Chapter 4 of this thesis, I proposed that the SRAL channel current observed in SR vesicles was an anion leak channel, which was also permeable to cations, and which existed in channel clusters within the SR. Figure 5.17 suggests that, in *Tric-a* KO tissue, the SRAL channel becomes more selective for Cl^-. It is possible, therefore, that rather than consisting of one channel type, the SRAL channel complex consists of a variety of channels, one of which is TRIC-A. These findings also suggest that the TRIC-A channel would be more selective for cations over anions and may be permeable to choline. One final possibility is that TRIC-A and TRIC-B are not the SR K^+ channels that are normally found gating in mammalian SR vesicles and that the identify of the SR K^+ channels has yet to be discovered. This leaves open the question as to why we don't

more frequently observe the types of single-channel current-fluctuations that are obtained after incorporating purified TRIC-A and TRIC-B proteins into artificial membranes. After all, TRIC-A is the most abundant ion channel in the SR and therefore unless the protein becomes damaged following purification or requires some kind of 'activation' we would expect to observe this channel frequently.

Chapter 6. Purified TRIC-A and TRIC-B proteins

6.1 Introduction

The only published eukaryotic TRIC structure is of the *c. elegans* TRIC-B1/B2 channel [112]. *C. elegans* is a type of nematode (roundworm), about 1 mm in length, that lives in temperate soil environments [200]. The *c. elegans* TRIC-B1 structure suggested a protein with three 7-TM monomers, each with a central pore [112]. Each TRIC-B1 monomer also contained a $PI(4,5)P_2$ molecule as part of the channel structure, with the charged head group forming part of the channel pore [112]. The pore of the TRIC-B1 protein was found to be an hour glass shape with two constrictions of <1.5 Å and a central reservoir of between 1.5-2.3 Å which contained binding sited for cations and water [112].

The *c. elegans* TRIC-B1 channels were found to gate to a fully open conductance of 153 pS in 210 mM symmetrical KCl solution and to two sub-conductance states at 33 % (45.8 pS) and 67 % (101.5 pS) which may correspond to the open levels of the monomeric pores [112]. The channel was also found to be Ca^{2+} activated from the cytosolic side, but inhibited by symmetrical Ca^{2+} [112].

Following the publication of their paper on the structure of the TRIC-B1 protein from *c. elegans* [112], the laboratory of Zhenfeng Liu (Laboratory of Protein and Peptide Pharmaceuticals &Laboratory of Proteomics, Institute of Biophysics, Chinese Academy of Sciences, Beijing 100101, China) sent us both the full length protein and a truncated version (as in the paper) of the protein containing only the amino acid chain from 1-247 of *c. elegans* TRIC-B1 reconstituted into liposomes. We then incorporated these liposomes into bilayers to investigate ion channel function. In addition, purified human TRIC-A protein, reconstituted into liposomes was obtained from our collaborators in the Carpenter laboratory (Structural Genomics Consortium, University of Oxford, UK).

The aim of this chapter therefore is to characterise the biophysical properties of channels observed from purified human TRIC-A and *c. elegans* TRIC-B1 preparations and to investigate if TRIC-like channels can be observed in native SR membranes using bilayer experimental data

6.2 Results

6.2.1 The study of reconstituted *c. elegans* TRIC-B1 protein

6.2.1.1 Initial experiments: The four channels

When the reconstituted *c. elegans* TRIC-B1 proteins were added to the bilayer, initially four distinct channels were observed. I have termed the channel as types I-IV. Below, the properties of these channels are detailed in order from the most common type observed to the least common. All four types were observed from liposomes containing both the full length and the truncated versions of the *c. elegans* TRIC-B1 protein. Due to the apparent similarity between the currents observed from liposomes containing the full length and the truncated versions of the channel, for the purpose of this thesis the data from these preparations have been merged.

6.2.1.2 The type I channel

An example of type I channel gating is shown in Figure 6.1. This was the most common channel type, observed in 11 of 23 bilayer experiments using liposomes containing the purified *c.* elegans TRIC-B1. The channels gated with high Po and dwelt predominantly in high-noise sub-conductance states.

Figure 6.2A shows the current-voltage relationship of the type I channel in symmetrical and asymmetrical KCl. The figure shows that the type I channel is more selective for cations over anions with a P_K/P_{Cl} = 22.7±9.2 (mean±SEM, n=7). The apparent single-channel conductance of

the Type I channel was observed to increase from 193±11 pS (mean±SEM, n=7) in symmetrical KCl to 353±10 pS (mean±SEM, n=7) in asymmetrical KCl, resulting from a non-parallel shift in the linear regression lines. It should also be noted that, although the data is fitted with a linear regression, the data follows a curve. Figure 6.2B shows a similar experiment; however, choline is the cation instead of K^+. The E_{rev} suggests that the channel is 16 times more selective for choline over Cl^- ($P_{choline}/P_{Cl}$ = 15.5±8.2). As with the KCl data, the data in choline-chloride is not linear and follows a curve. In symmetrical solutions, the apparent single-channel conductance was significantly smaller in symmetrical choline-chloride (54±2 pS, mean±SEM, n=4) when compared with symmetrical KCl (193±11 pS, mean±SEM, n=7).

Figure 6.2C shows how the conductance of the high-noise sub-conductance state changes with voltage. The sub-conductance current is expressed as a percentage of the apparent fully open channel current level. At more positive voltages, the sub-conductance state appeared to have a lower conductance, suggesting voltage sensitivity.

Figure 6.2D compares the relative permeabilities of K^+ and choline to Cl^- for the type I channel. The channel appeared more selective for K^+ and choline over Cl^-.

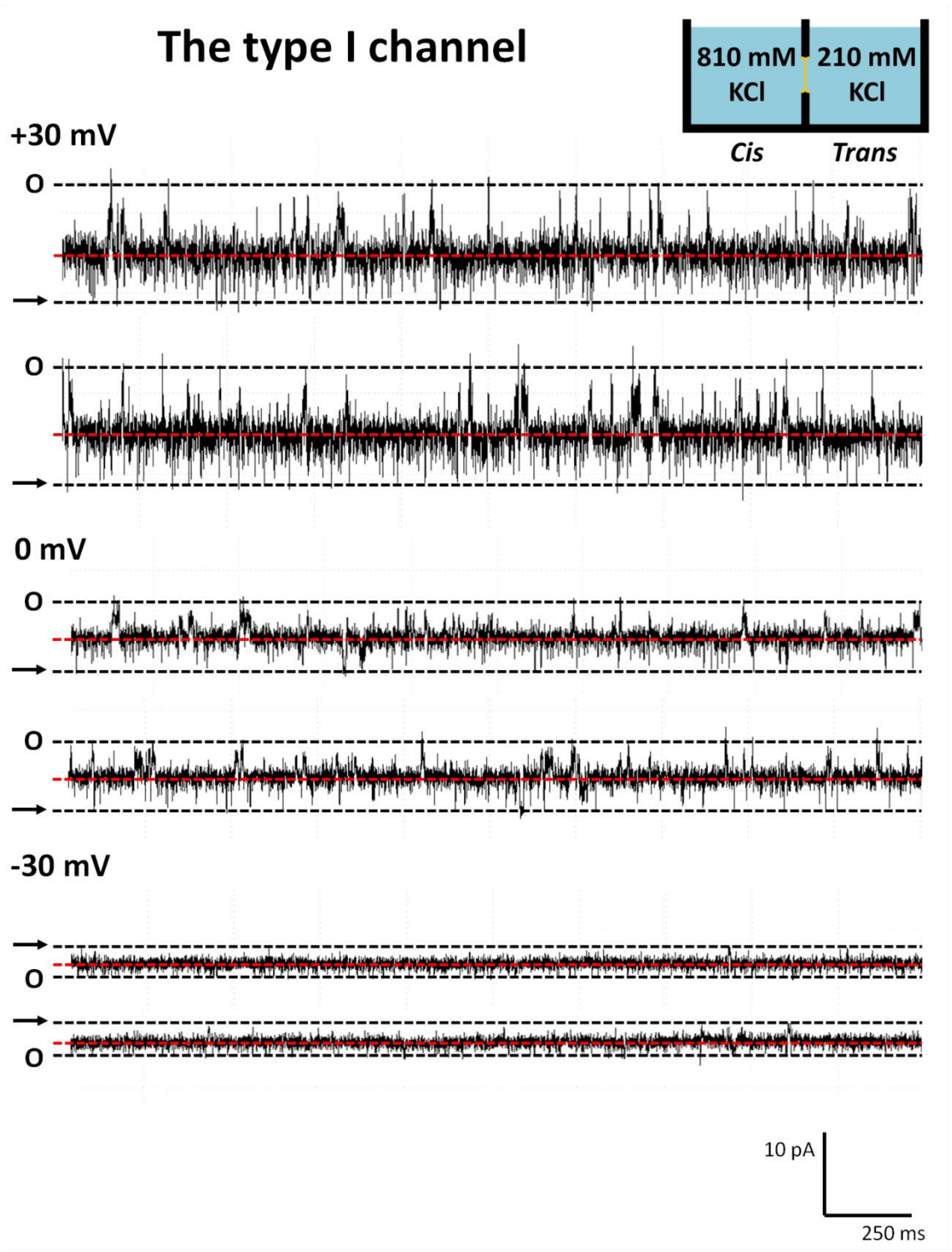
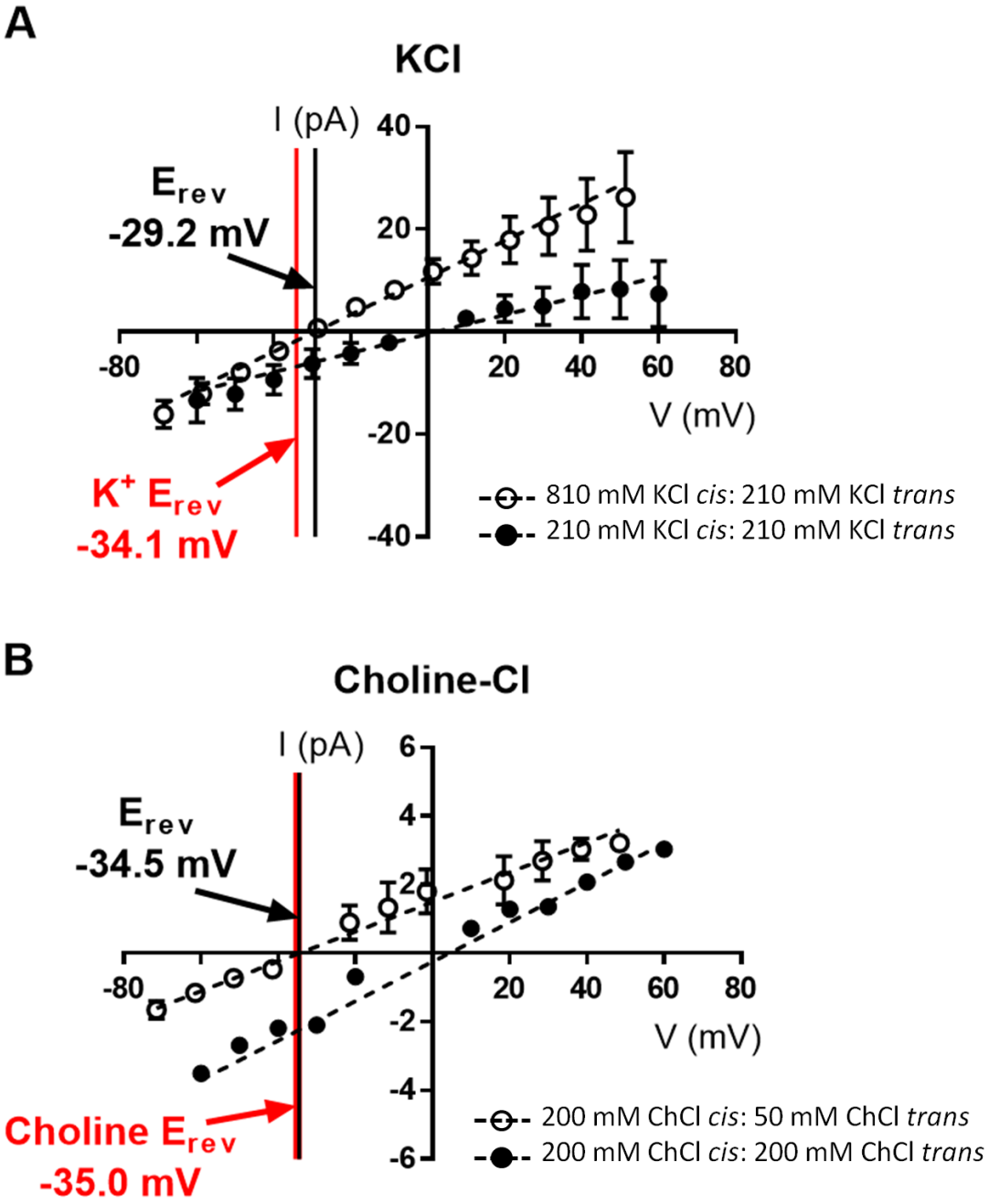
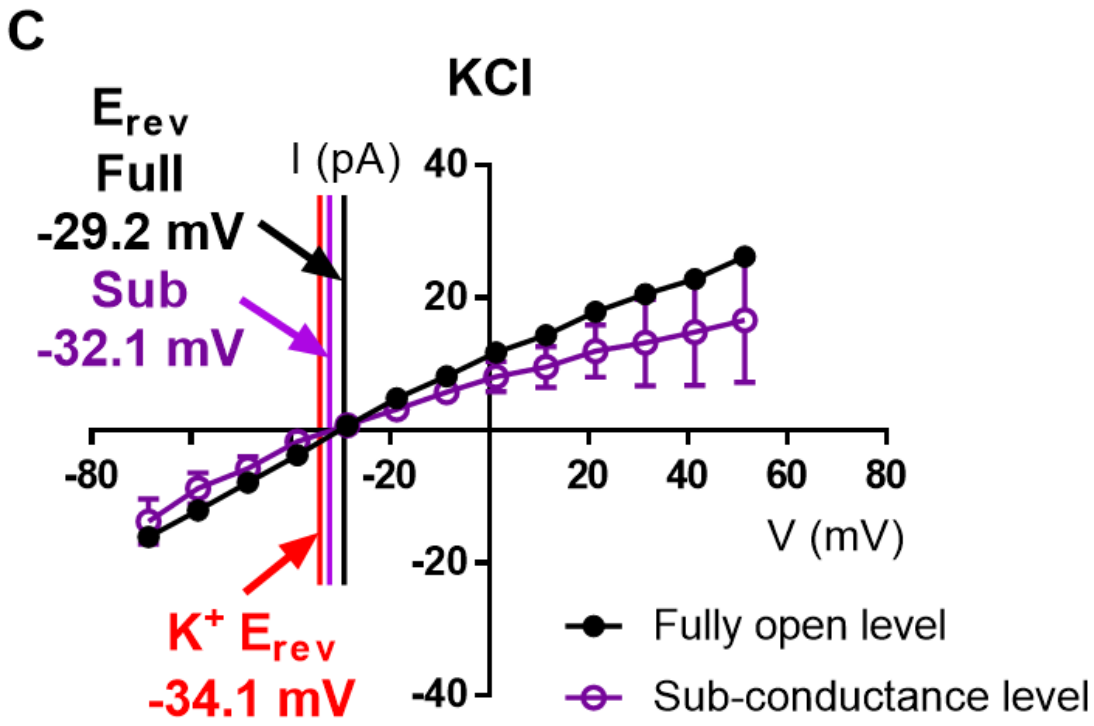

The type I channel
810 mM KCl
210 mM KCl
Cis
Trans
+30 mV
O
O
0 mV
O
O
-30 mV
O
O
10 pA
250 ms

Figure 6.1. Current-fluctuations through the type I channel
Current-fluctuations through the type I channel at +30 mV (top trace), 0 mV (middle trace) and -30 mV (bottom trace) in asymmetric solutions (*cis*: 810 mM KCl, 10 µM Ca^{2+}, 20 mM HEPES, pH 7.2; *trans*: 210 mM KCl, 10 µM Ca^{2+}, 20 mM HEPES, pH 7.2). The closed channel level is shown by an arrow and the fully open level by an O. The sub-conductance level is shown with a red broken line. The recordings are typical of 11 experiments.


A
KCl
I (pA)
40
20
-20
-40
-80
20
40
60
80
V (mV)
E rev
-29.2 mV
K+ E rev
-34.1 mV
810 mM KCl cis: 210 mM KCl trans
210 mM KCl cis: 210 mM KCl trans
B
Choline-Cl
I (pA)
6
4
2
-2
-4
-6
-80
20
40
60
80
V (mV)
E rev
-34.5 mV
Choline E rev
-35.0 mV
200 mM ChCl cis: 50 mM ChCl trans
200 mM ChCl cis: 200 mM ChCl trans


C
KCl
E_{rev}
Full
-29.2 mV
Sub
-32.1 mV
I (pA)
40
20
-20
-40
-80
-20
20
40
60
80
V (mV)
K^+ E_{rev}
-34.1 mV
Fully open level
Sub-conductance level

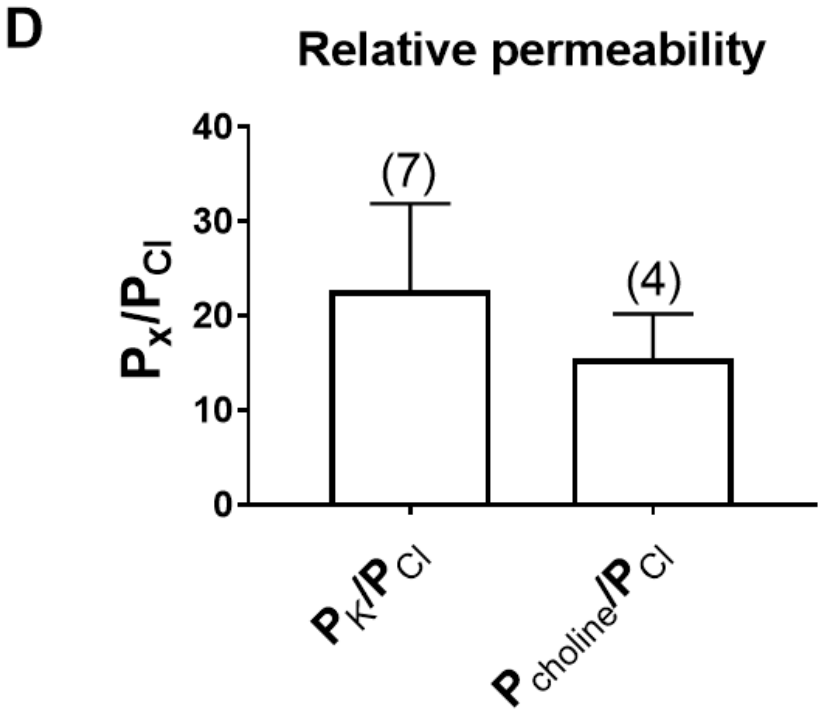

D
Relative permeability
P_x/P_{Cl}
40
30
20
10
0
(7)
(4)
P_K/P_{Cl}
$P_{choline}/P_{Cl}$

Figure 6.2. The permeability properties of the type I channel
(A) The current-voltage relationship for the type I channel in symmetrical (black, n=7) KCl and asymmetrical (purple, n=4) KCl. **(B)** Current-voltage relationship for the type I channel in symmetrical (black, n=1) choline-chloride (ChCl) and asymmetrical (purple, n=3) choline-chloride. **(C)** The current-voltage relationship of the type I channel sub-conductance state in asymmetric KCl. The solid black line shows the linear regression line for the fully open state for reference **(D)** The relative permeabilities of the apparent fully open channel level of the Type I channel in KCl and choline-chloride. The number of experiments is shown in brackets above each respective bar. Values are of the mean±SEM or mean±SD. Current-voltage relationships are fitted by means of a linear regression and the calculated cation E_{rev} is shown as a red vertical line on each graph. The E_{rev} for the channel is labelled on each graph by means of vertical line. Where not shown, error bars are within the symbols.

6.2.1.3 The type II channel

The type II channel was observed in 5 out of 23 experiments. This appeared as a leak in the bilayer made up from many small conductance channels gating together (Figure 6.3). The average or leak current was measured using noise analysis and the unitary conductance of the small individual channel was measured independently (Figure 6.4).

The leak current was larger in symmetrical 210 mM KCl (969.1±9.6 pS, mean±SEM, n=5) and smaller in symmetrical 350 mM choline-chloride (338.5±4.4 pS, mean±SD, n=3). Type II currents s were found to be more selective for cations over anions with a P_K/P_{Cl} value of 5.3±0.4 (mean±SEM, n=5) and a $P_{choline}/P_{Cl}$ value of 5.6 (mean, n=2).

The unitary current measurement for the type II channels was less easy to accurately measure. The measurements which were made revealed a single-channel conductance which was far smaller than that measured for the average current. In symmetrical 210 mM KCl the unitary conductance was 37.7±1.6 pS (mean±SEM, n=5) and 15.1±1.4 pS (mean±SD, n=3) in symmetrical 350 mM choline-Cl. The unitary current displayed an unusual permeability sequence of choline>Cl^->K^+.

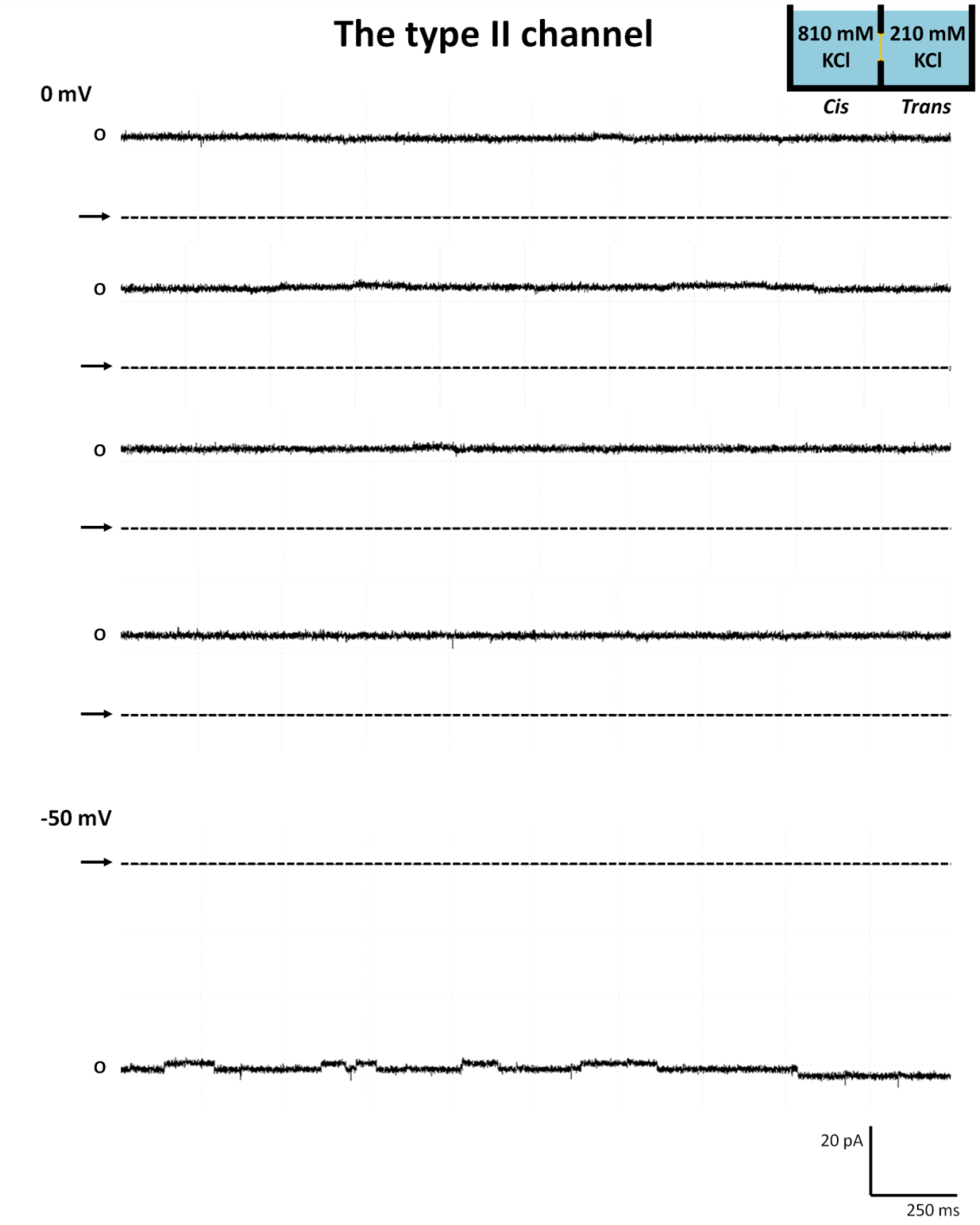
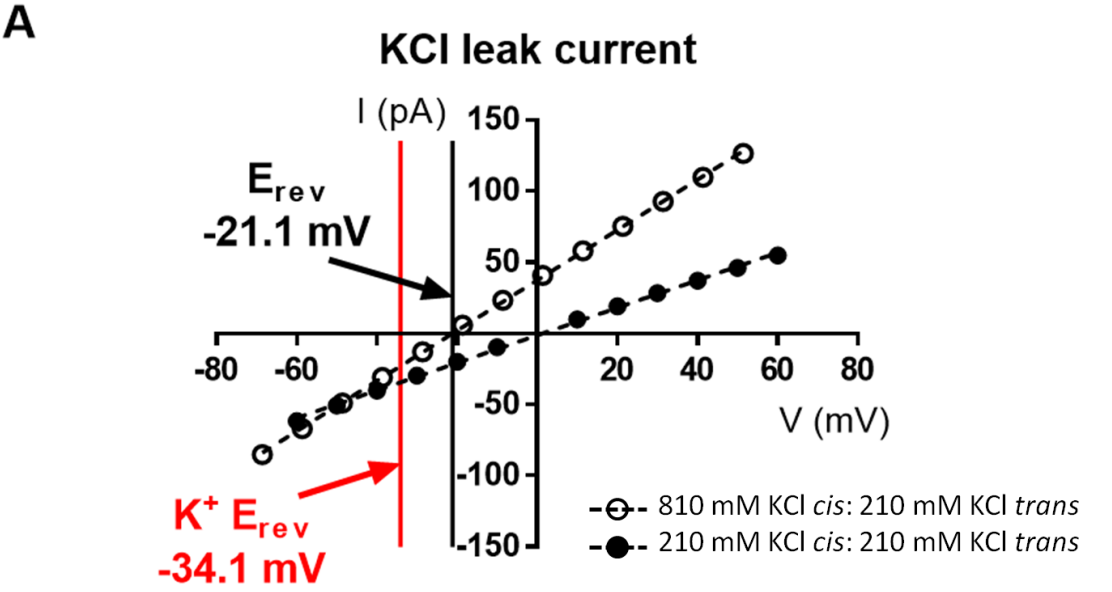
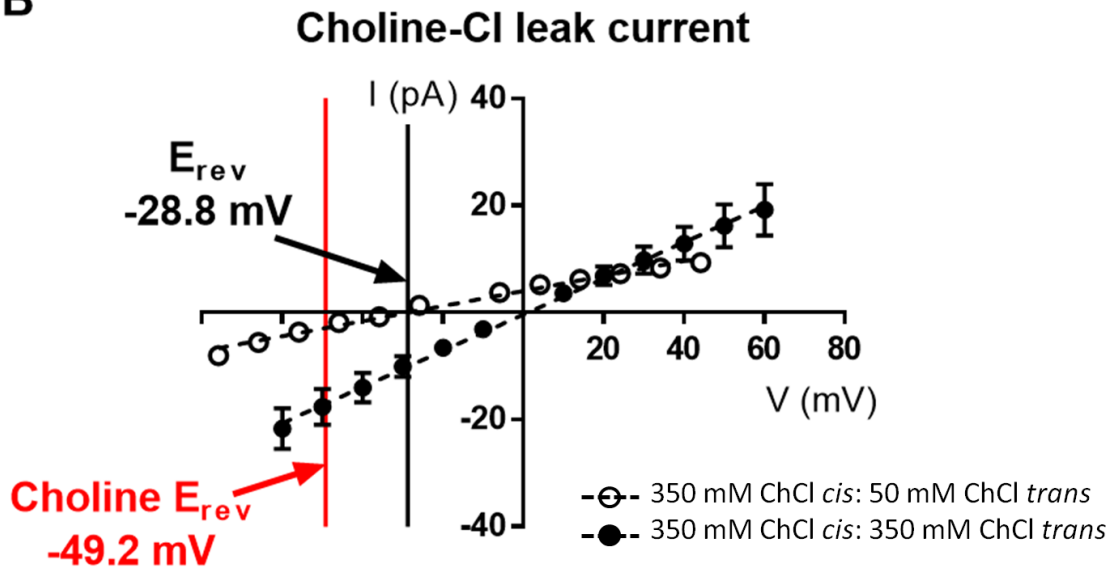


Figure 6.3. Current-fluctuations through the type II channel
Current-fluctuations at 0 mV (top traces) and -50 mV (bottom trace) in asymmetrical KCl through the type II channel. Recordings are representative of 5 experiments. The zero current level is shown by an arrow and the channel open level by O.

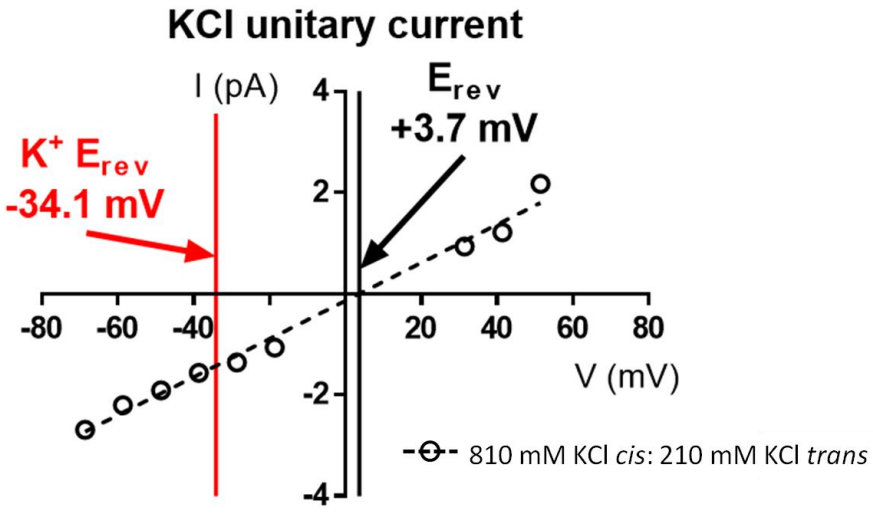
A


KCl leak current
I (pA)
150
100
50
-50
-100
-150
-80
-60
20
40
60
80
V (mV)
E rev
-21.1 mV
K+ E rev
-34.1 mV
810 mM KCl cis: 210 mM KCl trans
210 mM KCl cis: 210 mM KCl trans

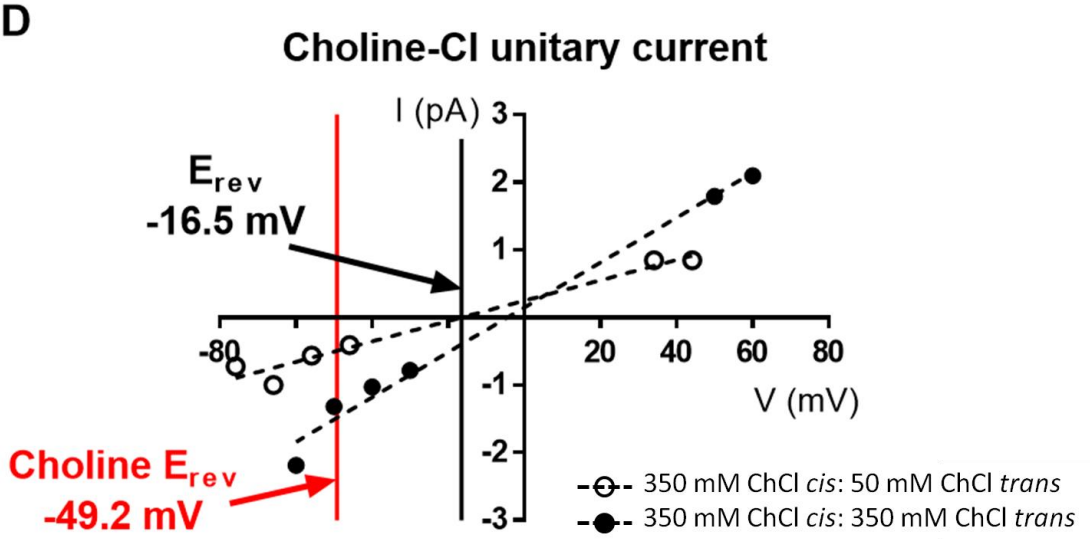
B


Choline-Cl leak current
I (pA)
40
20
-20
-40
20
40
60
80
V (mV)
E rev
-28.8 mV
Choline E rev
-49.2 mV
350 mM ChCl cis: 50 mM ChCl trans
350 mM ChCl cis: 350 mM ChCl trans

C


KCl unitary current
I (pA)
4
2
-2
-4
E_{rev}
+3.7 mV
K^+ E_{rev}
-34.1 mV
-80
-60
-40
20
40
60
80
V (mV)
810 mM KCl *cis*: 210 mM KCl *trans*

D


Choline-Cl unitary current
I (pA)
3
2
1
-1
-2
-3
E_{rev}
-16.5 mV
-80
20
40
60
80
V (mV)
Choline E_{rev}
-49.2 mV
350 mM ChCl *cis*: 50 mM ChCl *trans*
350 mM ChCl *cis*: 350 mM ChCl *trans*

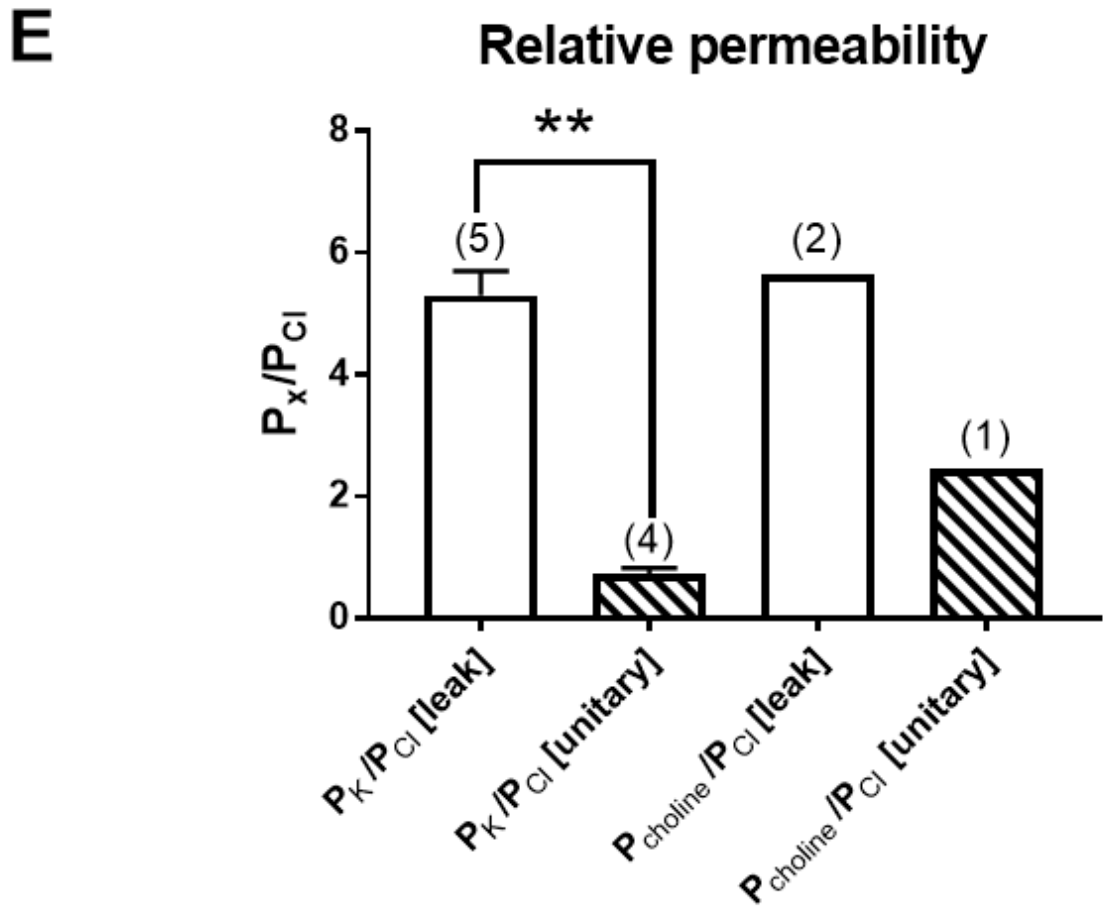


Figure 6.4. Permeability properties of the type II channel
(A, B) Current-voltage relationship for the average (leak) current through the type II channel calculated using noise analysis. Data is shown in symmetrical (open circles) KCl and asymmetrical (filled circles) KCl (A) and in symmetrical (open circles) choline-chloride (ChCl) and asymmetrical (closed circles) choline-chloride **(C, D)** Current voltage relationship for the unitary current through the type II channel in asymmetrical KCl **(C)** and in symmetrical (open circles) choline- chloride and asymmetrical (filled circles) choline-chloride . **(E)** The relative permeability ratios (P_x/P_{Cl}), of ions through the type II channel calculated for the average current (open bars) and the unitary current (shaded bars). The number of experiments is shown in brackets above each respective bar. Values are of the mean±SEM or mean±SD. Current-voltage relationships are fitted by means of a linear regression and the calculated cation E_{rev} is shown as a red vertical line on each graph. The E_{rev} of each channel is also labelled on each graph by black vertical line. Where not shown, error bars are within the symbols**.**

6.2.1.4 The Type III channel

A third type of channel, termed the type III channel, was observed in 4 bilayer experiments. An example of current-fluctuations through the channel is shown in Figure 6.5. The channel had a high Po with brief sojourns to a closed state. The 4 channels recorded all displayed similar gating patterns; however the channel permeability properties were inconsistent. All channels were permeable to both Cl^- and K^+, but their relative permeabilities to K^+ and Cl^- (P_K/P_{Cl}) ranged from 0.5 to 3.3 (Figure 6.5C).

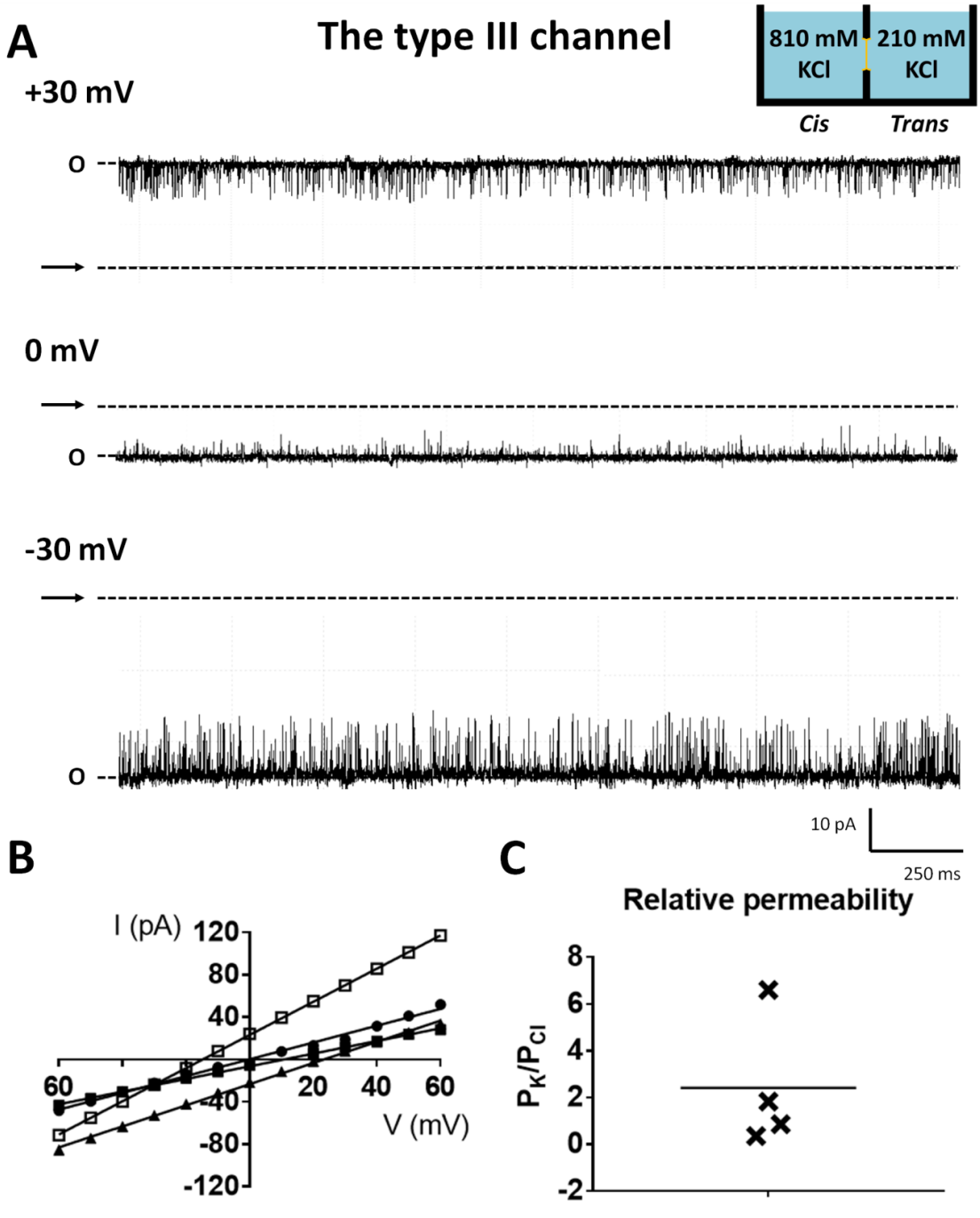


Figure 6.5. The type III channel
(A) Current-fluctuations through a type III channel at -30 mV, 0 mV and +30 mV holding potentials. The zero current level is shown with an arrow and the channel open level by an O. The experiment was recorded in asymmetrical KCl **(B)** Individual current voltage relationships of the type III channels. Values are of the mean±SD (n=4). **(C)** The P_K/P_{Cl} values for each type IV channel, showing the variation in data.

6.2.1.5 The Type IV channel

The least common channel, observed in only 3 out of 23 bilayer experiments, has been termed the type IV channel. An example of current-fluctuations through the type IV channel is shown in Figure 6.6. Although each of the three channels observed displayed differing biophysical properties, they were visually similar and thus have been grouped together. The channels exhibited a lower Po (+30 mV: 0.23±1.0, mean±SD, n=3) than the other channel types observed and the gating consisted of brief channel openings and closings. At more negative potentials, the channel openings were shorter and the Po decreased (-30 mV: 0.03±0.02, mean±SD, n=3). As with the type III channels, the channel permeability values varied highly between experiments (Figure 6.6C). The single-channel conductance was also found to be variable as is shown by the high standard deviation measurements in Figure 6.6B.

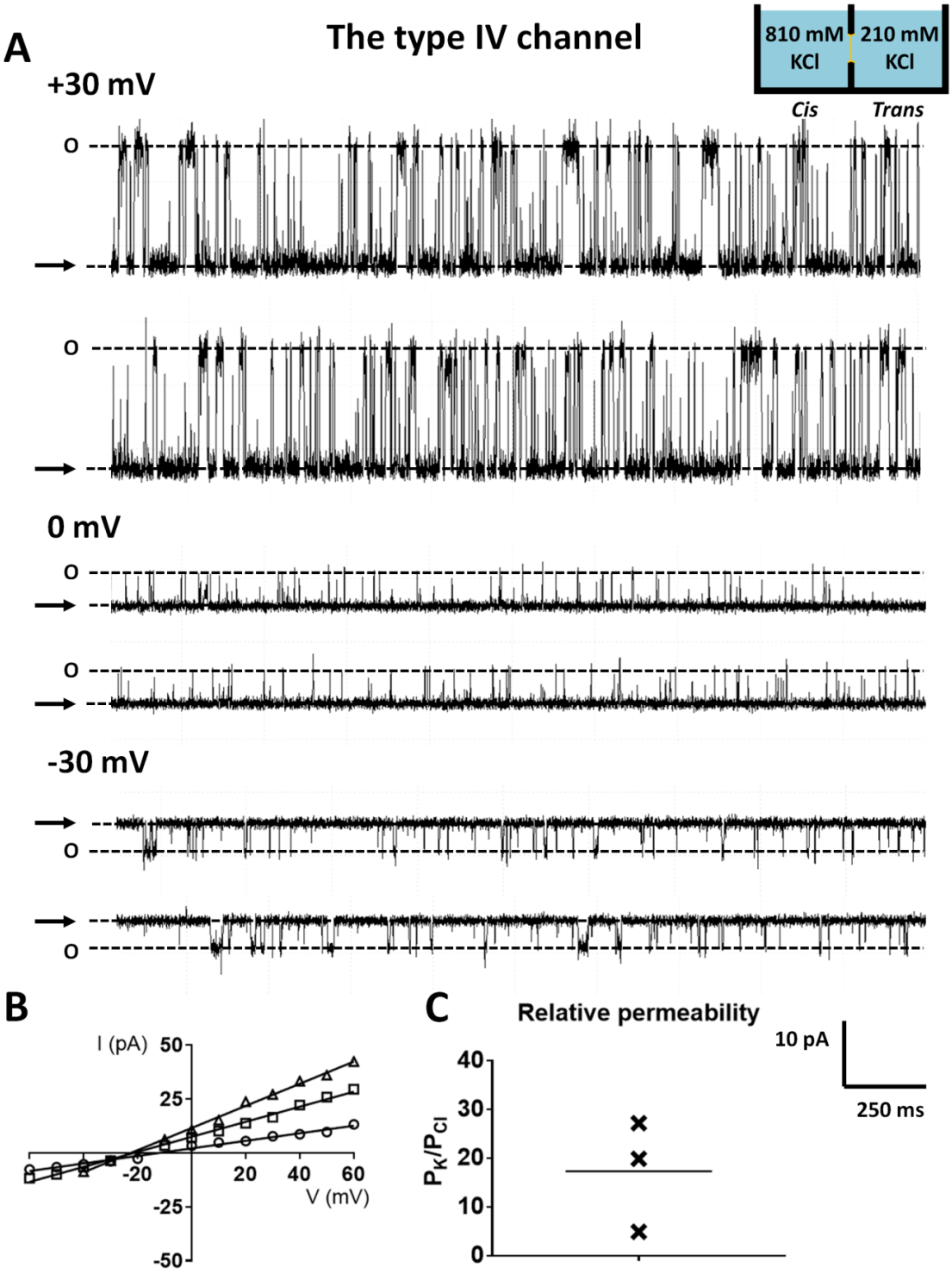


Figure 6.6. The type IV channel
(A) An example of current-fluctuations through a type IV channel at +30 mV, 0 mV, and -30 mV holding potentials in asymmetrical KCl. The channel closed levels are shown by an arrow and the open channel levels by O. **(B)** Individual current voltage relationships of the type IV channels. **(C)** The P_K/P_{Cl} values for each type IV channel, showing the variation in data.

6.2.2 Which Channel Type is the *c. elegans* TRIC-B1 channel?

In a purified protein preparation, only the purified channel should be present. It is therefore clear that three of the four channel types observed in the purified preparation are either artefacts, for example the result of lipid-detergent complexes, or contaminant proteins. Additional studies were therefore conducted to establish which channel type is the *c. elegans* TRIC-B1 channel.

6.2.3 Control liposome studies

The first study was undertaken with a control preparation consisting of reconstituted liposomes made from 90% asolectin (Sigma), 10% cholesterol (Avanti) (w:w) and 1 % β-DM (Sigma) (w:w). The control liposomes were incorporated into artificial PE bilayers using identical protocols as were used to fuse vesicles containing purified *c. elegans* TRIC-B1 proteins.

9 experiments were conducted using the control liposomes. In 7 of the experiments there were no incorporations of ion channels into the bilayer after 30 min of stirring. In 2 experiments, the following current-fluctuations were observed. These were similar to the Type III channels in the TRIC-B1 preparation. We can therefore conclude that the type III channel may be a contaminant protein or a contaminant of lipid and detergent. A similar rapid gating type of channel has previously been described by Accardi *et al.* in 2004 [201]

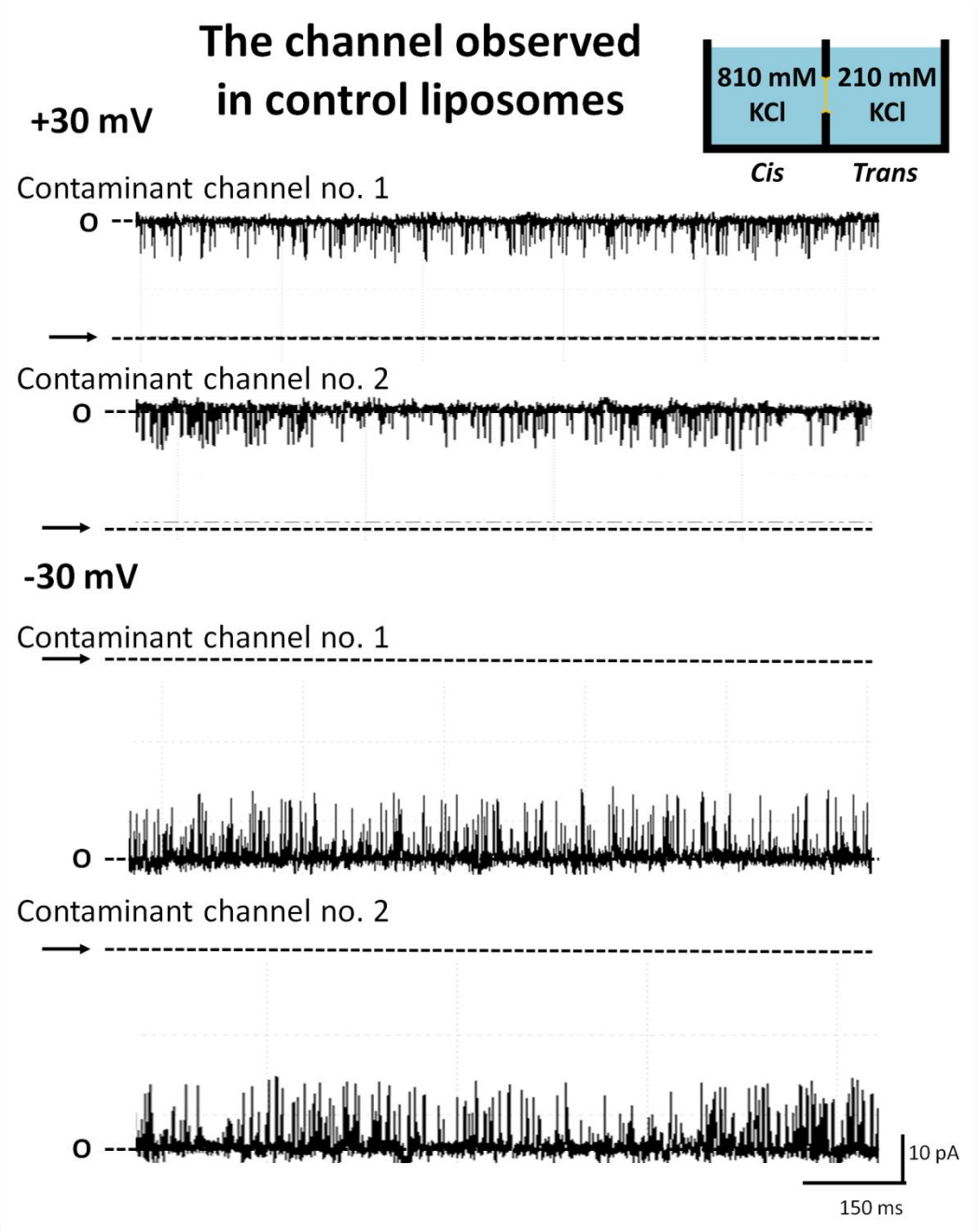


Figure 6.7 Current-fluctuations through the channels observed in control empty liposomes at ±30 mV

Current-fluctuations through two contaminant channels, termed 'Contaminant channel no.1' and 'Contaminant channel no.2', observed in control liposomes at holding potentials of +30 mV and -30 mV in asymmetrical KCl solutions. The zero current level is shown by an arrow ad the open channel level by O.

6.2.4 Extruded liposomes

A second study was performed where the liposomes containing the *c. elegans* TRIC B1 protein were extruded. Liposomes can have altered morphology when subjected to the freeze-thaw process which can result in liposomes which are large and multilamellar in structure and may affect the reconstitution into bilayers under voltage-clamp conditions [202]. Liposomes were therefore extruded through a 400 nm membrane using an Avanti Mini Extruder (Avanti).

Type I channel currents were the only currents observed in the extruded vesicles (n=8 experiments). It is possible that the Type II and Type IV could be artefacts caused by lipids/detergents.

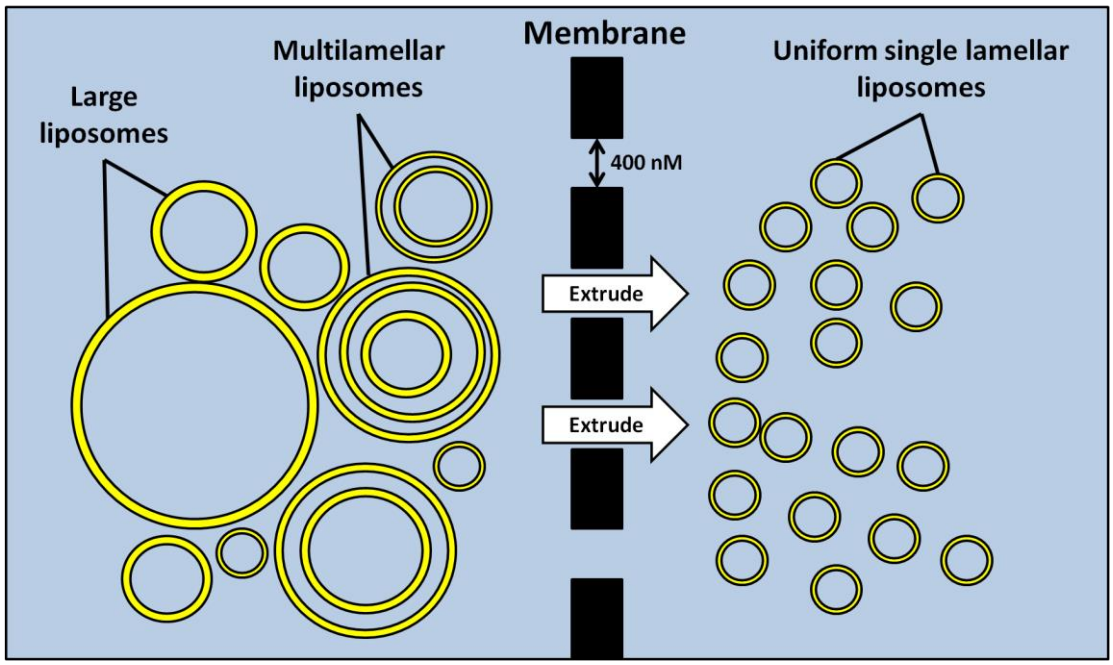


Figure 6.8. A schematic showing the state of liposomes before extrusion (left) and after extrusion (right) through a 400 nM membranes

6.2.5 Similarity to native SR channels

TRIC is an SR membrane protein and therefore, it is it possible that it is observed in bilayer experiments with native SR membrane vesicles. It has previously been suggested that the identity of the TRIC channels is that of SR K^+ channels [97]. Typical gating and single-channel conductance of the SR K^+ channel in mammalian SR appears to be different to that of the published data from the *c. elegans* TRIC-B1 experiments. However, the SR K^+ channel does sometimes gate to sub-conductance states in a manner which resembles that of the Type I channel. Examples of this type of gating where prolonged sub-conducting events occur are shown in Figure 6.9 (sheep cardiac SR K^+ channel in symmetrical 210 mM KPIPES) and in Figure 6.10 (mouse skeletal SR K^+ channel in symmetrical 210 mM KCl). It is possible that the type I channels are SR K^+ channels gating in a prolonged sub-conductance state. The sub-conductance state of the type I channels appears similar (around 70 % of the apparent fully open state) to the sub-conductance states observed in native SR K^+ channels. The sequence alignment in Figure 6.11 shows the sequence similarity between *c. elegans* TRIC-B1 and the mammalian TRIC-B channel, especially in the pore regions, suggesting that they might share similar permeability properties.

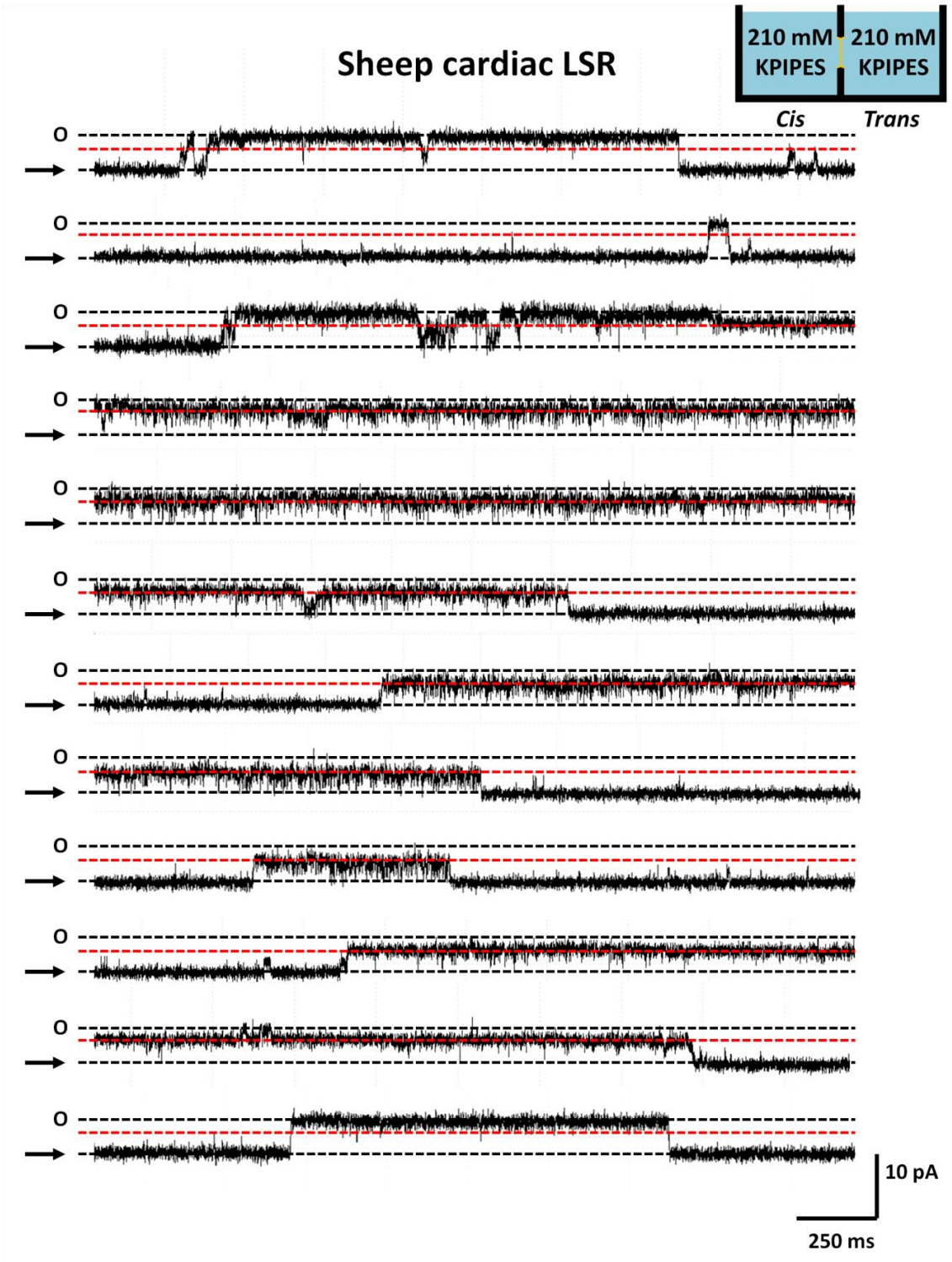


Figure 6.9 Native SR K^+ channel from sheep cardiac muscle
Current-fluctuations through a native sheep cardiac SR K^+ channel at +30 mV, showing sub-conductance gating similar to that of the type I channel seen in purified *c. elegans* TRIC-B1 preparations. The experiment was recorded in symmetrical 210 mM KPIPES. The channel closed level is shown by an arrow, the fully open channel level by O, and the level of the flickery sub-conductance state is shown by a red broken line.

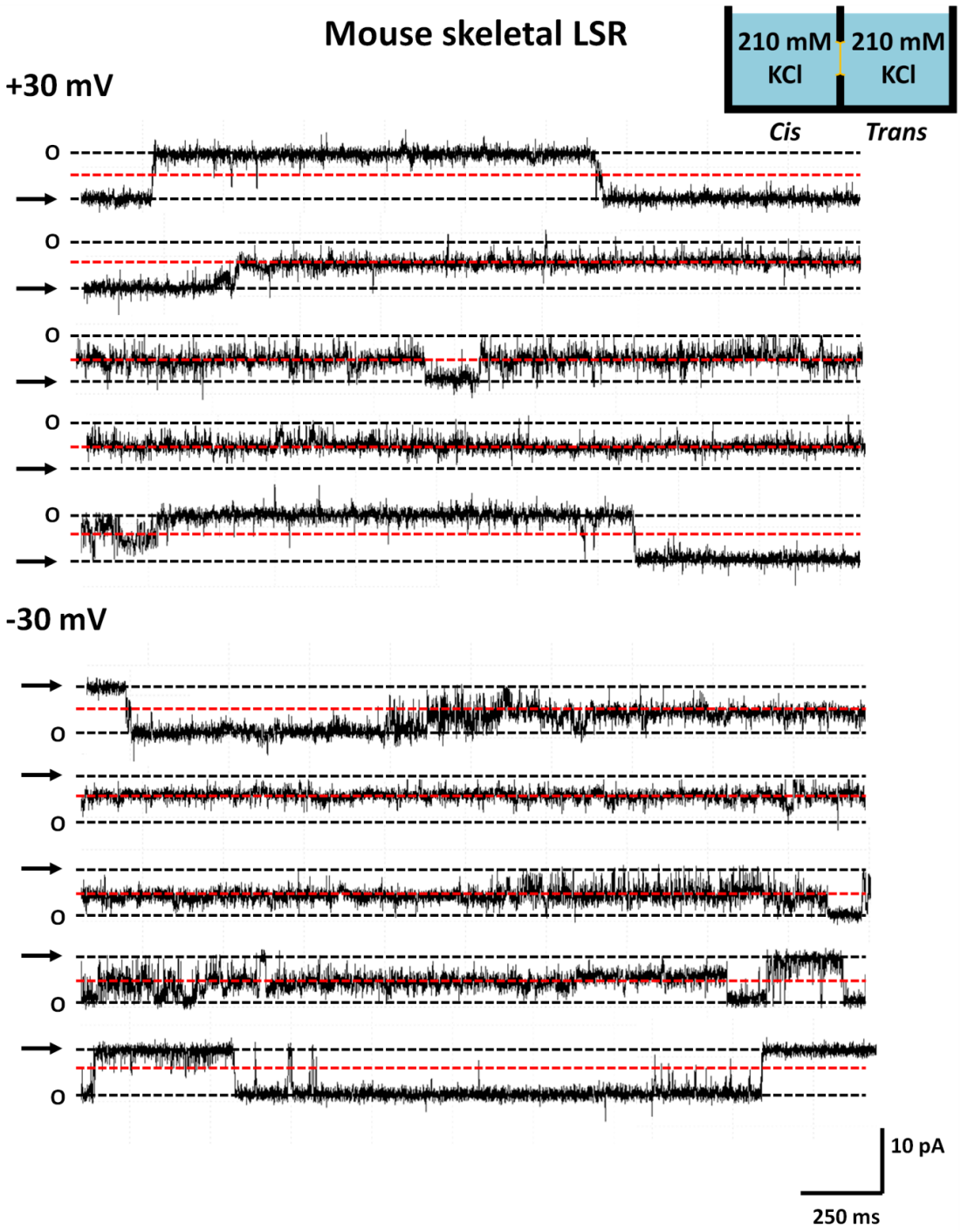


Figure 6.10. Native SR K^+ channel from mouse skeletal muscle
Current-fluctuations through a native mouse skeletal SR K^+ channel at +30 mV and -30 mV holding potentials showing sub-conductance gating similar to that of the type I channel seen in purified *c. elegans* TRIC-B1 preparations. The experiment was recorded in symmetrical 210 mM KCl. The channel closed level is shown by an arrow, the fully open channel level by an O, and the level of the flickery sub-conductance state is shown by a red broken line.

```
TM38B_HUMAN             1   ---------MDSPWDELALAFSRTSMFPFFDIAHYLVSVMAVKRQPGAAAL--AWKNPIS   49
TM38B_MOUSE             1   ---------MEYPWDDLTLAFSRTSMFPFFDIAHYLVSVMALKQRPGAVAA--AWNNPLA   49
W5PBF9_SHEEP            1   ---------MDSPWNELTLAFSRTSMFPFFDIAHYLVSVMALKHQPGAAAL--AWKNPLS   49
T38B1_CAEEL             1   MVVPESFQLDQEILLDAGAQLHRLKMYPYFDVAHYLLMIIEVRDDLGSAASIFSRKHPLS   60
                                      :    :    : * .*:*:**:****: :: ::   *:.*   : ::*::

TM38B_HUMAN            50   SWFTAMLHCFGGGILSCLLLAEPPLKFLANHTNILLASSIWYITFFCPHDLVSQGYSYLP  109
TM38B_MOUSE            50   SWLSAMLHCFGGGILSCMLLAESPLKFLTNHTNILLASSIWYIVFFCPRDLVSQGYSYQP  109
W5PBF9_SHEEP           50   SWFTAMLHCFGGGILSCVLLAEPPLRFLANNTNILLASSIWYIAFFCPYDLISQGYSFLP  109
T38B1_CAEEL            61   CWLSSMLMCFADAFLANFLLGEPVIAPFKRHDDIILATIIWYLVFYAPFDGIYKIAKITP  120
                            .*:::** **...:*: .**.*  :  : .: :*:**: ***:.*:.* * : :  .  *

TM38B_HUMAN           110   VQLLASGMKEVTRTWKIVGGVTHANSYYKNGWIVMIAIGWARGAGGTIITNFERLVKGDW  169
TM38B_MOUSE           110   IQFLAAGMKEVTRTWKIVGGVSDANSYYRNAWIVMIVVGWARGAGGAVVTACEQLLKGDW  169
W5PBF9_SHEEP          110   VQLLAAGMKEVTRTWKIVGGVTHANSYYKNGWIVMIAIGWARGAGGSIITNFEQLVKGCW  169
T38B1_CAEEL           121   VKCVLAVMKEVKRAYKVSHGVSHAAKLYPNSYIVQVLVGTAKGAGSGIVRTLEQLVRGVW  180
                            :: : : ****.*::*:  **:.* . * *.:** : :* *:***. ::   *:*::* *

TM38B_HUMAN           170   KPEGDEWLKMSYPAKVTLLGSVIFTFQHTQHLAISKHNLMFLYTI-FIVATKITMMTTQT  228
TM38B_MOUSE           170   KPEGDEWLKMSFPCKITLLGSIMFTFQHTRHLAISKHDLMFLYTI-FLVTIKVTMMMTKD  228
W5PBF9_SHEEP          170   KPEAEEWLKMSYPAKVTLLGSVIFTFQQTKHLAISKPNLMFLFTV-FLVATKITMMITET  228
T38B1_CAEEL           181   LPTHNELLRPSFATKACVVAASVLALEKSGTYLTAPHDLVYLVIVGFFVYFKLSAV-ILH  239
                             *  :* *: *:  *  ::.: :::::::     :  :*::*  : *:*  *:: :

TM38B_HUMAN           229   STMTFAPFEDTLSWMLFGWQ--Q---PFSSCEKKSEAKSPSNGVGSLASKPVDVASDNVK  283
TM38B_MOUSE           229   TAVTLTPFEDTLTRMLFGRRQQQ---QFSSSEKKTEVKPSSNGSASSASKRGAEPSGGAK  285
W5PBF9_SHEEP          229   AFMPFACFEDTLSRMLFGWQ--Q---QFSPVEKKSETKSSFNGTGSSTSKPGANASDKVK  283
T38B1_CAEEL           240   VTDPFAPIENLFCAIFMGGIWDAVSRALAASRDRRAAGAHSNENGSSISTPEKKDQ----  295
                               :: :*: :  :::*         ::  ..:  .    *  .*  *.    .

TM38B_HUMAN           284   KKHTKKNE                                                    291
TM38B_MOUSE           286   RHAKKED-                                                    292
W5PBF9_SHEEP          284   KKHSKKTE                                                    291
T38B1_CAEEL           296   --------                                                    295
```

Figure 6.11. A sequence alignment of the TRIC-B protein
The amino acid sequences alignment of TRIC-B proteins from human, mouse, sheep, and TRIC-B1 from *c. elegans* (CAEEL). Sequence similarity is shown shaded in grey. The red shaded areas are the amino acids thought to form part of the TRIC-B1 pore [112]. This figure was produced using the database and the online tools provided by Uniprot (http://www.uniprot.org/).

6.2.5.1 Similarities to other native proteins

Similarities exist between the type I channel and the possible TRIC-A channel observed in CHO cells overexpressing the human TRIC-A protein, in that both channels gate in a high noise sub-conductance state that is usually approximately 70 % of the apparent fully open channel level.

6.2.6 Properties of the type I protein

6.2.6.1 Further permeability studies

The type I channels display complex gating behaviour which was also observed for SR K^+ channels. The type I channel gating behaviour was therefore studied in more detail in an attempt to describe the conducting properties of the channel and to find a gating model that might describe the essential features and help to determine if TRIC channels are similar to or distinct from that of SR K^+ channels.

As discussed earlier in this chapter, the type I channel is selective for K^+ and choline over Cl^-. Figure 6.12 shows an experiment where a channel is gating in symmetrical 210 mM KCl solution. The *cis* and *trans* were then replaced with 210 mM NMDG-Cl and the current was observed to disappear, indicating that the channel may be impermeable to either Cl^- or NMDG or that the channel permeability was too low to measure. The current was partially rescued when the bath solutions were replaced with 210 mM $CaCl_2$, demonstrating that the Type I channel is permeable to Ca^{2+}, but with a lower conductance than occurs with K^+. This is not the case with the mammalian SR K^+ channel, where the channel is impermeable to Ca^{2+} [98]. The mammalian SR K^+ channel has also been reported to be impermeable to choline [102], which is permeant in the Type I channel. Thus the Type I channel from *c. elegans* appears to possess slightly different selectivity properties than those of mammalian SR K^+ channels.

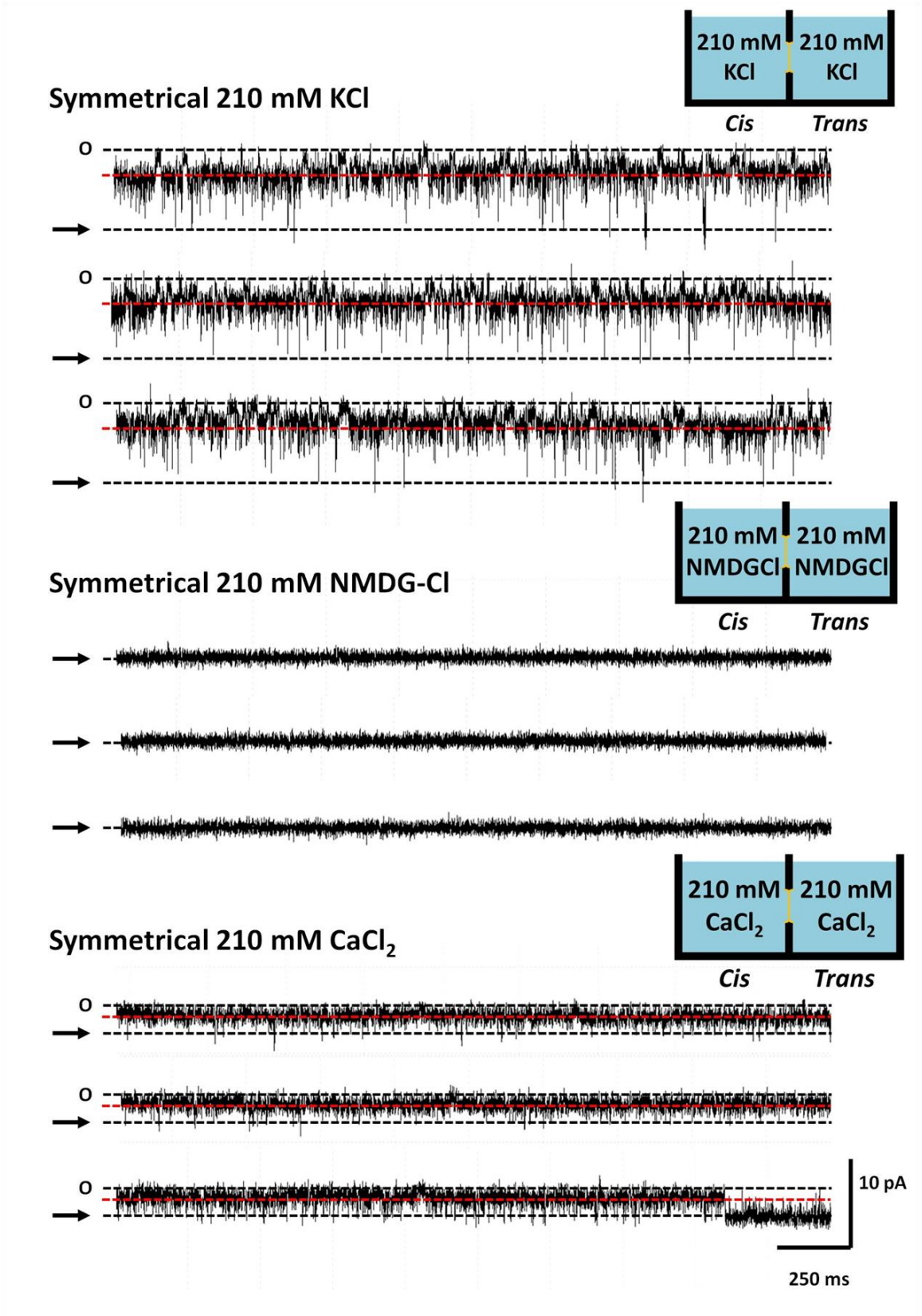

210 mM KCl
210 mM KCl
Cis
Trans
Symmetrical 210 mM KCl
o
o
o
210 mM NMDGCl
210 mM NMDGCl
Cis
Trans
Symmetrical 210 mM NMDG-Cl
210 mM CaCl2
210 mM CaCl2
Cis
Trans
Symmetrical 210 mM CaCl2
o
o
o
10 pA
250 ms

Figure 6.12 Current-fluctuations through the *c. elegans* TRIC-B1 channel
Current fluctuation through the Type I channel at a +30 mV holding potential in symmetrical 210 mM KCl, 210 mM NMDG-Cl (210 HCl, 10 µM Ca^{2+}, 10 mM HEPES, buffered to H 7.2 with NMDG), and 210 mM $CaCl_2$ (210 mM $CaCl_2$, 10 mM HEPES, buffered to pH 7.2 with Tris). The zero current level is shown with an arrow, the fully open channel state is shown with an O and the noisy sub-conductance level is shown with a red broken line.

6.2.6.2 Modelling the gating of the *c. elegans* TRIC-B1 protein

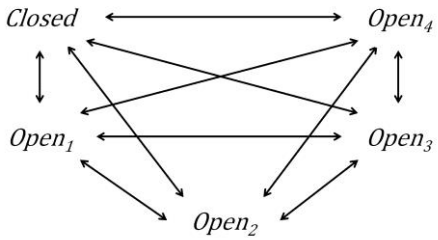
In order to gain insight into the gating of the purified TRIC channels, I produced a number of Markov models to model the gating. These models were purely speculative and should not be treated as accurate predictions of TRIC channel gating mechanisms.

A number of simple Markov models were designed and fitted to the data to ascertain the number of states which exist in the complex channel gating behaviour of the Type I channel. Linear Markov models were created with between 1 and 10 states and with each model increasing the number of possible states by 1. The models were fitted to an amplitude-histogram with an SKM algorithm using the QuB software suite [181] and each model was compared for the goodness of its fit to the data using a log-likelihood ratio test [185]. The best estimate for the number of states through which the Type I channel gates was 5 states (the most likely number of states in 6 out of 7 experiments). From this, a simple linear model was obtained and is shown below; the fit of the model to a representative Type I channel recording is shown in Figure 6.13.

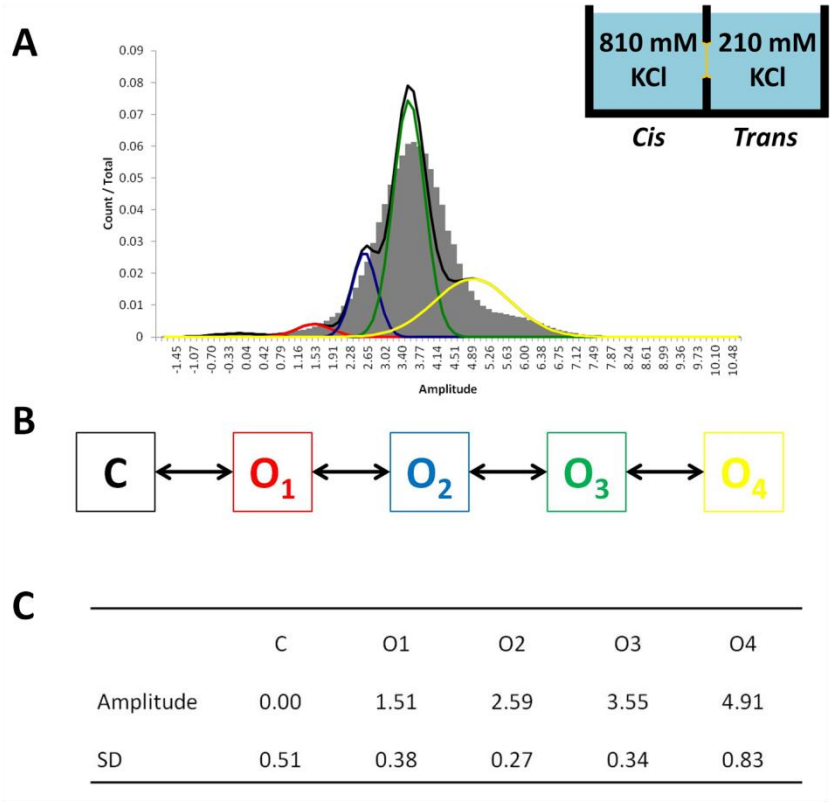
$$Closed \leftrightarrow Open_1 \leftrightarrow Open_2 \leftrightarrow Open_3 \leftrightarrow Open_4$$

Model M 4

The model consists of a closed state and four subsequent open states. It is possible, however, that the correct model is not linear. Model M 4 was therefore compared with a non-linear model, also with 5 states, but with the ability of the channel to move freely between any state as shown below. A log-likelihood ratio test comparing the two models showed that the linear model was a better fit for the data.



Model M 5



C

	C	O1	O2	O3	O4
Amplitude	0.00	1.51	2.59	3.55	4.91
SD	0.51	0.38	0.27	0.34	0.83

Figure 6.13. The 5-state model of *c. elegans* TRIC-B1 gating
(A) An amplitude-histogram for the Type I channel at 0 mV in asymmetrical KCl with the 5 state model fitted. **(B)** The 5 state model of Type I channel (Model M 4). The colours of each state corresponds to a Gaussian fit in **(A)**. **(C)** Details for Model M 4 in **(B)**.

6.2.6.3 An alternative mechanism for *c. elegans* TRIC-B1 channel gating

The TRIC protein is trimeric [81] and has been shown to have three separate, identical pores, one situated in each trimer [112]. Markov models were therefore designed with this channel structure in mind.

At the simplest level, three identical pores should result in three equal open levels: one fully open channel level where all three pores are fully open and two subsequent sub-conductance states where one or more of the pores are closed. Such a scenario would result in a single-channel trace and amplitude histogram similar to that shown in Figure 6.14.

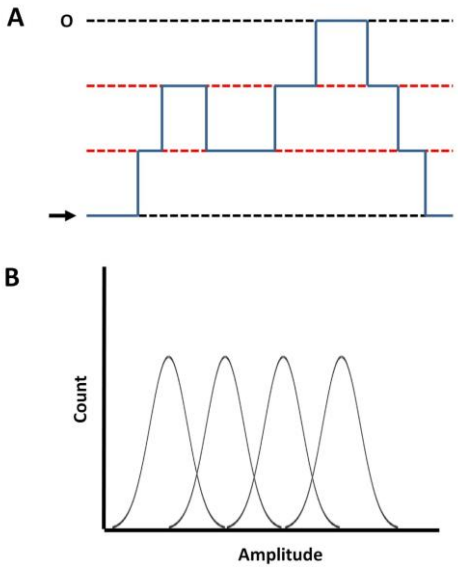


Figure 6.14. A simplified schematic showing how a single-channel recording and a amplitude histogram would appear if an ion channel with three identical pores were gating in the bilayer
(A) A schematic of a section of single-channel recording. The fully open channel level is shown with an O and the closed level is shown with an arrow. The sub-conductance states where <3 pores are open are shown by red broken lines. The channel traces is shown by a blue line. **(B)** A schematic of an amplitude histogram of the same channel.

If we consider the Type I channel, the gating pattern appears more complicated. As a result, a simple linear Markov model with three equal open channel levels representing each monomeric open level as shown below is not a good fit for the data as shown in the typical example of Figure 6.15.

$$Closed \leftrightarrow Open_1 \leftrightarrow Open_2 \leftrightarrow Open_3$$

Model M 6

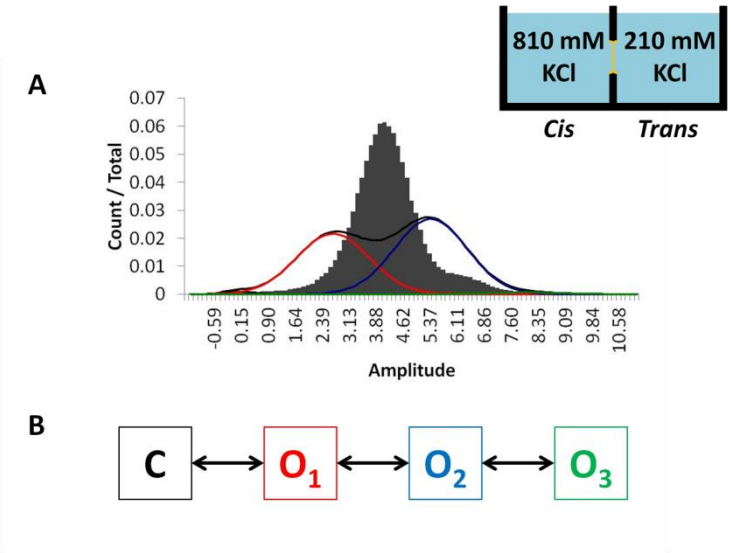


Figure 6.15. The 4-state model of *c. elegans* TRIC-B1 gating
(A) A representative amplitude-histogram for the type I channel at 0 mV in asymmetrical KCl with the 4 state model fitted. **(B)** The 4 state model of *c. elegans* TRIC-B1 (Model M 6). The colours of each state corresponds to a Gaussian fit in **(A)**.

A different model is therefore required. It is possible that the noisy sub-conductance state observed in the type I channel and in the native SR K^+ channel could be artefacts arising from filtering rapid transitions between full open and closed states. If events are too brief to resolve, a burst of openings may then appear as a sub-conductance event, the current amplitude of which will depend on open and closed rates [104]. This has also been suggested for various K^+ channels exhibiting sub-conductance openings [203]–[208]. If this were the case, a second Markov model could be created as shown below.

$$Closed \leftrightarrow Sub\ level_1 \leftrightarrow Open_1 \leftrightarrow Sub\ level_2 \leftrightarrow Open_2 \leftrightarrow Sub\ level_3 \leftrightarrow Open_3$$

Model M 7

This second model assumes that between each fully open state (*$Open_1$* to *$Open_2$* and *$Open_2$* to *$Open_3$*) there exists a "Sub level" artefact created by rapid gating between the open levels. If such a model is fitted to the *c. elegans* TRIC-B1 gating pattern, a much closer fit is observed (Figure 6.16). A log-likelihood ratio test was performed comparing the fit of Model M 4 and Model M 7. The test produced a p-value <0.001, suggesting that Model M 7 is a better fit for the data. It is therefore feasible that the sub-conductance levels observed in the Type I channel gating are time-averaged current levels caused by unresolved rapid gating between two open states or an open and closed state. The same model can also be fitted to skeletal SR K^+ channels gating predominantly in sub-conductance states and under the same experimental conditions (Figure 6.17). Thus, this could be used as evidence to suggest that TRIC-B is an SR K^+ channel.

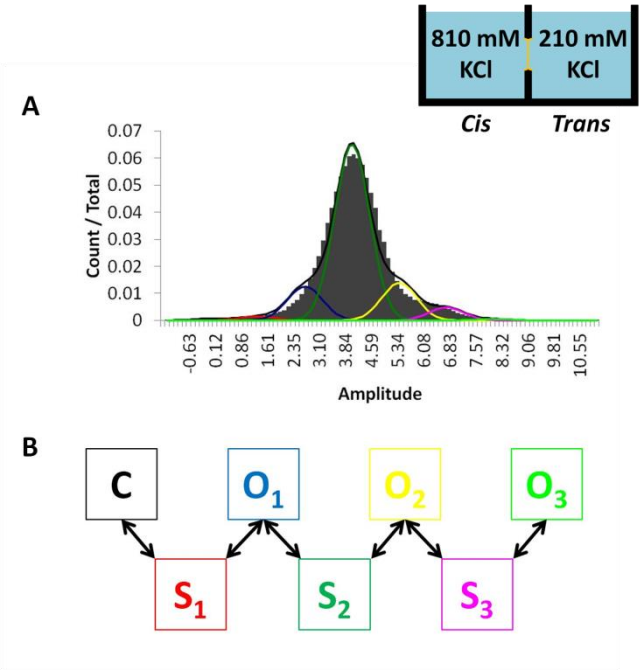
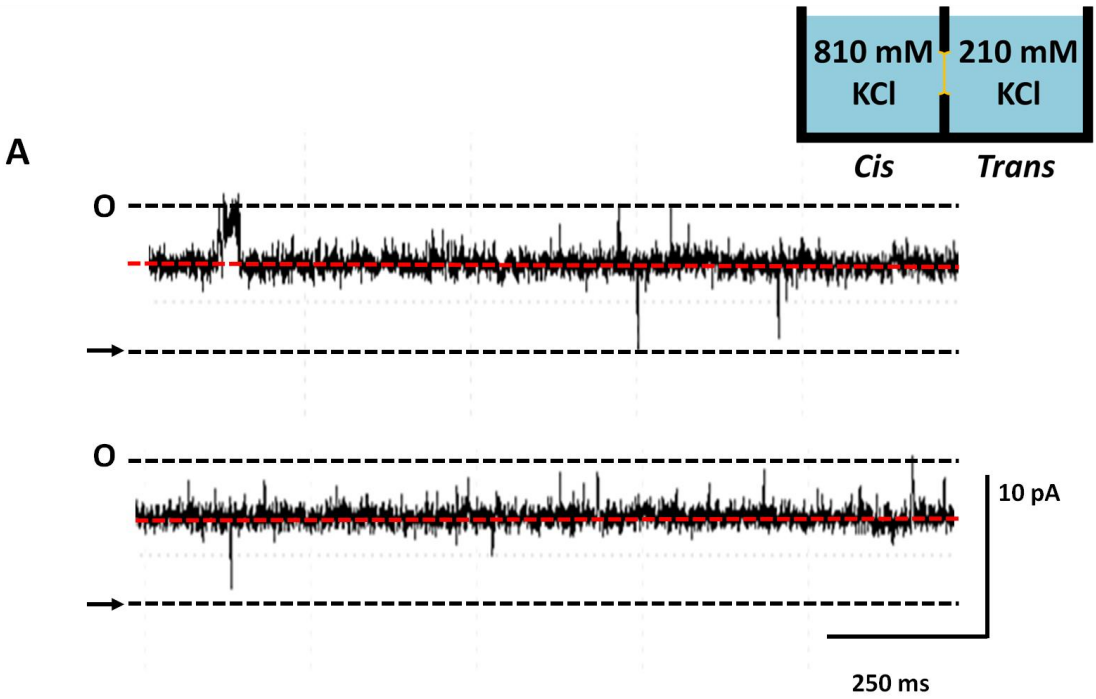
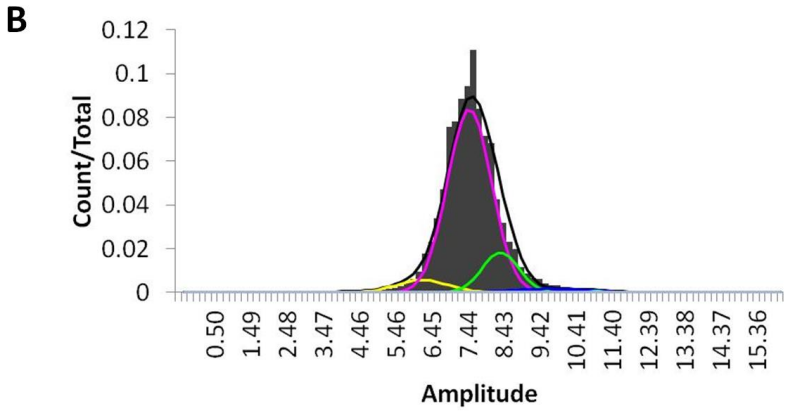


Figure 6.16. The 7-state model of *c. elegans* TRIC-B1 gating
(A) An amplitude-histogram for the Type I channel at 0 mV in asymmetrical KCl with the 7 state model fitted. **(B)** The 7 state model of The Type I channel gating (Model M 7) including the sub-conductance states (S_{1-3}) between each full state (C, O_{1-3}). The colours of each state corresponds to a Gaussian fit in **(A)**.


A
810 mM KCl
210 mM KCl
Cis
Trans
O
O
10 pA
250 ms


B
Count/Total
0.12
0.1
0.08
0.06
0.04
0.02
0
0.50
1.49
2.48
3.47
4.46
5.46
6.45
7.44
8.43
9.42
10.41
11.40
12.39
13.38
14.37
15.36
Amplitude

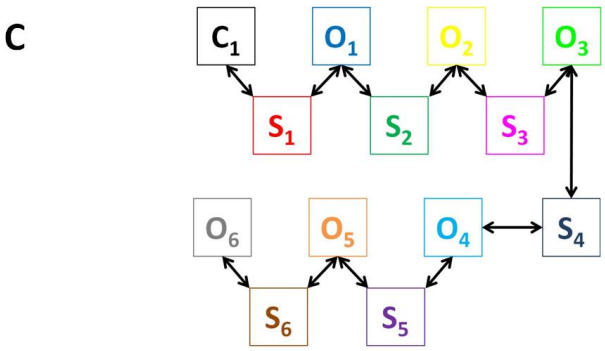

C
C1
O1
O2
O3
S1
S2
S3
O6
O5
O4
S4
S6
S5

Figure 6.17. The native TRIC channel from mouse skeletal muscle
(A) Current-fluctuations through two SR K^+ channels from mouse skeletal muscle which are gating in the sub-conductance state at 0 mV in asymmetrical KCl solutions The channel closed level is shown by an arrow and the fully open level by an O. The predominant sub-conductance state is shown with a red broken line. **(B)** An amplitude histogram of three minutes of recording of the channel shown in **(A)** and fitted with the model shown in **(C)**. The model in **(C)** has been modified to model two channels gating in the bilayer. The colour of each state in the model corresponds to a Gaussian fit on the histogram of the same colour.

6.2.6.4 Pharmacological evidence for the existence of sub-conductance unresolved fast gating

In order to further compare the similarities of purified TRIC channels with SR K^+ channels, the type I channel was recorded in the presence of 1 mM decamethonium in the *cis* chamber (Figure 6.18). Decamethonium is a pharmacological tool which is known to block K^+ channels by occluding the pore. Its blocking effects on the SR K^+ channel are well established [100]. An example of decamethonium block of the SR K^+ channels is shown in Figure 6.19. In the presence of decamethonium, the type I channel gated predominantly into the open channel levels and dwelt far less in the sub-conductance states. This can be seen in the recordings and the amplitude histograms in Figure 6.18. The channel opening to clear open states due to decamethonium allowed the single-channel conductance of the type I channels to be measured in symmetrical 210 mM KCl. The conductance of the channel was found to be 306.7 pS which was larger than that of mammalian SR K^+ channels (210 pS, Chapter 3). The effect that decamethonium has on the channel may suggest that, when decamethonium is present in the *cis* chamber, it occludes the pore of the *c. elegans* TRIC-B1 protein and prevents the fast gating required for the sub-conductance state. The effect of decamethonium on the type I channel is further discussed in the discussion section of this chapter.

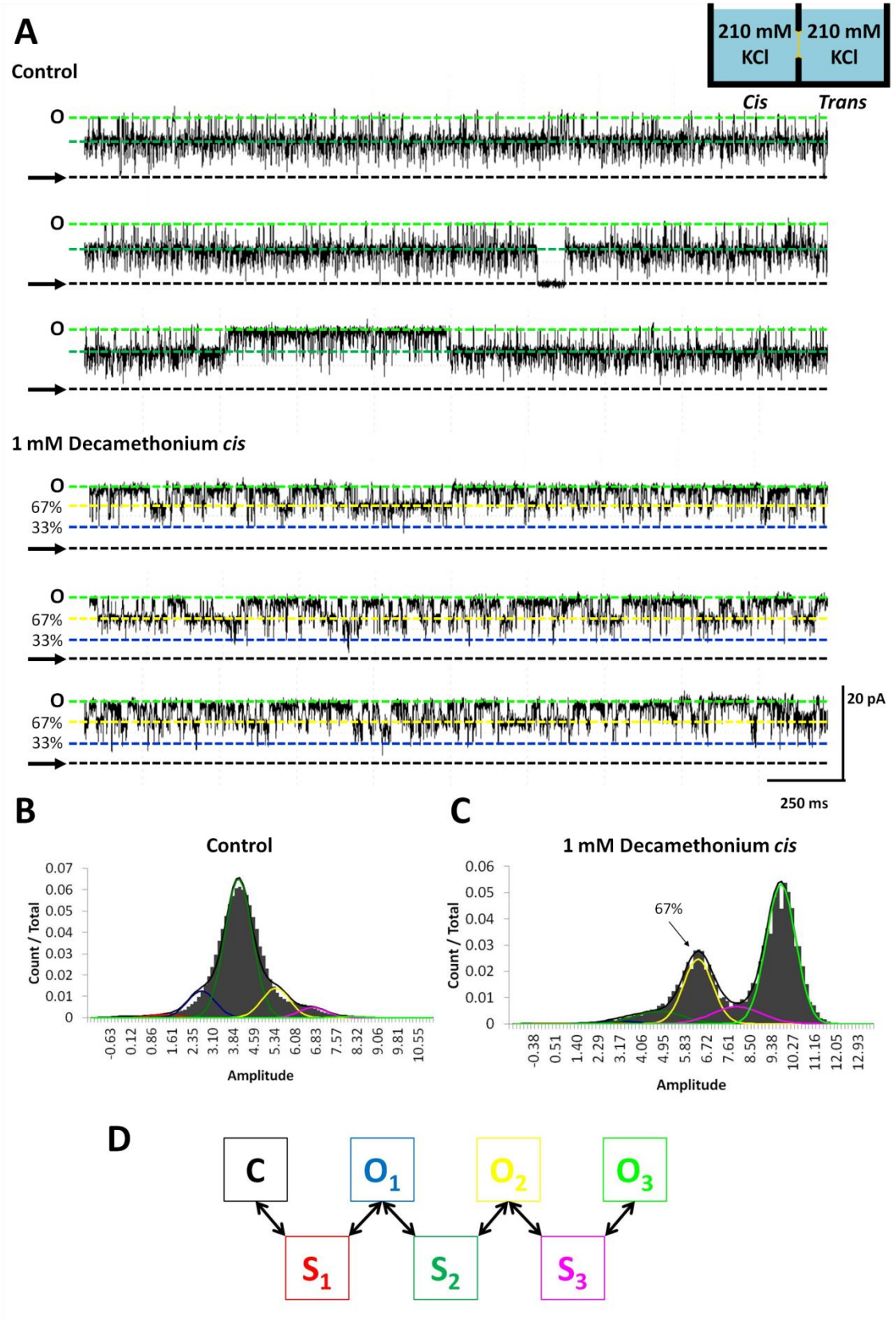

A
Control
210 mM KCl
210 mM KCl
Cis
Trans
O
1 mM Decamethonium cis
67%
33%
20 pA
250 ms
B
Control
Count / Total
Amplitude
C
1 mM Decamethonium cis
67%
Count / Total
Amplitude
D
C
O1
O2
O3
S1
S2
S3

Figure 6.18. The effect of decamethonium on the *c. elegans* TRIC-B1 channel
(A) Current-fluctuations through the Type I channel at +30 mV in symmetrical KCl solution. Recordings are shown in control conditions (top traces) and with 1 mM decamethonium added to the *cis* chamber (bottom traces). The channel closed level is shown by an arrow and the fully open level by O. Sub-conductance states are shown as a red broken line. **(B)** Amplitude histograms of three minutes of recording of the channels shown in the control recording in **(A)** and fitted with the model shown in **(D)**. **(C)** Amplitude histograms of three minutes of recording of the channels shown in **(A)** with 1 mM decamethonium *cis* and fitted with the model shown in **(D)**. The colour of each state in the model corresponds to a Gaussian fit on the histogram of the same colour.

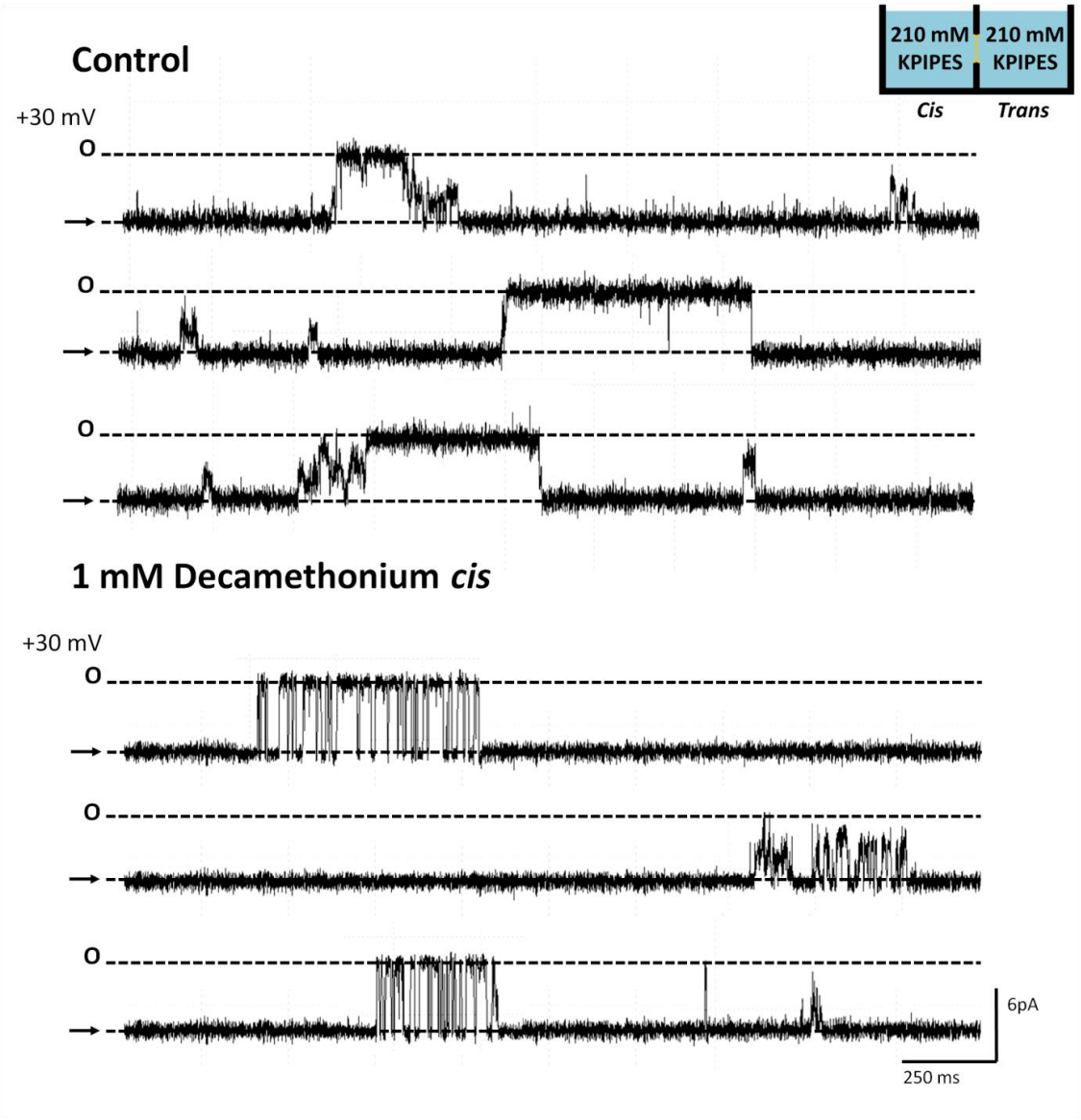


Figure 6.19. The effect of decamethonium on the mouse skeletal SR K^+ channel
Current-fluctuations through the a mouse skeletal SR K^+ channel at +30 mV under control conditions (top traces) and when 1 mM decamethonium was added to the *cis*/cytosolic side of the channel (bottom traces). Channel closed levels are shown by an arrow and apparent fully open levels by an O.

6.2.7 The purified human TRIC-A protein

Purified human TRIC-A protein, reconstituted into liposomes was obtained from our collaborators in the Carpenter laboratory (Structural Genomics Consortium, University of Oxford, UK). Unlike the *c. elegans* TRIC-B1 preparation, after incorporation into bilayers, only one type of channel was observed from the liposomes containing human TRIC-A channels. Figure 6.20 shows a representative single-channel recording of current-fluctuations through the channel at holding potentials of +30 mV, 0 mV and -30 mV. The human TRIC-A protein shared some gating pattern similarities to the *c. elegans* TRIC-B1 protein (Figure 6.1) and the possible TRIC-A protein observed in CHO cells over-expressing TRIC-A (Figure 5.1) such as gating predominantly in a high noise sub-conductance state and only briefly gating to the closed and the apparent fully open state.

6.2.7.1 Permeability properties of the human TRIC-A protein

Figure 6.21 shows the current-voltage relationships for the human TRIC-A protein in KCl and choline-Cl^-, calculated using the apparent fully open state of the channel, and the relative permeabilities for K^+ and choline compared to Cl^-. The current-voltage relationships were linear with conductance values of 709.8±16.0 pS (mean±SD, n=4) for the channel in KCl and 154.4±7.5 pS (mean±SD, n=3) in choline-chloride. The sub-conductance state of the channel was observed to be consistently at a level which was 70% of the apparent fully open channel level and had a conductance of 506.6±10.8 pS (mean±SD, n=4). The human TRIC-A protein was found to be more selective for K^+ and choline over Cl^- with a P_K/P_{Cl} value of 5.6±4.9 (mean±SD, n=4) and a $P_{choline}/P_{Cl}$ of 16.0±4.5 (mean±SD, n=3).

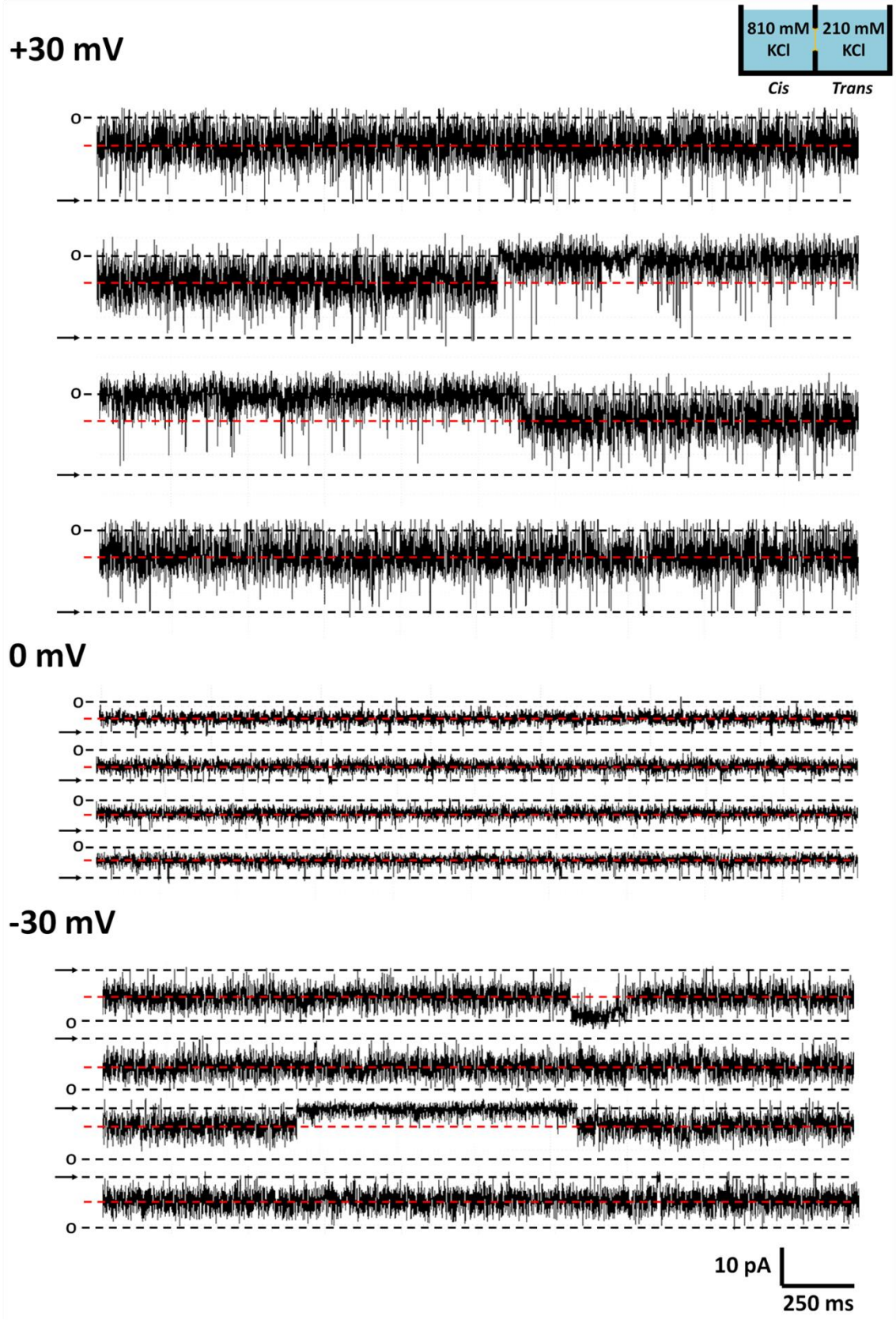
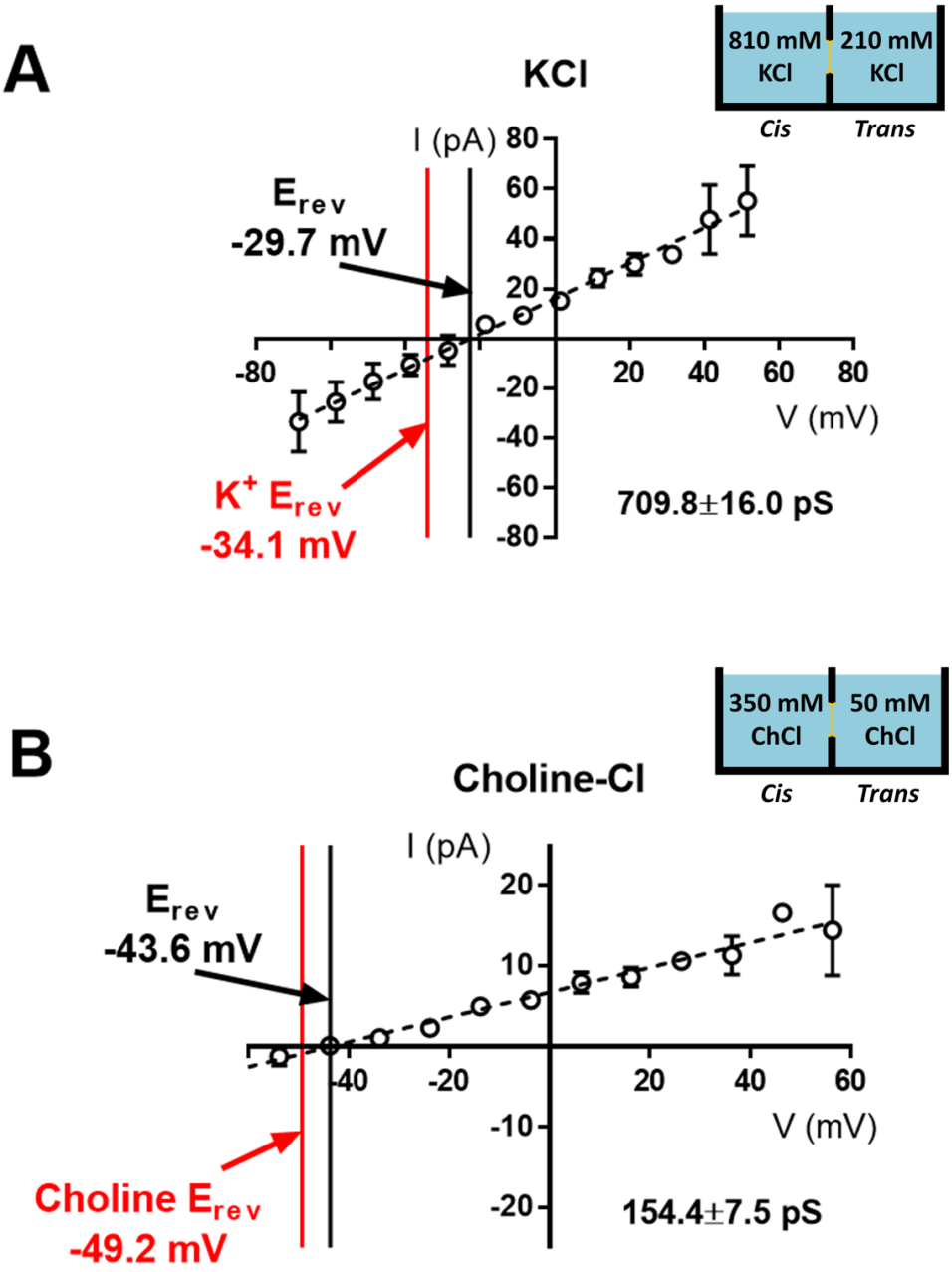

+30 mV
810 mM KCl
210 mM KCl
Cis
Trans
o
0 mV
-30 mV
10 pA
250 ms

Figure 6.20. Current-fluctuations through the human TRIC-A channel
Current-fluctuations through the purified human TRIC-A channel at the stated holding potentials. Experiments were conducted in asymmetrical conditions (*cis*: 810 mM KCl, 10 µM Ca^{2+}, 20 mM HEPES, pH 7.2; *trans*: 210 mM KCl, 10 µM Ca^{2+}, 20 mM HEPES, pH 7.2). The channel closed level is shown by an arrow and the apparent fully open level by O. Proposed sub-conductance states are shown by a red line. The recordings are representative of 7 experiments.


A
KCl
810 mM KCl
210 mM KCl
Cis
Trans
I (pA)
80
60
40
20
-20
-40
-60
-80
-80
20
40
60
80
V (mV)
E rev
-29.7 mV
K+ E rev
-34.1 mV
709.8±16.0 pS
B
Choline-Cl
350 mM ChCl
50 mM ChCl
Cis
Trans
I (pA)
20
10
-10
-20
-40
-20
20
40
60
V (mV)
E rev
-43.6 mV
Choline E rev
-49.2 mV
154.4±7.5 pS

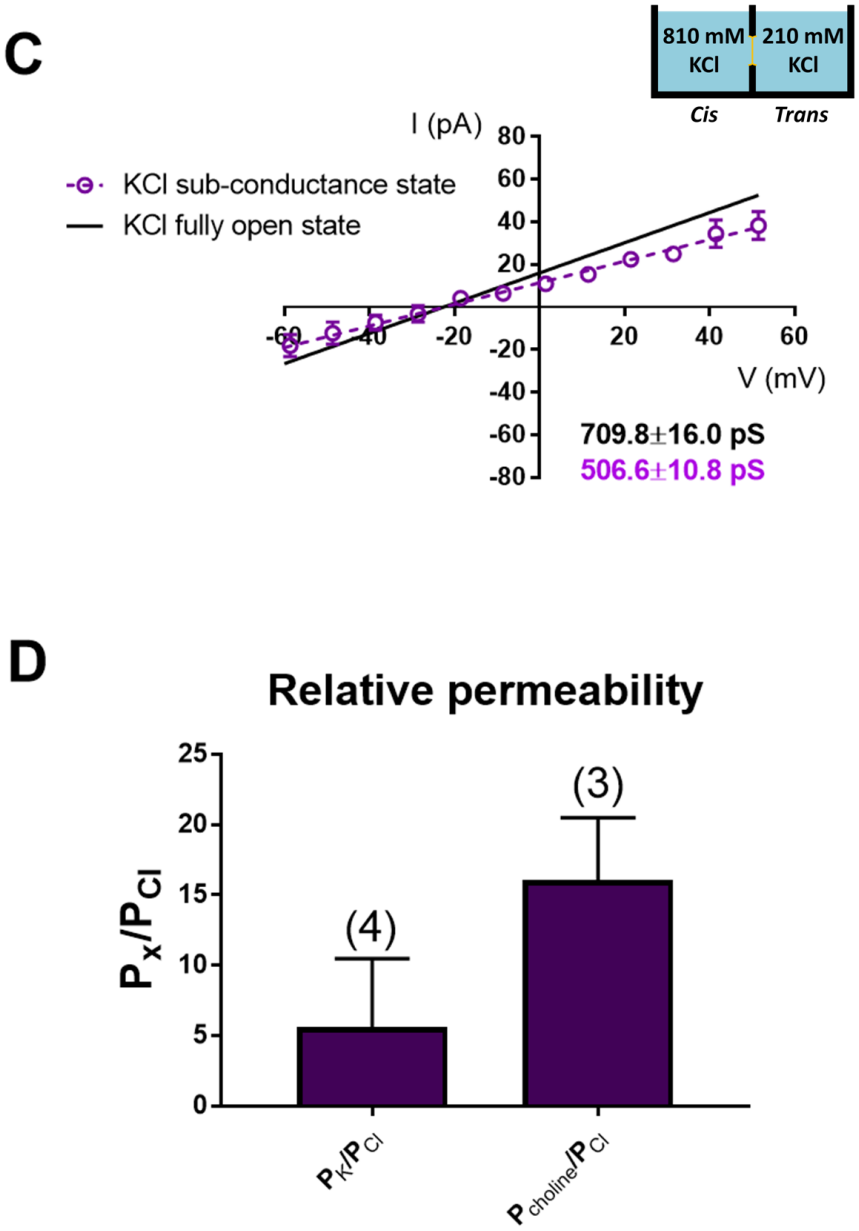


Figure 6.21. The permeability properties of the human TRIC-A channel
(A) Current-voltage relationship for the type I channel in asymmetrical KCl. **(B)** Current-voltage relationship for the type I channel in asymmetrical choline-Cl. **(C)** The current-voltage relationship of the type I channel sub-conductance state in asymmetric KCl. The solid black line shows the linear regression line for the fully open state for reference. The sub-conductance state E_{rev} was –22.6 **(D)** The relative permeabilities of the human TRIC-A channel in KCl and choline-Cl. The number of experiments is shown in brackets above each respective bar. Values are of the mean±SD. Current-voltage relationships are fitted by means of a linear regression, the cation E_{rev} is shown as a red vertical line on each graph, and the conductance value is shown in the lower right on each graph.

6.2.8 A comparison of the *c. elegans* TRIC-B1 and human TRIC-A channels

A visual comparison of the recordings in Figure 6.1 (*c. elegans* TRIC-B1) and Figure 6.20 (human TRIC-A) reveals that, although the two channels retain similarities, such as the gating in a high noise sub-conductance state and only brief fully open events, important differences exist. The human TRIC-A protein gates in a faster manner, especially at more negative potentials, and dwells in the closed channel state for longer periods compared to the *c. elegans* TRIC-B1 channel. This is demonstrated in Figure 6.22.

Further differences exist in the conductance properties of both the fully open and sub-conductance states of the channels. The human TRIC-A protein exhibits a larger fully open channel conductance in both KCl (TRIC-A: 709.8±1.6 pS, TRIC-B1: 352.6±9.5 pS, mean±SEM) and choline-chloride (TRIC-A: 154.4±7.5 pS, TRIC-B1: 41.7±1.8 pS, mean±SEM) when compared with the *c. elegans* TRIC-B1 (Figure 6.23). The sub-conductance levels observed in both channels also differed. When comparing the highest Po sub-conductance level for each channel, the human TRIC-A protein dwelt in a sub-conductance state which was consistently ~70 % of the fully open channel level, whereas the *c. elegans* TRIC-B1 channel sub-conductance levels were voltage sensitive, with negative holding potentials resulting in ~70 % sub-conductance levels and positive potentials resulting in sub-conductance levels at only ~30 % of the fully open channel level (Figure 6.23E).

Differences also existed in the permeability of the channels to Cl^-. While both proteins share similar permeability properties and pass both K^+, choline, and Cl^-, the human TRIC-A channel is more permeable to Cl^- when compared with the *c. elegans* TRIC-B1 channel (Figure 6.23F).

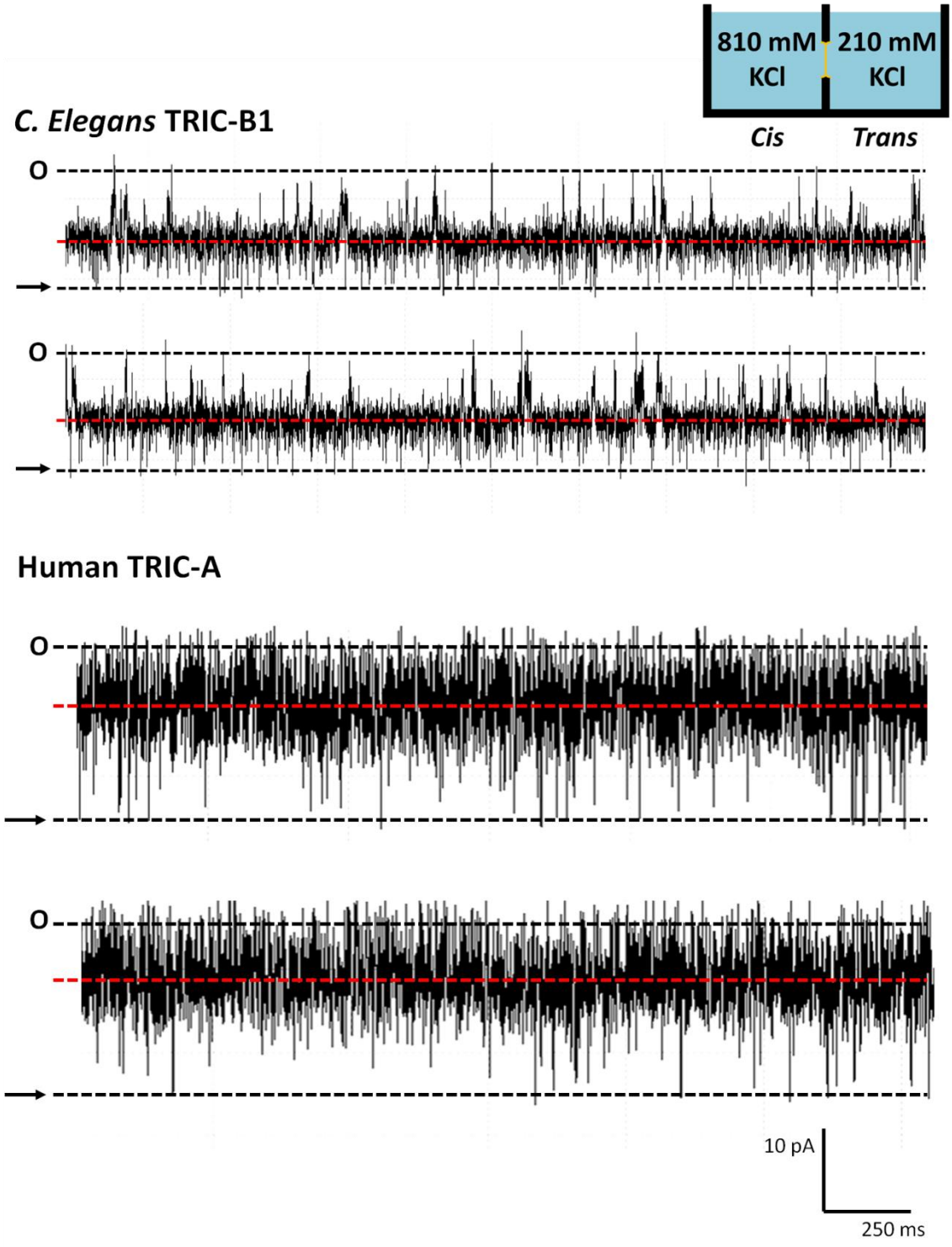
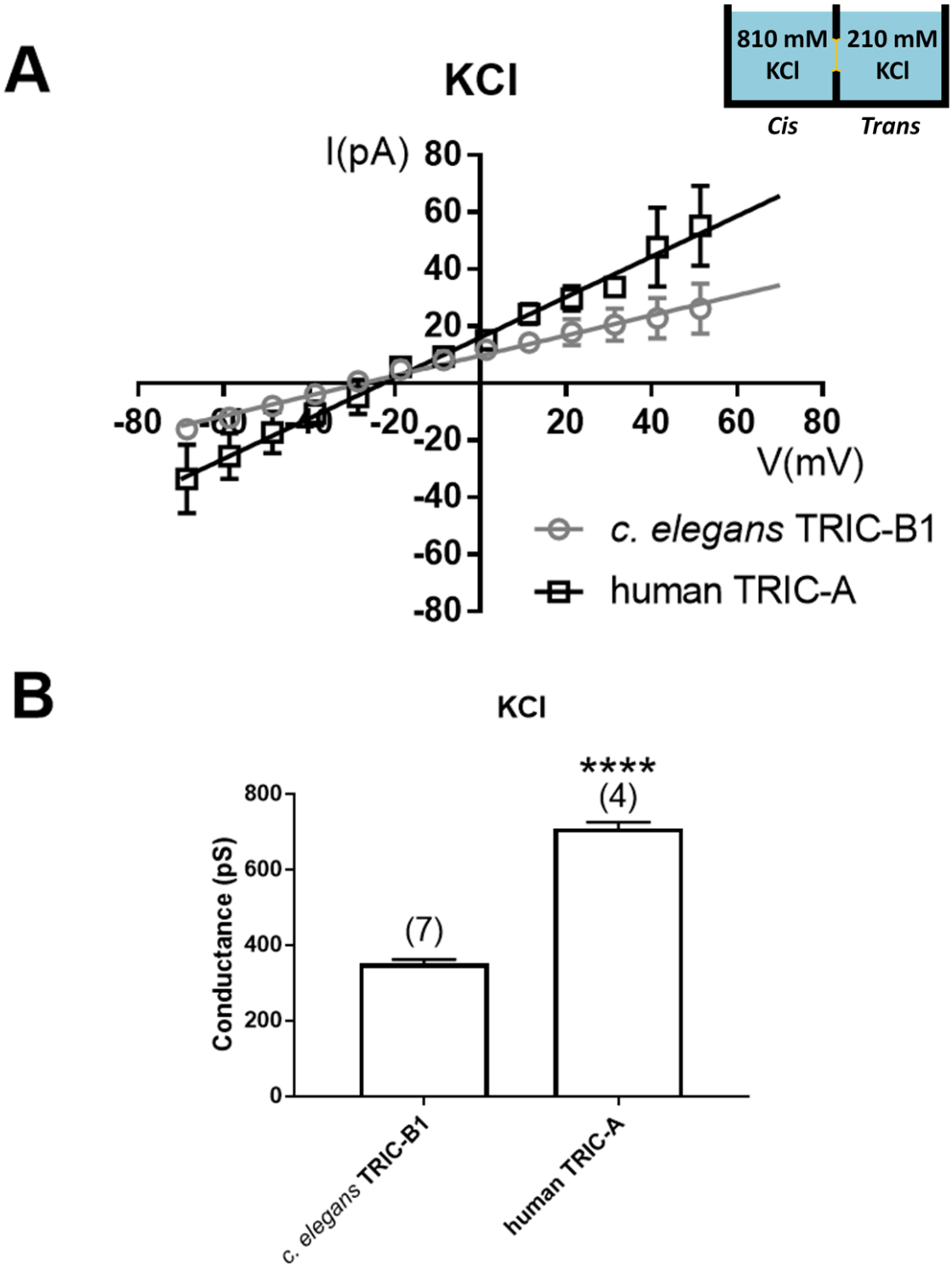
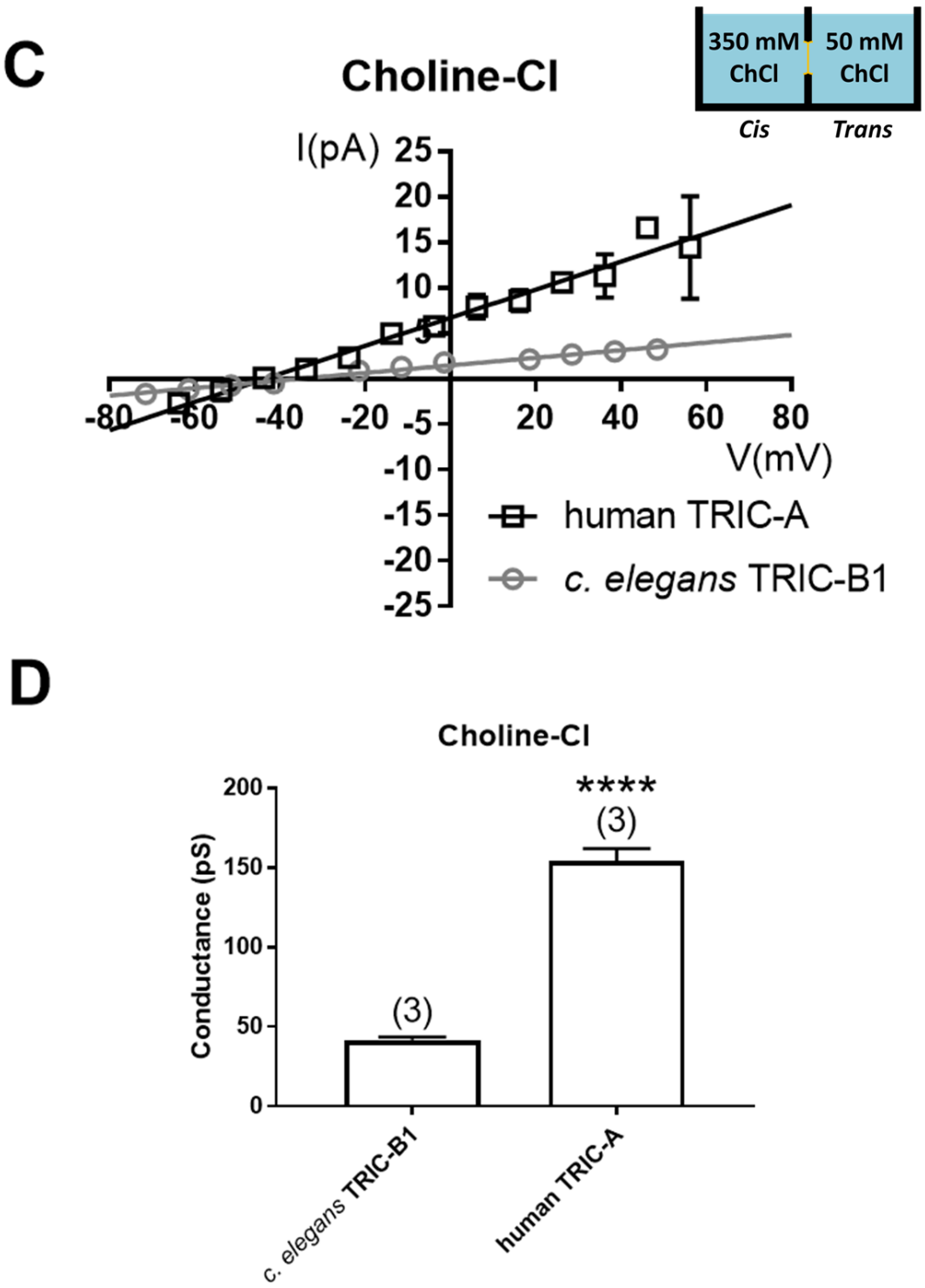


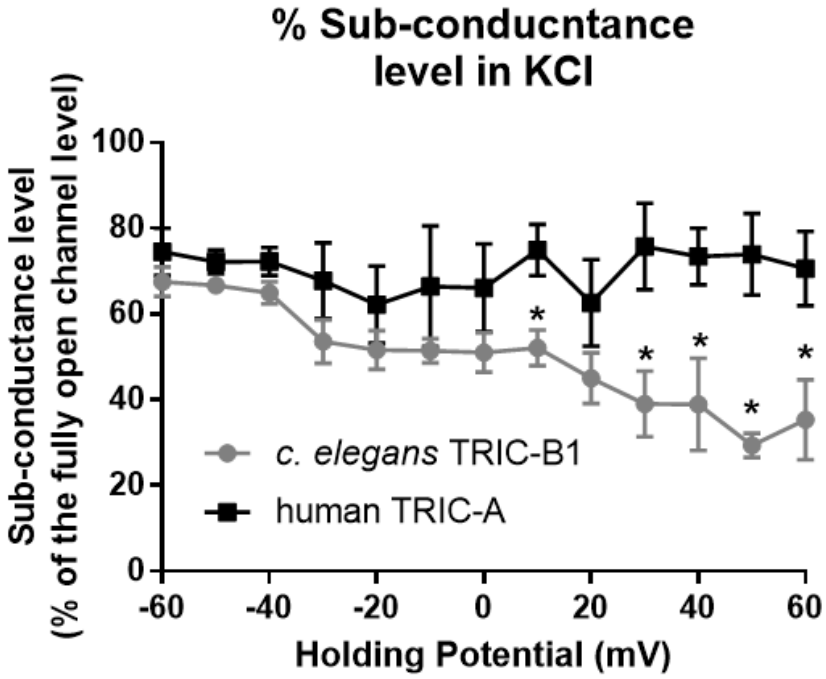
Figure 6.22. Current-fluctuations through the *c. elegans* TRIC-B1 channel and the human TRIC-A channel

Current-fluctuations through the *c. elegans* TRIC-B1 channel and the human TRIC-A channel in asymmetrical KCl and at a +30 mV holding potential. Channel closed levels are shown by an arrow and apparent fully open channel levels are shown by O. The proposed sub-conductance state is shown by a red broken line.


A
KCl
810 mM KCl
210 mM KCl
Cis
Trans
I(pA)
80
60
40
20
-20
-40
-60
-80
-80
-60
-40
-20
20
40
60
80
V(mV)
c. elegans TRIC-B1
human TRIC-A
B
KCl
****
(4)
(7)
800
600
400
200
0
Conductance (pS)
c. elegans TRIC-B1
human TRIC-A


C
Choline-Cl
350 mM ChCl
50 mM ChCl
Cis
Trans
I(pA)
25
20
15
10
5
-5
-10
-15
-20
-25
-80
-60
-40
-20
20
40
60
80
V(mV)
human TRIC-A
c. elegans TRIC-B1
D
Choline-Cl
Conductance (pS)
200
150
100
50
0
****
(3)
(3)
c. elegans TRIC-B1
human TRIC-A

E


% Sub-conducntance level in KCl
Sub-conductance level (% of the fully open channel level)
100
80
60
40
20
0
-60
-40
-20
0
20
40
60
Holding Potential (mV)
c. elegans TRIC-B1
human TRIC-A
*
*
*
*
*

F

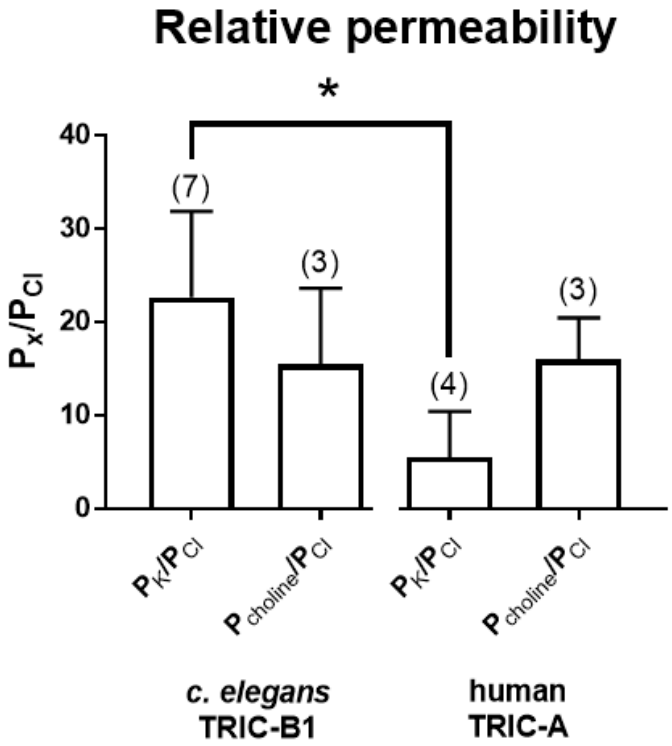

Relative permeability
*
40
30
20
10
0
P_x/P_{Cl}
(7)
(3)
(4)
(3)
P_K/P_{Cl}
$P_{choline}/P_{Cl}$
P_K/P_{Cl}
$P_{choline}/P_{Cl}$
c. elegans TRIC-B1
human TRIC-A

Figure 6.23. A comparison of the biophysical properties of the *c. elegans* TRIC-B1 and the human TRIC-A channels
(A) Current-voltage relationships of the *c. elegans* TRIC-B1 and human TRIC-A proteins in asymmetrical KCl (*cis*: 810 mM KCl, 10 µM Ca^{2+}, 20 mM HEPES, pH 7.2; *trans* : 210 mM KCl, 10 µM Ca^{2+}, 20 mM HEPES, pH 7.2). **(B)** A comparison of the single-channel conductance properties of the the *c. elegans* TRIC-B1 and human TRIC-A proteins in asymmetrical KCl. **(C)** Current-voltage relationships of the *c. elegans* TRIC-B1 and human TRIC-A proteins in asymmetrical choline-Cl (*cis*: 350 mM choline-Cl, 10 µM Ca^{2+}, 10 mM HEPES, buffered to pH 7.2 with Tris; *trans* : 50 mM choline-, 10 µM Ca^{2+}, 10 mM HEPES, buffered to pH 7.2 with Tris). **(D)** A comparison of the single-channel conductance properties of the the *c. elegans* TRIC-B1 and human TRIC-A proteins in asymmetrical choline-Cl. **(E)** How the sub-conductance level changes relative to the fully open channel level as voltage increases for the *c. elegans* TRIC-B1 (gray circles) and human TRIC-A (black squares) proteins. **(F)** A comparison of the permeability ratio (P_x/P_{Cl}) from the *c. elegans* TRIC-B1 and human TRIC-A proteins. Values are of the mean±SEM or mean±SD. The number of experiments conducted is indicated in brackets inside or above the respective bar.

6.3 Discussion

As discussed earlier in this chapter, four different channel types were observed in the *c. elegans* TRIC-B1 preparation. Establishing which channel type is the TRIC-B1 protein and which types are contaminants/artefacts was therefore necessary.

Type III channels were observed in control tissue and therefore can be discounted from the study. The type IV channel was not observed in bilayer experiments after the liposomes had been extruded, and its biophysical properties varied widely between experiments. It is therefore possible that the type IV channel is an artefact of the lipid bilayer. The type II channel, like the type IV channel, was not observed in extruded liposomes; however, unlike the type IV channel, the channel properties were found to be more uniform. It is feasible that this channel could be a result of multiple TRIC-B1 channels gating together in the bilayer.

The type I channel was the most common channel observed and it was present in all liposome preparations apart from empty liposome controls. The type I channel single-channel properties were uniform and the channel displayed similar gating to that of the other possible TRIC-A channel observed in Chapter 5 of this thesis (Figure 5.1). Considering the data presented in this chapter, I speculate that the most likely candidate for the *c. elegans* TRIC-B1 protein is the type I channel.

6.3.1 Permeability of the Type I channel/*c. elegans* TRIC-B1

This chapter has demonstrated that the *c. elegans* TRIC-B1 channel is more selective for cations over anions, but does pass both. A greater understanding of the channel pore properties can be gained by studying the current-voltage relationships and pharmacological properties of the channel in more detail. If we consider the current-voltage relationships shown in Figure 6.2, as expected, in symmetrical KCl and choline-chloride, the current-voltage relationship passes through 0. Also, as expected for a cation channel, when the cation concentration of the *cis* chamber is raised relative to the *trans* chamber, a shift to the left of the graph is observed. The pore of the *c. elegans* TRIC-B1 channel is more complex, however. The data follows a curve, rather than a linear pattern and the rightward shift is not parallel. Figure 6.24 shows the data re-plotted to demonstrate these properties more clearly.

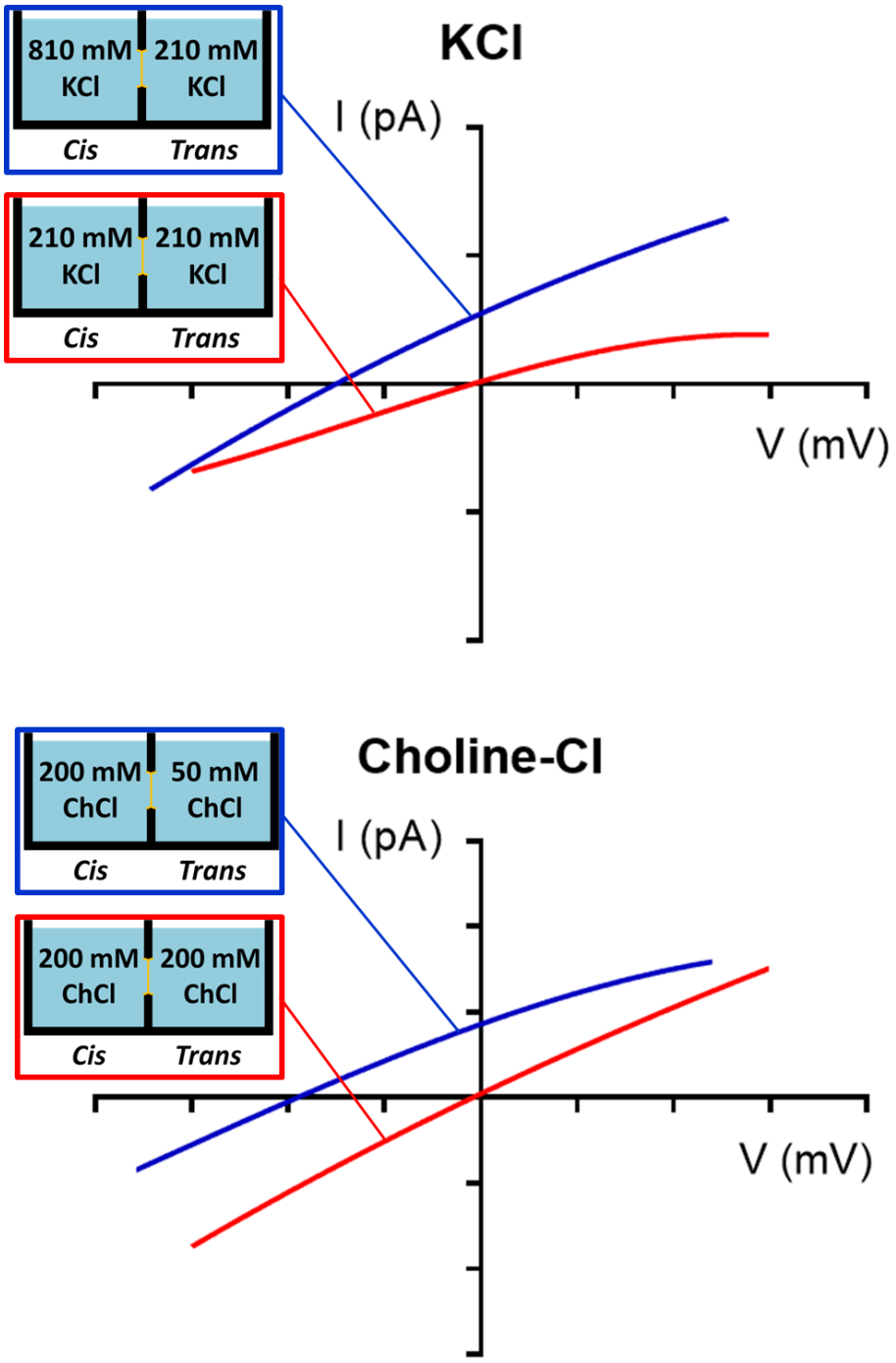


Figure 6.24. Current-voltage relationships for the *c. elegans* TRIC-B1 channel in KCl and choline-chloride showing the shift from symmetrical solutions (red) to asymmetrical solutions (blue)

It is possible that such a shift is observed due to two factors. Firstly, when a pore is selective for multiple ions present in the surrounding solution, it is possible that competition for the pore occurs which will alter with holding potential, resulting in a curved IV plot. This effect is amplified with higher ionic concentrations. Secondly, although the pore passes both Cl^- and K^+, it is more selective for K^+. When the ionic concentration is increased asymmetrically, this effect is also amplified, resulting in an unbalanced increase in current at positive potentials and a non-parallel shift.

Figure 6.2B shows that the *c. elegans* TRIC-B1 channel is almost entirely selective for choline over Cl^-. This finding is apparently contradictory to the data obtained in KCl, where some Cl^- was observed to pass through the channel. It is possible however, that choline occludes the pore as well as passing through it. At high choline concentrations, choline ions would therefore prevent Cl^- from permeating through the pore, and the channel would appear entirely selective for choline. Evidence for this is found in the small conductance of the channel in choline-chloride compared to KCl, and the non-parallel shift between asymmetrical and symmetrical solutions.

Figure 6.12 also shows that Ca^{2+} passes through the *c. elegans* TRIC-B1 channel, but with a lower conductance than K^+. The data also suggests that in NMDG-chloride no ions permeate the channel. The data obtained in NMDG-chloride could be due to NMDG occluding the pore, in a similar way to that of choline, but unlike choline, NMDG is not permeant.

Considering these channel properties, a number of predictions can be made about the physical properties of the channel pore. For the purpose of this discussion, I have assumed that the *c. elegans* TRIC-B1 protein contains three identical pores as has been suggested in the structure of the channel [112].

The table below details the approximate dimensions of ions (dehydrated) used for this study as a comparison of size.

Ion	Length (Å)	Width (Å)	Depth (Å)	Reference
K^+	2.66	2.66	2.66	[209]
Cl^-	3.62	3.62	3.62	[209]
Ca^{2+}	1.98	1.98	1.98	[209]
Choline	7.49	5.02	4.49	[194]
NMDG	13.06	5.58	5.33	[194]

Table 3. Approximate dimensions of ions used in *c. elegans* TRIC-B1 experiments

At its simplest form, the ability of an ion to permeate the pore is dependent on the size of both the ion and the pore, and whether the pore is large enough at its narrowest point to allow the ion to pass through. Considering monovalent cations, K^+ passes through the pore of the *c. elegans* TRIC-B1 channel with a high conductance, indicating that the pore is a minimum of 2.66 Å wide. Similarly choline, with a minimum diameter of 5.02 Å also passes through the pore, suggesting a pore diameter of at least 5.02 Å. As has been suggested in this chapter, NMDG blocks the pore. As choline is small enough to pass through and NMDG is large enough to block the pore, an estimate for the pore diameter at its narrowest point would be between 5.02 Å and 5.58 Å (the smallest diameters of choline and NMDG). This is a larger pore radius than that of the published structure, where the pore diameter was estimated at 3.0 Å to 4.6 Å [112]. It should be noted that the resolution of the TRIC-B1 structure was 3.3 Å. It is also possible that the published structure is that of the closed channel conformation and that the open confirmation would exhibit a pore diameter closer to that predicted above.

It is also possible to use the *c. elegans* TRIC-B1 data to suggest the selectivity properties of the channel pore. Ion channel selectivity is defined by the amino acid sequence which makes up the selectivity filter of the pore. These residues can filter ions from the surrounding solutions based on their ionic size (as discussed above) and valency. Experimental data for the *c. elegans* TRIC-B1 suggests that the channel selectivity filter allows both cations and anions to permeate

the pore, but with a higher selectivity for cations. According to the published structure of the *c. elegans* TRIC-B1, two negatively charged residues are present in the proposed pore region, D72 and E130. E130 is highly conserved in mammalian TRIC proteins and binds the $PI(4,5)P_2$ molecule in the TRIC-B1 protein. The D27 residue is not conserved. In human TRIC-A and TRIC-B, it is replaced by uncharged serine and glycine residues, respectively. The lack of a charged residue at this point may result in different ion selectivity in the human TRIC isoforms when compared with those from *c. elegans*. It should be noted that positively charged residues are highly conserved in all TRIC isoforms.

Ca^{2+} passes through the pore, but with a lower conductance compared to K^+. It is possible that this is due to Ca^{2+} having a higher hydration enthalpy. The hydration enthalpy is a measure of the ability of an ion to bind to water molecules in solution. In order for an ion to pass through most channel pores, the ion must be partly or fully de-hydrated; the hydration enthalpy is the energy required to achieve this for any given ion. Due to its double charge and small size, Ca^{2+} has a relatively high hydration enthalpy (-397 Kcal/mol [209]) compared to K^+ (-85 Kcal/mol [209]). It therefore requires more energy to remove Ca^{2+} from solution than it does K^+ and as such, K^+ ions are more permeant than Ca^{2+}.

Due to the large size of the pore, however, it is possible that ions could pass through in a partial or even fully hydrated state. The hydrated diameter of K^+, Cl^- and Ca^{2+} are 6.3 Å, 5.4 Å and 6.96Å, respectively [209]. While the diameters of the fully hydrated K^+ and Ca^{2+} ions are too large to fit through the predicted pore diameter, it is feasible that the pore of the *c. elegans* TRIC-B1 channel could allow a fully hydrated Cl^- ion to permeate, suggesting a possible pathway for Cl^- current through the channel.

6.3.2 Gating of the *c. elegans* TRIC-B1 channel

I have speculated in this chapter that the complex gating of the *c. elegans* TRIC-B1 channel could be caused by rapid gating between the fully open states of each monomeric pore. One limitation of electrophysiological techniques is the resolution at which data can be recorded. Some ion channel gating events may be too brief to accurately measure and thus can result in apparent sub-conductance states. This has also been suggested for various K^+ channels exhibiting sub-conductance openings [203]–[208]. In this chapter I have suggested that a model, which takes this into account by including an extra state between each monomeric open level, could be the best fit for the data. Further to this, I added the potassium channel pore blocker, decamethonium, to the *cis* side of the channel. Decamethonium caused the *c. elegans* TRIC-B1 channel to gate mainly to the suggested monomeric open channel levels, removing the 'sub-conductance' state gating which may be caused by rapid channel gating rather than a defined pore structure. I speculate that decamethonium achieved this by entering the pore and propping it open without fully blocking K^+ current, thus causing slower blocking events and preventing the rapid gating between open-open and open-closed states that can be observed without decamethonium. A schematic of a possible mechanism for the block of TRIC channels by a folded decamethonium molecule, as suggested by Coronado and Miller in 1980 for SR K^+ channel block [100], is shown in Figure 6.25. It should be noted, however, that the model proposed by Coronado and Miller was based on block from the luminal (*trans*) channel side and that they did not observe block from the cytosolic side as we do (Figure 6.19). This experiment was only performed once and needs repeating. Further experiments are also required to characterise the concentration and voltage-dependence of the decamethonium effect before we can conclude any mechanism with certainty.

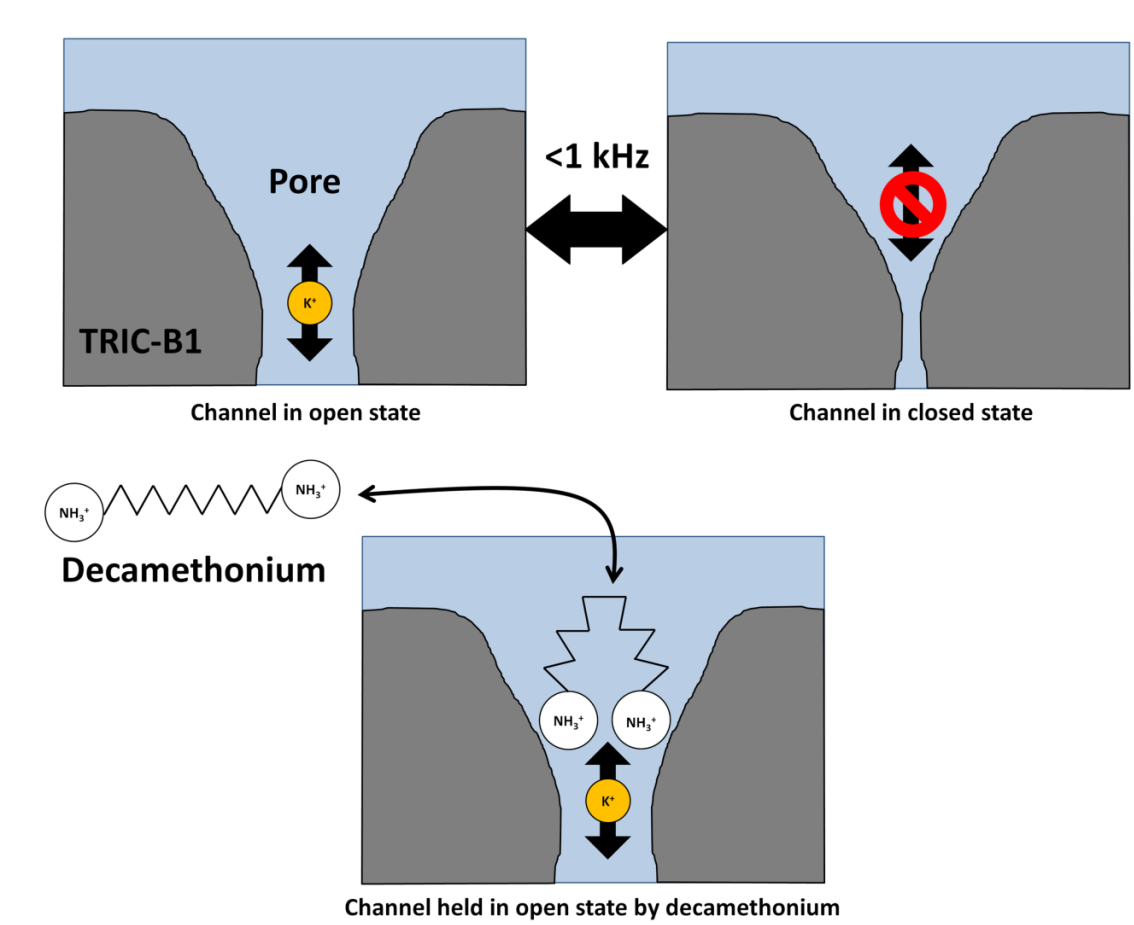


Figure 6.25. A schematic of how decamethonium block could alter the channel behaviour of the TRIC-B1 channel

6.3.3 Comparison to published data

Three papers have recently been published describing the structure of the TRIC protein [111]–[113]. Figure 6.26 includes extracts from the papers showing the single-channel gating of the TRIC channel. None of the figures in these papers show currents which resembles the channels that I recorded from the *c. elegans* TRIC-B1 and report smaller conductance values of 150-160 pS [112][113]. This is especially surprising, as Figure 6.26A shows data from the group from which we obtained the *c. elegans* TRIC-B1.

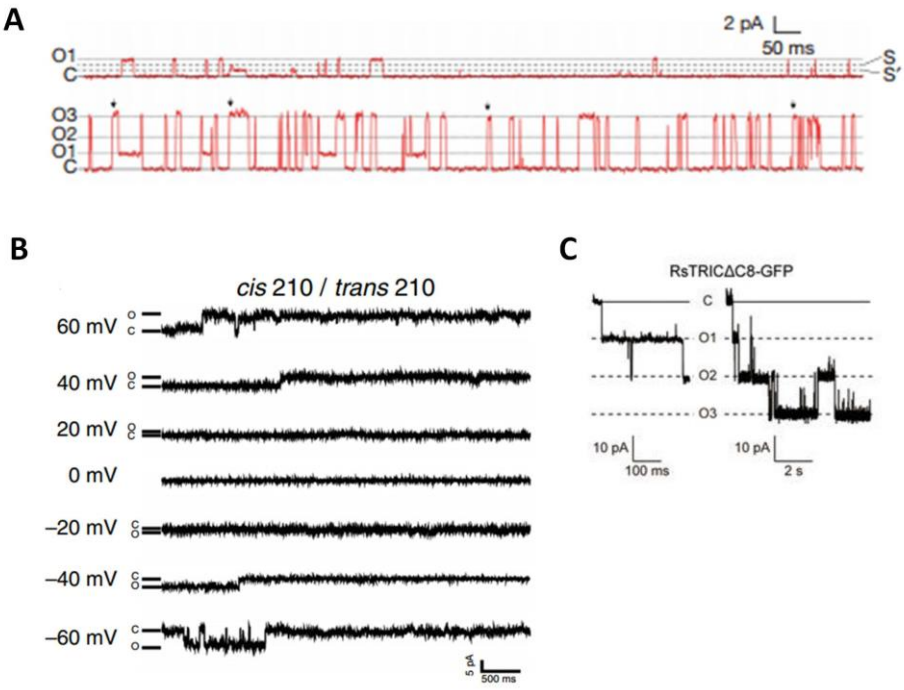


Figure 6.26. Published electrophysiological data of TRIC channels
(A) *c.elegans* TRIC-B1 from Yang *et al.* 2016. Recordings were made in 210 mM symmetrical solutions and the single-channel conductance was 153.2 pS [112]. **(B)** Prokaryotic SaTRIC from Su *et al.* 2016. Recordings were made in 210 mM symmetrical solutions and the single-channel conductance was 159pS [113]. **(C)** Prokaryotic RsTRIC from Kasuya *et al.* 2017. Solutions and conductance values are not stated in the paper [111].

6.3.4 Is TRIC responsible for SR K^+ channel currents?

One of the key aims of this thesis was to establish whether the SR K^+ channels, observed in planar lipid bilayer experiments, are TRIC channels. In this chapter, I have described mammalian SR K^+ channel gating behaviour which exhibits some similarities to that of the purified *c. elegans* TRIC-B1 and human TRIC-A channels. Both the mammalian SR K^+ channels, shown in Figure 6.9 and Figure 6.10, and the purified TRIC channels gate predominantly to a high-noise sub-conductance state at around 70% of the apparent fully open channel level. The channels only gate briefly to the closed level and the apparent fully open channel level. Where the channels differ significantly, however, is in the permeability properties. The mammalian SR K^+ channel has been shown to be impermeable to Cl^- [72][97], Ca^{2+} [72][98][99] and choline [90], all of which pass through both the purified *c. elegans* TRIC-B1 and human TRIC-A channels. It is unclear whether this is due to differences between species (although the pore regions are largely conserved), or whether the TRIC channel is damaged during the purification technique, resulting in a less selective pore. It is clear that, although some of the evidence in this chapter supports TRIC proteins being SR K^+ channels as are observed in bilayer recordings, further experiments are required to fully establish this.

6.4 Further experiments

If time and resources allowed, this project would be developed further. It would be useful to develop a more effective way of studying the TRIC preparation where only the Type I channel is present; this could be accomplished by dialysation to minimise the detergent present in the bilayer or by extrusion of liposomes prior to experimentation as this seemed to remove unwanted currents. Studying the proteins in bilayers containing different lipids may also achieve this. Alternatively, the proteins could be expressed through other systems such as a cell-free wheat-germ system which should eliminate other ion channels. Further study into the

permeability of the *c. elegans* TRIC-B1 would also be interesting, especially to study ions known to permeate the SR K^+ channel such as Na^+ and Cs^+. If possible, the isolation of native ER/SR from *c. elegans* and a study of the SR K^+ channels present could answer questions about species differences. The development and the study of pure preparations other TRIC isoforms such as human TRIC-B would also help on the understanding of the differences between TRIC isoforms, and the study of purified mouse or sheep TRICA/B would allow a more direct comparison with native tissue.

Chapter 7. SR channels from *Mg23* KO mouse tissue

7.1 Introduction

MG23 is an ion channel which was first identified by the laboratory of Hiroshi Takeshima in 1998 [162]. The channel is abundantly expressed in the membranes of the ER/SR, especially in fast-twitch striated muscle fibres [151]. Although a physiological role for MG23 has not yet been established, it has been suggested that MG23 may play a role in promoting apoptosis by generating lethal signals from the SR/ER [158][159]. Structurally, EM microscopy techniques have suggested that MG23 proteins come together to form a large bowl-shaped structure in the SR membrane [164]. Single-channel analysis of purified MG23 proteins found it to be a cation selective channel with a low Po and gate with brief open events to a fully open state. An example of purified MG23 single-channel events is shown in Figure 7.1A. Multiple MG23 channels were also observed to gate in the bilayer. Current-fluctuations through multiple purified MG23 channels are shown in Figure 7.1B. Despite these findings, currents from the MG23 channel are yet to be identified in native SR, and it is unclear whether any potential role for this channel exists in EC coupling.

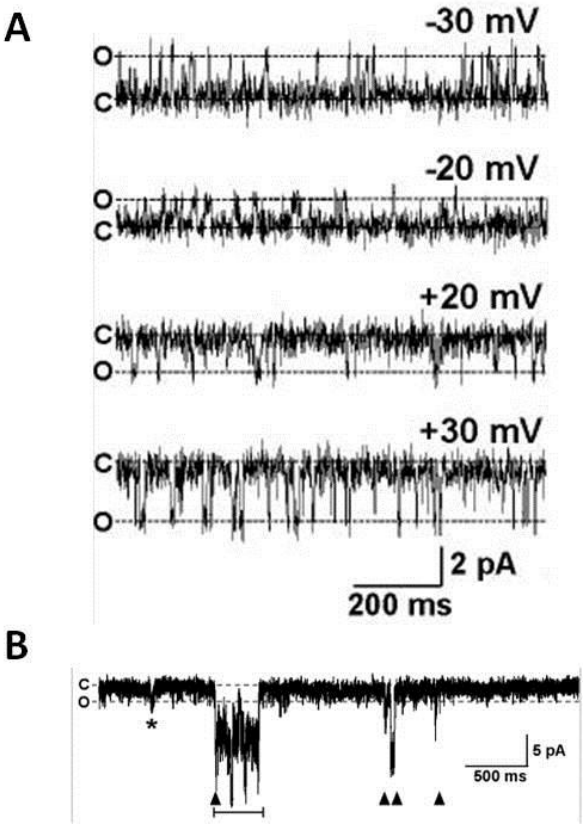


Figure 7.1. Current-fluctuations through purified MG23 channels
This figure was taken from Venturi *et al.* 2011 [164]. Recordings were made in 260 mM K^+.

In an attempt to further study the role of MG23, an *Mg23* KO mouse was produced by the Takeshima laboratory (Department of Biological Chemistry, Kyoto University, Kyoto, Japan). *Mg23* KO mice displayed a weaker Ca^{2+} uptake activity, especially in fast-twitch muscle, and the mice were observed to lose weight with age, a condition thought to be due to muscle atrophy [151]. It is possible that MG23 plays a role in EC-coupling and may interact with other ion channels in the SR. In order to study the SR ion channels, to observe any differences in *Mg23* KO muscle, the SR from skeletal muscle of the Mg23 KO mouse was isolated and studied in the bilayer system.

The aims of this chapter are therefore to investigate possible differences between WT and *Mg23* KO SR ion channel function and, by comparing *Mg23* KO SR currents to those of WT SR, to investigate a distinct current which could be caused by the MG23 channel.

7.2 Results

7.2.1 SR K^+ channel from *Mg23* KO mice

SR vesicles isolated from *Mg23* KO mouse skeletal muscle tissue were studied and compared with recordings from WT mouse skeletal mouse tissue. Figure 7.2A shows current-fluctuations through skeletal SR K^+ channels from WT and *Mg23* KO mouse skeletal muscle. A visual comparison of the recordings revealed no obvious differences between the gating pattern of SR K^+ channels from *Mg23* KO and WT tissue. Single-channel analysis found the conductance to be smaller in channels from *Mg23* KO tissue compared with WT channels, but this was not found to be significantly different, as is shown in Figure 7.3A. Additionally, the Po of the SR K^+ channel from *Mg23* KO mice was higher than that of SR K^+ channels from WT mice at both positive and negative potentials Figure 7.3B.

More detailed analysis of the single-channel events of SR K^+ channels from WT and *Mg23* KO tissue was therefore conducted to try to find a mechanism for the high Po observed in SR K^+ channels from *Mg23* KO mice. Figure 7.4 and Figure 7.5 compare the gating properties of the SR K^+ channel from WT and *Mg23* KO tissue. Figure 7.4 demonstrates that that the Po difference between WT and *Mg23* KO channels was due to a higher Po of the fully open state (Figure 7.4E and F). The Po of the sub-conductance level remained unchanged (Figure 7.4C and D). At -30 mV, the SR K^+ channel was found to spend significantly more time in the fully open state in channels from *Mg23* KO mice compared with WT which resulted in the voltage sensitivity of the SR K^+ channel, observed ubiquitously in SR K^+ channels from WT mice, not being present in SR K^+ channels from *Mg23* KO tissue. The frequency of SR K^+ channel events

was also found to be significantly higher in channels from *Mg23* KO tissue when compared with those from WT tissue; this was reflected in a change of sub-conductance event frequency from 6.7±3.5 Hz (mean±SEM, n=13) in WT to 14.8±2.1 Hz (mean±SEM, n=4) in channels from *Mg23* KO tissue. Similarly, the frequency of fully open channel events changed from 1.4±0.6 Hz (mean±SEM, n=13) in WT to 5.1±3.3 Hz (mean±SEM, n=4) in *Mg23* KO channels. In addition to having a higher frequency, the mean dwell times of SR K^+ channel events were shorter in channels from *Mg23* KO tissue (Figure 7.5D, E & F), including a 20 fold decrease in the duration of time between each event.

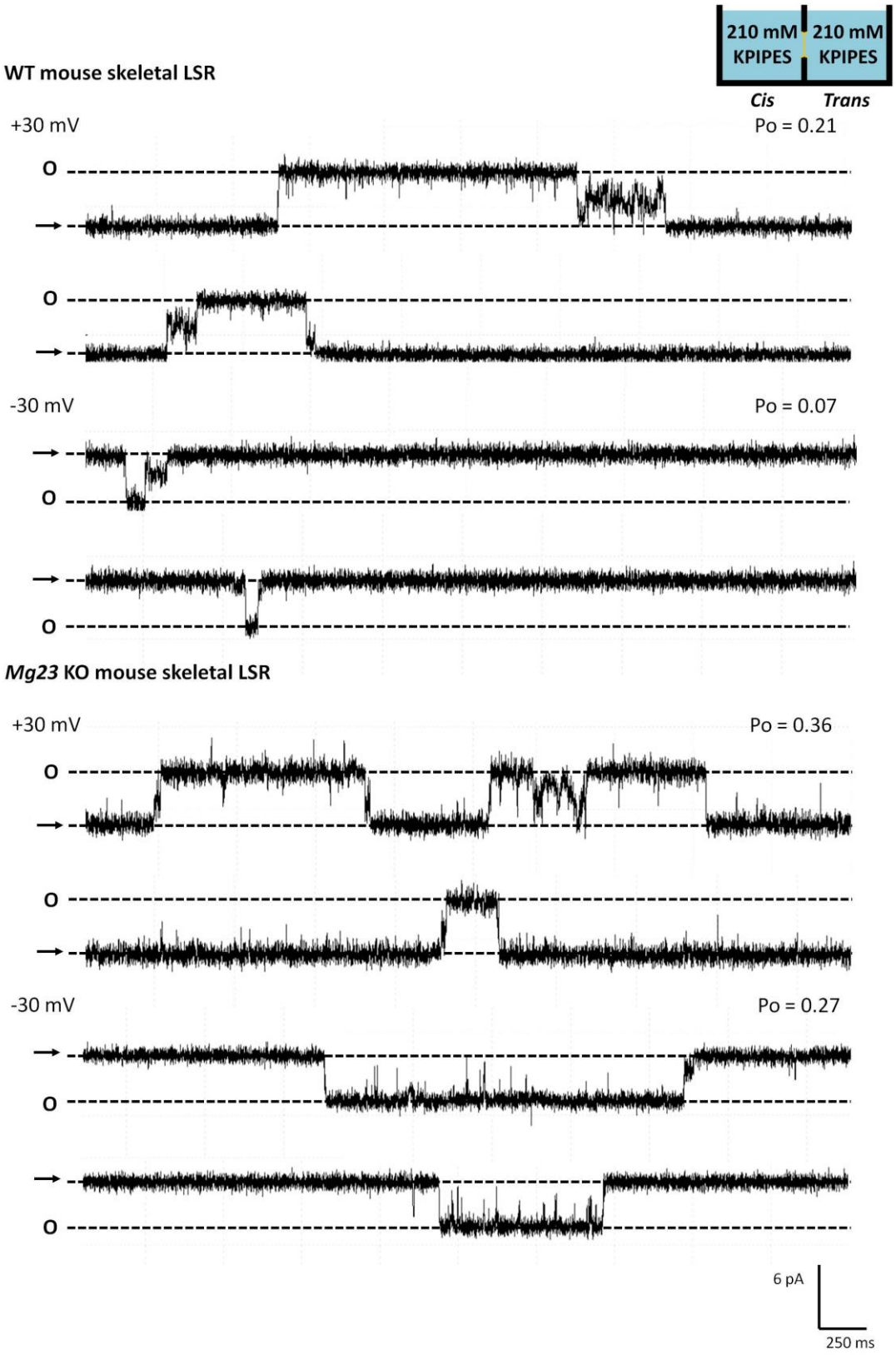

210 mM KPIPES
210 mM KPIPES
Cis
Trans
WT mouse skeletal LSR
+30 mV
Po = 0.21
O
O
-30 mV
Po = 0.07
O
O
Mg23 KO mouse skeletal LSR
+30 mV
Po = 0.36
O
O
-30 mV
Po = 0.27
O
O
6 pA
250 ms

Figure 7.2. The SR K^+ channel from WT and *Mg23* KO mouse skeletal muscle
(A) Current-fluctuations through the mouse skeletal muscle SR K^+ channel from WT mice (top traces) and *Mg23* KO mice (bottom traces) at +30 mV and -30 mV. The recordings are representative of 25 experiments in WT and 11 experiments in *Mg23* KO and were taken in symmetrical 210 mM K^+, 10 µM Ca^{2+}, buffered to pH 7.2 with PIPES. The channel open level is labelled O and the closed level is shown with an arrow. Po values are measured over three minutes. **(B)** The current-voltage relationship for mouse skeletal muscle SR K^+ channels from WT (black circles, n=25) and *Mg23* KO (green squares, n=11) mice. The conductance values are mean±SEM and calculated using a linear regression (Prism). **(C)** The conductance values for the SR K^+ channel from WT (white, n=25) and *Mg23* KO (green, n=11) plotted for comparison. Values are of the mean±SEM.

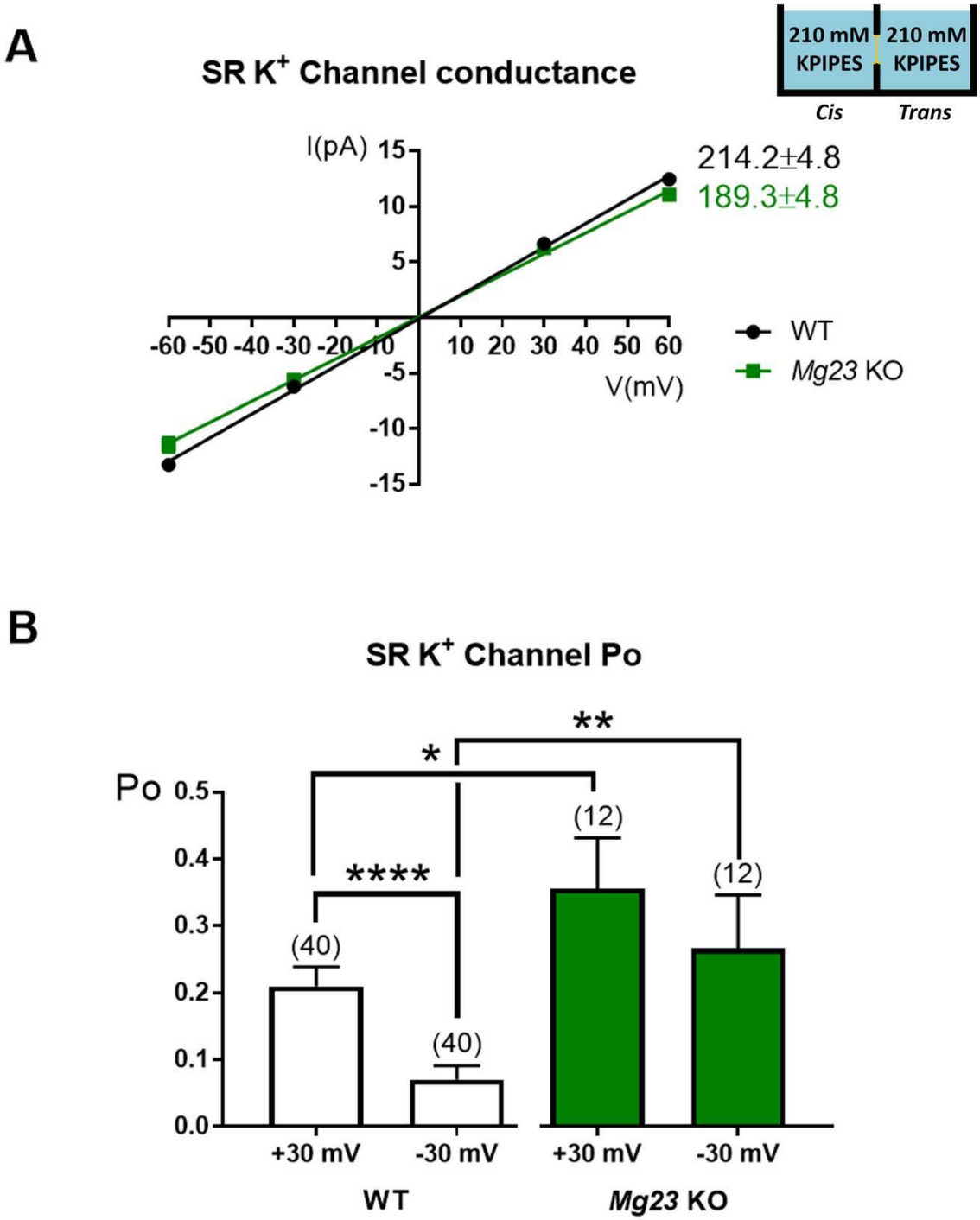


Figure 7.3. Gating properties of the SR K^+ channel from WT and *Mg23* KO tissue
(A) Current-voltage relationship for the SR K^+ channel from WT (black, n=19) and *Mg23* KO (green, n=12) mice. Values are the mean±SEM. Where not seen, error bars are within the point. **(B)** The Po of the SR K^+ channel at ±30 mV from WT (white) and *Mg23* KO (green) mice. Values are the mean±SEM. The number of experiments is shown in brackets above the respective bar.

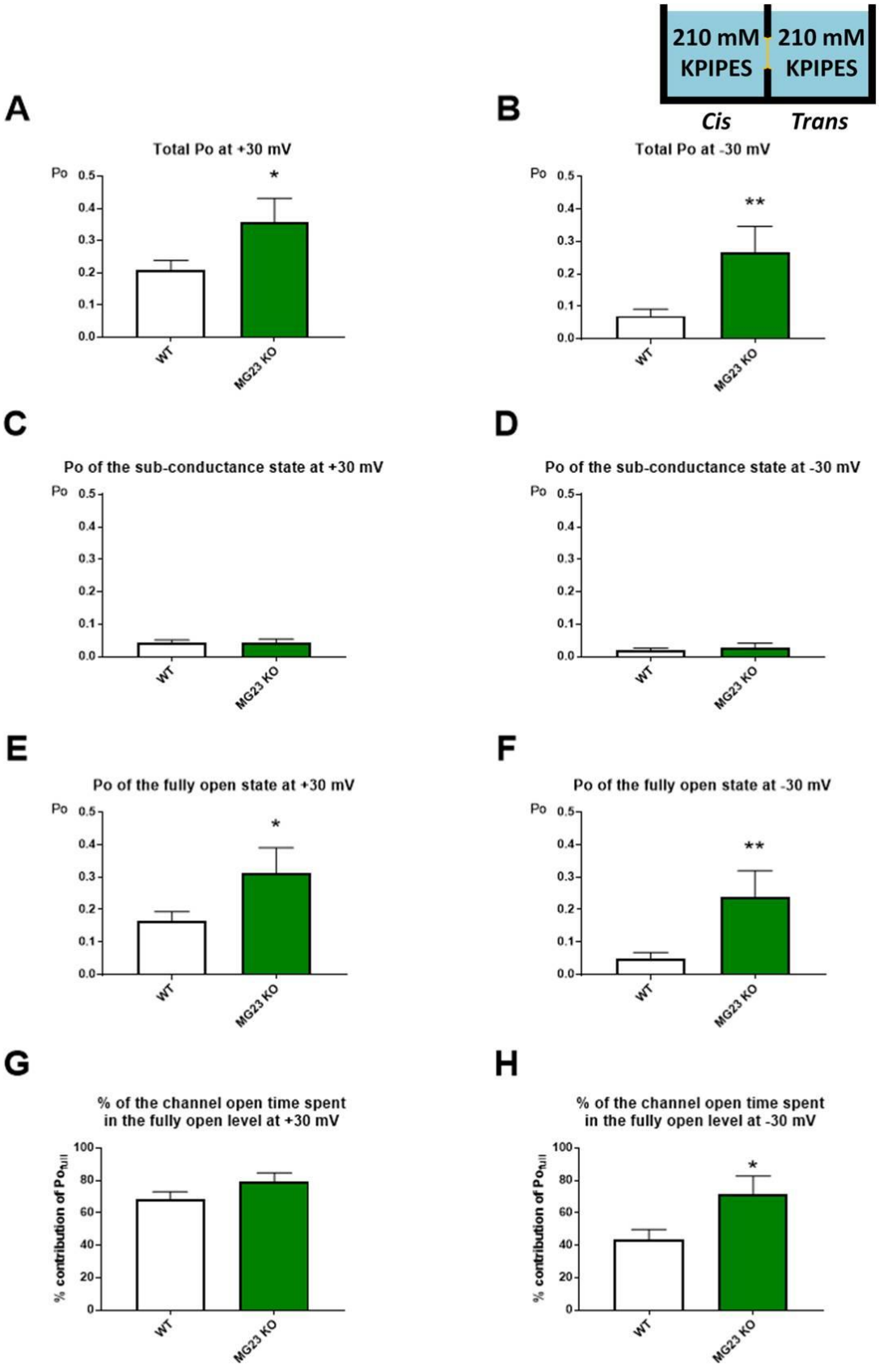

A
Total Po at +30 mV
Po
0.5
0.4
0.3
0.2
0.1
0.0
*
WT
MG23 KO
B
210 mM KPIPES
210 mM KPIPES
Cis
Trans
Total Po at -30 mV
Po
0.5
0.4
0.3
0.2
0.1
0.0
**
WT
MG23 KO
C
Po of the sub-conductance state at +30 mV
Po
0.5
0.4
0.3
0.2
0.1
0.0
WT
MG23 KO
D
Po of the sub-conductance state at -30 mV
Po
0.5
0.4
0.3
0.2
0.1
0.0
WT
MG23 KO
E
Po of the fully open state at +30 mV
Po
0.5
0.4
0.3
0.2
0.1
0.0
*
WT
MG23 KO
F
Po of the fully open state at -30 mV
Po
0.5
0.4
0.3
0.2
0.1
0.0
**
WT
MG23 KO
G
% of the channel open time spent in the fully open level at +30 mV
% contribution of Po full
100
80
60
40
20
0
WT
MG23 KO
H
% of the channel open time spent in the fully open level at -30 mV
% contribution of Po full
100
80
60
40
20
0
*
WT
MG23 KO

Figure 7.4. The gating properties of the mouse skeletal muscle SR K^+ channel from WT and *Mg23* KO mice

(A, B, C) The Po of the mouse skeletal muscle SR K^+ channel from WT (white, n=25) and *Mg23* KO (green, n=11) mice at +30 mV for the sub-conductance state (A), the fully open state (B) and the total channel open time (C). (D) The % of channel open time which was spent in the sub-conductance state in WT (White) and *Mg23* KO (green). (D, E, F, G) The data analysis was repeated for the channels at -30 mV. Data was collected in symmetrical 210 mM K^+, 10 µM Ca^{2+}, buffered to pH 7.2 with PIPES. Values are of the mean±SEM.

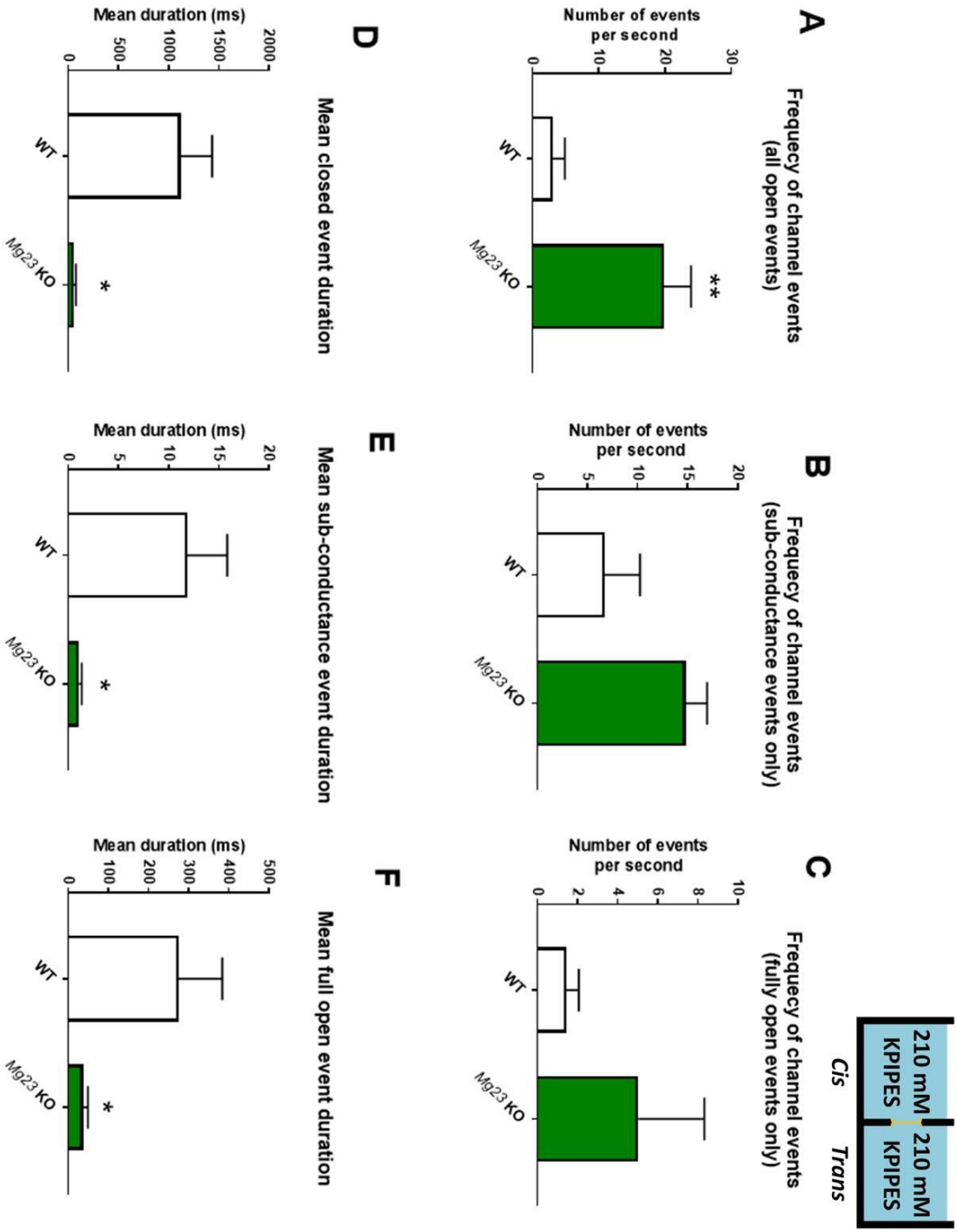


Figure 7.5. Event analysis of SR K^+ channels from WT and *Mg23* KO mouse skeletal muscle
WT data is shown in white (n=19) and *Mg23* KO data is shown in green (n=4). Data was recorded at +30 mV. **(A)** The frequency of all channel events. **(B)** The frequency of channel events to the sub-conductance level. **(C)** The frequency of channel events to the fully open channel level. **(D, E, F)** the mean event duration for closed events **(D)**, sub-conductance events **(E)** and fully open events **(F)**. Values are the mean±SEM.

7.2.2 The SR K^+ channel from *Mg23* KO tissue gates in a cooperative manner

Figure 7.6 shows how the Po of the SR K^+ channel from WT and *Mg23* KO mice changes depending on the number of channels gating in the bilayer. SR K^+ channels from *Mg23* KO tissue were found to gate with increased Po as the number of channels in the bilayer increased. This could be an indication that SR K^+ channels from *Mg23* KO mice gate in a cooperative manner. Figure 7.7 demonstrates that, as with SR K^+ channels from *Tric-a* KO mice, the SR K^+ channels from *Mg23* KO mice did not follow a binomial distribution. This finding is further supported by Figure 7.8 which demonstrates the degree to which SR K^+ channels from *Mg23* KO tissue do not gate independently. Evidence suggests, therefore, that cooperative gating exists between the SR K^+ channels from *Mg23* KO mice.

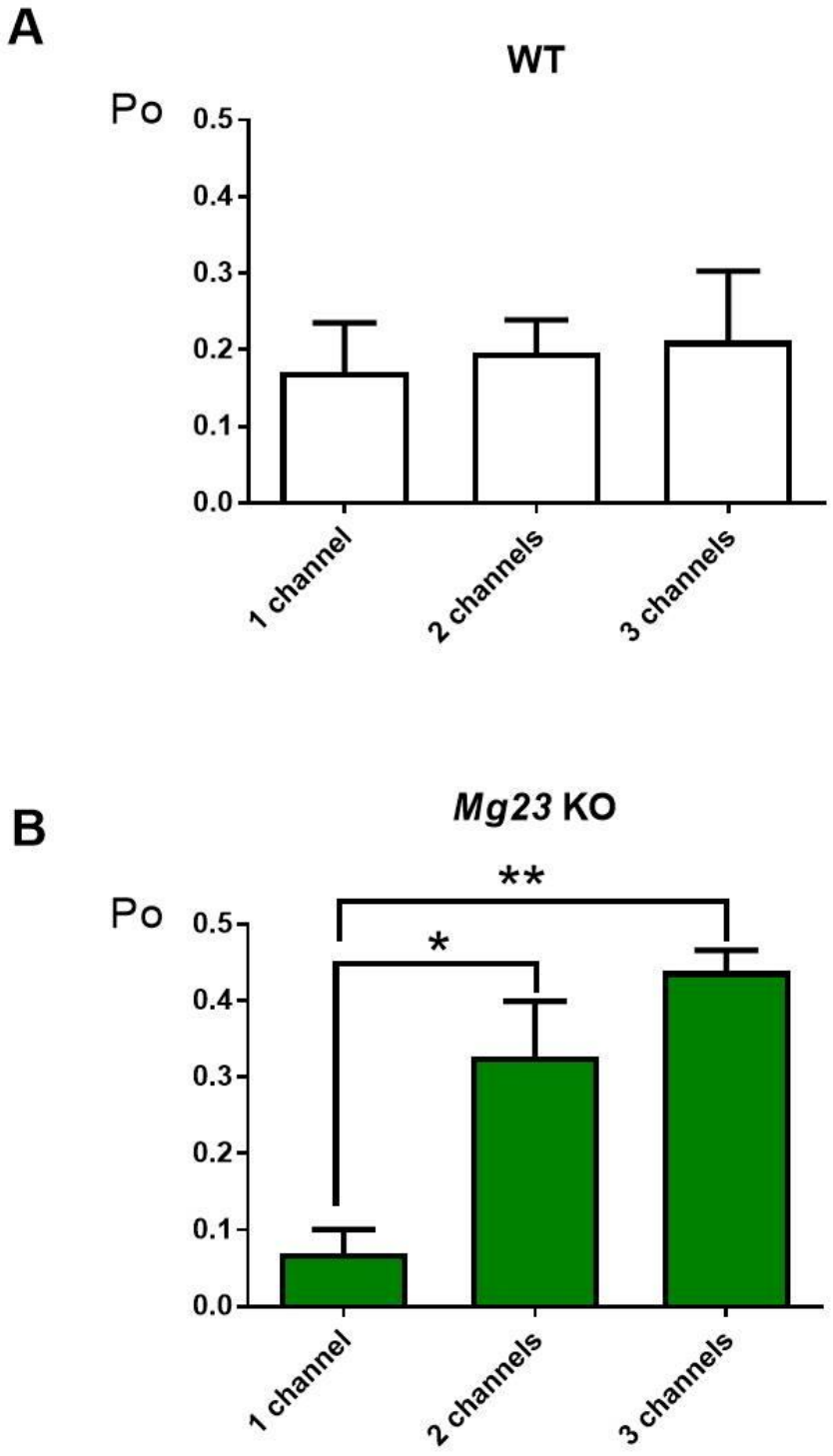


Figure 7.6. The Po of the SR K^+ channel as a function of the number of channels gating in the bilayer

(A) The Po of WT SR K^+ channels when 1 channel (n=19), 2 channels (n=31) or 3 channels (n=8) were gating in the bilayer. **(B)** The Po of SR K^+ channels from *Mg23* KO tissue when 1 channel (n=4), 2 channels (n=4) or 3 channels (n=4) were gating in the bilayer. Data was recorded at +30 mV. Values are the mean±SEM.

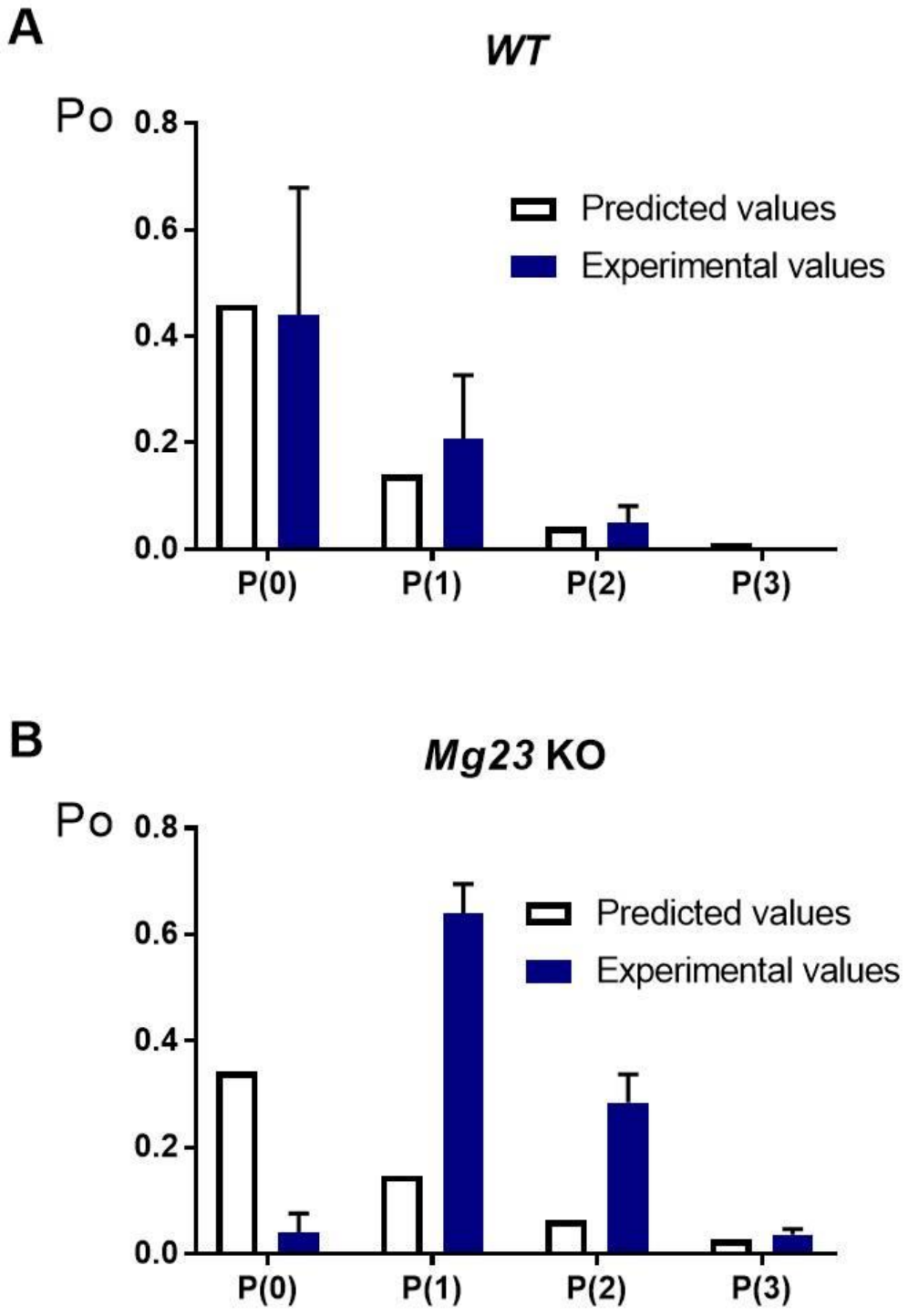


Figure 7.7 The binomial statistical prediction for three SR K^+ channels gating in the bilayer
(A) WT, n=5. **(B)** *Mg23* KO, n=4. The white bars show the binomial statistical prediction of the Po of the closed channel level (P(0)) and of each open channel level (P(1), P(2), P(3)) if three SR K^+ channels are gating together in the bilayer at +30 mV. Predicted values were calculated using the Po from single SR K^+ channel experiments (WT = 0.23, *Mg23* KO = 0.33). Blue bars represent the equivalent experimental data. Values are of the mean±SEM.

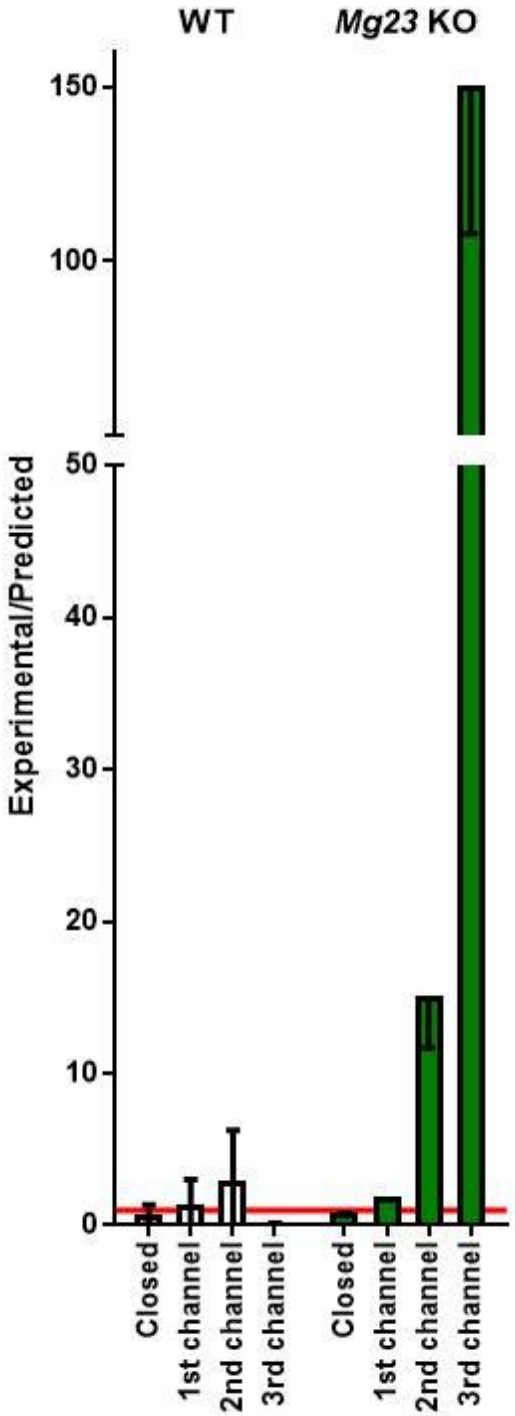


Figure 7.8. A comparison of experimental data to the binomial statistical prediction
The ratio of experimental Po to the Po predicted through the binomial equation is plotted for SR K^+ channel experiments from WT (white bars) and *Mg23* KO (green bars) where three channels are gating together in the bilayer at +30 mV. The red line represents the point where Experimental/predicted Po values are equal to one and thus follows a binomial distribution.

7.2.3 RyR1 channels from *Mg23* KO mice

The RyR1 channel from *Mg23* KO tissue did not have a different Po or conductance compared to WT tissue (Figure 7.9).

7.2.4 Cl^- currents from *Mg23* KO mice

A Cl^- current was observed and recorded after the first Cl^- channel fusion event of SR vesicles from *Mg23* KO tissue. The current is shown in Figure 7.10 and was similar to that of the SRAL channel described in Chapter 4 of this thesis. The current was therefore compared with the WT SRAL channel currents. Figure 7.11A shows the average current recorded by noise analysis through apparent SRAL channels from WT and *Mg23* KO tissue. Cl^- currents from *Mg23* KO tissue were found to be smaller than those recorded from WT tissue. This could indicate a smaller concentration of SRAL channels in each vesicle from *Mg23* KO mice. The $P_{choline}/P_{Cl}$ was not found to be different in WT tissue compared to *Mg23* KO tissue, however (Figure 7.11B).

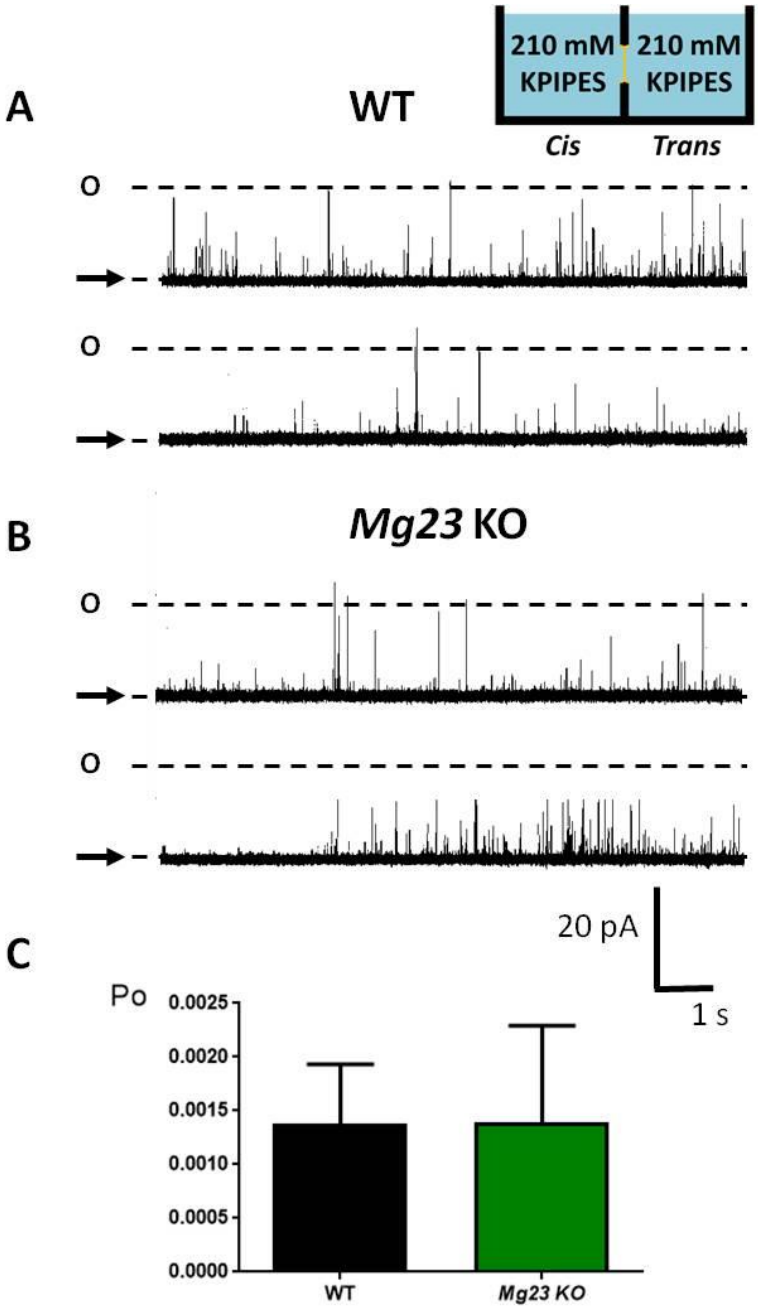


Figure 7.9. RyR1 channels from WT and *Mg23* KO tissue
Representative recordings of the RyR1 channel from WT **(A)** and *Mg23* KO **(B)** mice. Recordings were made in symmetrical 210 mM KPIPES. The channel fully open level is shown by O and the closed level by an arrow. **(C)** A comparison of the Po values for RyR1 channels from WT (black, n=23) and *Mg23* KO (green, n=4) mice. Values are of the mean±SEM.

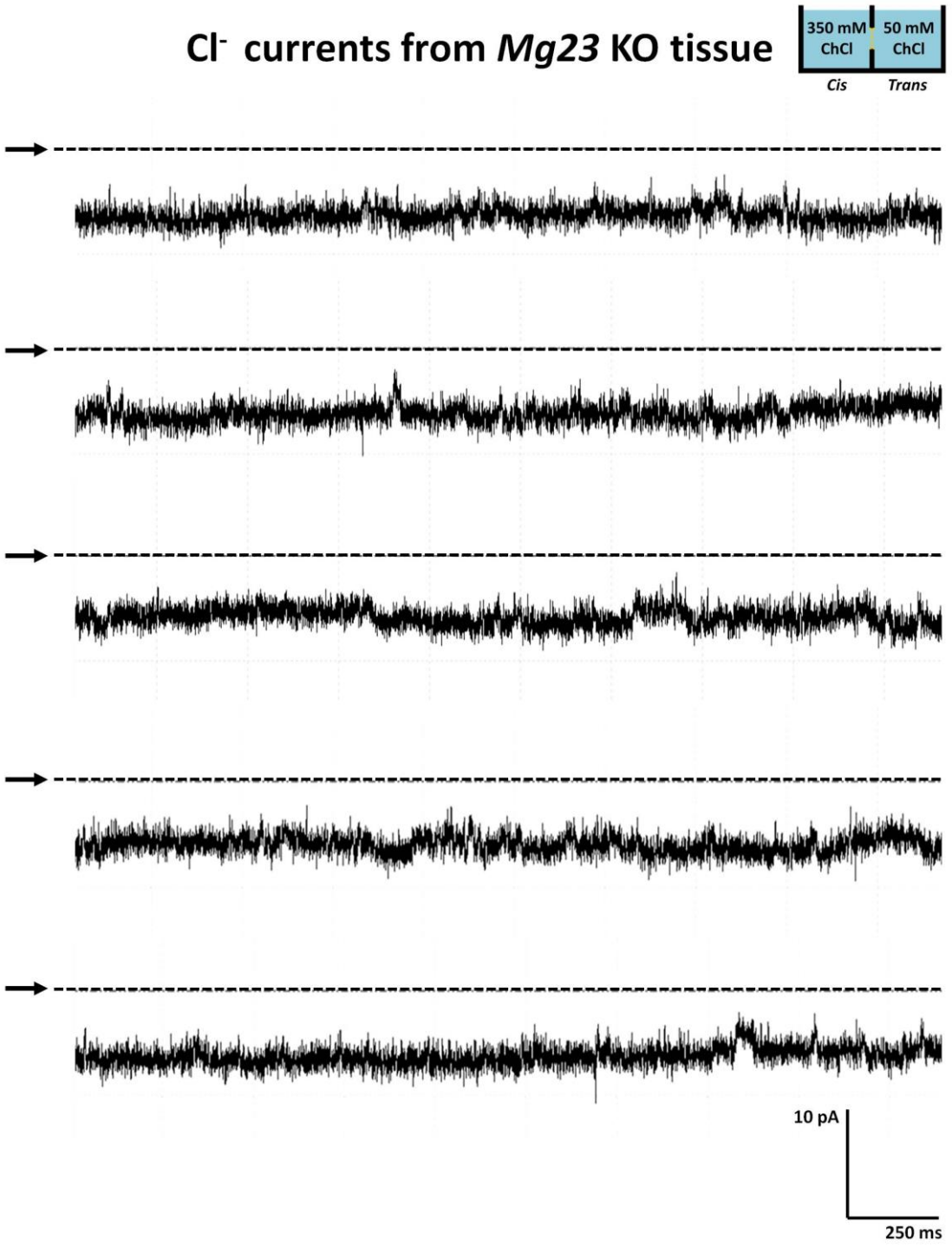


Figure 7.10. Representative recordings of SR Cl^- currents observed in *Mg23* KO tissue
Channel closed levels are shown by an arrow.

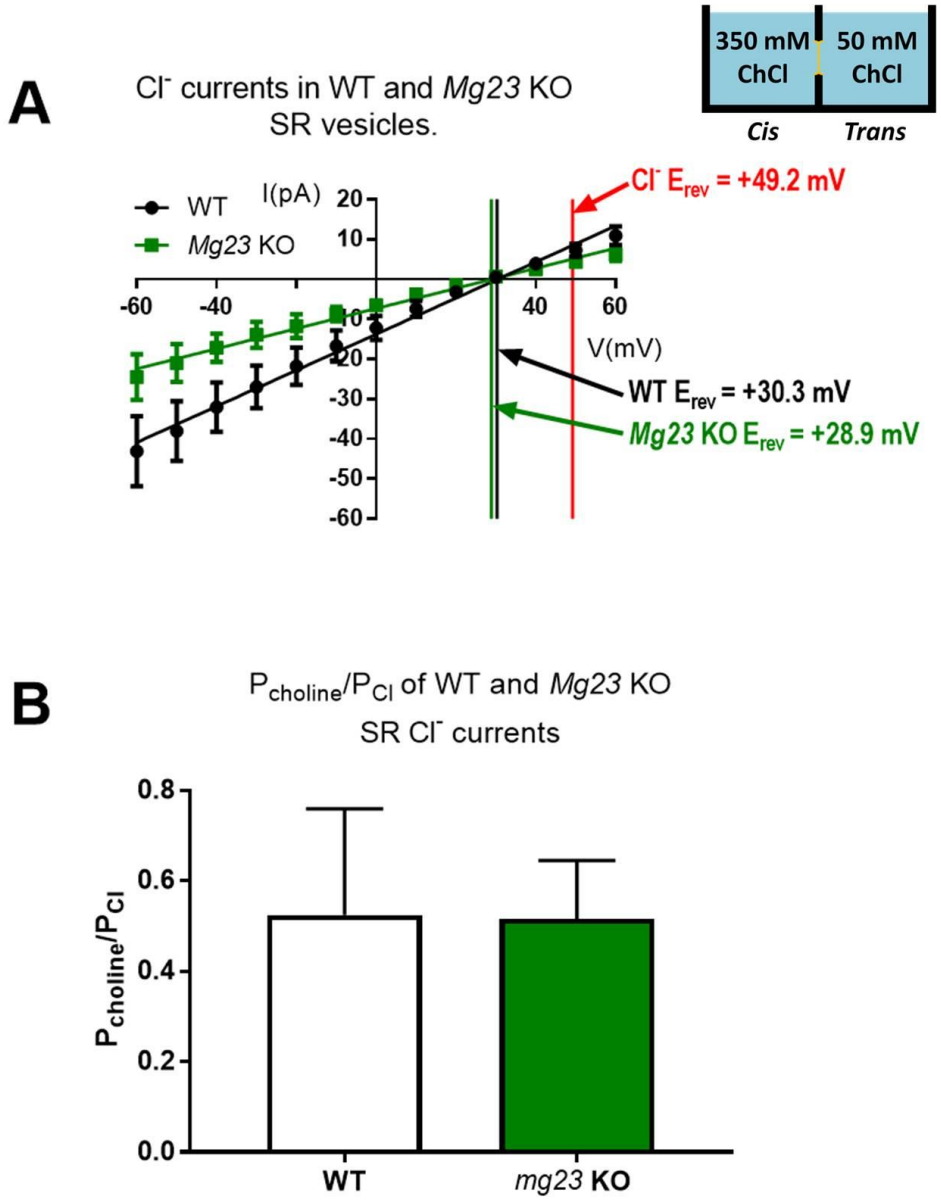


Figure 7.11. Permeability properties of SR Cl^- currents from WT and *Mg23* KO mouse skeletal muscle

(A) The current-voltage relationship for average currents through SR Cl^-/SRAL channel currents calculated by noise analysis from WT (black, n=6) and *Mg23* KO (green, n=4) mouse skeletal muscle. Experiments were conducted in asymmetrical choline-chloride solutions. The E_{rev} values for Cl^- and each data set are indicated by a vertical line **(B).** The relative permeability of choline to Cl^- ($P_{choline}/P_{Cl}$) for SR Cl^- currents/SRAL channels from WT and *Mg23* KO tissue. Values are of the mean±SEM.

7.2.5 The effect of the cytotoxic small molecule, C-6, on SR ion channels

One of the aims of this chapter was to identify the MG23 protein as a distinct current in the SR. We therefore treated bilayers, into which were fused SR vesicles from WT or *Mg23* KO mice, with potential ligands of MG23. One such molecule is the cytotoxic small molecule, C-6 (Figure 7.12), a compound which was developed as an anti-cancer drug which induces cell death in breast cancer cell lines due to the release of excess Ca^{2+} from the ER [210]. C-6 was discontinued due to it inducing high levels of SR stress [210]. C-6 has been shown to associate with the MG23 protein [211]. It is possible that C-6 could activate/inhibit/regulate MG23. SR membranes from *Mg23* KO mouse skeletal muscle were therefore treated with the C-6 and compared with effects on WT mouse skeletal tissue.

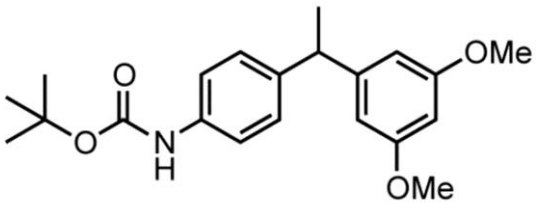


Figure 7.12. The structure of C-6
This structure was adapted from Vaden (2015) [211]

C-6 was found not to activate any novel type of channel in WT SR and caused no obvious change in SR K^+ channel gating (n=2). Figure 7.13 shows however that when 200 µM C-6 was added to the *cis* side of the mouse RyR1 channel, activation of the channel occurred. C-6 also reduced the channel conductance of RyR1.

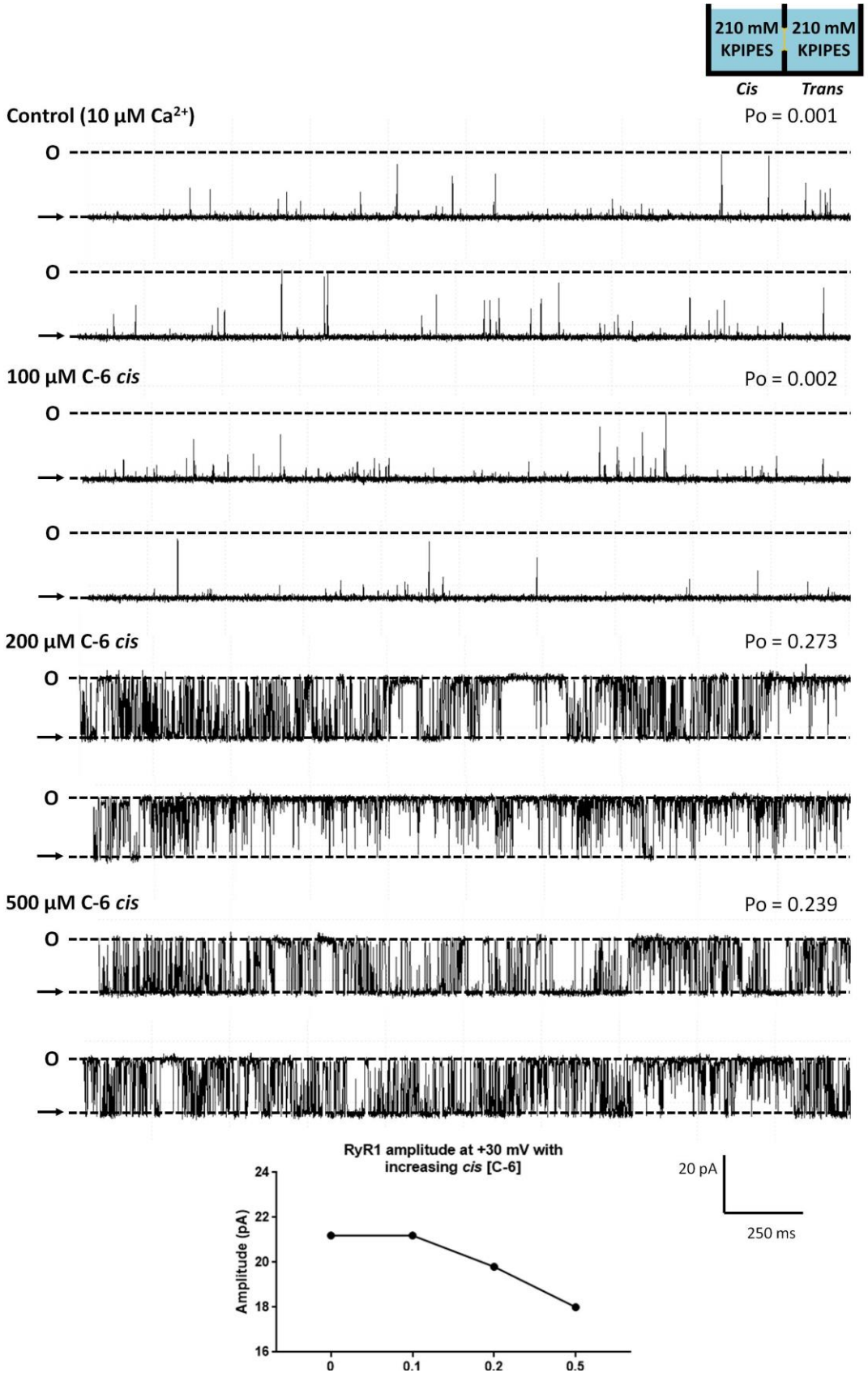

210 mM KPIPES
210 mM KPIPES
Cis
Trans
Control (10 µM Ca2+)
Po = 0.001
O
O
100 µM C-6 cis
Po = 0.002
O
O
200 µM C-6 cis
Po = 0.273
O
O
500 µM C-6 cis
Po = 0.239
O
O
RyR1 amplitude at +30 mV with increasing cis [C-6]
Amplitude (pA)
24
22
20
18
16
0
0.1
0.2
0.5
20 pA
250 ms

Figure 7.13. The effect of C-6 on the RyR1 channel.
Current-fluctuations through an RyR1 channel from mouse skeletal HSR at +30 mV with increasing concentrations of *cis* C-6. This effect was observed in two experiments, one performed by myself with K^+ as the permeant ion, and the other performed by Dr Sam El-Ajouz with Ca^{2+} as the permeant ion. The experiment was recorded is in symmetrical 210 mM K^+, 10 µM Ca^{2+}, buffered to pH 7.2 with PIPES. The channel open level is shown by O and the closed level by an arrow. Beneath the traces is a plot of how the RyR1 channel open level current decreases with higher *cis* [C-6] (n=1).

7.2.6 pH may be an activator of MG23

It has been suggested that an alkaline pH may be a promoter of ER/SR stress [212]. It is possible that, if C-6 interacts with MG23 and causes ER/SR stress, then other ER/SR stress promoters may be activators of MG23. Artificial bilayers which contained fused SR vesicles from *Mg23* KO mice or WT mice were therefore subjected to a *cis*/cytosolic alkaline pH. Artificial membranes containing SR membranes from WT mice were found to be unstable (broke easily) when the pH of the bath solution was altered from pH 7.2 to pH 9.2. Such a change often resulted in a current similar to that shown in Figure 7.14C and was followed by the bilayer breaking and the termination of the experiment (n=11). This was found not to be the case when the bilayer contained SR from *Mg23* KO mice (n=7).

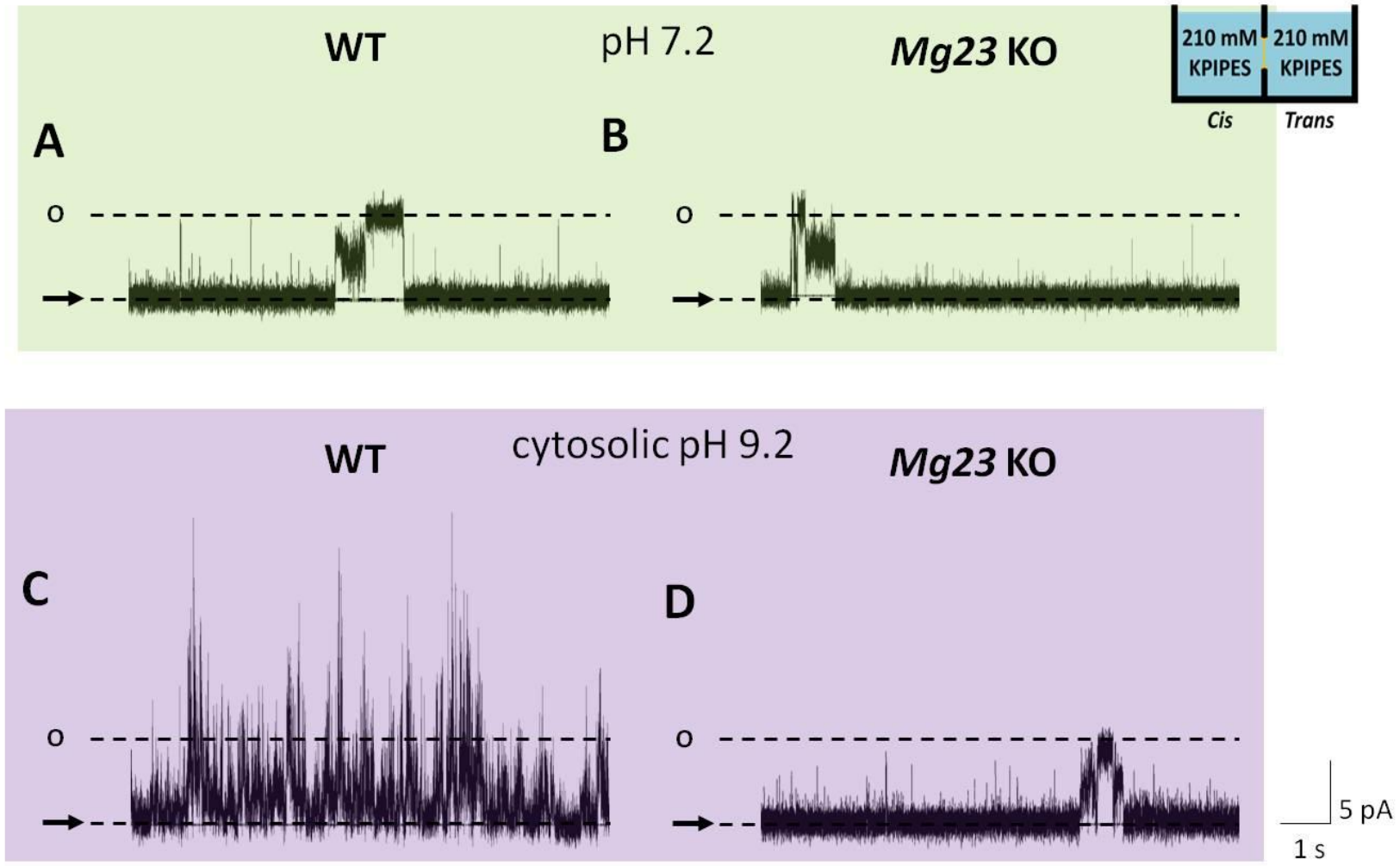

WT
pH 7.2
Mg23 KO
210 mM KPIPES
210 mM KPIPES
Cis
Trans
A
B
o
o
WT
cytosolic pH 9.2
Mg23 KO
C
D
o
o
5 pA
1 s

Figure 7.14. The effect of pH 9.2 on membranes containing SR proteins from *Mg23* KO mice and WT mice

Representative recordings in pH 7.2 **(A, B)** and pH 9.2 **(C, D)** taken from membranes containing SR vesicles from WT **(A, C)** and *Mg23* KO **(B, D)** mice. Recordings were made in 210 mM KPIPES. The open level of the SR K^+ channel is shown by O and the closed channel level by an arrow.

7.3 Discussion

This chapter has aimed to investigate the biophysical properties of SR channels in *Mg23* KO tissue and compare them to SR channels from WT tissue. SR K^+ channels were found to exhibit a higher Po in *Mg23* KO tissue with more and faster channel gating events to the fully open channel level than SR K^+ channels from WT tissue (Figure 7.3, Figure 7.4, Figure 7.5). These findings suggest that MG23 may interact directly with SR K^+ channels in the bilayer to alter channel Po, possibly in a regulatory capacity. It is also possible that MG23 could behave as a low Po SR K^+ channel and that removing the channel, leaves only higher Po channels to gate in the bilayer. Other channels, similar to MG23, are thought to exist in the SR which could be other SR K^+ channels. The BRI3-binding protein (BRI3BP) is one such example [163][151]. Our collaborator, Hiroshi Takeshima, is in the process of developing MG23/BRI3 BP double KO mice and it is hoped that the SR from these animals would be studied in the bilayer.

SR K^+ channels from *Mg23* KO tissue exhibited cooperative gating in a similar way to SR K^+ channels from *Tric*-a KO tissue (Figure 7.6, Figure 7.7, Figure 7.8). It is possible that this is further evidence for SR membrane crowding as discussed in Chapter 5, and that the abundance and spatial arrangements of the proteins in the SR membrane normally prevents direct interaction between SR K^+ channels.

The gating patterns of RyR1 channels and currents from first Cl^- fusion events from *MG23* KO tissue compared with WT channels were found to be similar. These findings suggest that MG23 may not interact with the RyR1 channel or direct physical interactions do not modulate channel function. Figure 7.11 also makes it seem unlikely that MG23 is one of the commonly observed SR Cl^- channels that I described in Chapter 4. However, my work on these channels was not extensive and there maybe additional cation or anion channels that are not normally observed in muscle SR under the conditions of my experiments. For example, a channel may

be only activated by a specific trigger(s) such as voltage, Ca^{2+}, Zn^{2+}, Cu^{2+}/Cu^{3+}, pH change, oxidation, phosphorylation, binding of calmodulin or other factors and hence the channel is not normally gating in a bilayer experiment.

This chapter sought to investigate the pharmacology of the MG23 channel as well as its effects on other SR channels. The compound C-6 is thought to bind to the MG23 protein and it could therefore have a pharmacological effect on the channel. C-6 was not found to activate any SR channels apart from RyR1. This may be the mechanism of action by which C-6 induces cell death.

In addition to C-6, it was thought that MG23 could be activated by a high luminal (*trans*) pH, as high pH levels have been associated with ER/SR stress [212]. Figure 7.14C shows current-fluctuations in the presence of high pH (9.2), observed to open in membranes containing WT SR, but not *Mg23* KO SR. These currents were visually similar to the proposed gating pattern of multiple MG23 channels [165]. Unfortunately, as the bilayer often broke after observing such currents, further analysis could not be carried out. The increased stability of bilayers containing SR from *Mg23* KO mice was used to study the effect of pH 9.2 on the SR K^+ channel described in Chapter 3 of this thesis.

Chapter 8. Conclusions

This thesis has focused on the study of the biophysical properties of SR ion channels through the use of planar lipid bilayer techniques. Channels such as the TRIC channels are thought to provide a countercurrent during EC-coupling, which is crucial for Ca^{2+} release from the SR, and channels such as MG23 and TRIC may maintain the SR membrane potential close to 0 mV, ensuring that ionic concentrations across the SR are equilibrated. These ion channels were therefore studied in this thesis in order to better understand the EC-coupling process and ionic flux across the membrane of the SR.

Chapters 3 and 4 of these thesis studied SR K^+ currents and SR Cl^- currents observed after the incorporation of native SR vesicles into artificial bilayers. In Chapter 3, I compared the properties of SR K^+ channels from various mammalian muscle tissues. I found that the typical gating pattern of SR K^+ channels, described in detail previously [104] [105], was essentially unchanged between the different tissues studied. I speculated that the SR K^+ channels from mouse, sheep and rabbit may share a high degree of sequence homology, especially in the pore region.

Sheep cardiac SR K^+ channels were found to gate with a lower conductance than SR K^+ channels from mouse or rabbit muscle. I concluded that this is due to a species difference, rather than a difference between skeletal and cardiac muscle, evidenced by no difference being observed between mouse skeletal and cardiac muscle SR K^+ channel currents.

Chapter 3 also investigated the pharmacological properties of SR K^+ channel currents with the aim of finding as specific ligand. No specific ligand was found; however, I found that increasing Ca^{2+} and Ni^{2+}, but not Mg^{2+} concentrations on the luminal side of the channel reduced the Po of the fully open channel level at positive potentials and prevented SR K^+ channels from

exhibiting voltage-sensitivity. Ca^{2+} and Mg^{2+} were also observed to cause 'smooth block' of K^+ currents through the SR K^+ channel, from both the luminal and cytosolic sides. I speculated that Ca^{2+} had a dual effect on SR K^+ channels. Ca^{2+} (and other divalent cations such as Mg^{2+}) could block the pore of SR K^+ channels at millimolar concentrations, and a Ca^{2+} binding site on the luminal side of SR K^+ channels may act to regulate the channels during EC-coupling. Evidence suggested that the Ca^{2+} binding site was accessible to Ca^{2+} and Ni^{2+}, but not Mg^{2+}. I further speculated a degree of asymmetry in the pore of SR K^+ channels, as evidenced by variations in cytosolic and luminal blocking effects of Ca^{2+} and Mg^{2+}. Increased luminal pH was observed to cause similar gating effects to Ca^{2+} and Ni^{2+} and suggest pH sensitivity of SR K^+ channel currents; however it was unclear whether this was a similar mechanism to that of Ca^{2+} regulation. I found that ATP did not alter SR K^+ channel activity from the cytosolic side.

In Chapter 4 of this thesis, I studied the SR Cl^- currents observed in bilayers after incorporation of native SR vesicles into the bilayer. These currents had previously been observed in the Sitsapesan laboratory and were observed to incorporate together with RyRs; however they have not yet been studied. I therefore sort to characterise the SR Cl^- currents under a range of conditions. Three SR Cl^- channel currents were identified; I termed these the SRAS channel, the SRAL channel, and the Type 3 SR Cl^- channel. The SRAS channel was found to be a Cl^--selective channel and gated with clear sub-conductance states and shared similarity to previously described SR Cl^--selective ion channels [86], [116], [118]–[123]. Due to the lack of data however, I could not speculate as to whether these channels were the same. The SRAL channel was observed in the bilayer after the first Cl^- fusion event. The channel current was akin to that of a leak current and was found to exhibit non-selective, porin-like permeability properties, passing both anions and large cations such as NMDG. This was similar to previous non-selective SR Cl^- channels observed in bilayer experiments [117], [124]–[126]. I speculated that this 'channel' was more likely a channel cluster formed from a number of SR ion channels, one

of which may be TRIC-A as discussed in Chapter 5 of this thesis. The Type 3 SR Cl^- channel was only observed twice in the bilayer and so analysis of the channel was limited. The gating pattern was similar to that of TRIC channels described in Chapters 5 and 6 of this thesis. It is possible, therefore that this current was produced by a TRIC channel gating in the bilayer. I found that little evidence existed to suggest that the SR Cl^- channel currents observed from native SR could be identified as any of the currently known SR Cl^- channels such as the CFTR, VDAC or CLIC1 channels. I speculated therefore that the SRAS and SRAL channels could represent as yet unidentified SR Cl^- channels.

Chapter 5 and Chapter 6 of this thesis studied two SR K^+ channels, TRIC-A and TRIC-B. The chapters focused on studying TRIC channels from native membranes and changes in native SR proteins from *Tric-a* KO tissue (Chapter 5), and on studying purified TRIC channels (Chapter 6).

In Chapter 6 of this thesis, I studied purified TRIC-B1 channels from *c. elegans* and purified human TRIC-A proteins. I observed channels which gated predominantly to a high-noise sub-conductance state and which were permeable to K^+, Cl^-, and choline. The channels from purified TRIC-A preparations exhibited a higher permeability to Cl^- compared with those from *c. elegans* TRIC-B1 preparations. I concluded that these currents were TRIC channels and speculated that the sub-conductance gating may be attributed to rapid gating between open states caused by the three monomeric pores of TRIC channels. The action of decamethonium on the currents from *c. elegans* TRIC-B1 provided evidence for this theory. Based on these currents, I identified TRIC-like gating in SR K^+ channel recordings from both native SR cardiac and skeletal membranes, and CHO cells over-expressing TRIC-A, speculating that these may be due to TRIC channels gating in the bilayer. These native channels exhibited K^+-selectivity which led me to further speculate that the conditions or protein folding of TRIC channels in native membranes may cause TRIC to function as a K^+-selective channel where it does not from purified preparations. I further speculated about the pore dimensions of the purified TRIC

channels and postulated that the pore may be wide enough to facilitate the transport of fully hydrated Cl^- ions and that this may be the mechanism by which the channels pass Cl^-.

In Chapter 5, I compared the SR K^+ and Cl^- channels from *Tric-a* KO mouse tissue to those from WT mouse tissue. The gating of SR Cl^- channels from *Tric-a* KO muscle is discussed above. SR K^+ channels from *Tric-a* KO tissue exhibited lower Po and more channel events to the sub-conductance level. Here I proposed two theories. I proposed that the SR K^+ channel currents observed in *Tric-a* KO muscle were currents through the TRIC-B channel only, and that this channel exhibited differences to TRIC-A. Alternatively, I proposed that TRIC-A may act to stimulate K^+ flow across the SR membrane through SR K^+ channels and that this explained the lower Po of SR K^+ channels observed in *Tric-a* KO tissue. In Chapter 7, I described similar experiments conducted with *Mg23* KO SR membranes. In experiments using *Mg23* KO SR, the Po of SR K^+ channels were increased. I speculated that MG23 may play a role in limiting K^+ flow across SR membranes and that channel-channel interactions and regulation between TRIC-A and MG23, and SR K^+ channels in the SR was possible.

SR K^+ channels from *Tric*-a KO and *Mg23* KO mice also exhibited coupled gating where they did not in WT tissue. It would appear that when either TRIC-A or MG23 are not present in the SR, the SR K^+ channels can associate and gate in a cooperative manner. It is possible that this is evidence of SR membrane 'crowding' and that SR K^+ channels cannot associate due to the large channel density.

Chapter 7 also studies some possible pharmacological properties of MG23. The small molecule C-6 which is thought associate with MG23 [211] was found not to activate any novel ion channel in the SR. C-6 was observed to activate RyR channels, however, and I speculated that this may be the mechanism by which C-6 promotes cell death in cancer cells. In Chapter 7, I

also suggest that an alkaline pH may activate MG23 and thus may play a role in promoting MG23 to trigger cell death.

In conclusion, the overall aim of this thesis was to study the intracellular ion channels which may be involved in providing a counter-current during Ca^{2+} flux in EC-coupling. I have studied the properties of SR K^+ channels, which are likely candidates for providing counter-currents by K^+ influx into the SR during EC-coupling. I identified modulators for these channels in the form of high luminal Ca^{2+}, Ni^{2+}, and pH. I have also studied the two SR K^+ channels, TRIC-A and TRIC-B. I characterised purified TRIC proteins in the bilayer and suggested a mechanism for channel gating. I also identified how SR K^+ channels are altered in tissue devoid of TRIC-A or MG23, and provided evidence of ion channel crowding in the SR. Further to this, I have also described three novel SR Cl^- channels which may provide counter-currents through Cl^- efflux from the SR during EC-coupling.

References

[1] M. Brini, T. Calì, D. Ottolini, and E. Carafoli, “Intracellular Calcium Homeostasis and Signaling,” Springer, Dordrecht, 2013, pp. 119–168.

[2] M. F. Schneider and W. K. Chandler, “Voltage dependent charge movement in skeletal muscle: a possible step in excitation-contraction coupling,” *Nature*, vol. 242, pp. 244–246, 1973.

[3] M. Endo, “Calcium release from the sarcoplasmic reticulum.,” *Physiol. Rev.*, vol. 57, no. 1, pp. 71–108, Jan. 1977.

[4] C. Caputo, “Excitation and Contraction Processes in Muscle,” *Annu. Rev. Biophys. Bioeng.*, vol. 7, no. 1, pp. 63–83, Jun. 1978.

[5] W. Melzer, A. Herrmann-Frank, and H. C. Lüttgau, “The role of Ca2+ ions in excitation-contraction coupling of skeletal muscle fibres,” *Biochim. Biophys. Acta - Rev. Biomembr.*, vol. 1241, no. 1, pp. 59–116, May 1995.

[6] M. W. Berchtold, H. Brinkmeier, and M. Müntener, “Calcium ion in skeletal muscle: its crucial role for muscle function, plasticity, and disease.,” *Physiol. Rev.*, vol. 80, no. 3, pp. 1215–65, Jul. 2000.

[7] A. Fabiato and F. Fabiato, “Contractions induced by a calcium-triggered release of calcium from the sarcoplasmic reticulum of single skinned cardiac cells,” *J. Physiol.*, vol. 249, pp. 469–495, 1975.

[8] D. M. Bers, *Excitation-contraction coupling and cardiac contractile force*, vol. second. Dordrecht: Kluwer, 1991.

[9] C. Franzini-Armstrong and A. O. Jorgensen, “Structure and development of E-C coupling units in skeletal muscle,” *Annu. Rev. Physiol.*, vol. 56, pp. 509–534, 1994.

[10] A. Saito, S. Seiler, A. Chu, and S. Fleischer, “Preparation and morphology of sarcoplasmic reticulum terminal cisternae from rabbit skeletal muscle,” *J.Cell Biol.*, vol. 99, pp. 875–885, 1984.

[11] B. Costello, C. Chadwick, A. Saito, A. Chu, A. Maurer, and S. Fleischer, “Characterization of the junctional face membrane from terminal cisternae of sarcoplasmic reticulum,” *J.Cell Biol.*, vol. 103, pp. 741–753, 1986.

[12] S. Treves, M. Vukcevic, M. Maj, R. Thurnheer, B. Mosca, and F. Zorzato, “Minor sarcoplasmic reticulum membrane components that modulate excitation-contraction coupling in striated muscles.,” *J. Physiol.*, vol. 587, no. Pt 13, pp. 3071–9, Jul. 2009.

[13] A. H. Caswell and J. P. Brunschwig, “Identification and extraction of proteins that compose the triad junction of skeletal muscle,” *J.Cell Biol.*, vol. 99, pp. 929–939, 1984.

[14] C. Franzini-Armstrong and G. Nunzi, “Junctional feet and particles in the triads of a fast-twitch muscle fibre,” *J. Muscle Res. Cell Motil.*, vol. 4, pp. 233–252, 1983.

[15] P. H. Jewett, S. D. Leonard, and J. R. Sommer, “Chicken cardiac muscle: its elusive extended junctional sarcoplasmic reticulum and sarcoplasmic reticulum fenestrations.,” *J. Cell Biol.*, vol. 56, no. 2, pp. 595–600, Feb. 1973.

[16] J. R. Sommer and E. A. Johnson, “Comparative ultrastructure of cardiac cell membrane specializations. A review.,” *Am. J. Cardiol.*, vol. 25, no. 2, pp. 184–94, Feb. 1970.

[17] J. R. Sommer and R. A. Waugh, “The ultrastructure of the mammalian cardiac muscle cell--with special emphasis on the tubular membrane systems. A review.,” *Am. J. Pathol.*, vol. 82, no. 1, pp. 192–232, Jan. 1976.

[18] S. Komazaki, K. Ito, H. Takeshima, and H. Nakamura, “Deficiency of triad formation in developing skeletal muscle cells lacking junctophilin type 1.,” *FEBS Lett.*, vol. 524, no. 1–3, pp. 225–9, Jul. 2002.

[19] C. Franzini-Armstrong and F. Protasi, “Ryanodine receptors of striated muscles: A complex channel capable of multiple interactions,” *Physiol. Rev.*, vol. 77, pp. 699–729, 1997.

[20] T. Tanabe, K. G. Beam, J. A. Powell, and S. Numa, “Restoration of excitation-contraction coupling and slow calcium current in dysgenic muscle by dihydropyridine receptor complementary DNA,” *Nature*, vol. 336, pp. 134–139, 1988.

[21] B. E. Flucher, H. Takekura, and C. Franzini-Armstrong, “Development of the excitation-contraction coupling apparatus in skeletal muscle: Association of sarcoplasmic reticulum and transverse tubules with myofibrils,” *Dev. Biol.*, vol. 160, pp. 135–147, 1993.

[22] E. Rios and G. Pizarro, “Voltage sensor of excitation-contraction coupling in skeletal muscle,” *Physiol. Rev.*, vol. 71, pp. 849–907, 1991.

[23] E. Rios, J. J. Ma, and A. Gonzalez, “The mechanical hypothesis of excitation-contraction (EC) coupling in skeletal muscle,” *J. Muscle Res. Cell Motil.*, vol. 12, pp. 127–135, 1991.

[24] T. Tanabe, K. G. Beam, B. A. Adams, T. Niidome, and S. Numa, “Regions of the skeletal muscle dihydropyridine receptor critical for excitation-contraction coupling,” *Nature*, vol. 346, pp. 567–569, 1990.

[25] M. F. Schneider, “Control of calcium release in functioning skeletal muscle fibers,” *Annu. Rev. Physiol.*, vol. 56, pp. 463–484, 1994.

[26] X. Lu, l Xu, and G. Meissner, “Activation of the skeletal muscle calcium release channel by a cytoplasmic loop of the dihydropyridine receptor,” *J.Biol.Chem.*, vol. 269, pp. 6511–6516, 1994.

[27] G. B. Gurrola, C. Ar,valo, R. Sreekumar, A. J. Lokuta, J. W. Walker, and H. H. Valdivia, “Activation of Ryanodine Receptors by Imperatoxin A and a Peptide Segment of the II-III Loop of the Dihydropyridine Receptor,” *J.Biol.Chem.*, vol. 274, pp. 7879–7886, 1999.

[28] H. Takeshima *et al.*, “Excitation-contraction uncoupling and muscular degeneration in mice lacking functional skeletal muscle ryanodine-receptor gene,” *Nature*, vol. 369, pp. 556–559, 1994.

[29] G. Meissner, “Isolation and characterization of two types of sarcoplasmic reticulum vesicles,” *Biochim. Biophys. Acta - Biomembr.*, vol. 389, pp. 51–68, 1975.

[30] N. Callamaras and I. Parker, “Radial localization of inositol 1,4,5-trisphosphate-sensitive Ca 2+ release sites in Xenopus oocytes resolved by axial confocal linescan imaging,” *J. Gen. Physiol.*, vol. 113, pp. 199–213, 1999.

[31] R. M. Kawamoto, J. P. Brunschwig, and A. H. Caswell, “Localization by immunoelectron microscopy of spanning protein of triad junction in terminal cisternae/triad vesicles.,” *J. Muscle Res. Cell Motil.*, vol. 9, no. 4, pp. 334–43, Aug. 1988.

[32] B. A. Block, T. Imagawa, K. P. Campbell, and C. Franzini-Armstrong, “Structural evidence for direct interaction between the molecular components of the transverse tubule/sarcoplasmic reticulum junction in skeletal muscle,” *J.Cell Biol.*, vol. 107, pp. 2587–2600, 1988.

[33] F. A. Lai, H. P. Erickson, E. Rousseau, Q. Y. Liu, and G. Meissner, “Evidence for a Ca 2+ channel within the ryanodine receptor complex from cardiac sarcoplasmic reticulum,” *Biochem. Biophys. Res. Commun.*, vol. 151, pp. 441–449, 1988.

[34] M. Inui, A. Saito, and S. Fleischer, *Isolation of the ryanodine receptor from cardiac sarcoplasmic reticulum and identity with the feet structures*. J.Biol.Chem., 1987.

[35] H. Takeshima *et al.*, “Primary structure and expression from complementary DNA of skeletal muscle ryanodine receptor,” *Nature*, vol. 339, pp. 439–445, 1989.

[36] M. Nabauer, G. Callewaert, L. Cleemann, and M. Morad, “Regulation of calcium release is gated by calcium current, not gating charge, in cardiac myocytes,” *Science (80-.).*, vol. 244, pp. 800–803, 1989.

[37] A. Fabiato, “Calcium-induced release of calcium from the cardiac sarcoplasmic reticulum,” *Am. J. Physiol.*, vol. 245, pp. C1–C14, 1983.

[38] A. Fabiato, “Simulated calcium current can both cause calcium loading in and trigger the calcium release from the sarcoplasmic reticulum of a skinned cardiac Purkinje cell,” *J. Gen. Physiol.*, vol. 85, pp. 291–320, 1985.

[39] T. L. Rich, G. A. Langer, and M. G. Klassen, “Two components of coupling calcium in single ventricular cell of rabbits and rats,” *Am. J. Physiol.*, vol. 254, pp. H937–H946, 1988.

[40] M. Endo, A. Fabiato, and F. Fabiato, “Calcium release from the sarcoplasmic reticulum,” *Physiol. Rev.*, vol. 57, no. 1, pp. 71–108, 1977.

[41] A. Fabiato and F. Fabiato, “Contractions induced by a calcium-triggered release of calcium from the sarcoplasmic reticulum of single skinned cardiac cells.,” *J. Physiol.*, vol. 249, no. 3, pp. 469–95, Aug. 1975.

[42] M. Nabauer, G. C. Ellis-Davies, J. H. Kaplan, and M. Morad, “Modulation of Ca2+ channel selectivity and cardiac contraction by photorelease of Ca2+,” *Am. J. Physiol.*, vol. 256, pp. H916–H920, 1989.

[43] K. Narita, T. Akita, J. Hachisuka, S. M. Huang, K. Ochi, and K. Kuba, “Functional coupling of Ca 2+ channels to ryanodine receptors at presynaptic terminals - Amplification of exocytosis and plasticity,” *J. Gen. Physiol.*, vol. 115, pp. 519–532, 2000.

[44] D. M. Bers, “Cardiac excitation-contraction coupling,” *Nature*, vol. 415, pp. 198–205, 2002.

[45] K. Ito *et al.*, “Deficiency of triad junction and contraction in mutant skeletal muscle lacking junctophilin type 1.,” *J. Cell Biol.*, vol. 154, no. 5, pp. 1059–67, Sep. 2001.

[46] M. Nishi *et al.*, “Motor discoordination in mutant mice lacking junctophilin type 3.,” *Biochem. Biophys. Res. Commun.*, vol. 292, no. 2, pp. 318–24, Mar. 2002.

[47] A. H. Caswell, N. R. Brandt, J. P. Brunschwig, and S. Purkerson, “Localization and partial characterization of the oligomeric disulfide-linked molecular weight 95 000 protein (triadin) which binds the ryanodine and dihydropyridine receptors in skeletal muscle triadic vesicles,” *Biochemistry*, vol. 30, pp. 7507–7513, 1991.

[48] B. C. Knollmann, “New roles of calsequestrin and triadin in cardiac muscle,” *J. Physiol.*, vol. 587, no. 13, pp. 3081–3087, Jul. 2009.

[49] N. Chopra *et al.*, “Ablation of triadin causes loss of cardiac Ca2+ release units, impaired excitation-contraction coupling, and cardiac arrhythmias.,” *Proc. Natl. Acad. Sci. U. S. A.*, vol. 106, no. 18, pp. 7636–41, May 2009.

[50] M. Shimuta, S. Komazaki, M. Nishi, M. Iino, K. Nakagawara, and H. Takeshima, “Structure and expression of mitsugumin29 gene.,” *FEBS Lett.*, vol. 431, no. 2, pp. 263–7, Jul. 1998.

[51] H. Takeshima *et al.*, “Mitsugumin29, a novel synaptophysin family member from the triad junction in skeletal muscle,” *Biochem. J.*, vol. 331, pp. 317–322, 1998.

[52] M. A. P. Brotto, R. Y. Nagaraj, L. S. Brotto, H. Takeshima, J. J. Ma, and T. M. Nosek, “Defective maintenance of intracellular Ca2+ homeostasis is linked to increased muscle fatigability in the MG29 null mice.,” *Cell Res.*, vol. 14, no. 5, pp. 373–8, Oct. 2004.

[53] S. Dally, E. Corvazier, R. Bredoux, R. Bobe, and J. Enouf, “Multiple and diverse coexpression, location, and regulation of additional SERCA2 and SERCA3 isoforms in nonfailing and failing human heart.,” *J. Mol. Cell. Cardiol.*, vol. 48, no. 4, pp. 633–44, Apr. 2010.

[54] M. Periasamy, P. Bhupathy, and G. J. Babu, “Regulation of sarcoplasmic reticulum Ca2+ ATPase pump expression and its relevance to cardiac muscle physiology and pathology.,” *Cardiovasc. Res.*, vol. 77, no. 2, pp. 265–73, Jan. 2008.

[55] E. Carafoli, “Calcium pump of the plasma membrane,” *Physiol. Rev.*, vol. 71, pp. 129–153, 1991.

[56] E. E. Strehler and D. A. Zacharias, “Role of alternative splicing in generating isoform diversity among plasma membrane calcium pumps.,” *Physiol. Rev.*, vol. 81, no. 1, pp. 21–50, Jan. 2001.

[57] M. P. Blaustein and W. J. Lederer, “Sodium calcium exchange: Its physiological implications,” *Physiol. Rev.*, vol. 79, pp. 763–854, 1999.

[58] C. M. Terracciano, A. I. Souza, K. D. Philipson, and K. T. MacLeod, “Na+-Ca2+ exchange and sarcoplasmic reticular Ca2+ regulation in ventricular myocytes from transgenic mice overexpressing the Na+-Ca2+ exchanger.,” *J. Physiol.*, vol. 512 (Pt 3), pp. 651–67, Nov. 1998.

[59] R. H. Adrian and L. D. Peachey, “Reconstruction of the action potential of frog sartorius muscle.,” *J. Physiol.*, vol. 235, no. 1, pp. 103–31, Nov. 1973.

[60] J. Vergara, F. Bezanilla, and B. M. Salzberg, “Nile blue fluorescence signals from cut single muscle fibers under voltage or current clamp conditions.,” *J. Gen. Physiol.*, vol. 72, no. 6, pp. 775–800, Dec. 1978.

[61] P. Labarca and C. Miller, “A K+-selective, three-state channel from fragmented sarcoplasmic reticulum of frog leg muscle,” *J. Membr. Biol.*, vol. 61, pp. 31–38, 1981.

[62] G. Meissner, “Monovalent ion and calcium ion fluxes in sarcoplasmic reticulum,” *Mol. Cell. Biochem.*, vol. 55, no. 1, pp. 65–82, 1983.

[63] A. M. Garcia and C. Miller, “Channel mediated monovalent cation-fluxes in isolated sarcoplasmic reticulum vesicles,” *J. Gen. Physiol.*, vol. 83, pp. 819–839, 1984.

[64] C. Miller, R. L. Rosenberg, and R. L. Rosenbcrg, “A voltage-gated cation conductance channel from fragmented sarcoplasmic reticulum. Effects of transition metal ions,” *Biochemistry*, vol. 18, pp. 1138–1145, 1979.

[65] A. V Somlyo, H. Gonzalez-Serratos, H. Shuman, G. McClellan, and A. P. Somlyo, “Calcium release and ionic changes in the sarcoplasmic reticulum of tetanized muscle: an electron probe study,” *J. Cell Biol.*, vol. 90, pp. 577–594, 1981.

[66] R. H. Fink and C. Veigel, “Calcium uptake and release modulated by counter-ion conductances in the sarcoplasmic reticulum of skeletal muscle,” *Acta Physiol. Scand.*, vol. 156, no. 3, pp. 387–396, 1996.

[67] D. Gillespie and M. Fill, “Intracellular Calcium Release Channels Mediate Their Own Countercurrent: The Ryanodine Receptor Case Study,” *Biophys. J.*, vol. 95, no. 8, pp. 3706–3714, Oct. 2008.

[68] C. W. Abramcheck and P. M. Best, “Physiological role and selectivity of the in situ potassium channel of the sarcoplasmic reticulum in skinned frog skeletal muscle fibers,” *J. Gen. Physiol.*, vol. 93, pp. 1–21, 1989.

[69] A. F. Dulhunty, P. R. Junankar, K. R. Eager, G. P. Ahern, and D. R. Laver, “Ion channels in the sarcoplasmic reticulum of striated muscle,” *Acta Physiol. Scand.*, vol. 156, pp. 375–385, 1996.

[70] H. Oetliker, “Energetical considerations related to calcium release from the sarcoplasmic reticulum in skeletal muscle.,” *Biomed. Biochim. Acta*, vol. 48, no. 5–6, pp. S313-8, 1989.

[71] A. Szewczyk, “The intracellular potassium and chloride channels: properties, pharmacology and function (review).,” *Mol. Membr. Biol.*, vol. 15, no. 2, pp. 49–58.

[72] C. Miller, “Voltage-gated cation conductance channel from fragmented sarcoplasmic reticulum: steady-state electrical properties.,” *J. Membr. Biol.*, vol. 40, no. 1, pp. 1–23, Apr. 1978.

[73] D. McKinley and G. Meissner, “Evidence for a K + , Na + permeable channel in sarcoplasmic reticulum,” *J. Membr. Biol.*, vol. 44, pp. 159–186, 1978.

[74] T. Kometani and M. Kasai, “Ionic permeability of sarcoplasmic reticulum vesicles measured by light scattering method.,” *J. Membr. Biol.*, vol. 41, no. 4, pp. 295–308, Jul. 1978.

[75] R. Coronado, R. L. Rosenberg, and C. Miller, “Ionic selectivity, saturation, and block in a K+-selective channel from sarcoplasmic reticulum.,” *J. Gen. Physiol.*, vol. 76, no. 4, pp. 425–46, Oct. 1980.

[76] C. Miller, “Integral membrane channels: studies in model membranes.,” *Physiol. Rev.*, vol. 63, no. 4, pp. 1209–42, Oct. 1983.

[77] S. Cukierman, G. Yellen, and C. Miller, “The K+ channel of sarcoplasmic reticulum. A new look at Cs+ block.,” *Biophys. J.*, vol. 48, no. 3, pp. 477–84, Sep. 1985.

[78] P. Stein and P. Palade, “Sarcoballs: Direct access to sarcoplasmic reticulum Ca 2+ channels in skinned frog muscle fibers,” *Biophys. J.*, vol. 54, pp. 357–363, 1988.

[79] G. D. Hals, P. G. Stein, and P. T. Palade, “Single channel characteristics of a high conductance anion channel in "sarcoballs".,” *J. Gen. Physiol.*, vol. 93, no. 3, pp. 385–410, Mar. 1989.

[80] J. Wang and P. M. Best, “Characterization of the potassium channel from frog skeletal muscle sarcoplasmic reticulum membrane,” *J. Physiol.*, vol. 477, no. 1994, pp. 279–290, 1994.

[81] M. Yazawa *et al.*, “TRIC channels are essential for Ca2+ handling in intracellular stores.,” *Nature*, vol. 448, no. 7149, pp. 78–82, Jul. 2007.

[82] R. H. A. Fink and D. G. Stephenson, “Ca 2+ -movements in muscle modulated by the state of K + -channels in the sarcoplasmic reticulum membranes,” *Pflugers Arch. Eur. J. Physiol.*, vol. 409, pp. 374–380, 1987.

[83] D. Yamazaki *et al.*, “Essential role of the TRIC-B channel in Ca2+ handling of alveolar epithelial cells and in perinatal lung maturation.,” *Development*, vol. 136, no. 14, pp. 2355–61, Jul. 2009.

[84] D. Yamazaki *et al.*, “TRIC-A channels in vascular smooth muscle contribute to blood pressure maintenance,” *Cell Metab.*, vol. 14, no. 2, pp. 231–241, Aug. 2011.

[85] X. Zhao *et al.*, “Ca2+ overload and sarcoplasmic reticulum instability in tric-a null skeletal muscle.,” *J. Biol. Chem.*, vol. 285, no. 48, pp. 37370–37376, Nov. 2010.

[86] E. Rousseau, M. Roberson, and G. Meissner, “Properties of single chloride selective channel from sarcoplasmic reticulum,” *Eur. Biophys. J.*, vol. 16, pp. 143–151, 1988.

[87] A. V Somlyo, G. McClellan, H. Gonzalez-Serratos, and A. P. Somlyo, “Electron probe X-ray microanalysis of post-tetanic Ca2+ and Mg2+ movements across the sarcoplasmic reticulum in situ,” *J. Biol. Chem.*, vol. 260, no. 11, pp. 6801–6807, 1985.

[88] F. Kamp, P. Donoso, and C. Hidalgo, “Changes in luminal pH caused by calcium release in sarcoplasmic reticulum vesicles,” *Biophys. J.*, vol. 74, no. 1, pp. 290–296, 1998.

[89] D. Gillespie, J. Giri, and M. Fill, “Reinterpreting the anomalous mole fraction effect: the ryanodine receptor case study,” *Biophys. J.*, vol. 97, no. 8, pp. 2212–2221, 2009.

[90] R. Coronado and C. Miller, “Conduction and block by organic cations in a K+-selective channel from sarcoplasmic reticulum incorporated into planar phospholipid bilayers.,” *J. Gen. Physiol.*, vol. 79, no. 4, pp. 529–47, Apr. 1982.

[91] J. A. Hill Jr., R. Coronado, and H. C. Strauss, “Potassium channel of cardiac sarcoplasmic reticulum is a multi-ion channel,” *Biophys. J.*, vol. 55, no. 1, pp. 35–45, 1989.

[92] B. Tomlins and A. J. Williams, “Solubilisation and reconstitution of the rabbit skeletal muscle sarcoplasmic reticulum K+ channel into liposomes suitable for patch clamp studies,” *Pflugers Arch. (European J. Physiol.*, vol. 407, pp. 341–347, 1986.

[93] M. A. Gray, B. Tomlins, R. A. P. Montgomery, and A. J. Williams, “Structural aspects of the sarcoplasmic reticulum K + channel revealed by gallamine block,” *Biophys. J.*, vol. 54, no. 2, pp. 233–239, Aug. 1988.

[94] A. J. Williams and B. Tomlins, “Solubilization and reconstitution of the K + -selective channel of rabbit skeletal muscle sarcoplasmic reticulum,” *Biochem. Soc. Trans.*, vol. 13, pp. 1247–1248, 1985.

[95] J. A. Fox and S. Ciani, “Experimental and theoretical studies on Tl + interactions with the cation-selective channel of the sarcoplasmic reticulum,” *J. Membr. Biol.*, vol. 84, pp. 9–23, 1985.

[96] B. Tomlins, A. J. Williams, and R. A. P. Montgomery, “The characterization of a monovalent cation selective channel of mammalian cardiac muscle sarcoplasmic reticulum,” *J. Membr. Biol.*, vol. 80, pp. 191–199, 1984.

[97] S. J. Pitt *et al.*, “Charade of the SR K+-channel: two ion-channels, TRIC-A and TRIC-B, masquerade as a single K+-channel.,” *Biophys. J.*, vol. 99, no. 2, pp. 417–26, Jul. 2010.

[98] Q. Y. Liu and H. C. Strauss, “Blockade of cardiac sarcoplasmic reticulum K + channel by Ca 2+ : Two-binding-site model of blockade,” *Biophys. J.*, vol. 60, pp. 198–203, 1991.

[99] A. Uehara, M. Yasukochi, and I. Imanaga, “Calcium modulation of single SR potassium channel currents in heart muscle,” *J. Mol. Cell. Cardiol.*, vol. 26, pp. 195–202, 1994.

[100] R. Coronado and C. Miller, “Decamethonium and hexamethonium block K+ channels of sarcoplasmic reticulum,” *Nature*, vol. 288, no. 5790, pp. 495–497, 1980.

[101] Q. Y. Liu, R. L. Rasmusson, Q. X. Liu, and H. C. Strauss, “Voltage-dependent, open channel blockade of the cardiac sarcoplasmic reticulum potassium channel by 4-aminopyridine.,” *Can. J. Cardiol.*, vol. 14, no. 2, pp. 275–80, Feb. 1998.

[102] C. Miller, “Bis-quaternary ammonium blockers as structural probes of the sarcoplasmic reticulum K+ channel.,” *J. Gen. Physiol.*, vol. 79, no. 5, pp. 869–91, May 1982.

[103] J. A. Fox, “Conductance and selectivity properties of a substate of the rabbit sarcoplasmic reticulum channel,” *Biophys. J.*, vol. 47, pp. 573–576, 1985.

[104] A. Matyjaszkiewicz *et al.*, “Subconductance Gating and Voltage Sensitivity of Sarcoplasmic Reticulum K+ Channels: A Modeling Approach,” *Biophys. J.*, vol. 109, no. 2, pp. 265–276, 2015.

[105] E. Venturi *et al.*, “TRIC-B channels display labile gating: evidence from the TRIC-A knockout mouse model.,” *Pflugers Arch.*, vol. 465, no. 8, pp. 1135–48, Aug. 2013.

[106] E. Venturi, R. Sitsapesan, D. Yamazaki, and H. Takeshima, “TRIC channels supporting efficient Ca2+ release from intracellular stores,” *Pflügers Arch. - Eur. J. Physiol.*, vol. 465, no. 2, pp. 1–9, Feb. 2012.

[107] A. Uehara, M. Yasukohchi, S. Ogata, and I. Imanaga, “Activation by intracellular calcium of a potassium channel in cardiac sarcoplasmic reticulum,” *Pflugers Arch. Eur. J. Physiol.*, vol. 417, pp. 651–653, 1991.

[108] R. Shaheen *et al.*, “Study of autosomal recessive osteogenesis imperfecta in Arabia reveals a novel locus defined by *TMEM38B* mutation,” *J. Med. Genet.*, vol. 49, no. 10, pp. 630–635, Oct. 2012.

[109] E. Rubinato *et al.*, “A novel deletion mutation involving TMEM38B in a patient with autosomal recessive osteogenesis imperfecta,” *Gene*, vol. 545, no. 2, pp. 290–292, Jul. 2014.

[110] M. Volodarsky *et al.*, “A deletion mutation in TMEM38B associated with autosomal recessive osteogenesis imperfecta.,” *Hum. Mutat.*, vol. 34, no. 4, pp. 582–6, Apr. 2013.

[111] G. Kasuya *et al.*, “Crystal structures of the TRIC trimeric intracellular cation channel orthologues,” *Cell Res.*, vol. 26, no. 12, pp. 1288–1301, Dec. 2016.

[112] H. Yang, M. Hu, J. Guo, X. Ou, T. Cai, and Z. Liu, “Pore architecture of TRIC channels and insights into their gating mechanism,” *Nature*, vol. 538, no. 7626, pp. 537–541, Oct. 2016.

[113] M. Su *et al.*, “Structural basis for conductance through TRIC cation channels,” *Nat. Commun.*, vol. 8, 2017.

[114] A. L. Silverio and M. H. Saier Jr., “Bioinformatic characterization of the trimeric intracellular cation-specific channel protein family,” *J. Membr. Biol.*, vol. 241, no. 2, pp. 77–101, 2011.

[115] S. R. M. Holmberg and A. J. Williams, “Single channel recordings from human cardiac sarcoplasmic reticulum,” *Circ. Res.*, vol. 65, pp. 1445–1449, 1989.

[116] E. Rousseau, “Single chloride-selective channel from cardiac sarcoplasmic reticulum studied in planar lipid bilayers.,” *J. Membr. Biol.*, vol. 110, no. 1, pp. 39–47, Aug. 1989.

[117] T. Ide, H. Sakamoto, T. Morita, T. Taguchi, and M. Kasai, “Purification of a Cl-(-)channel protein of sarcoplasmic reticulum by assaying the channel activity in the planar lipid bilayer system.,” *Biochem. Biophys. Res. Commun.*, vol. 176, no. 1, pp. 38–44, Apr. 1991.

[118] C. Townsend and R. L. Rosenberg, “Characterization of a chloride channel reconstituted from cardiac sarcoplasmic reticulum,” *J. Membr. Biol.*, vol. 147, pp. 121–136, 1995.

[119] A. Decrouy, M. Juteau, and E. Rousseau, “Examination of the role of phosphorylation and phospholamban in the regulation of the cardiac sarcoplasmic reticulum Cl - channel,” *J. Membr. Biol.*, vol. 146, pp. 315–326, 1995.

[120] J. I. Kourie, D. R. Laver, G. P. Ahern, and A. F. Dulhunty, “A calcium-activated chloride channel in sarcoplasmic reticulum vesicles from rabbit skeletal muscle,” *Am. J. Physiol.*, vol. 270, pp. C1675–C1686, 1996.

[121] J. I. Kourie, D. R. Laver, P. R. Junankar, P. W. Gage, and A. F. Dulhunty, “Characteristics of two types of chloride channel in sarcoplasmic reticulum vesicles from rabbit skeletal muscle,” *Biophys. J.*, vol. 70, pp. 202–221, 1996.

[122] S. Kawano, F. Nakamura, T. Tanaka, and M. Hiraoka, “Cardiac sarcoplasmic reticulum chloride channels regulated by protein kinase A,” *Circ. Res.*, vol. 71, pp. 585–589, 1992.

[123] S. Kawano and M. Hiraoka, “Protein kinase A-activated chloride channel is inhibited by the Ca 2+ -calmodulin complex in cardiac sarcoplasmic reticulum,” *Circ. Res.*, vol. 73, pp. 751–757, 1993.

[124] J. S. Smith, R. Coronado, and G. Meissner, “Single-channel calcium and barium currents of large and small conductance from sarcoplasmic reticulum,” *Biophys. J.*, vol. 50, pp. 921–928, 1986.

[125] M. Tanifuji, M. Sokabe, and M. Kasai, “An anion channel of sarcoplasmic reticulum incorporated into planar lipid bilayers. Single channel behavior and conductance,” *J. Membr. Biol.*, vol. 99, pp. 103–111, 1987.

[126] M. Sukhareva, J. Morrissette, and R. Coronado, “Mechanism of chloride-dependent release of Ca 2+ in the sarcoplasmic reticulum of rabbit skeletal muscle,” *Biophys. J.*, vol. 67, pp. 751–765, 1994.

[127] G. P. Ahern and D. R. Laver, “ATP inhibition and rectification of a Ca2+-activated anion channel in sarcoplasmic reticulum of skeletal muscle.,” *Biophys. J.*, vol. 74, no. 5, pp. 2335–51, May 1998.

[128] J. I. Kourie, “ATP-sensitive Voltage- and Calcium-dependent Chloride Channels in Sarcoplasmic Reticulum Vesicles from Rabbit Skeletal Muscle,” *J. Membr. Biol.*, vol. 157, pp. 39–51, 1997.

[129] J. I. Kourie, “pH-modulation of chloride channels from the sarcoplasmic reticulum of skeletal muscle.,” *J. Membr. Biol.*, vol. 167, no. 1, pp. 73–83, Jan. 1999.

[130] S. Kawano, A. Kuruma, Y. Hirayama, and M. Hiraoka, “Anion permeability and conduction of adenine nucleotides through a chloride channel in cardiac sarcoplasmic reticulum,” *J.Biol.Chem.*, vol. 274, pp. 2085–2092, 1999.

[131] M. Divangahi *et al.*, “Lack of CFTR in skeletal muscle predisposes to muscle wasting and diaphragm muscle pump failure in cystic fibrosis mice.,” *PLoS Genet.*, vol. 5, no. 7, p. e1000586, Jul. 2009.

[132] A. A. L. B. WELSH, M. J., L.-C. TSUI, T. F. BOAT, “Cystic fibrosis,” in *The Metabolic and Molecular Basis of Inherited Disease*, 1995, pp. 3799–3876.

[133] D. N. Sheppard and M. J. Welsh, “Structure and function of the CFTR chloride channel.,” *Physiol. Rev.*, vol. 79, no. 1 Suppl, pp. S23-45, Jan. 1999.

[134] V. Shoshan-Barmatz *et al.*, “VDAC/porin is present in sarcoplasmic reticulum from skeletal muscle,” *FEBS Lett.*, vol. 386, pp. 205–210, 1996.

[135] V. Shoshan-Barmatz and D. Gincel, “The voltage-dependent anion channel: characterization, modulation, and role in mitochondrial function in cell life and death.,” *Cell Biochem. Biophys.*, vol. 39, no. 3, pp. 279–92, 2003.

[136] M. J. Sampson, R. S. Lovell, D. B. Davison, and W. J. Craigen, “A Novel Mouse Mitochondrial Voltage-Dependent Anion Channel Gene Localizes to Chromosome 8,” *Genomics*, vol. 36, no. 1, pp. 192–196, Aug. 1996.

[137] K. Zeth, “Structure and evolution of mitochondrial outer membrane proteins of β-barrel topology,” *Biochim. Biophys. Acta - Bioenerg.*, vol. 1797, no. 6–7, pp. 1292–1299, Jun. 2010.

[138] D. C. Bay, M. Hafez, M. J. Young, and D. A. Court, “Phylogenetic and coevolutionary analysis of the β-barrel protein family comprised of mitochondrial porin (VDAC) and Tom40,” *Biochim. Biophys. Acta - Biomembr.*, vol. 1818, no. 6, pp. 1502–1519, Jun. 2012.

[139] V. Shoshan-Barmatz and A. Israelson, “The voltage-dependent anion channel in endoplasmic/sarcoplasmic reticulum: characterization, modulation and possible function.,” *J. Membr. Biol.*, vol. 204, no. 2, pp. 57–66, Mar. 2005.

[140] S. J. Harrop *et al.*, “Crystal structure of a soluble form of the intracellular chloride ion channel CLIC1 (NCC27) at 1.4-A resolution.,” *J. Biol. Chem.*, vol. 276, no. 48, pp. 44993–5000, Nov. 2001.

[141] B. A. Cromer, C. J. Morton, P. G. Board, and M. W. Parker, “From glutathione transferase to pore in a CLIC.,” *Eur. Biophys. J.*, vol. 31, no. 5, pp. 356–64, Sep. 2002.

[142] R. Tonini *et al.*, “Functional characterization of the NCC27 nuclear protein in stable transfected CHO-K1 cells.,” *FASEB J.*, vol. 14, no. 9, pp. 1171–8, Jun. 2000.

[143] B. M. Tulk, P. H. Schlesinger, S. A. Kapadia, and J. C. Edwards, “CLIC-1 functions as a chloride channel when expressed and purified from bacteria.,” *J. Biol. Chem.*, vol. 275, no. 35, pp. 26986–93, Sep. 2000.

[144] S. M. Valenzuela *et al.*, “The nuclear chloride ion channel NCC27 is involved in regulation of the cell cycle.,” *J. Physiol.*, vol. 529 Pt 3, pp. 541–52, Dec. 2000.

[145] K. Warton *et al.*, “Recombinant CLIC1 (NCC27) assembles in lipid bilayers via a pH-dependent two-state process to form chloride ion channels with identical characteristics to those observed in Chinese hamster ovary cells expressing CLIC1.,” *J. Biol. Chem.*, vol. 277, no. 29, pp. 26003–11, Jul. 2002.

[146] H. Singh and R. H. Ashley, “Redox regulation of CLIC1 by cysteine residues associated with the putative channel pore.,” *Biophys. J.*, vol. 90, no. 5, pp. 1628–38, Mar. 2006.

[147] D. A. Board PG, Coggan M, Watson S, Gage PW, “CLIC-2 modulates cardiac ryanodine receptor Ca2+ release channels,” *Int. J. Biochem. Cell Biol.*, vol. 36, no. 8, pp. 1599–1612, Aug. 2004.

[148] A. F. Dulhunty, P. Pouliquin, M. Coggan, P. W. Gage, and P. G. Board, “A recently identified member of the glutathione transferase structural family modifies cardiac RyR2 substate activity, coupled gating and activation by Ca2+ and ATP.,” *Biochem. J.*, vol. 390, no. Pt 1, pp. 333–43, Aug. 2005.

[149] J. F. Cotten and M. J. Welsh, “Covalent modification of the regulatory domain irreversibly stimulates cystic fibrosis transmembrane conductance regulator.,” *J. Biol. Chem.*, vol. 272, no. 41, pp. 25617–22, Oct. 1997.

[150] T. Yamazaki *et al.*, “Augmentation of drug-induced cell death by ER protein BRI3BP.,” *Biochem. Biophys. Res. Commun.*, vol. 362, no. 4, pp. 971–5, Nov. 2007.

[151] N. K. & H. T. Miyuki Nishi, Yu Takahashi, “Reduced function of fast-twitch muscle fibers in Mg23-Knockout mice,” in *GRC conference, Les Diablerets, Switzerland*, 2017, p. Poster presentation.

[152] F. Vanden Abeele *et al.*, “Functional implications of calcium permeability of the channel formed by pannexin 1,” *J. Cell Biol.*, vol. 174, no. 4, pp. 535–546, Aug. 2006.

[153] C. Ambrosi *et al.*, “Pannexin1 and Pannexin2 Channels Show Quaternary Similarities to Connexons and Different Oligomerization Numbers from Each Other,” *J. Biol. Chem.*, vol. 285, no. 32, pp. 24420–24431, Aug. 2010.

[154] M. Ishikawa, T. Iwamoto, T. Nakamura, A. Doyle, S. Fukumoto, and Y. Yamada, “Pannexin 3 functions as an ER Ca^{2+} channel, hemichannel, and gap junction to promote osteoblast differentiation,” *J. Cell Biol.*, vol. 193, no. 7, pp. 1257–1274, Jun. 2011.

[155] H. Tu *et al.*, “Presenilins Form ER Ca2+ Leak Channels, a Function Disrupted by Familial Alzheimer’s Disease-Linked Mutations,” *Cell*, vol. 126, no. 5, pp. 981–993, Sep. 2006.

[156] H. Zhang, S. Sun, A. Herreman, B. De Strooper, and I. Bezprozvanny, “Role of Presenilins in Neuronal Calcium Homeostasis,” *J. Neurosci.*, vol. 30, no. 25, pp. 8566–8580, Jun. 2010.

[157] X.-P. Dong, X. Wang, and H. Xu, “TRP channels of intracellular membranes,” *J. Neurochem.*, vol. 113, no. 2, pp. 313–328, Apr. 2010.

[158] T. Yamazaki, N. Sasaki, M. Nishi, and H. Takeshima, “Facilitation of DNA damage-induced apoptosis by endoplasmic reticulum protein mitsugumin23,” *Biochem. Biophys. Res. Commun.*, vol. 392, no. 2, pp. 196–200, Feb. 2010.

[159] A. Yamashita, T. Taniwaki, Y. Kaikoi, and T. Yamazaki, “Protective role of the endoplasmic reticulum protein mitsugumin23 against ultraviolet C-induced cell death,” *FEBS Lett.*, vol. 587, no. 9, pp. 1299–1303, May 2013.

[160] I. K. H. Poon *et al.*, “Unexpected link between an antibiotic, pannexin channels and apoptosis,” *Nature*, vol. 507, no. 7492, pp. 329–334, Mar. 2014.

[161] G. K. Atkin-Smith *et al.*, “A novel mechanism of generating extracellular vesicles during apoptosis via a beads-on-a-string membrane structure,” *Nat. Commun.*, vol. 6, p. 7439, Jun. 2015.

[162] M. Nishi, S. Komazaki, M. Iino, K. Kangawa, and H. Takeshima, “Mitsugumin23, a novel transmembrane protein on endoplasmic reticulum and nuclear membranes,” *FEBS Lett.*, vol. 432, pp. 191–196, 1998.

[163] L. Lin, Y. Wu, C. Li, and S. Zhao, “Cloning, tissue expression pattern, and chromosome location of a novel human gene BRI3BP.,” *Biochem. Genet.*, vol. 39, no. 11–12, pp. 369–77, Dec. 2001.

[164] E. Venturi *et al.*, “Mitsugumin 23 Forms a Massive Bowl-Shaped Assembly and Cation-Conducting Channel,” *Biochemistry*, vol. 50, no. 13, pp. 2623–2632, Apr. 2011.

[165] E. Venturi *et al.*, “Mitsugumin 23 forms a massive bowl-shaped assembly and cation-conducting channel,” *Biochemistry*, vol. 50, no. 13, pp. 2623–2632, 2011.

[166] L. R. Jones, H. R. Besch Jr., J. W. Fleming, M. M. McConnaughey, and A. M. Watanabe, “Separation of Vesicles of Cardiac Sarcolemma from Vesicles of Cardiac Sarcoplasmic Reticulum,” *J. Biol. Chem.*, vol. 254, pp. 530–539, 1979.

[167] M. M. Bradford, “A rapid and sensitive method for the quantitation of microgram quantities of protein utilizing the principle of protein-dye binding,” *Anal. Biochem.*, vol. 72, no. 1–2, pp. 248–254, May 1976.

[168] P. Mueller, D. O. Rudin, H. T. Tien, and W. C. Wescott, “Resconstitution of excitable cell membrane structure in vitro,” *Circulation*, vol. 26, pp. 1167–1171, 1962.

[169] V. A. Parsegian, “Ion-membrane interactions as structural forces.,” *Ann. N. Y. Acad. Sci.*, vol. 264, pp. 161–71, Dec. 1975.

[170] D. M. Andrews, E. D. Manev, and D. A. Haydon, “Composition and energy relationships for some thin lipid films, and the chain conformation in monolayers at liquid-liquid interfaces,” *Spec. Discuss. Faraday Soc.*, vol. 1, no. 0, p. 46, Jan. 1970.

[171] C. Miller, “Ion channel structure and function,” *Science (80-.).*, vol. 258, pp. 240–241, 1992.

[172] A. L. Hodgkin and A. F. Huxley, “A quantitative description of membrane current and its application to conduction and excitation in nerve,” *J. Physiol.*, vol. 117, pp. 500–544,

1952.

[173] M. H. Akabas, F. S. Cohen, and A. Finkelstein, “Separation of the osmotically driven fusion event from vesicle-planar membrane attachment in a model system for exocytosis,” *J.Cell Biol.*, vol. 98, pp. 1063–1071, 1984.

[174] J. Zimmerberg, F. S. Cohen, and A. Finkelstein, “Fusion of phospholipid vesicles with planar phospholipid bilayer membranes. I. Discharge of vesicular contents across the planar membrane,” *J. Gen. Physiol.*, vol. 75, pp. 241–250, 1980.

[175] A. Saito, S. Seiler, A. Chu, and S. Fleischer, “Preparation and morphology of sarcoplasmic reticulum terminal cisternae from rabbit skeletal muscle.,” *J. Cell Biol.*, vol. 99, no. 3, pp. 875–85, Sep. 1984.

[176] R. Sitsapesan and A. J. Williams, “Gating of the native and purified cardiac SR Ca(2+)-release channel with monovalent cations as permeant species.,” *Biophys. J.*, vol. 67, no. 4, pp. 1484–94, Oct. 1994.

[177] P. H. Barry and J. W. Lynch, “Liquid junction potentials and small cell effects in patch-clamp analysis,” *J. Membr. Biol.*, vol. 121, pp. 101–117, 1991.

[178] D. M. Bers, “A simple method for the accurate determination of free [Ca] in Ca-EGTA solutions,” *Am. J. Physiol.*, vol. 242, pp. 404–408, 1982.

[179] H.Nyquist, “Certain topics in telegraph transmission theory,” *Trans. A.I.E.E.*, vol. 47(2), pp. 617–644, 1928.

[180] C. E. Shannon, “A Mathematical Theory of Communication,” *Bell Syst. Tech. J.*, vol. 27, no. 4, pp. 623–656, Oct. 1948.

[181] F. Qin, “Restoration of single-channel currents using the segmental k-means method based on hidden Markov modeling,” *Biophys. J.*, vol. 86, no. 3, pp. 1488–1501, 2004.

[182] S. H. Chung, J. B. Moore, L. G. Xia, L. S. Premkumar, and P. W. Gage, “Characterization of single channel currents using digital signal processing techniques based on Hidden Markov Models.,” *Philos. Trans. R. Soc. Lond. B. Biol. Sci.*, vol. 329, no. 1254, pp. 265–85, Sep. 1990.

[183] J. Forney GD, “The viterbi algorithm,” in *Proceedings of the IEEE*, 1973, p. 61(3):268-78.

[184] D. Colquhoun and A. G. Hawkes, “The principles of the stochastic interpretation of Ion-channel mechanisms,” in *Single-channel recording*, vol. 2, B. Sakmann and E. Neher, Eds. New York & London: Plenum, 1995, pp. 135–175.

[185] A. R. Stepanyuk, A. L. Borisyuk, and P. V Belan, “Efficient maximum likelihood estimation of kinetic rate constants from macroscopic currents.,” *PLoS One*, vol. 6, no. 12, p. e29731, 2011.

[186] P. E. D. R. O. Labarca, R. Coronado, C. Miller, R. Coronado, and C. Miller, “Thermodynamic and kinetic studies of the gating behaviour of a K + -selective channel from the sarcoplasmic reticulum membrane,” *J. Gen. Physiol.*, vol. 76, no. 4, pp. 397–424, Oct. 1980.

[187] A. Tinker, A. R. G. Lindsay, and A. J. Williams, “Cation conduction in the cardiac sarcoplasmic reticulum calcium-release channel under physiological and pathophysiological conditions,” *Cardiovasc. Res.*, vol. 27, pp. 1820–1825, 1993.

[188] T. Guo *et al.*, “Sarcoplasmic reticulum K(+) (TRIC) channel does not carry essential countercurrent during Ca(2+) release,” *Biophys. J.*, vol. 105, no. 5, pp. 1151–1160, 2013.

[189] F. O. Brien, “Biophysical characterisation of the mechanisms regulating sarcoplasmic reticulum K + channel gating,” University of Oxford, 2015.

[190] F. O. Brien, “Biophysical characterisation of the mechanisms regulating sarcoplasmic reticulum K + channel gating,” no. November, 2015.

[191] A. Tinker, A. R. G. Lindsay, and A. J. Williams, “Cation conduction in the calcium release channel of the cardiac sarcoplasmic reticulum under physiological and pathophysiological conditions,” pp. 1820–1825, 1993.

[192] B. Hille, *Ionic channels of excitable membranes*, Third., vol. 2. Sunderland, MA.: Sinauer, 1992.

[193] Q. Liu and H. C. Strauss, “two-binding-site model of blockade,” vol. 60, no. July, pp. 198–203, 1991.

[194] M. Barann, K. Schmidt, M. Göthert, B. W. Urban, and H. Bönisch, “Influence of sodium substitutes on 5-HT-mediated effects at mouse 5-HT3 receptors.,” *Br. J. Pharmacol.*, vol. 142, no. 3, pp. 501–8, Jun. 2004.

[195] S. El-Ajouz *et al.*, “Dampened activity of ryanodine receptor channels in mutant skeletal muscle lacking TRIC-A.,” *J. Physiol.*, vol. 595, no. 14, pp. 4769–4784, Jul. 2017.

[196] J. Patlak and R. Horn, “Effect of N-Bromoacetamide on Single Sodium Channel Currents in Excised Membrane Patches.”

[197] K. Witschas *et al.*, “Dampened Activity of Single Ryanodine Receptor Channels in Mice Devoid of TRIC-A,” *Biophys. J.*, vol. 110, no. 3, p. 266a, Feb. 2016.

[198] F. Despa, “Endoplasmic reticulum overcrowding as a mechanism of beta-cell dysfunction in diabetes.,” *Biophys. J.*, vol. 98, no. 8, pp. 1641–8, Apr. 2010.

[199] S. R. McGuffee and A. H. Elcock, “Diffusion, Crowding & Protein Stability in a Dynamic Molecular Model of the Bacterial Cytoplasm,” *PLoS Comput. Biol.*, vol. 6, no. 3, p. e1000694, Mar. 2010.

[200] W. Wood, *The Nematode Caenorhabditis elegans*. Cold Spring Harbor Laboratory Press, 1988.

[201] A. Accardi, L. Kolmakova-Partensky, C. Williams, and C. Miller, “Ionic currents mediated by a prokaryotic homologue of CLC Cl- channels.,” *J. Gen. Physiol.*, vol. 123, no. 2, pp. 109–19, Feb. 2004.

[202] S. Sriwongsitanont and M. Ueno, “Effect of Freeze-Thawing Process on the Size and Lamellarity of PEG-Lipid Liposomes,” *Open Colloid Sci. J.*, vol. 4, pp. 1–6, 2011.

[203] J. a Hill *et al.*, “Open-channel subconductance state of K+ channel from cardiac sarcoplasmic reticulum.,” *Am. J. Physiol.*, vol. 258, no. 1 Pt 2, pp. H159-64, Jan. 1990.

[204] M. L. Chapman, H. M. A. VanDongen, and A. M. J. Vandongen, “Activation-dependent subconductance levels in the drk1 K channel suggest a subunit basis for ion permeation and gating,” *Biophys. J.*, vol. 72, pp. 708–719, 1997.

[205] L. Shang, S. V. Ranson, and S. J. Tucker, “Kir5.1 underlies long-lived subconductance levels in heteromeric Kir4.1/Kir5.1 channels from Xenopus tropicalis,” *Biochem. Biophys. Res. Commun.*, vol. 388, no. 3, pp. 501–505, Oct. 2009.

[206] J. Zheng and F. J. Sigworth, “Intermediate conductances during deactivation of heteromultimeric Shaker potassium channels.,” *J. Gen. Physiol.*, vol. 112, no. 4, pp. 457–74, Oct. 1998.

[207] F. Bezanilla, “The Origin of Subconductance Levels in Voltage-gated K^+ Channels,” *J. Gen. Physiol.*, vol. 126, no. 2, pp. 83–86, Aug. 2005.

[208] W. B. Ferguson, O. B. McManus, and K. L. Magleby, “Opening and closing transitions for BK channels often occur in two steps via sojourns through a brief lifetime subconductance state,” *Biophys. J.*, vol. 65, pp. 702–714, 1993.

[209] B. Hille, “Ion Channels of Excitable Membranes (Second Edition).” .

[210] R. M. Vaden, K. M. Gligorich, R. Jana, M. S. Sigman, and B. E. Welm, “The small molecule C-6 is selectively cytotoxic against breast cancer cells and its biological action is characterized by mitochondrial defects and endoplasmic reticulum stress.,” *Breast Cancer Res.*, vol. 16, no. 6, p. 472, 2014.

[211] R. M. Vaden, “A CHEMICAL BIOLOGY APPROACH TOWARDS THE DEVELOPMENT OF STRATEGIES TO TARGET DRUG REFRACTORY BREAST CANCER,” The University of Utah, 2015.

[212] H. Wang, Y. Liang, B. Zhang, W. Zheng, L. Xing, and M. Li, “Alkaline stress triggers an immediate calcium fluctuation in Candida albicans mediated by Rim101p and Crz1p transcription factors,” *FEMS Yeast Res.*, vol. 11, no. 5, pp. 430–439, Aug. 2011.